UNIVERSITY OF SOUTHAMPTON

Techniques, Results & Analysis of the *INTEGRAL*/IBIS Soft Gamma-Ray Survey

Elizabeth Joanne Barlow

Submitted for the degree of Doctor of Philosophy

SCHOOL OF PHYSICS AND ASTRONOMY
FACULTY OF SCIENCE

April 11, 2006

UNIVERSITY OF SOUTHAMPTON

ABSTRACT

FACULTY OF SCIENCE

SCHOOL OF PHYSICS AND ASTRONOMY

Doctor of Philosophy

Techniques, Results & Analysis of the *INTEGRAL*/IBIS Soft Gamma-Ray Survey

by Elizabeth Joanne Barlow

This thesis presents results from the soft gamma-ray survey performed with the IBIS telescope during the first three years of the *INTEGRAL* mission. Gamma-ray emission mechanisms and the types of astronomical objects emitting in the IBIS detection range are reviewed, together with the technologies developed to detect them. The imaging capability of IBIS is achieved by a coded mask aperture above the detector planes. The mask is supported by a honeycomb structure; systematic variations in reconstructed source fluxes have been found and attributed to the transparency of this structure. The instrument's response to off-axis sources has been investigated and a correction model developed using dedicated Crab observations.

For the first time, a catalogue of objects emitting in the 20–100 keV energy regime has been produced down to a limiting sensitivity of 1 mCrab. The first IBIS catalogue presents 123 sources and is superceded by a second catalogue which includes 209, the majority of which are Galactic X-ray binaries. Techniques for the production of the catalogues and survey results, including average spectral characteristics of the sources, are discussed. 25% of the these sources are currently unclassified. Analysis of one such source, the transient black hole candidate IGR J17285-2922, is presented.

The IBIS/ISGRI survey also detects a small sample of cataclysmic variable stars. A cross-correlation performed between supplementary IBIS data and a CV catalogue has revealed eight more CV detections. It is shown that IBIS is more likely to detect CVs of intermediate polar and asynchronous polar sub-types, both of which are rare classes of object.

Contents

List of Figures

List of Tables

Declaration

The work presented in this thesis has been carried out by the author whilst in canditure for a research degree at the University of Southampton between February 2003 and January 2006. The determination of the energy resolution of IBIS Compton Mode by the author, described in Chapter 3, has been published in Bird et al. (2003). The average off-axis correction developed by the author and presented in Chapter 4 has been released as part of the *INTEGRAL* OSA software v.4.0 after verification and acceptance by the *INTEGRAL* Science Data Centre. The MMM code used for the calibration work in Chapter 4 was developed at Southampton by Dave Willis and modified by the author. The work described in Chapter 5 was carried out with the IBIS Survey Team (of which the author is a member) and includes work published as part of Bird et al. (2005); (2006) and Dean et al. (2005). All of Chapter 6 has been published as Barlow et al. (2005). All other research has not previously been presented and has been performed solely by the author.

Publications:

Bird, A.J., **Barlow, E.J.**, Bassani, L., et al. "The Second IBIS/ISGRI Soft Gamma-Ray Survey Catalog" 2006 ApJ 636, 765

Dean, A.J., Bazzano, A., Hill, A.B, Stephen, J.B., Bassani, L., **Barlow, E.J.**, et al. "Global Characteristics of the first IBIS/ISGRI catalogue sources" 2005 A&A 443 485

Barlow, E.J., Bird, A.J., Clark, D.J., et al. "Detection and analysis of a new INTEGRAL hard X-ray transient, IGR J17285-2922" 2005 A&A 437L 27B

Bird, A.J., **Barlow, E.J.**, Bassani, L., et al. "The First IBIS/ISGRI Soft Gamma-Ray Galactic Plane Survey Catalog" 2004 ApJ 607L 33B

Bird, A.J., **Barlow, E.J.**, Bazzano, A., et al. "IBIS ground calibration" 2003 A&A 411L 159B

Publications:

Bird, A.J., **Barlow, E.J.**, Bassani, L., et al. "The Second IBIS/ISGRI Soft Gamma-Ray Survey Catalog" 2006 ApJ 636, 765

Dean, A.J., Bazzano, A., Hill, A.B, Stephen, J.B., Bassani, L., **Barlow, E.J.**, et al. "Global Characteristics of the first IBIS/ISGRI catalogue sources" 2005 A&A 443 485

Barlow, E.J., Bird, A.J., Clark, D.J., et al. "Detection and analysis of a new INTEGRAL hard X-ray transient, IGR J17285-2922" 2005 A&A 437L 27B

Bird, A.J., **Barlow, E.J.**, Bassani, L., et al. "The First IBIS/ISGRI Soft Gamma-Ray Galactic Plane Survey Catalog" 2004 ApJ 607L 33B

Bird, A.J., **Barlow, E.J.**, Bazzano, A., et al. "IBIS ground calibration" 2003 A&A 411L 159B

Acknowledgements

I would like to start by thanking Tony Dean for his motivating and enthusiastic supervison and for giving me the opportunity to return to academic study. I would also like to acknowledge the help and guidance of Tony (Ralph) Bird who has been unstinting in his assistance with every aspect of my work for this thesis, for which I am very grateful.

Additionally, I would like to thank all members of the Astronomy Group at Southampton, especially Remon Cornelisse for his help in understanding various neutron star related topics, Christian Knigge and Retha Pretorius for invaluable discussions about CVs and José Luis Galache for assistance with all things Lomb Scargle. Special thanks go to my office-mates Adam Hill, Vito Sguera and Manuela Molina for their individual expertise and countless entertaining discussions, Dave Willis for his much appreciated advice and humour and Vanessa Godfrey for being a great friend and dinner party host.

I am deeply grateful towards my Mum and Dad, Andrew and Katherine for their unfailing support and encouragement. I cannot imagine belonging to a more inspirational and supportive family. I would also like to thank Clare and Patrick Foss-Smith for their kindness, especially throughout the last few months. Final and greatest thanks go, as always, to my beloved Charlie, to whom this thesis is dedicated.

Chapter 1

Introduction: Gamma-ray Astronomy

1.1 Motivation and Structure of Thesis

To observe the gamma-ray sky, one must first overcome certain challenges. Not only are gamma-rays unable to be focused with conventional optics, but the opacity of the Earth's atmosphere makes the ground based study of this radiation impossible for all but the highest energies (>100 GeV). As a result of these challenges, gamma-ray astronomy has a comparatively short history and is therefore a rich and interesting area to investigate. Efforts are rewarded with insights into the most energetic of processes occurring in our Galaxy, the sources of which are reviewed in this chapter. Following on from this, Chapter 2 will detail the techniques for detecting and imaging gamma-rays and will introduce the *INTEGRAL* observatory. Over the last three years the IBIS instrument on board *INTEGRAL* has enabled new advances to be made in the imaging of the soft gamma-ray sky. Chapters 3 and 4 will concentrate on the important task of calibrating the IBIS telescope. This work is vital if meaningful results are to be gained from *INTEGRAL* data.

The unprecedented sensitivity of the imager IBIS has been instrumental in producing the most in-depth view of the sky in the 20–100 keV energy range. The first IBIS catalogue consists of guaranteed time observations along the Galactic plane and deep exposure of the Galactic centre while the second catalogue is the result of increased exposure (nearly 2 years of observations) away from the plane and improved processing and analysis techniques. These methods are discussed in Chapter 5 alongside an average spectral analysis of the global sample. It has been found, from observations with *INTEGRAL*, that close binary systems are the major contributors to the low energy gamma-ray luminosity of the Galaxy and that as a consequence of this, diffuse interstellar mechanisms are relatively unimportant. It is also found that a significant proportion of the discrete sources that are observed in the soft gamma-ray domain are of a 'new' population of sources previously unnoticed in the X-ray band. This population includes a sub-set of binaries characterised by a high level of intrinsic absorption. Chapter 6 investigates the nature of an unclassified *INTEGRAL* source discovered during the survey, IGR J17285–2922, which is a potential black hole candidate. Additionally, it is found that IBIS detects a small sample of cataclysmic variable systems, the temporal and spectral characteristics of which are investigated in Chapter 7. The final chapter will summarise the main findings of the work presented here.

The classification of photon energy ranges is to some extent arbitrary and considerable overlap is especially noted in literature between hard X-ray and soft gamma-rays, where the former can possess energies anywhere between 1 and 100 keV. Alternatively, X-ray and gamma-ray photons can be distinguished by their respective emission mechanisms, whereby the latter are described as such if they originated from nuclear processes, for example. Therefore, to avoid confusion in this thesis and to highlight the energy range of the IBIS instrument, the phrase 'soft gamma-rays' is used to refer to photons above 15 keV and extending to $\sim$100's keV.

1.2 Gamma-ray production mechanisms

- **Bremsstrahlung Radiation** - occurs from the "braking" of an electron in the electrostatic field of an atomic nucleus, ion or molecule, producing a photon. Thermal bremsstrahlung radiation is emitted when the inital energy distribution of electrons is thermal, *e.g.* in a hot ionised plasma where the distribution of the emitted photon energies reflects the initial electron energy distribution. The resulting photon spectrum can therefore be used to determine the temperature of the plasma.

- **Synchroton Radiation** - or magneto-bremsstrahlung is the relativistic case of cyclotron radiation where an energetic charged particle is accelerated in the influence of a magnetic field emitting a photon with a characteristic gyrofrequency. The resulting emission is polarised and concentrated in a narrow beam in the direction of the path of the electron. The intensity of the synchrotron radiation is dependent on the strength of the magnetic field and the energy of the accelerated particles. If the initial energy distribtion of the charged particles is a power-law, the resulting synchrotron emission will also have a power-law distribution (*i.e.* non-thermal). Pulsars (high magnetic field rotating neutron stars) are sources of high energy synchrotron radiation; the pulsar is expelling energetic electrons which interact with its magnetic field.

- **Inverse Compton Scattering** - from the interaction between an energetic electron and a photon, where energy of electron$\gg$energy of photon. This process requires high photon densities (e.g. microwave background). High energy electrons can upscatter an infra-red photon to gamma-ray energies, resulting in a power law spectrum.

- **Radioactive Decay** - produce spectral lines at the characteristic energy of the nuclear energy levels. Examples of isotopes with long lifetimes which emit gamma-rays from processes associated with stellar evolution are listed in Table 1.1.

- **Electron–Positron Annihilation** - this process forms two photons with energies equivalent to the rest mass of an electron (511 keV) $e^+ + e^- \rightarrow \gamma + \gamma$. The emission process is complicated for the positronium state where three photon decay results in a spectrum with a long tail below the 511 keV line. Positrons can be generated via nucleosynthesis in supernovae (see Table 1.1), cosmic rays interacting with interstellar medium (ISM) and pair production in pulsars and/or black holes.
- **Nuclear interactions** - collisions between cosmic rays (relativistic protons and nuclei) and atomic nuclei and molecules of the interstellar gas produce neutral pions, the decay of which produce emission >100 MeV. This is an important process in the production of diffuse gamma-ray photons.

1.3 Astrophysical Sources of Gamma-rays

The Galactic plane has been found to be a strong source of gamma-rays. The emission is derived from a large number of discrete sources and weaker truly diffuse component. This section will provide an overview of the wealth of Galactic sources emitting above 20 keV in the context of their observational characteristics. The discrete source luminosity is dominated by close binary systems which have evolved such that the compact object is a neutron star (NS), black hole (BH) or possible a white dwarf. The main aim of this thesis is to study the spectral and timing characteristics of these sources so as to better understand their underlying processes. Soft gamma-ray emission from binaries where the compact object is a white dwarf (cataclysmic variables) will be reviewed in Chapter 7. A brief description of the types of extragalactic sources is included in Sec. 1.3.4.

1.3.1 X-ray Binaries - Accretion powered emitters

Accretion of material onto a compact object as seen in X-ray binaries is the principal source of energy that leads to the production of high energy radiation in our Galaxy. The total accretion luminosity onto a compact object can be estimated by considering the gravitational potential energy E released by the accretion of mass m onto the surface of a compact object of mass M and radius R given by:

$$E_{acc} = \frac{GMm}{R} \text{ erg} \tag{1.1}$$

where the accretion luminosity for an accretion rate $\dot{m}$ is:

$$L_{acc} = \frac{GM\dot{m}}{R} \text{ erg s}^{-1} \tag{1.2}$$

At high luminosities, the accretion rate is controlled by the outward pressure transferred from the radiation on the accreting material via Thomson scattering (non-relativistic case of Compton scattering). If the outward force equals the inward gravitational force, accretion will stop. This is called the Eddington Limit which implies a limit on L for spherical accretion and can be represented by:

$$L_{Edd} = \frac{4\pi GMmc}{\sigma_e} = 1.3 \times 10^{38} \left(\frac{M}{\mathrm{M}_\odot}\right) \text{ erg } s^{-1} \tag{1.3}$$

where M is the mass of the accreting compact object, m is the mass of an accreting particle (~proton mass) and σ_e is the Thomson cross-secton for scattering electrons. By assuming that all the gravitational potential energy of the accreting material is turned into thermal energy for a system accreting at the Eddington limit, an upper limit for the spectral range of emission can be estimated. For an accreting neutron star, it is found that photons can be expected to have energies between 1 keV (based on the blackbody temperature) and 50 MeV (Frank, King &Raine 2002).

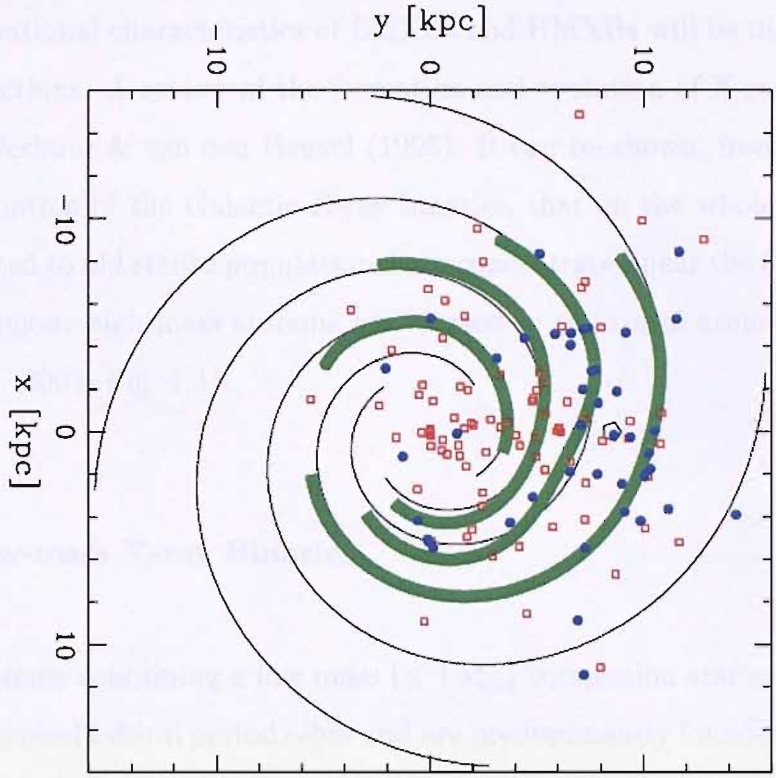

Figure 1.1: Distribution of low mass (open squares) and high mass (filled circles) X-ray binaries superimposed on spiral-armed models of the Galaxy. The Sun is marked by the pentagon *(From Grimm et al. 2002)*.

X-ray binary systems make up the dominating class of Galactic soft-gamma ray emitting objects and accrete via the following two modes:

- **Roche Lobe Overflow** - where a low mass star has evolved to fill its Roche lobe and is transferring mass via the inner Lagrangian point, forming a disk around the compact object, resulting in a low-mass X-ray binary (LMXB)
- **Stellar Wind Accretion** - a compact object orbiting a massive star captures material from the star's stellar wind (or ejected circumstellar disk in the case of emission-line B-type (Be) star), creating a high-mass X-ray binary (HMXB). Some HMXB systems can be a hybrid of stellar wind accretion and RL overflow.

The observational characteristics of LMXBs and HMXBs will be discussed in the proceeding sections. A review of the formation and evolution of X-ray binaries can be found in Verbunt & van den Heuvel (1995). It can be shown, from studying the spatial distribution of the Galactic X-ray binaries, that on the whole the low-mass systems (related to old stellar populations) are concentrated near the Galactic bulge, while the younger, high-mass systems are located in the spiral arms of the Galaxy (Grimm et al. 2002; Fig. 1.1).

1.3.1.1 Low-mass X-ray Binaries

These are systems containing a low mass ($\leq 1\,\mathrm{M}_{\odot}$) companion star orbiting around a NS or BH, typical orbital period ~hrs and are predominantly found in the Galactic bulge and in globular clusters. The compact object is accreting material via Roche lobe overflow. The Roche lobe of a star describes the volume within which matter is dominated by the gravitational pull of the star. The point at which the Roche lobes of the two stars in a binary meet is called the inner Lagrangian point (L1 in Fig. 1.2). Material is transferred from the companion star via the L1 point by an accretion stream and forms an accretion disk around the primary as a result of the conservation of angular momentum. Half of the total luminosity available from accretion is radiated by the disk which is bright in the ultraviolet (Charles & Seward 1995). X-ray and soft gamma-ray emission results from the inner, high temperature part of the disk (boundary layer) and has been detected up to 100's of keV, in many cases the emission spectrum can be described by a simple power-law model.

Spectral characteristics (in the X-ray band) of individual LMXBs with a NS as the compact object can be highly variable and can be tracked using a colour-colour diagram (CD), revealing two distinct sub-classes of LMXB: Z-type and Atoll sources according to the shape traced out by the CD (see Fig. 1.3; see van der Klis 1995

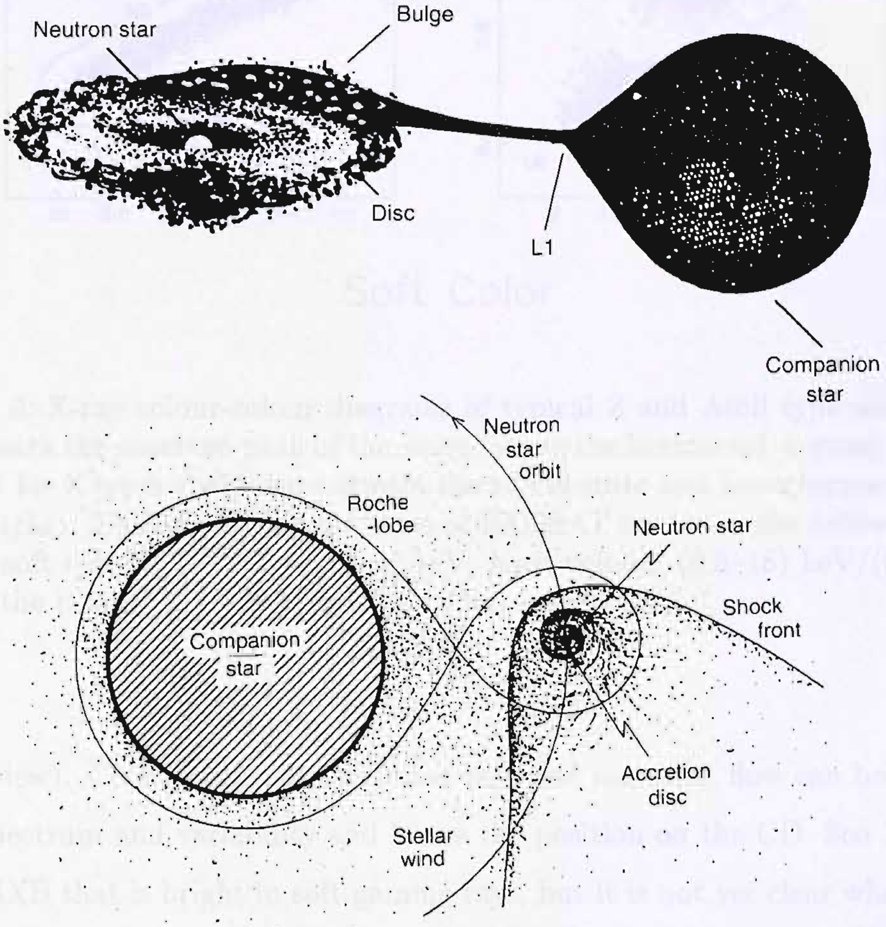

Figure 1.2: Schematic of the two types of X-ray binaries. Top: a low-mass X-ray binary, where the NS is surrounded by an accretion disk. The companion star is filling its Roche lobe and is transfering material via the inner Lagrangian point. A bulge or 'hot-spot' occurs where the accretion stream impacts the accretion disk. Bottom: a high mass star is shedding material via a powerful stellar wind which is captured by an orbiting NS. *(Picture Credit: Charles & Seward 1995, adapted from EXOSAT observatory/ESA)*

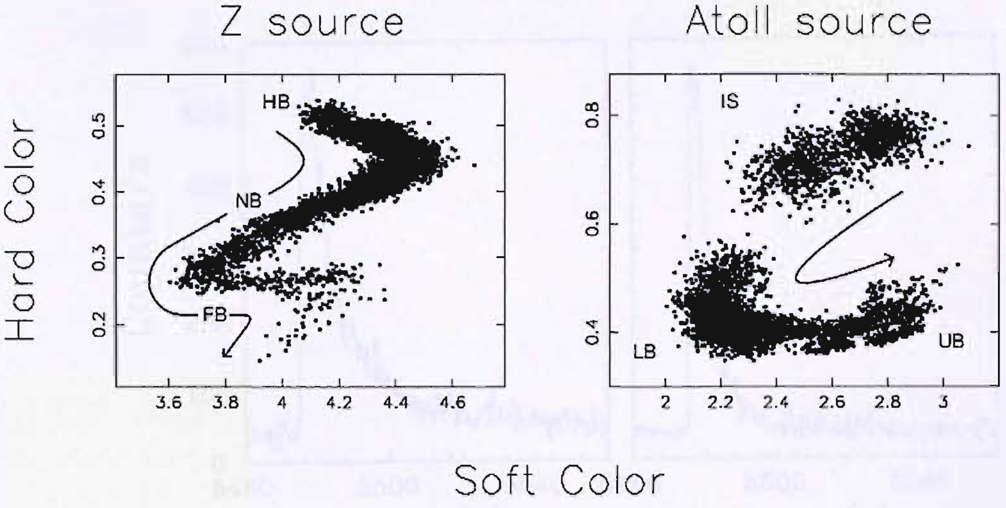

Figure 1.3: X-ray colour-colour diagrams of typical Z and Atoll type sources. The arrows mark the observed path of the source along the horizontal, normal and flaring branches for Z types (left) and between the island state and lower/upper banana in Atolls (right). The colours are the ratio of EXOSAT counts in the following energy bands - soft colour: (3–5) keV/(1–3) keV, hard colour: (6.5–18) keV/(5–6.5) keV and are the ratio of EXOSAT counts in *(Wijnands 2001).*

for a review). Changes in mass accretion rate and accretion flow can be linked the X-ray spectrum and variability and hence the position on the CD. Sco X-1 is a Z-type LMXB that is bright in soft-gamma rays, but it is not yet clear whether these spectral changes can be observed at gamma-ray energies. Such observations would help in determining the origin of the emission (thermal and non-thermal) for these objects which may be linked to the intrinsic luminosity of the source.

Many LMXB (mostly Atoll types) display bright Eddington-limited transient events, displaying a black-body spectrum. These are called Type I X-ray Bursts and are the result of build up of material on the surface of a NS (see Strohmayer & Bildsten 2003 for an in-depth account). As hydrogen is accreted on the NS it undegoes nuclear fusion burning producing a layer of helium. The helium undergoes hydrostatic compression until it reaches a critical point resulting in a thermonuclear

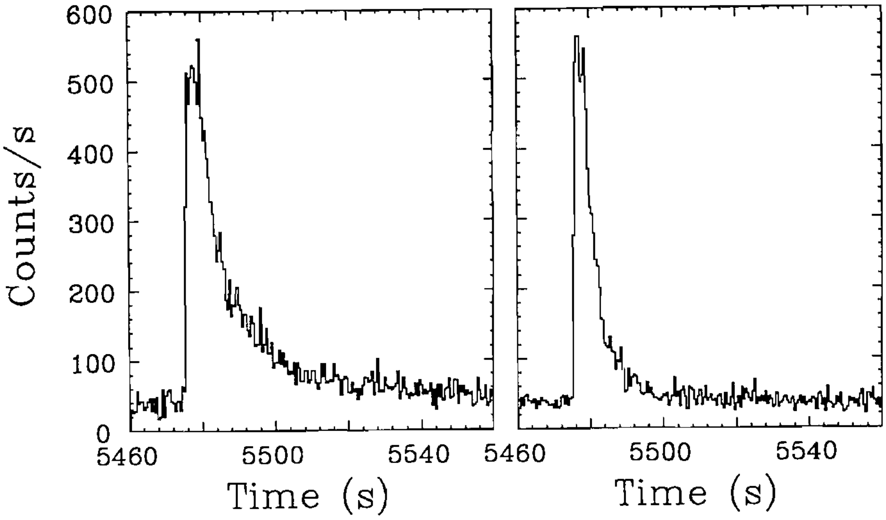

Figure 1.4: A single X-ray burst from 4U1702-429 as observed with *EXOSAT* in two energy bands: 1.2–5.3 keV (left) and 5.3–19.0 keV (right). The softening of the X-ray burst spectrum is apparent as the long tail in the low-energy profile during the burst decay *(adapted from Lewin et al. 1993)*.

flash. The burst timescale is fast (10-100 s) and the longer the times between bursts, the more powerful the burst (van Paradijs et al. 1988). The burst is detectable in the X-ray and soft gamma-ray regime (peaking in the X-ray) and the associated light-curve is usually characterised by a fast-rise followed by exponential decay (see Fig. 1.4). The spectrum of a burst can be described by a black-body spectrum, the temperature of which increases during the rise in flux (as the surface of the NS is heated) and decreases during the decay phase (kT$\sim$2–3 keV) from the cooling of the NS photosphere (Lewin et al. 1993). As a result, the decay times are shorter at higher energies (Fig. 1.4). If a LMXB is observed to undergo Type I bursts then this is conclusive proof that the compact is a NS and not a BH as they imply the presence of a surface on the compact object. These bursts are unique to LMXB as the higher magnetic field of younger NS in HMXBs hinders the build up of material on the NS. In LMXBs, accretion over long timescales (10^7 to 10^9 yr) has suppressed the magnetic field of the NS (making the fields typically $\leq 10^8$G). A small group of

LMXB have been discovered to be pulsating very rapidly as a result of prolonged accretion causing the old NS to spin up; these objects have been named accreting millisecond pulsars (see Psaltis 2004 for a review). These pulses are particularly visible during bursting episodes in transient systems, *e.g.* SAX J1808.1-3658 (Wijnands & van der Klis 1998).

1.3.1.2 High-mass X-ray Binaries

A HMXB consists of a massive ($> 10\,\mathrm{M}_\odot$), early type star accreting onto a compact companion, usually a NS. Although stellar wind accretion is a less efficient accretion mechanism compared to Roche lobe overflow, the massive companion stars are seen to possess intense (mass loss rates of $10^{-6}\,\mathrm{M}_\odot \mathrm{y}^{-1}$) and highly supersonic ($>10^3$km s-1) stellar winds, which causes a bow-shock in front of the NS (see Fig. 1.2). Supergiant (SG) systems have binary orbits with periods between 1–15 d, while Be systems have more highly eccentric orbits with periods $\sim$ 10–100 d (White, Nagase & Parmar 1995). These young systems are found predominantly in the Galactic disk where the star forming regions are located. If the compact object is a NS with a strong magnetic field (as is likely in young systems), the accretion disk gets disrupted near to the surface of the NS. In this case, material is channelled along the magnetic field lines and is accreted along the poles, where a hot spot forms with temperatures of 10^7K (kT>1keV) or more. Here, in a similar manner to the rotation-powered pulsars described in Sec. 1.3.2, beams of emission sweep the sky and are detected as pulsations if the magnetic pole is oriented towards the Earth. The average spectra are non-thermal, roughly power-law in shape with an exponential cut-off at $\sim$20 keV (Fillipova et al. 2004). Additionally, the detection of cyclotron lines enables the magnetic field of the NS to be measured. Systems where the companion is a Be star are generally transient objects, for which the outbursts are connected to the eccentricity of the orbit or episodes of mass ejection from the star. Recently, *INTEGRAL* has discovered a 'new' population of obscured HMXB, characterised by high photoelectric absorption, that is much greater than the interstellar column density in their line of sight (see Walter et al. 2004a; Negueruela 2004).

1.3.1.3 Neutron Star or Black Hole?

The first strong evidence for the existence of a black hole (BH) in a binary system was found in the HMXB Cyg X-1. Radial velocity measurments of the supergiant companion star inferred that the compact object is $10.1\,\mathrm{M}_{\odot}$ (Herrero et al. 1995), greater than the accepted mass limit for a NS ($\sim 3\,\mathrm{M}_{\odot}$). This is by far the most robust method of determining the nature of a compact object, but accurately measuring the radial velocity of the secondary can be difficult, especially for low mass systems as the companion is faint and the emission may be dominated by a large accretion disk. Therefore, alternative evidence for the presence of a BH (or NS) must be obtained. As explained in the previous section, the detection of X-ray bursts or pulsations is indicative of an object with a surface and/or a magnetic field and hence NS, but it is not always possible to observe the systems undergoing such bursts. As yet, there are no corresponding clear signatures of a BH. Other observational phenomenon that strongly points towards the existence of a BH are characteristic spectral state changes. Distinct spectral states have been inferred from observations of confirmed BH-binaries which can be described by the geometry of the accretion disk and/or different accretion modes and have the following spectral characteristics (see Fig. 1.5; Esin et al. 1997; for a review see McClintock & Remillard 2004):

- **Very high state** - characterised by a very steep power-law (Γ >2.4) with luminosities approaching the Eddington Limit.

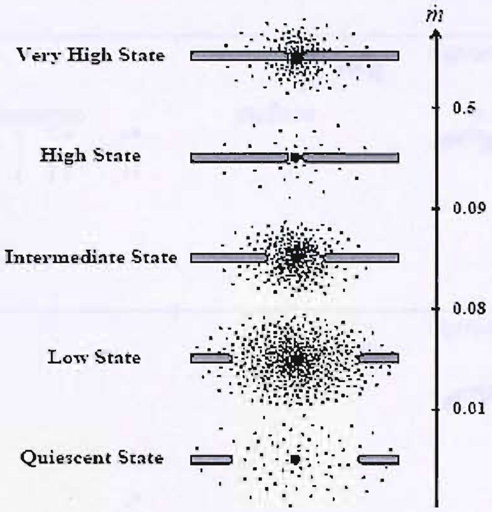

Figure 1.5: Spectral states of a BH-binary as a function of total Eddington-scaled mass accretion rate ($\dot{m}$) as represented by the accretion disk and accretion flow/corona (dots) *(Esin et al. 1997)*.

- **High/soft state** - this state is dominated by a soft thermal disk component below 10 keV and a steep power-law spectrum (Γ=2.1–4.8).
- **Intermediate state** - the intermediate states can exist during the transitions from the high/soft to the low/hard state and can be very short lived ~days, *e.g.* GX339–4 (Belloni 2004)
- **Low/hard state** - spectrum is dominated by a power-law spectrum, flatter than in the high/soft state (Γ=1.5–2.1) with a cut-off at ~100 keV which can be described as the Comptonisation of soft photons by a hot plasma, possibly a corona surrounding the BH. The accretion disk is believed to be truncated due to the absence of a thermal component.
- **Quiescent state** - disk is truncated further from the BH resulting in a very low luminosity ($\sim 10^{31}$erg s^{-1}) state, making detection difficult with current gamma-ray telescopes. The X-ray spectrum can be described as non-thermal and hard (Γ=1.5–2.1).

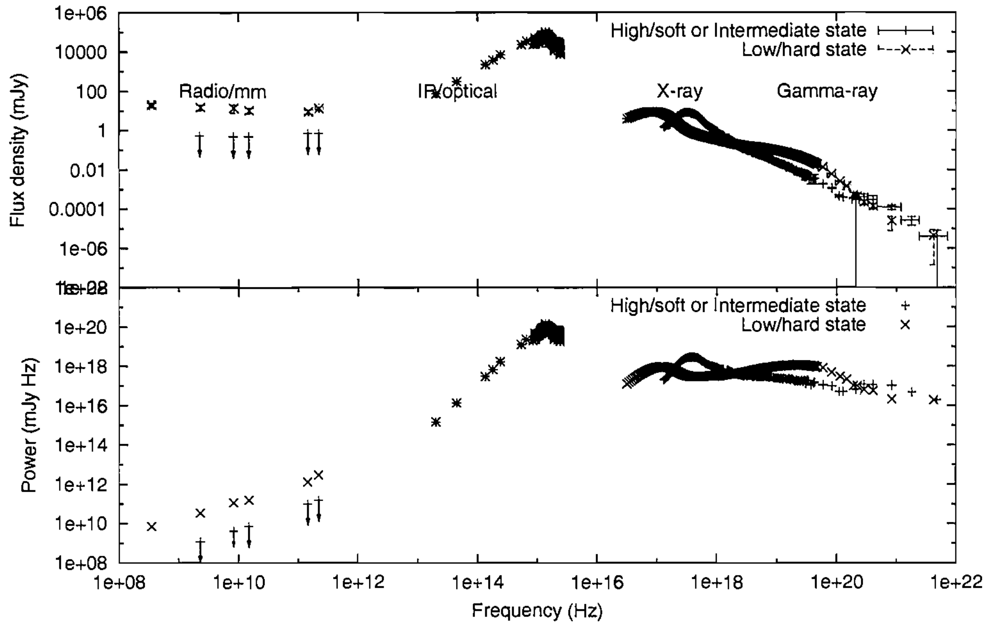

Figure 1.6: Broadband spectra of Cyg X-1 from radio to gamma-ray energies in flux density and spectral power-law representations, illustrating the suppression of radio-mm emission during the high/soft state. The low/hard state has an X-ray spectrum which peaks in power at ~100 keV and the IR/optical regime is dominated by the OB companion star which is unchanging between states. The >1 MeV gamma-ray flux is comparable in both states. *(adapted from Fender & Maccarone 2004)*

Radio observations of bright BH-binaries have discovered powerful radio-emitting outflows associated with these systems and there is now strong evidence that this phenomenon forms a key part of the accretion behaviour in certain states of X-ray binaries. These objects (*e.g.* GRS 1915+105; Mirabel & Rodriguez 1994) are called microquasars, drawing from the obvious analogy between jet emitting active galaxies. Although there is no direct evidence of X-ray and gamma-ray emission from the actual jet, there is now evidence of a strong coupling between the observed radio and X-ray luminosities, where the jet is strongly detected in the low/hard spectral state, but seems to be quenched during the high/soft phase (Gallo, Fender & Pooley 2003). Figure 1.6 displays the broadband spectra of Cyg X-1 illustrating the high/soft and low/hard spectral states. For a review of the high energy emission from microquasars see Fender & Maccarone 2004.Binary systems showing observational characteristics similar to 'confirmed' BH-binaries but whose nature cannot be established through mass evaluation are called BH candidates (BHC). Further detections of both BH and candidate systems, especially in the soft gamma-ray regime, are important in order to understand the emssion processes and observed spectral states of X-ray binaries and to help distinguish between those containing a NS or a BH.

1.3.2 Supernovae and Related Products

The life of a star is controlled by its mass and a sequence of nuclear fusion reactions ($H \rightarrow He \rightarrow C \rightarrow O, Ne, Si \rightarrow^{56} Fe$). The energy produced in these reactions counteracts the gravitational force of the star, but when all the fuel in the star's core is exhausted the star may collapse, leading to a supernova (SN) explosion (^{56}Fe is the most strongly bound nucleus, further fusion requires energy input) . A Type Ia SN occurs as a nuclear explosion in a binary system where accretion onto a white dwarf results in the white dwarf reaching its critical mass ($\sim 1.4\,\mathrm{M}_\odot$). Ignition takes place under degenerate conditions and may result in the complete disruption of the star. A Type Ib SN is thought to be caused by the gravitational core collapse of an intermediate mass (initial stellar mass $\sim$several $\mathrm{M}_\odot$) star which has lost its outer layer of Hydrogen (*i.e.* Wolf-Rayet type), while the core implosion of an even more massive star (initial mass greater than $8\,\mathrm{M}_\odot$) produces a Type II SN. During the collapse, the star's iron core is squeezed under great temperature and pressure, causing neutronization to take place ($p + e \rightarrow n + \nu$). If the neutron degeneracy is capable of stopping further infall then a neutron star will be formed, otherise a black hole is created (typically when core mass $<\sim 2.5\ \mathrm{M}_\odot$). As the result of the core collapse, a shock wave propagates outwards and transfers energy

Isotope	Lifetime	Decay Chain	Line energy (keV)	Source
^{7}Be	77 days	^{7}Be→^{7}Li	478	Novae
^{56}Ni	111 days	^{56}Ni→^{56}Co→^{56}Fe	847, 1238	Supernovae
^{57}Ni	390 days	^{57}Ni→^{57}Co→^{57}Fe	122	Supernovae
^{22}Na	3.8 yrs	^{22}Na→^{22}Na+e^{+}	511, 1275	Novae
^{44}Ti	89 yrs	^{44}Ti→^{44}Sc→^{44}Ca	68, 78, 1156	Supernovae
^{26}Al	10^{6} yrs	^{26}Al→^{25}Mg+e^{+}	511, 1809	Novae, Supernovae, stars
^{60}Fe	2×10^{6} yrs	^{60}Fe→^{60}Co	1173. 1332	Supernovae

Table 1.1: Isotopes producing gamma-ray spectral lines.

to the outer layers of the star, which are blown off into the interstellar medium (ISM). The ejected shell of material subsequently expands and interacts with the ISM, forming a nebula, continually cooling until it has radiated all of its heat away over timescale $\sim 10^5$y. Radioactive isotopes generated by the massive stars and associated SN explosion are included in Table 1.1. By measuring the time profile of ^{56}Ni spectral line, the expansion of a SN envelope can be measured. At the other end of the timescale, the long decay-time isotope ^{26}Al can be used as a tracer for star formation and SN occurance rates and reflects the integrated nucleosynthesis activity from supernovae, novae, and massive-star wind ejection (*e.g.* Wolf-Rayet stars). Recent work by Diehl et al. (2006) using the fine gamma-ray spectroscopy capability of the *INTEGRAL* satellite, have measured the distribution of ^{26}Al in the galaxy and correlated the associated line shift with the rotation of the galaxy. This implies that the ^{26}Al isotope is being created throughout the Galaxy, most probably in on-going star formation regions, which leads to estimates of a star formation rate of ~7 new stars per year and 1 SN every 50 years (Diehl et al. 2006; see Fig. 1.8).

A pulsar is a rapidly rotating, highly magnetic neutron star which can be formed in a core-collapse SN explosion. These rotation powered objects (as opposed to accretion powered pulsars, see Sec. 1.3.1.2) emit jets of relativistic particles (electron-

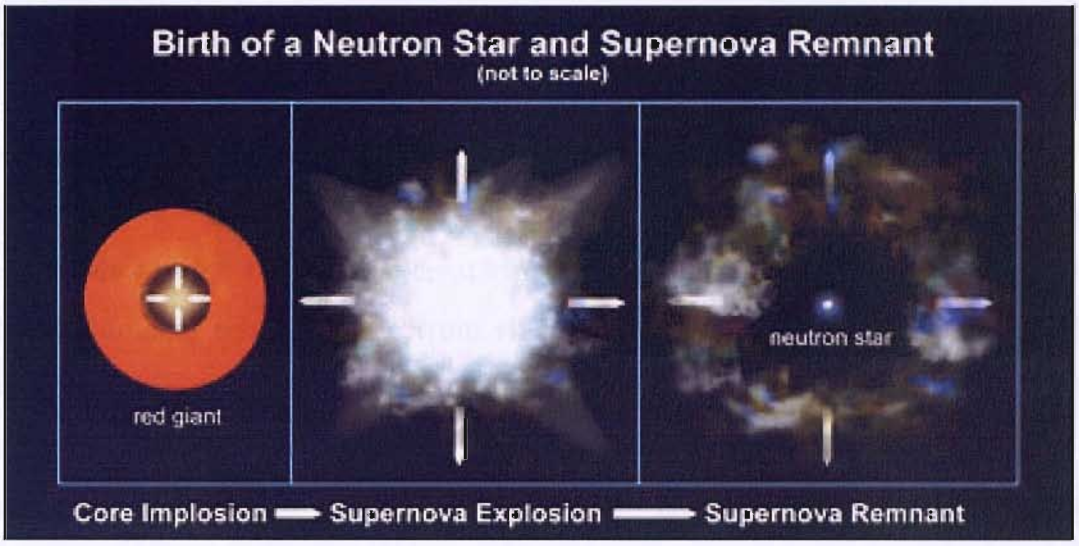

Figure 1.7: The birth of a neutron star *(Picture Credit: NASA/CXC/SAO)*

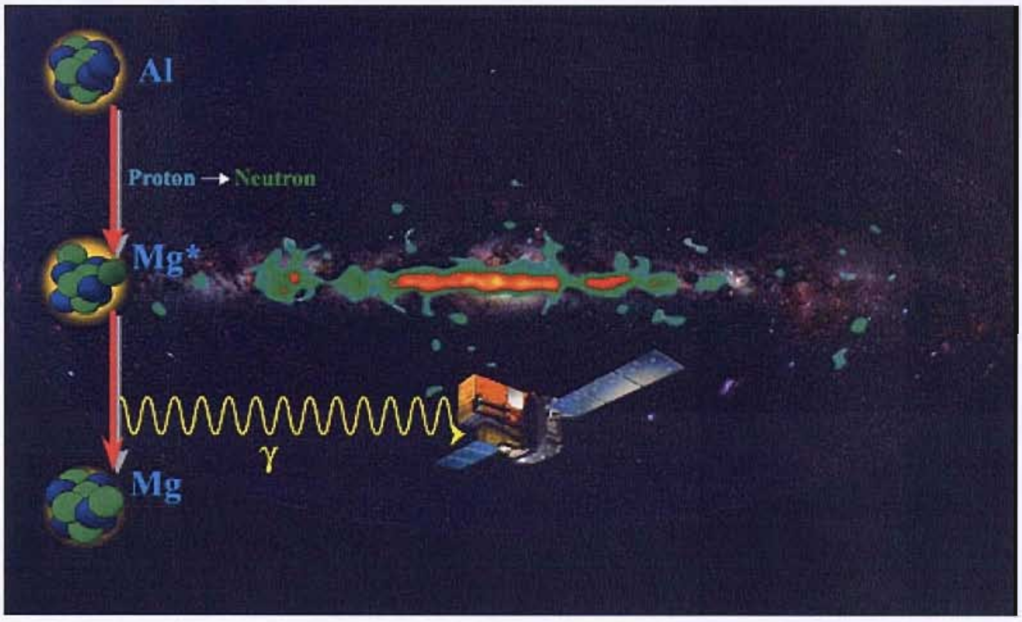

Figure 1.8: ^{26}Al in the Galaxy. An optical image of the Galaxy overlaid with *CGRO*/COMPTEL image of ^{26}Al highlighting star formation regions. *(Picture Credit: Roland Diehl/MPE)*

position pairs) from the magnetic poles (see Kaspi et al. 2004 for a detailed review). If there is an offset between magnetic and spin axis and one of the magnetic poles falls within the line of sight of the earth, pulsed emission is observed. Although the dominant emission is usually in radio wavelengths, soft X-ray emission can be produced from residual heat of the neutron star formation and non-thermal X-rays and/or soft gamma-rays can be created from the upscattering of lower energy (e.g. radio) photons by relativistic electrons via inverse Compton scattering. Additionally, radio synchrotron emission (sometimes extending to extremely high energy gamma-ray wavelengths) is produced as the result of the highly relativistic magnetised wind emitting from the pulsar interacting with the surrounding medium, termed a pulsar wind nebula (PWN). Out of the several hundred known radio pulsars detected less than ten have been detected in gamma-rays.

1.3.2.1 The Crab Pulsar

The Crab is the strongest persistent discrete source of gamma-rays in the sky and was first observed in the optical, as a SN explosion in 1054 AD. The object is observable at all wavelengths and in X-rays the object manifests itself as a bright jet emitting pulsar and synchrotron wind nebula (Fig. 1.9). The bright rings observed in the surrounding nebula are thought to be due to thermal shocks (Hester et al. 2002). At soft gamma-ray energies the dominating radiation is the pulsed emission (period ~0.033 s) with a characteristic double peak profile which has been previously studied with many high energy instruments *e.g. HEAO-1*/A4 in the 18–200 keV range (Knight 1982) and *CGRO*/COMPTEL above 500 keV (Kuiper et a. 2001). It has also been used for verifying the absolute timing capabilities of the high-energy instruments on-board *INTEGRAL* (Kuiper et al. 2003). The Crab also is regularly used as a calibration source in the X-ray and gamma-ray regimes as, in longer observations, the bright emission can be considered constant. The broad-band high

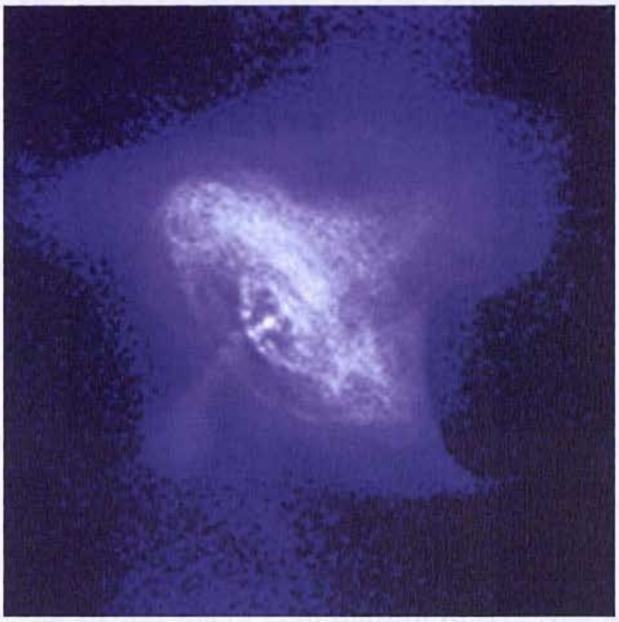

Figure 1.9: Crab in X-rays showing the pulsar jet and associated nebula *(Picture Credit: NASA/CXC/SAO)*.

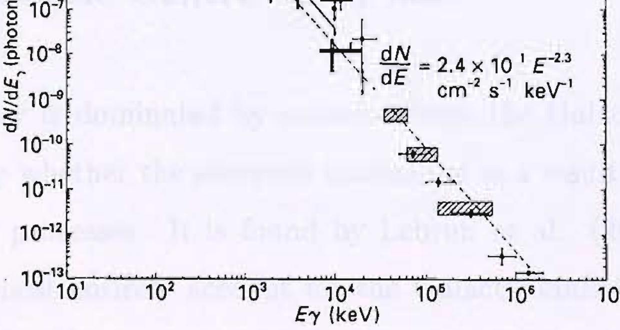

Figure 1.10: Total Crab emission and spectrum *(Zombeck 1990)*.

energy spectrum of the Crab is displayed in Fig. 1.10 and has a convenient near uniform power density spectrum with slope ~2. The unit of milliCrab can be used as a measure of source flux and has become ubiquitious in gamma-ray astronomy.

1.3.2.2 Magnetars

Neutron stars with extreme magnetic fields ($> 10^{14}$ G) are termed magnetars. Both Soft Gamma-ray Repeaters (SGR) and Anomalous X-ray Pulsars (AXP) are described as being systems containing potential magnetars. SGRs are characterised, as suggested by the name, by repetitive bursts in the soft gamma-ray regime. They were first thought to be a sub-type of Gamma-ray Bursts (see Sec. 1.3.4), but have softer emission and are observed to have persistent X-ray emission from which pulses have been detected. AXPs were discovered as unusual spinning-down pulsars with no optical counterparts. Recent observations have detected bursts from these systems, which imply that SGR and AXP may be a similar sort of object, where the extreme NS magnetic field is powering both the persistent and burst emission. For a comprehensive review of these objects see Woods & Thompson (2004).

1.3.3 The Galactic Centre and Plane

The high energy sky is dominated by emission from the Galactic plane and it is interesting to study whether the observed continuum is a result of discrete sources or diffuse emission processes. It is found by Lebrun et al. (2004) that observed discrete sources almost entirely account for the Galactic emission in soft gamma-rays (Fig. 1.11) with only a very low level of contribution needed from interstellar processes. Furthermore, Strong et al. (2005) has used the second *INTEGRAL* /IBIS catalogue (see Chapter 5) to study the contribution of point sources be-

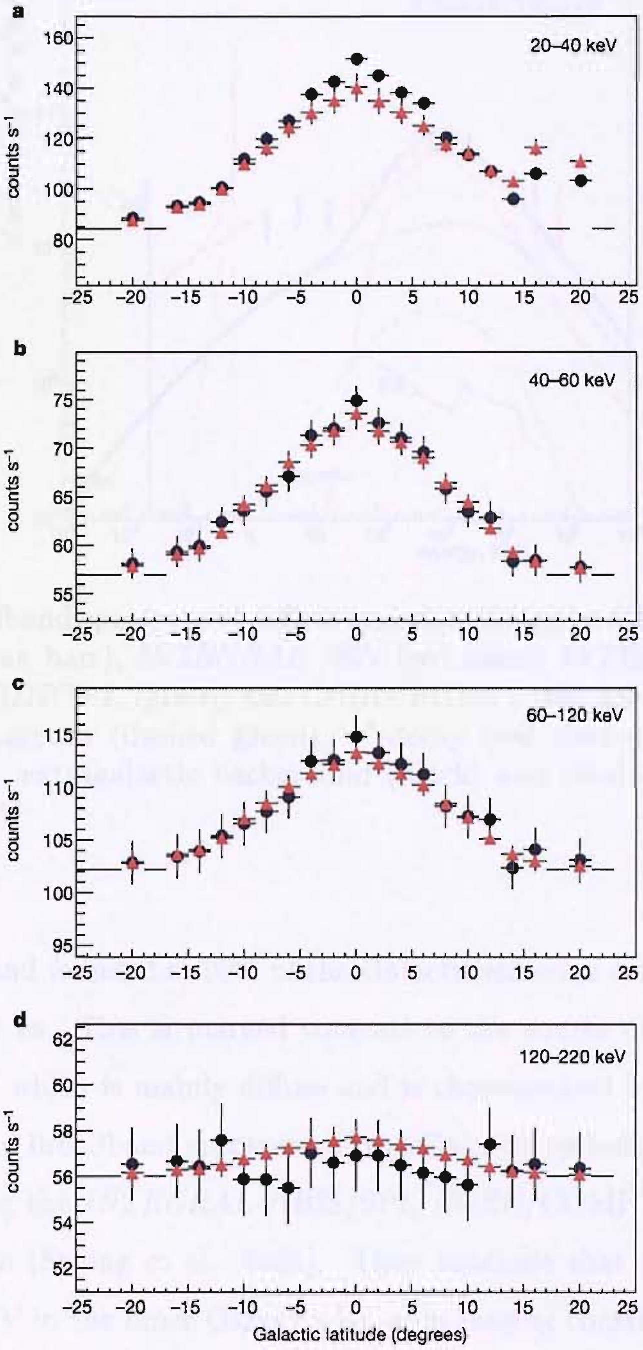

Figure 1.11: Latitude profiles of the Galactic emission in the central regions where $|l|<20°$, showing background-corrected detector count rates (black circles) and detected source counts (red triangles) *(Lebrun et al. 2004)*.

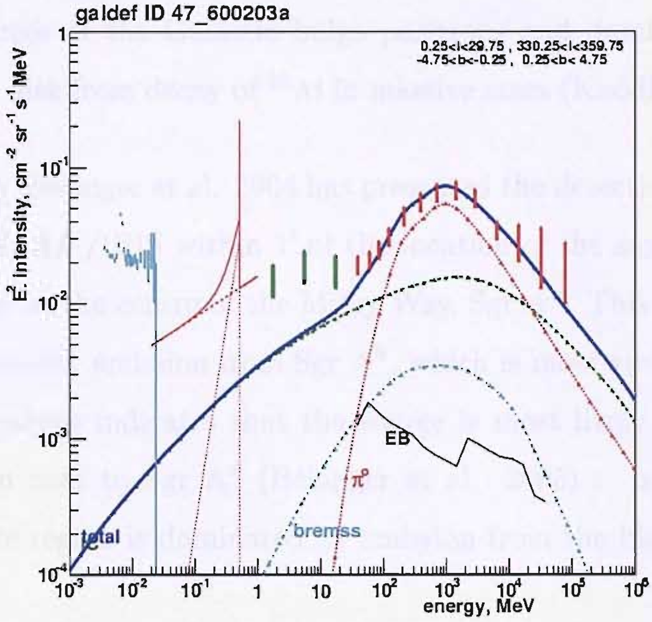

Figure 1.12: Broadband spectrum of diffuse emission along the Galactic plane. Data is from *RXTE* (cyan bars), *INTEGRAL* /SPI (red lines), *INTEGRAL* /IBIS (magenta), *CGRO*/COMPTEL (green) and *CGRO*/EGRET (red bars). Emission models are inverse Compton (dashed green), π^0-decay (red dotted), bremsstrahlung (cyan dashed-dot), extragalactic background (black) and total model (dark blue) *(Strong et al. 2005)*.

tween 20–60 keV and found that 90% of the Galactic emission can be accounted for by detectable sources. This is marked contrast to the source of continuum emission below 20 keV which is mainly diffuse and is characterised by a soft spectrum. Fig. 1.12 shows the broadband spectrum of the Galactic emission between 10 keV and 100 GeV using the *INTEGRAL* /IBIS/SPI, *CGRO*/COMPTEL/EGRET and *RXTE* instruments (Strong et al. 2005). They conclude that positron processes dominate >300 keV in the inner Galaxy with a decreasing contribution from point sources as energy increases.

The central bulge of the Galaxy as a source of positrons has been investigated by mapping the 511 keV line emission using the *INTEGRAL* /SPI. Results suggest that old stellar populations (Type Ia supernovae and/or low-mass X-ray binaries) are the main sources of the Galactic bulge positrons and dominate the 511 keV emission from the disk from decay of ^{26}Al in massive stars (Knödlseder et al. 2005).

Finally, work by Bélanger et al. 2004 has presented the detection of IGR J17456-2901 with *INTEGRAL* /IBIS within 1′ of the location of the supermassive ($\sim 3 \times 10^6$ M$_\odot$) black hole at the centre of the Milky Way, Sgr A*. This would be the first detection of gamma-ray emission from Sgr A*, which is most easily detected in the radio. Further analysis indicates that the source is most likely a compact region of diffuse emission near to Sgr A* (Bélanger et al. 2005) . In soft gamma-rays the Galactic centre region is dominated by emission from the black hole candidate 1E 1740.7–2942.

1.3.4 Extra-galactic Sources

It is not intended to give a lengthly review of the different types of extra-galactic objects here since the science thrust of this thesis is concerned with Galactic objects. However, it is interesting to study the comparisions between AGN and Galactic binaries and in particular how the emission processes scale with black hole mass which can be performed using observations in the soft gamma-ray domain.

1.3.4.1 Active Galactic Nuclei

Away from the Galactic plane, bright and highly variable emission is observed from Active Galactic Nuclei (AGN). These objects are characterised by energetic emission from an accreting central supermassive (M$\sim 10^7$ M$_\odot$) black hole, which is able to outshine its host galaxy. A multi-wavelength review of AGN can be found in Risaliti & Elvis (2004). The different sub-types of AGN can be unified by considering the geometry and inclination angle of the system (see Fig. 1.13; Urry & Padovani

1995). Seyfert galaxies are AGN where the host galaxy can also be observed. They are less luminous and less distant compared to Quasars (QSOs) which appear as bright point sources in optical observations. Seyfert 1 galaxies are oriented so that the broad-line emission from the inner parts of the system can be observed, but if the galaxy is viewed edge- or near edge-on, the inner regions are obscured by the optically thick torus. In this case, the emission is strongly scattered and the system is classed as a Seyfert 2 or narrow-line galaxy (see Véron-Cetty & Véron (2003) for a review of Seyfert classifications). High-energy non-thermal photons are created through synchrotron and inverse Compton processes and the soft gamma-ray spectrum of both Seyfert 1 and 2 galaxies can be described with a hard power-law (Γ ~1.5) with some evidence for an exponential cut-off at ~80–300 keV (Risaliti & Elvis 2004). Additionally, soft gamma-ray observations are revealing absorbed (high column density) Seyfert galaxies missed in X-ray and lower wavelength studies (Bassani et al. 2006). Such observations are important in order to create more accurate models of the X-ray background.

AGN can also be sub-divided into radio loud and radio quiet varieties. Radio loud galaxies are ~10% of the total AGN population and in some cases can possess large and significant radio lobes, while radio quiet AGN generally have smaller scale, less relativistic jets. The jets are produced near the black hole and if oriented towards the Earth, the AGN is classed as a Blazar. Beaming of the jet is inferred by the rapid variability of emission (in all wavelengths) or by superluminal motions on VLBI (Very Long Baseline Interferometry) scales. Gamma-ray photons are produced in these jets from the inverse Compton scattering of photons by electrons in the beam. It is possible to learn about AGN by studying Galactic binaries; *e.g.* the relative proximity of Galactic microquasars enable the processes involved in jet emission to be studied more easily. Essentially, both systems contain an accreting compact object, but with the AGN black hole being typically a million to a billion times more massive than a black hole in a Galactic binary.

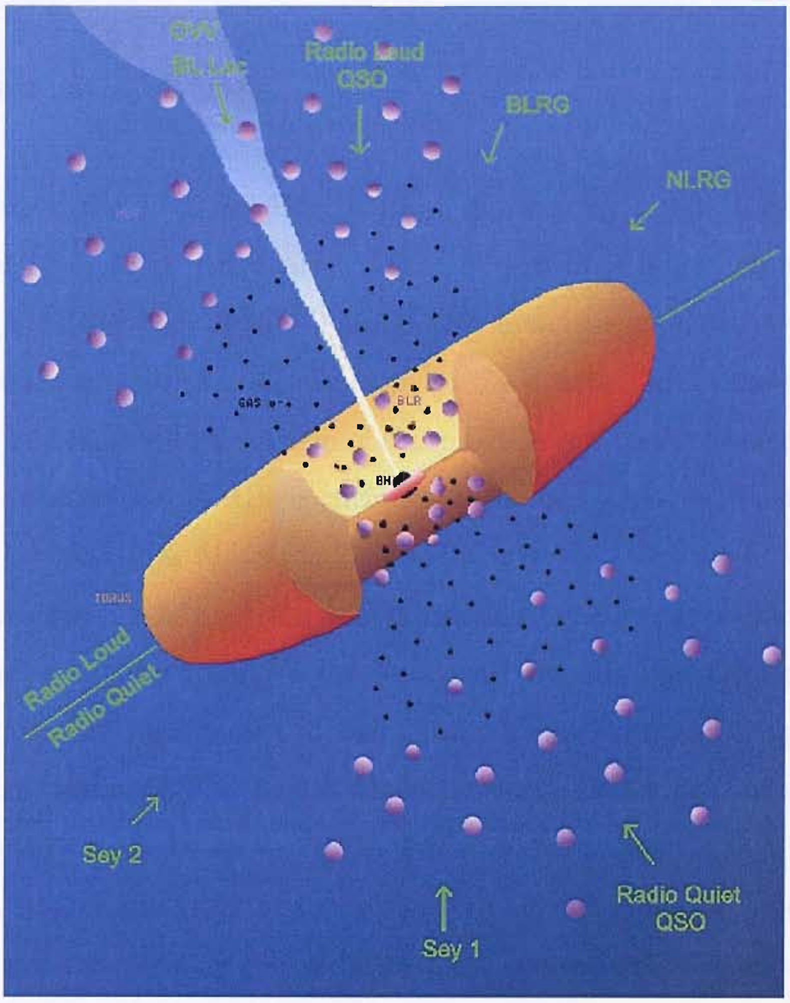

Figure 1.13: Unification model of Active Galactic Nuclei *(Picture Credit: adapted from Urry & Padovani 1995)* .

Gamma-rays have also been observed from clusters of galaxies, most likely as the result of inverse Compton processes between the microwave background and energetic electrons accelerated to relativistic speeds by shocks in the intercluster medium, *e.g.* Coma Cluster (Fusco-Femiano et al.1999).

1.3.4.2 Gamma-ray Bursts

First detected by the Vela Satellite in 1969, gamma-ray burst (GRB) events are characteristed by a short timescale (~20 s) release of a huge amount of energy $\sim 10^{51-53}$erg s^{-1} (Fishman 1995). The BATSE instrument on the *CGRO* mission detected ~1 burst per day and the isotropy of the events implies the extra-galactic nature of the bursts. While the origin of short GRBs is thought to be due to NS-NS mergers, the origin of long GRBs is currently explained with the "Standard fireball model" (see *e.g.* Zhang & Mészáros 2004 for a review). This model describes the collapse of a massive ($> 30\,M_\odot$) star which produces synchrotron radiation observed as gamma-rays from the result of shocks caused by colliding "shells" of matter. Afterglows which can be detected in radio, optical and X-ray wavelengths can help identify the host galaxy of the bursts which are currently thought to occur in star-forming regions (*e.g.* Costa et al. 1997). For a recent review on GRBs see Hurley et al. (2002). Although the detection of GRBs is one of the main objectives of the *INTEGRAL* mission, this subject is beyond the scope of this thesis and has only been included for completeness.

1.4 Summary

This chapter has described the types of objects which can be observed at energies above 20 keV and has shown that all of the discrete sources can be linked to the presence of a compact object, *e.g.* black hole or neutron star. A schematic showing the different types of emitting objects is displayed in Fig. 1.14. Apart from SGR, the Galactic objects described above are historically classified according to their X-ray (<20 keV) emission. Soft gamma-ray observations are important to understanding fully the origin and mechanisms for the high energy emission which will help determine more physical models for the observed spectra. The next chapter of this thesis will describe the methods by which soft-gamma ray emission can be detected and will introduce the *INTEGRAL* mission through which many new high energy sources have being unveiled.

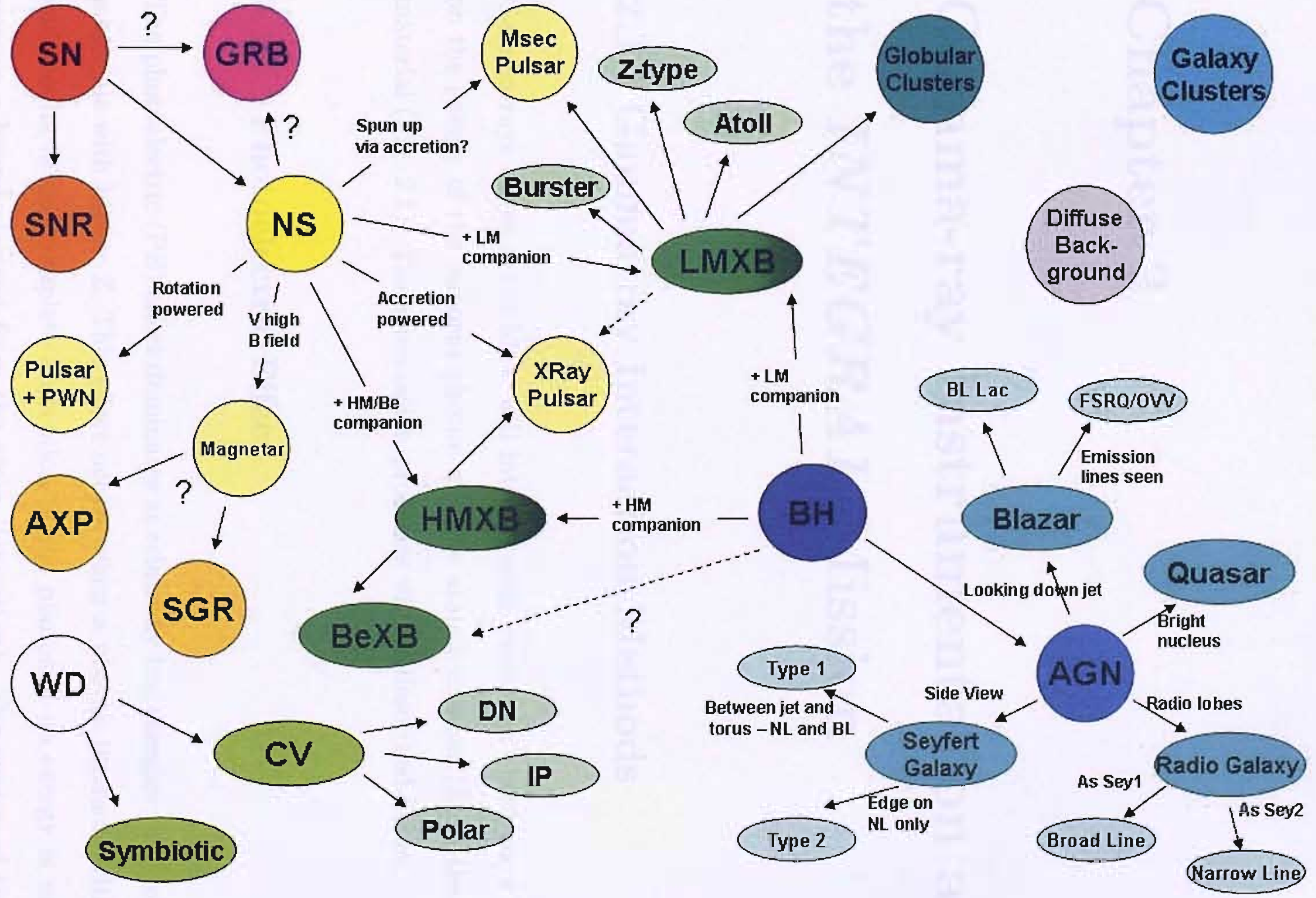

Figure 1.14: Astronomical sources of gamma-ray emission. The colour grading on the LMXB and HMXB objects represent the distinction between those with a NS primary (bright green) and BH-binaries (dark green).

Chapter 2

Gamma-ray Instrumentation and the *INTEGRAL* Mission

2.1 Gamma-ray Interaction Methods

Gamma-rays below ~100 MeV will interact with matter in three ways depending on the energy of the incident photon and the atomic number (Z) of the absorbing material (Fig. 2.1). The attenuation processes will be described below.

2.1.1 Photoelectric Effect

The photoelectric (PE) effect dominates at relatively low energies (<1MeV) and for materials with higher Z. This effect occurs when a photon interacts with an atom and results in the complete absorption of the photon if its energy is sufficient to remove a bound electron from the atom (ionisation). The energy of the expelled electron E_e can be expressed as the energy of the photon minus the binding energy

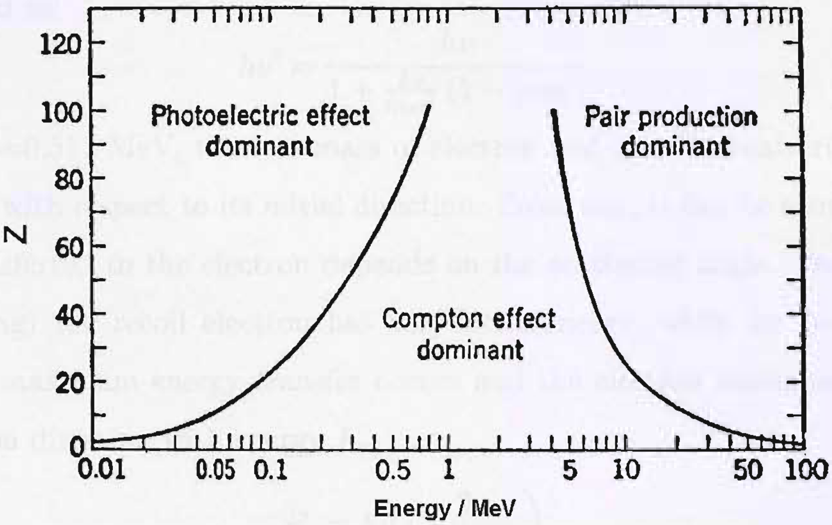

Figure 2.1: Gamma-ray interaction processes as a function of energy and atomic number of absorber material.

of the electron:

$$E_e = h\nu - E_{binding} \tag{2.1}$$

The electron will then transfer its energy to the surrounding material. Meanwhile, the ionised atom will recombine with another electron, emitting an X-ray photon with a characteristic energy (fluorescence) which is also absorbed, resulting in all of the initial photon energy being absorbed in the material.

2.1.2 Compton Scattering

Compton scattering is the dominant gamma-ray attenuation process at energies of ~1 MeV when the binding energy of an electron in an atom becomes less important and the electron can be considered free. When a photon is incident upon a free electron a transfer of energy occurs leaving the photon with a fraction of its initial energy. If the initial photon energy E=hν, the energy of the scattered photon can be expressed as:

$$h\nu' = \frac{h\nu}{1 + \frac{h\nu}{m_e c^2}\left(1 - cos\phi\right)} \tag{2.2}$$

where $m_e c^2$=0.511 MeV, the rest mass of electron and ϕ is the scattering angle of the photon with respect to its initial direction. From this, it can be shown that the energy transferred to the electron depends on the scattering angle. For ϕ=0° (i.e. no scattering) the recoil electron has very little energy, while for ϕ=180° (back scattering) maximum energy transfer occurs and the electron continues along the inital photon direction with energy E_e:

$$E_e = h\nu\left(\frac{2\alpha}{1 + 2\alpha}\right) \tag{2.3}$$

where $\alpha = \frac{h\nu}{m_e c^2}$. As a result of these differences in scattering angle, Compton scattering produces a continuum spectrum of energy displayed in Fig. 2.2. The Compton edge labelled corresponds to the maximum scatter scenario (ϕ=180°), while the total absorption peak corresponds to the initial photon energy from either PE absorption or multiple Compton scatterings. The back-scatter peak occurs at an energy equivalent to the difference between the energy of the Compton edge and total absorption peak and is due to a maximally scattered photon depositing the remainder of its energy.

The angular distribution of the scattered photons can be defined by the Klein-Nishina formula for the differential scattering cross-section:

$$\frac{d\sigma}{d\Omega} = Zr_e^2\left(\frac{1}{1 + \alpha\left(1 - cos\phi\right)}\right)^2\left(\frac{1 + cos^2\phi}{2}\right)\left(1 + \frac{\alpha^2\left(1 - cos\phi\right)^2}{\left(1 + cos^2\phi\right)\left(1 + \alpha\left(1 - cos\phi\right)\right)}\right) \tag{2.4}$$

where r_e is electron radius. The equation predicts that high energy photons will be preferentially scattered in the forward direction, with ϕ decreasing as energy increases. At lower energies (~100 keV) the scattered photons will be scattered almost isotropically. The distributions for a range of photon energies is shown in Fig. 2.3.

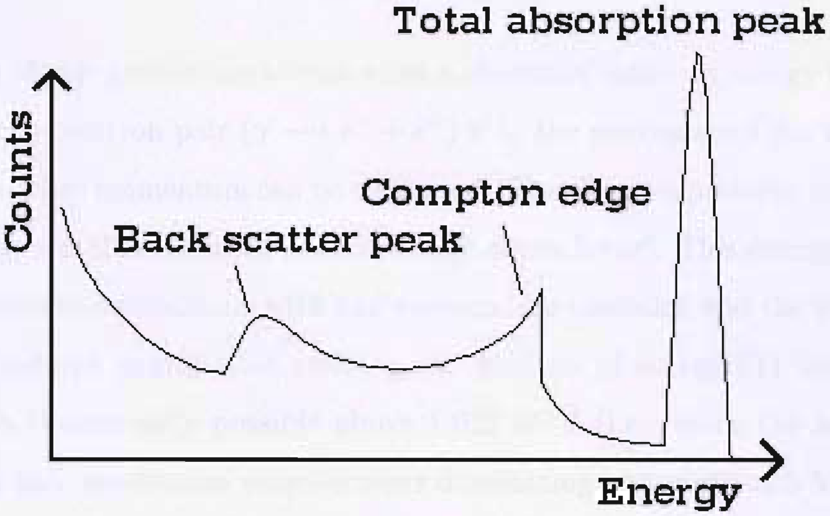

Figure 2.2: Pictorial representation of Compton spectrum for a mono-energetic source.

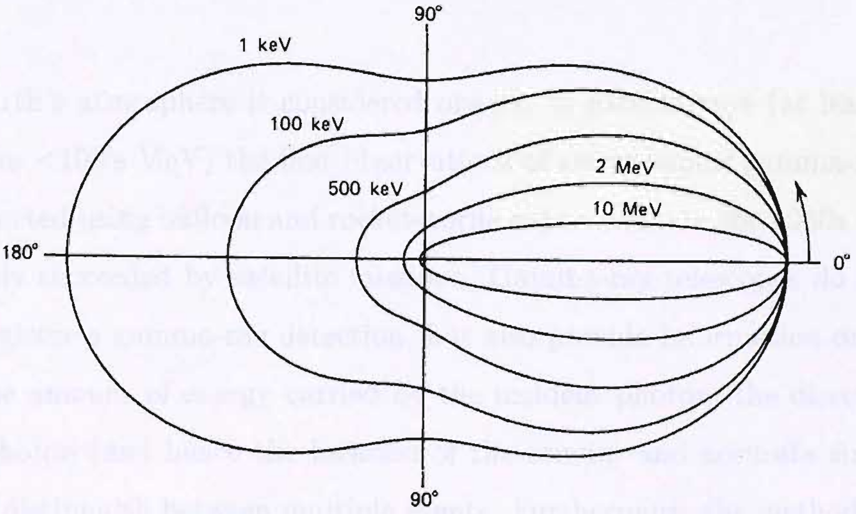

Figure 2.3: Polar plot of the number of photons (incident from the left) Compton scattered into a unit solid angle at the scattering angle (ϕ), for a range of energies (*adapted from Knoll 1989*).

2.1.3 Pair Production

The process of pair production occurs when a photon of sufficient energy is converted into a electron-positron pair ($\gamma \longrightarrow e^- + e^+$) if in the proximity of the nucleus of a third atom so that momentum can be conserved. The electron-positron pair will have kinetic energy equal to the inital photon energy minus $2m_ec^2$. This energy will be lost through Coulomb interactions with any surrounding electrons and the positron will eventually undergo annihilation creating two photons of energy 511 keV.Although this effect is theoretically possible above 1.022 MeV (i.e. twice the rest mass of an electron) pair production only becomes dominating above about 5 MeV. As the remainder of this review will be concerned with the detection of gamma-rays in the 20 keV–1 MeV energy range, pair production is not particularly relevant here.

2.2 Gamma-ray Telescopes

As the Earth's atmosphere is considered opaque to gamma-rays (at least for photon energies <100's MeV) the first observations of astronomical gamma-ray sources were conducted using balloon and rocket-borne experiments in the 1960s which were later largely succeeded by satellite missions. Gamma-ray telescopes do not simply need to register a gamma-ray detection, but also provide information on the event such as the amount of energy carried by the incident photon, the direction of the incident photon (and hence the location of the source) and accurate timing information to distinguish between multiple events. Furthermore, the methods by which gamma-rays can be imaged are affected by the inability to use conventional optics to focus such penetrating radiation above ~15 keV. Additionally, gamma-ray detectors are liable to significant contamination from background events outside the earth's atmosphere, thereby affecting the design of the telescope and making shielding an important consideration.

The telescope performance can be measured using the following properties:

- Detector efficiency defines the fraction of incoming photons of energy E_γ that will interact in the detector: $\varepsilon(E_\gamma) = 1 - e^{-\mu x}$ (counts per photon), where x is the thickness of the detector and μ is the total absorption coefficient. μ describes the probability that a gamma-ray photon will interact per unit length and is the sum of the probabilities from the three interaction modes ($\mu = \mu_{photoelectric} + \mu_{Compton\ scattering} + \mu_{pair\ production}$).
- Spectral resolution usually quoted as full width half maximum (FWHM) of the pulse height spectrum of a detector and provides a measure of how accurately the energy of an incident photon can be determined.
- Timing resolution depends on speed of electronic pulse readout and subsequent data transmission from detector and determines how accurately the arrival time of a photon can be determined.
- Angular resolution is a measure of how accurately the telescope can distinguish between two sources.
- Point source location accuracy defines how precisely the location of a point source can be determined.
- Field of view describes the amount of sky the telescope is able to image in a single observation.

The following sections will briefly outline the types of detectors and shielding systems used in gamma-ray telescopes and detail the imaging techniques commonly used in the soft gamma-ray energy band (20 keV–1 MeV).

2.2.1 Detector Types

When gamma-rays interact with matter they transfer some or all of their energy to the material. Gamma-ray detectors use materials in which the energy deposited produces a measurable change via an increase in temperature, production of electronic charge, a chemical change or emission of ultraviolet or optical photons. Commonly used astronomical detectors are discussed here, for further information see Leo (1992); Knoll (1989) .

A gas counter detector consists of a chamber of gas across which an electric field is applied. An incident gamma-ray is able to ionise the gas via the PE effect and produce an electron-ion pair which will move under the influence of the applied voltage. The most commmonly used type of gas counter in astronomical instruments is called a proportional counter, and uses an applied voltage between 250–500 keV. In this case, the drifting electrons will gain sufficient kinetic energy to further ionise neutral atoms in the gas producing even more electrons, the resulting signal being proportional to the initial photon energy. A certain amount of positional information can be gained from a proportional counter by placing a grid of wire anodes over the detector. These detectors are limited to an energy range up to ~150 keV.

A second type of gamma-ray detector is a semiconductor diode which works on a similar principle to a gas counter but operates at higher energies (typically few keV to MeV). An interacting gamma-ray photon will generate electron-hole pairs which will drift in the presence of an applied electric field. As the charges move, the detector suffers a drop in voltage which can be measured as the output pulse. The ISGRI detector on board the *INTEGRAL* satellite is such a semiconductor detector and is made up of Cadmium Telluride (CdTe). CdTe has advantages over other semiconductor materials (*e.g.* Germaninum) because it does not need to be cooled. However, it does suffer from 'charge trapping' caused by the drifting electrons and holes being trapped by imperfections in the CdTe crystal. Fortunately, a measurement of the rise-time of the signal allows this effect to be corrected for.

Thirdly, scintillation counters exploit the ability of certain materials to emit low-energy photons when struck by a high-energy charged particle. A gamma-ray photon can interact with the material and produce charged particles via the PE effect, Compton scattering or pair production, which will cause the material to scintillate, generating a pulse of visible/UV light. This pulse is then converted into a measurable detection by a photomultoplier tube (PMT) or a solid-state photo-diode. Scintillators can be of organic or inorganic material. Organic scintillators can exist in crystal form (*e.g.* Anthracene; Barlow 1969), or as a plastic if imbedded in a polymer, liquid if dissolved in a solvent and have faster response times, but produce relatively low light yields and are of lower density (*i.e.* less stopping power). Therefore, the most popular scintillators in gamma-ray astronomy are the higher density inorganic materials such as Sodium Iodide (NaI), Caesium Iodide (CsI) and Bismuth Germanate (BGO) which cover a similar (but slightly extended) energy range to semiconductor diode detectors. BGO has a high density relative to other inorganic scintillators and is therefore often used in active shielding. Position-sensitive detectors can be produced by using pixellated detector planes where the spatial resolution is the size of the scintillation pixels or semiconductor crystals.

2.2.2 Shielding

The responsibility of the shielding system is to reduce the amount of background radiation being detected and hence to improve the instrument sensitivity. There are two main types of shielding for an astronomical detector: passive and active. A passive shielding system uses a high atomic number material such as lead or tungsten to block charged particles and photons outside of the field of view. At low energies

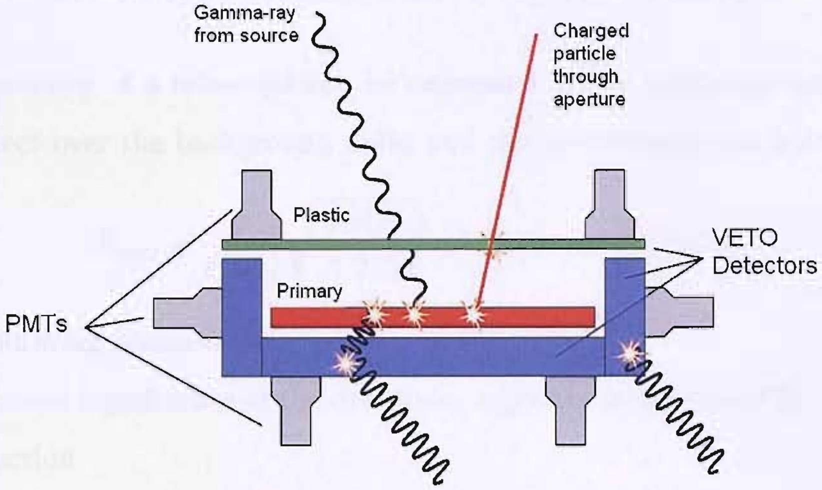

Figure 2.4: An example veto active shielding configuration consisting of BGO/PMT shielding underneath and to the sides of the primary detector and plastic scintallator/PMT placed above the telescope aperture. Both the charged particle and one of the non-source photons are vetoed out, a second non-source photon being absorbed outright by the BGO.

(<few hundreds of keV) passive shielding (*e.g.* a simple collimator) is used to absorb photons fully. With increasing photon energy, this becomes impractical due to the increasing heaviness of the amount of absorbing material needed. An active shielding system does not block the unwanted radiation, but instead uses a scattering event in a surrounding detector to act as a veto so that any simultaneous event in the primary detector can be rejected. Therefore, if there is a coincident event in the veto and detector, it is assumed to have come from outside the telescope field of view and is discarded. As this method does not require the full energy of the photon to be absorbed, it is a much more efficient especially at high energies. Examples of veto detector configurations include BGO plus PMT which is only useful above ~15 keV as the BGO has a low light output and a plastic scintillator/PMT set up which is commonly placed across the detector aperture for the veto of charged particles as it will not cause interactions with gamma-rays. See Fig. 2.4 for an example active shielding assemblage. A phoswich detector is a type of scintillator where veto and

detector systems have the same readout PMT (Lum et al. 1994).

The sensitivity of a telescope can be expressed as the minimum source flux it is able to detect over the background noise and can be estimated as follows:

$$F_{min} = \frac{\sigma}{\varepsilon(E_\gamma)}\sqrt{\frac{4B(E_\gamma)}{A\,T\Delta E}}\ \text{photons cm}^{-2}\text{s}^{-1}\text{keV}^{-1} \qquad (2.5)$$

with the following parameters:

σ - statistical significance of the detection, typically minimum of 3σ for confirmed source detection

$\varepsilon(E_\gamma)$ - gamma-ray detection efficiency of the detector for photon energy (E_γ) as defined earlier

$B(E_\gamma)$ - background noise in the detector system at photon energy (E_γ)

A - sensitive area of the telescope open to the incoming gamma-ray photons in cm^2

T - observation exposure time in seconds

ΔE - energy band of observation in keV

From this expression it can be seen that for the same exposure and bandwidth the telescope sensitivity can be improved by increasing the detector efficiency (*i.e.* increasing its thickness) and/or increasing the size A of the detector. Because of the square root factor, to increase the sensitivity of the telescope by a factor of three the area must be increased by approximately a factor 10. Unfortunately, for a non-focusing telescope as a result of increasing the detector size, the amount of background noise effecting the instrument also increases (approximately in line with the detector volume). Furthermore, increasing the size of the detector has serious repercussions with regards to the payload of the spacecraft. Below 100 keV, the background is dominated by cosmic diffuse photons incident through the telescope aperture whilst around 1 MeV the leaking of photons through the shielding system becomes the dominating effect. Additional background events above 100 keV are caused by cosmic ray interactions (spallation and neutron induced) in the telescope, whose rates are highly dependent on the area of the detector. Therefore, for lower energy gamma-ray instruments, the size of the telescope aperture has a significant effect on the amount of background contaminating the observations and efficiency can be improved more effectively by increasing the thickness of the detectors than by increasing the thickness of the veto shielding.

2.2.3 Imaging Techniques

Imaging is an important capability for a gamma-ray telescope as it enables a confident source detection, especially in crowded regions where it is difficult to distinguish between many source signals. By creating an image, more than one source can be observed at the same time and it becomes possible to make serendipitious detections of new and transient objects. Furthermore, sensitivity can be increased by using longer exposure times as, in most cases, an estimate of the background is made at the same time as the observation.

For energies up to ~10 keV, grazing incidence optics can be employed to focus X-rays (*e.g. XMM-Newton*; Aschenbach & Braeuninger 1988). As photon energy increases further this technique is limited by the grazing angle, which increases the focal length (and hence telescope size) to an impractical value (*e.g. ASCA* satellite, 0.7–10 keV, has a focal length of 3.5m; Serlemitsos et al. 1995). However, in the laboratory, a gamma-ray lens based on Bragg diffraction has demonstrated a potential technology for future Gamma-ray missions (von Ballmoos et al. 2001).

The following sections will discuss three commonly employed methods of gamma-ray imaging in the 20 keV to 1 MeV energy range.

2.2.3.1 Compton Telescopes

A Compton telescope uses a double layer detector construction to track the behaviour of a scattered gamma-ray photon and uses the Compton kinematics to reconstruct the incident photon direction. The top layer is constructed of a lower density detector to encourage Compton scattering of the photon. The lower layer consists of a higher Z material to prevent further scattering by ensuring all the remaining photon energy is deposited via the PE effect. The detectors will individually record the energy and position of each interaction and by using Eqn. 2.2 the scattering angle of the photon can be determined. This is then used to define an event circle for each photon within which the source is said to be located. See Chapter 3 for a detailed description of the kinematics involved. Images can be produced by projecting the resulting event circles back onto a grid, which will intersect at the location of the source.

An example of a Compton telescope was COMPTEL on-board the *Compton Gamma-ray Observatory (CGRO)* which operated between 800 keV–30 MeV with an angular resolution of ~1° and uses a liquid scintillator (NE 213A) as the upper detector layer and a NaI scintillator as the lower layer (Schoenfelder et al. 1996). The double layered detector system in the IBIS telescope on-board the *INTEGRAL* mission also has the capacity to image by this method. However, the primary role is not to use Compton scattering as a direct imaging method, but to use the event circle to limit the background events (see Chapter 3 for details).

2.2.3.2 Collimators and Temporal Modulation Imaging

The simplest imaging configuration uses a collimator to restrict the amount of sky that the detector can see. The angular resolution is therefore equal to the field of view of the telescope. As an extension of this method, temporal modulation involves coding the position of source using its detection by the telescope as a function of time, which is achieved by scanning the collimator across the sky. As a source is scanned, the detector measures the rise and fall of the flux as a function of time, thereby determining the position of the source. The *HEAO-1* A4 experiment is an example of a scanned collimated detector system. The primary result from A4 is an all-sky survey in the 20–180 keV range in which 72 sources were detected (Levine et al. 1984). The survey took place during 1978–9 and used 2 NaI/CsI phoswich scintillation detectors with the satellite in spinning mode so that the entire sky can took 6 months. The field of view (1.5° ×20°) of each detector was defined by passive mechanical slat collimators and active CsI collimators and veto shields inclined at +/- 60° to the satellite equatorial plane. In a scanning modulation collimator (SMC) angular resolution is improved by adding grids of wires placed across the detector which act as transmission windows. Similarly for a rotational modulation collimator (RMC), where the collimator itself rotates about an axis. The *HEAO-1* A3 experiment is an example of an SMC which operated in the 2–10 keV energy range (Gursky et al 1978). The chief disadvantage of these systems is that the intrinsic variability of a source is lost during the temporal modulation of the flux. This can be overcome by using phoswich RMC, which consists of a segmented phoswich detector in conjunction with a single grid of wires. The variability induced by the imaging system can therefore be determined by subtracting data from one set of detector 'strips' from the data from the other set, as done by the WATCH burst monitor on-board *GRANAT* (Brandt, Lund, and Rao 1990). The earth occultation technique performs limited ($\sim$ 1°) angular resolution imaging by using the earth as temporal modulator. The source flux is determined by measuring the step in count rate profile as the source sets below or rises above the earth's limb. This method has been employed with the BATSE experiment on-board *CGRO* producing an all sky survey based on 9 years of observations between 1991–2000 (Shaw et al. 2004).

2.2.3.3 Coded Mask Apertures

A coded mask is a tool for imaging which spatially modulates the source signal. In conjunction with a pixellated detector plane, this technique is able to create images of arcminute resolution in the 10 keV–10 MeV energy regime, thereby spanning the range between the capability of grazing incidence X-ray telescopes and Compton telescopes. Building from the basic principle of a pin-hole camera, a coded mask consists of an optimal distribution of opaque and transparent elements through which a source will project a shadow onto the detector plane (shadowgram). This pattern will change depending on the position of the source in the sky and thus, by knowing the pointing of the telescope, an image of the area of sky can be reconstructed by correlating the recorded image with a decoding array derived from the mask pattern (also see in't Zand 1992, for alternative deconvolution methods). In the soft gamma-ray domain, the optimal transparency of the mask pattern is 50% due to the high levels of background. A simplified model of a coded mask imaging system is shown in Fig. 2.5.

The angular resolution of a coded mask telescope dθ is defined by:

$$d\theta = tan^{-1}\left(\frac{C}{H}\right) \tag{2.6}$$

where C is the mask element size and H is the mask-to-detector distance. The point source location accuracy of a source significance σ is:

$$d\phi = \frac{tan^{-1}\left(\frac{D}{H}\right)}{\sigma} \tag{2.7}$$

where D is the detector pixel size $\leq$C. The point source location accuracy of a source can be improved by fitting a point spread function to the image. The fit to this function can be improved by increasing the number of detector pixels per mask element.

Mission	Instrument	Energy range	Field of view	Angular Resolution
GRANAT	SIGMA	30 keV–1.3 MeV	5°×5°	10′
BeppoSAX	WFC	2–30 keV	20°×20°	5′
INTEGRAL	IBIS	20 keV–10 MeV	29°×29°	12′
Swift	BAT	15–150 keV	2 sr	17′

Table 2.1: Properties of coded mask telescopes. See text for details and references.

The most prevalent mask design is a repeating pattern based on cyclic difference sets. A uniformly redundant array (URA) is a configuration where each spatial frequency between the mask elements is sampled the same amount of times and more than once, as opposed to non-uniformly redundant array (NRA) where every spatial frequency is sampled just once. Assuming a perfect imaging system, a URA mask produces a system point spread function (SPSF) with flat sidelobes. This method is successful in the fully-coded field of view (where the entire basic pattern shadow falls onto the detector), but in the partially coded field of view (or in a non-perfect system), the autocorrelation function will produce systematic noise which complicates the deconvolution process and the SPSF will have peaks in the sidelobes corresponding to ghost sources. URAs can be mapped onto both square and hexagonal grids, termed modified URA (MURA) and hexagonal URA (HURA) respectively, examples of which can be seen in Fig. 2.6. For an in depth discussion of coded mask techniques see in't Zand (1992) and Skinner & Ponman (1994).

The *GRANAT* mission was launched in 1989 and was in orbit until 1998 during which time it observed approximately one quarter of the sky and made a deep exposure of the Galactic centre region (~9 Ms). The Russian/French SIGMA telscope (Paul et al. 1991) on-board *GRANAT* was the first of its kind to use the coded aperture reconstruction technique for imaging the sky in soft gamma-rays (30 keV–1.3 MeV) with a maximum sensitivity in the 40–100 keV energy band. SIGMA detected a number of new sources including the BH-binary GRS 1915+105 (Bouchet

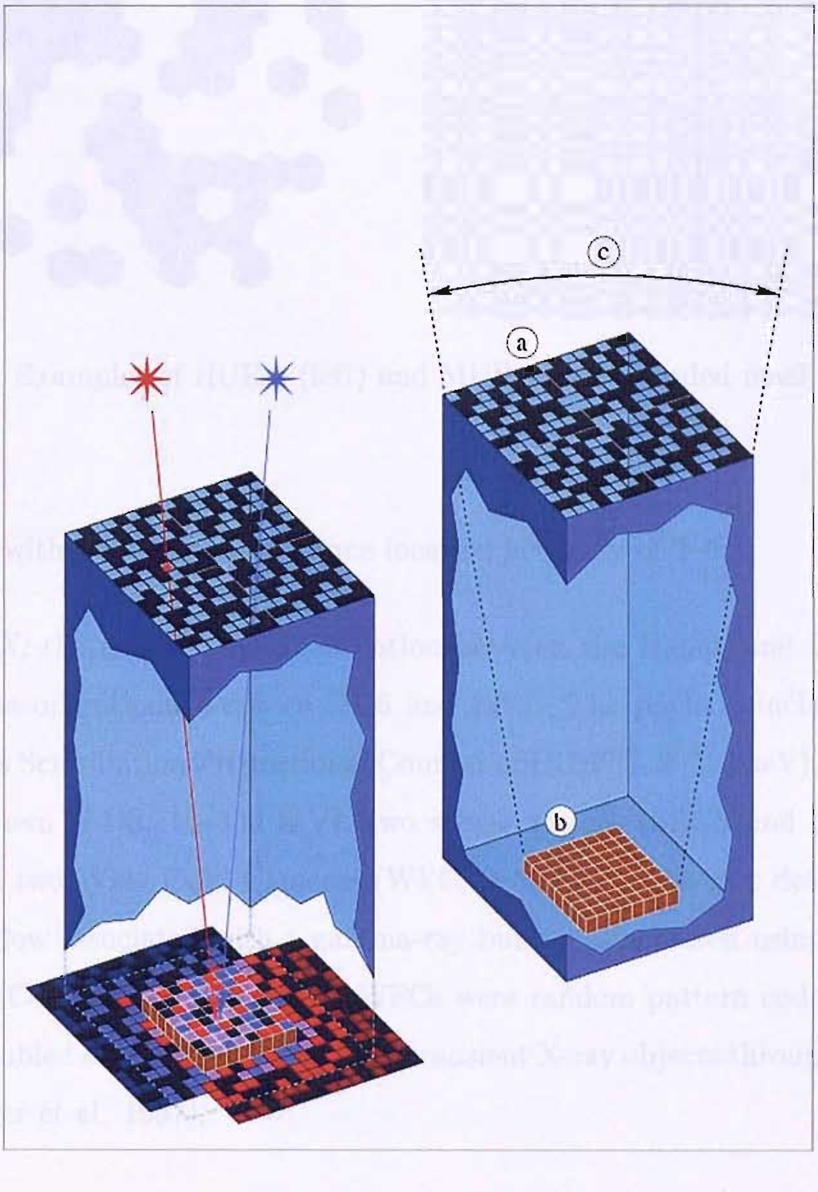

Figure 2.5: Layout of the IBIS coded mask system illustrating (a) the coded mask aperture, (b) pixellated detector plane and (c) field of view of the telescope. The superimposition of the shadows created by two sources though the mask is shown in the left hand diagram *(Picture Credit: ISDC)*.

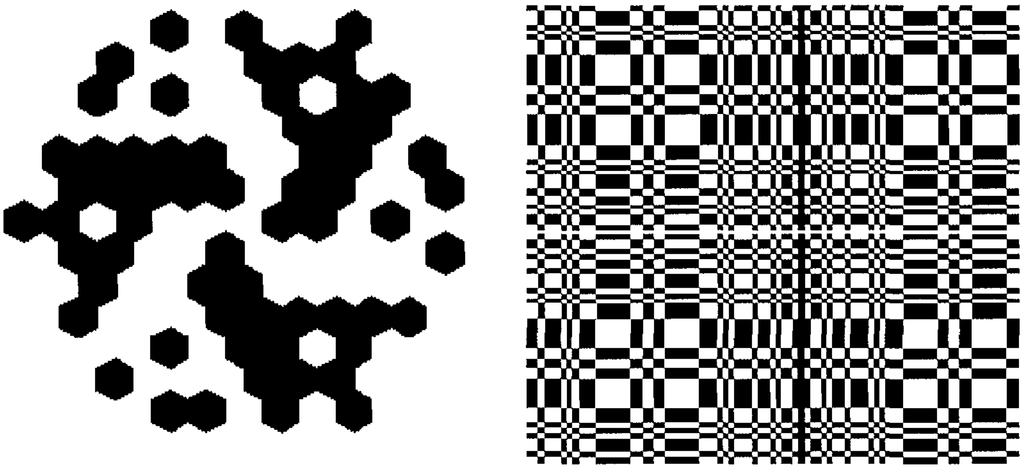

Figure 2.6: Examples of HURA (left) and MURA (right) coded mask patterns.

et al. 1993) with a typical point source location accuracy of 2–3′.

BeppoSAX, the result of a collaboration between the Italian and Dutch space agencies, was operational between 1996 and 2002. The payload included a High Pressure Gas Scintillation Proportional Counter (HPGSPC, 3–120 keV), a Phoswich detector system (PDS, 15–300 keV), two spectrometers (LECS and MECS, 0.1–10 keV) and two Wide Field Cameras (WFC, 2–30 keV). The first detection of an X-ray afterglow associated with a gamma-ray burst was achieved using the MECS instrument (Costa et al. 1997). The WFCs were random pattern coded mask imagers and enabled extensive monitoring of transient X-ray objects through a 20° field of view (Jager et al. 1997).

The NASA *Swift* mission (Gehrels et al. 2004) was launched recently in November 2004 with the primary goal of studying GRBs. The Burst Alert Telescope (BAT, Barthelmy et al. 2004) has a 2 sr field of view (partially coded) and acts as a burst trigger at which point the rapid slew capability of the observatory enables the burst site to be observed promptly with the optical/UV and X-ray instruments on-board. As a consequence of this functionality, the BAT is also being used to generate an all-sky survey in the energy range 15–150 keV with similar sensitivity to the *INTEGRAL*/IBIS survey (see Chapter 5). These surveys will complement each other well due to the different observational strategies of the two missions.

The *INTEGRAL*/IBIS telescope is reviewed in detail in Sec. 2.3 below and a comparison of the relative sensitivities of the instruments described above is given in Chapter 5 (Table 5.1).

2.3 The *INTEGRAL* Mission

The INTErnational Gamma-Ray Astrophysical Laboratory (*INTEGRAL*) was launched from a Proton rocket on 17th October 2002 from the Baikonur Cosmodrome in Kazakhstan. Designated a medium-sized ESA mission, the observatory aims to undertake the fine imaging of astrophysical objects along with spectroscopy of diffuse and line emission in the soft gamma-ray regime (20 keV–10 MeV). *INTEGRAL* is placed in a 72 hr eccentric orbit enabling the spacecraft to spend 80% of the time at above an altitude of 60 000 km, thereby avoiding unwanted radiation from the Earth's proton and electron belts. This section will introduce the IBIS telescope, which is the particular concern of this thesis, detailing both the imaging and detector systems together with the shielding methods employed to reduce background contamination. Fig. 2.7 illustrates the main components of the satellite.

2.3.1 IBIS - The Imager on-Board the *INTEGRAL* Satellite

The imager, IBIS, consists of two pixellated detector planes placed in parallel beneath a coded mask aperture system and is designed for the fine imaging and precise location of soft gamma-ray sources in the energy range 20 keV–10 MeV. The

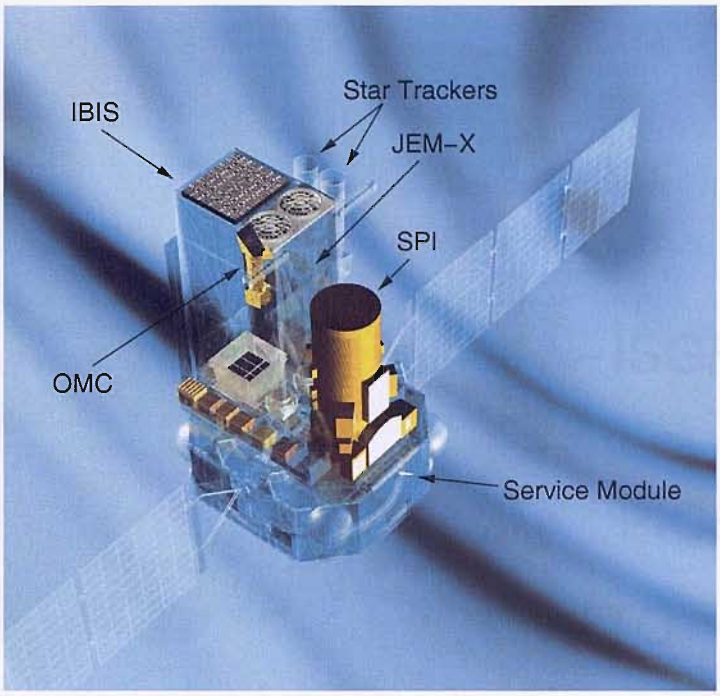

Figure 2.7: The *INTEGRAL* satellite.

telescope shielding system is composed of a combined collimator and VETO assemblage. The detector characteristics are listed in Table 2.2 and a representation of the detector arrangement is shown in Fig. 2.8. The imager operates with two detectors ISGRI (*INTEGRAL* Soft Gamma-Ray Imager) and PICsIT (PIxellated Caesium Iodide Telescope), covering complementary energy ranges (15 keV–1 MeV, 175 keV–10 MeV respectively) allowing the detection of both high and low energy gamma-rays. Information for this review is taken from Ubertini et al. (2003) and ISDC (2005) unless otherwise stated.

2.3.1.1 Detectors

ISGRI, the upper detector layer, consists of 16384 CdTe detectors organised into 8 identical modules, each containing 32×64 pixels (Lebrun et al. 2003). Each

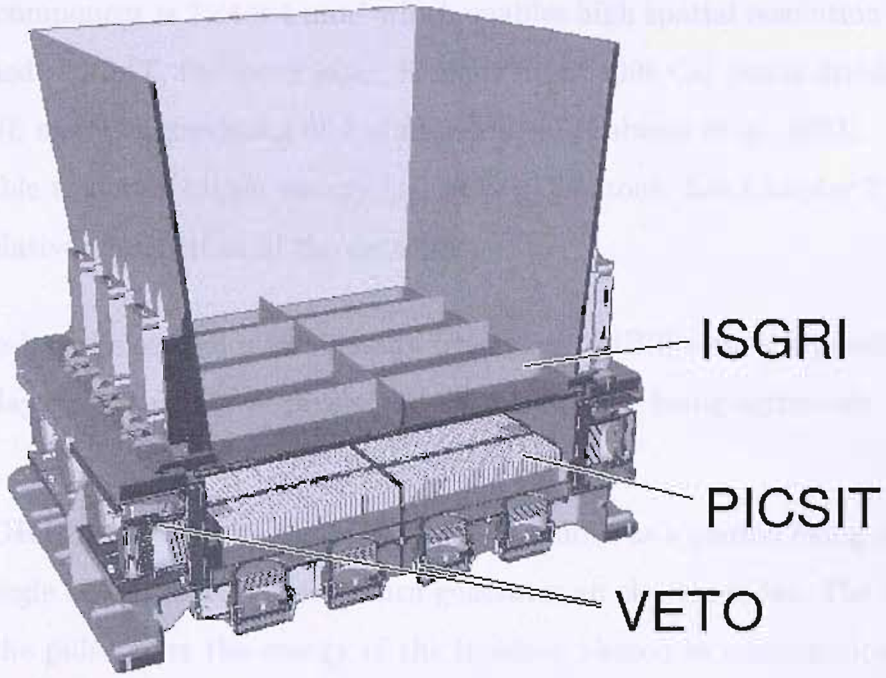

Figure 2.8: Cutaway of the IBIS instrument showing the PICsIT and ISGRI detector planes and shielding systems. Above the detector planes is the lower part of the collimating system (hopper).

Parameter	Value
Energy Range	15 keV–10 MeV
Sensitive Area	2600 cm^2 CdTe (ISGRI); 2890 cm^2 (PICsIT)
Energy resolution	9% (@100 keV); 10% (@1 MeV)
Field of view	9° (fully coded); 19° (50%)
Continuum sensitivity 3σ, 10^6 s (ph cm^{-2}s^{-1})	3.8×10^{-7} (@100 keV); 5.0×10^{-7} (@1 MeV)
Line sensitivity 3σ, 10^6 s (ph cm^{-2}s^{-1})	1.3×10^{-5} (@100 keV); 3.8×10^{-4} (@1 MeV)
Angular resolution	12′
Point source location accuracy	30″
Timing resolution	61μs (for E <1 MeV and Compton Mode); 1 ms (Spectral timing, no imaging); 2000 s (E>175 keV with imaging)

Table 2.2: Table of IBIS characteristics *(Ubertini et al. 2003).*

detector component is 2×4 × 4 mm^3 which enables high spatial resolution images to be obtained. PICsIT, the lower layer, is made up of 4096 CsI pixels divided into 16 modules (8 modules consisting of 2 semi-modules) (Labanti et al. 2003). This layer is more able to detect higher energy (>100 keV) photons. See Chapter 3 (Fig. 3.1) for the relative sensitivities of the detectors.

The on-board electronics can classify five types of IBIS events depending on the detector layer and number of pixels in each sub-module being activated:

- **ISGRI single event** - An ISGRI event is defined as a photon being stopped by a single ISGRI pixel which in turn generates an electric pulse. The amplitude of the pulse gives the energy of the incident photon in combination with the pulse rise time. If more than one pixel in the same module is excited at the same time, the events are rejected.
- **PICsIT single event** - In this case, a photon does not interact with the top detector layer (ISGRI) but is stopped by the lower layer producing a single scintillation flash from which the energy of the photon can be determined.
- **PICsIT multiple event** - PICsIT is capable of detecting photons that have scattered between two or more pixels in an array. The photon energy from a multiple event is determined from the sum of the energy deposits from each of the pixels. The site of the most energetic interaction is taken to be the detected position of the photon.
- **Compton event** - A Compton event occurs when a photon, after interaction with one of the layers, also deposits energy in the other detector. Compton single and multiple events can be detected in the case of adjacent PICsIT pixels being excited. In Compton mode, the telescope is able to span an extended energy range and Compton kinematics can be applied to track the incoming

photon scattered between the detector planes defining an event circle. This can then be used to increase the signal-to-noise of a detection, see Chapter 3.

2.3.1.2 Coded Mask

The IBIS coded mask is a square array (dimensions 1064 × 1064 × 16 mm^3) of 9025 cells in a MURA configuration (see Fig 2.9). 50% of the cells are tungsten elements of size 11.2 × 11.2 mm^2 which are opaque to photons in the operational range of the telescope. The remaining 50% cells are open, with an off-axis transparency of 60% at 20 keV. The mask is supported by a honeycomb structure which is detailed in Chapter 4. The coded mask produces a shadowgram in which photons from both the source and background are distributed. Cross-correlation techniques enable an image to be deconvolved for the fully coded field of view. Additional cleaning takes place to reconstruct the image for the partially coded field of view as detailed in Goldwurm et al. (2003).

2.3.1.3 Collimator and Veto

The collimating system consists of a hopper (see Fig. 2.8), the four walls of the payload module and four strips of 1mm thick tungsten around the edge of the mask. This creates a passive shield which limits the solid angle of the IBIS detector up to hundredss of keV. An anti-coincidence BGO scintillator VETO system is used to reject background events and shields the underneath and sides of the telescope to the top level of the ISGRI detector.

Figure 2.9: IBIS coded mask.

2.3.2 Spectrometer and other instruments

The IBIS imager is joined by three further instruments, the spectrometer (SPI) and two monitoring cameras (optical and X-ray):

- **SPI - SPectrometer on *INTEGRAL*** - provides fine spectral analysis of both discrete and extended gamma-ray sources over an energy range of 20 keV–8 MeV with a 16° field of view (fully coded) and 2° angular resolution. The spectrometer consists of an array of 19 individual hexagonal high-purity germanium detectors cooled to 85 K. Cosmic rays incident on the detector will damage the germanium crystals therefore the unit is temporarily heated up approximately every 6 months to recover spectral resultion. The SPI coded mask is composed of 3 cm thick tungsten hexagonal elements in a HURA pattern with 120° rotational symmetry, placed 1.7 m above the detector plane and having 80% transparency at 50 keV. A BGO anti-coincidence shield acts as a veto system for events caused by photons and particles entering from the telescope side. A plastic scintillator placed under the coded mask detects charged particles coming through the telescope field of view and also provides a veto signal. The veto shielding can be used as a burst trigger and for polarisation studies. (Vedrenne et al. 2003)

- **JEM-X - Joint European X-ray Monitor** - consists of two identical X-ray monitors (JEM-X 1 & 2) sensitive in the energy range between 3–35 keV. The field of view of each instrument is 4.8° (fully coded) with an angular resolution of $3'$. This telescope also employs a coded mask imaging system, the mask placed 3.4 m above the monitors. The mask is a 535 mm diameter HURA pattern with a transparency of 25%. The detectors themselves are collimated gas chambers filled with xenon (90%) and methane (10%).The collimator helps reduce events caused by the cosmic diffuse X-ray background (Lund et al. 2003). The window of the detector, below the collimator, is made of thin beryllium foil which allows a good transmission of X-rays whilst being impermeable to the detector gas. In-flight, the detector has experienced a loss in sensitivity due to changes in gas gain leading to a large fraction of events being classed as background and hence rejected (ISDC 2004).

- **OMC - Optical Monitoring Camera** - consists of an Johnson V filter optical system focused onto a large format CCD (1024×2048 pixels). The filter is centred on 550 nm with a limiting sensitivity ~18 mag. The telescope has a field of view of 5° and angular resolution of $23''$(Mas-Hesse et al. 2003).

2.4 Summary

This chapter has introduced the techniques by which astronomical gamma-ray sources can be detected and imaged. Specifically, it has been shown that the IBIS imager on board the *INTEGRAL* mission, a coded mask telescope, consitutes an improvement in imaging capability over past missions due to its large field of view and improved angular resolution. The surveying capability of the instrument will be demonstrated in Chapter 5. Meanwhile, the next two chapters will present work undertaken as part of the calibration of the IBIS telescope, namely determining the energy resolution of the Compton mode (Chapter 3) and correcting for the off-axis response of the telescope (Chapter 4).

Chapter 3

Investigation of IBIS Compton Mode

3.1 Introduction

This work was performed as part of the IBIS ground calibration campaign, the aims of which include verifying scientific performance, determining the spatial and spectral characteristics of the instrument and providing inputs for response matrix generation. One such input is the energy resolution as a function of energy for the detector planes, ISGRI and PICsIT.

As introduced in Chapter 2, the IBIS imaging instrument consists of two detectors, ISGRI and PICsIT, sensitive in complementary energy ranges and able to be used as independent devices or together in Compton mode. A Compton mode event is defined when a single photon interacts, and deposits energy, in both the ISGRI and PICsIT detectors. This chapter will describe the ground calibration work performed to determine the spectral characteristics and energy resolution of this mode.

The following section will give a outline of IBIS Compton mode and describe the source spectra reconstructed from the calibration runs. Section 3.2.3 will describe how the individual energy resolutions of the ISGRI and PICsIT detectors can be used to determine the energy resolution of Compton mode.

3.2 Compton Mode

The ISGRI detector is most sensitive below 200 keV, above which the efficiency starts to degrade (see Fig. 3.1, dotted line), and while the energy range of PICsIT is higher (~175 keV–10 MeV, dashed line in Fig. 3.1) these events are histogrammed on-board, as the *INTEGRAL* telemetry rate is too low to transmit all events, resulting in some loss of spectral information. All ISGRI events are transmitted using photon-by-photon mode (PPM), as the energy reconstruction is complicated and a complete spectral reconstruction cannot be performed prior to transmission. Therefore, Compton mode was developed to improve the sensitivity of the IBIS instrument over the intermediate ISGRI/PICsIT energy range (~200 keV to above 5 MeV). Compton mode detects photons scattered between the two detectors and thus is able to detect photons at a higher energy than with ISGRI alone. Additionally, an on-board selection algorithm is able to significantly reduce the level of background events, potentially providing much improved sensitivity. The selection algorithm exploits the Compton kinematics of the scattering to select only those photons arriving within a specified field of view. As a consequence of this, these events can now be transmitted in full unlike PICsIT events.

A Compton single event is defined as one deposit in ISGRI and one in PICsIT, whereas a Compton multiple event is one deposit in ISGRI and more than one in PICsIT (*cf.* PICsIT single and multiple events). Consider a photon that deposits

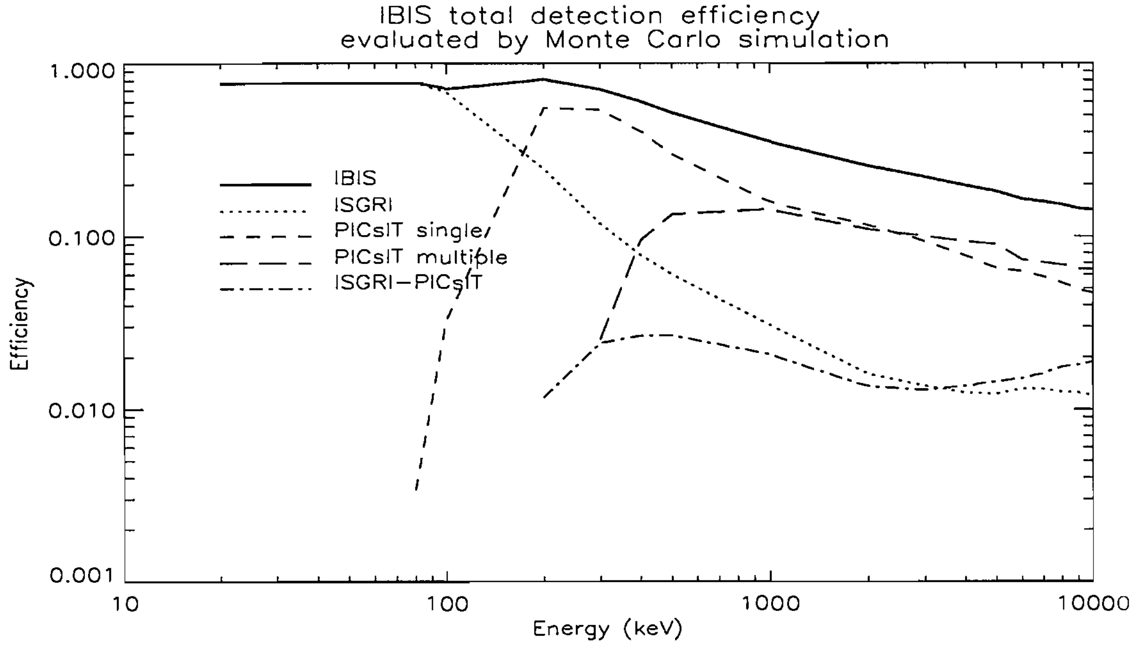

Figure 3.1: Detection Efficiency of the modes of IBIS.

energy E_i in ISGRI at $A(Y_i,Z_i)$ then Compton scatters and gets fully absorbed in PICsIT at $B(Y_p,Z_p)$, depositing the remainder of its energy E_p (see Fig. 3.2). The total energy of the photon is therefore $E_i + E_p$. The scattering angle, ϕ, of the Compton event can be calculated from Equation 3.1 which defines the event annulus and the geometrical scattering angle (between scattered photon direction and telescope axis), θ, from Equation 3.3. The selection algorithm defines two parameters, the Compton selection angle Φ and the Compton selection energy E_{sel}. If $\theta - \phi > \Phi$ then the photon is said to originate from outside the field of view (FOV) of the telescope and is rejected (Equation 3.5). If the event cone and the FOV cone intersect ($\theta - \phi \leq \Phi$) then the event is said to have possibly originated within the telescope field of view and is accepted as a source Compton event. The Compton selection energy E_{sel} specifies a high energy threshold above which the algorithm is not performed, usually 1 MeV. The telescope and passive shielding components are considered transparent to photons above this energy and all Compton events can be considered valid.

What has just been described is a simple case of forward scattering. In practice it is very difficult to determine whether the photon interacts with ISGRI first (forward scatter, Fig. 3.2) or PICsIT first (back scatter, Fig. 3.3). Events occuring in CdTe detectors (ISGRI) exhibit a rise-time dependent on the depth of the interaction in the detector material, where the deeper the interaction the longer the rise time. It can be shown that the lower energy photons expected to interact with ISGRI are most likely to interact shallowly in ISGRI. Therefore, it can be shown that low energy ISGRI events with long rise times are more likely to have been the result of back scatters. Alternatively, each Compton event can be described as both a forward and back scatter with two event cones being calculated and, if valid solutions exist, tested in conjunction with the compton selection Equations 3.5 and 3.6.
Compton scattering angle, ϕ for forward scattering:

$$\cos\phi = 1 - \left(\frac{m_o c^2}{E_p} + \frac{m_o c^2}{E_p + E_i}\right) \tag{3.1}$$

and back scattering:

$$\cos\phi = 1 - \left(\frac{m_o c^2}{E_i} + \frac{m_o c^2}{E_p + E_i}\right) \tag{3.2}$$

Geometrical scattering angle, θ for forward scattering:

$$\tan\theta = \frac{BC}{AC} \tag{3.3}$$

and back scattering:

$$\tan(\pi - \theta) = \frac{BC}{AC} \tag{3.4}$$

Where BC is the horizontal distance between the centers of triggered ISGRI and PICsIT pixels and AC is the distance between the detector planes (see Fig. 3.2 and 3.3).

Compton selection algorithm:

If E > E_{sel} no compton selection is performed, else test for forward scattering:

If,

$$\theta - \phi > \Phi \tag{3.5}$$

event is rejected, else test for back scattering:

If,

$$\theta - (\pi - \phi) > \Phi \tag{3.6}$$

the event is rejected, else event is accepted (modified from Laurent 1998).

3.2.1 Compton Calibration Data

The Compton calibration work described in this chapter makes use of data from two of the IBIS calibration campaigns - the instrument phase in Laben and a final Payload calibration (PLGC) in ESTEC. A range of radioactive test sources were employed, providing spectral lines between 356 keV and 2754 keV, in addition to dedicated background runs taken throughout the campaigns. The runs at Laben included configurations for verifying the Compton selection function (see Sec. 3.2.4 and Table 3.1). Operating separately during ground calibration, ISGRI had an energy range of ~15 keV–800 keV and PICsIT of ~175 keV–10 MeV. Working together in Compton mode produced a similar energy range of ~190 keV–10 MeV.

3.2.2 Compton Energy Spectra Reconstruction

To determine the spectrum of Compton events as recorded by the IBIS telescope, a value for Compton energy for each interaction must be calculated. This is simply the

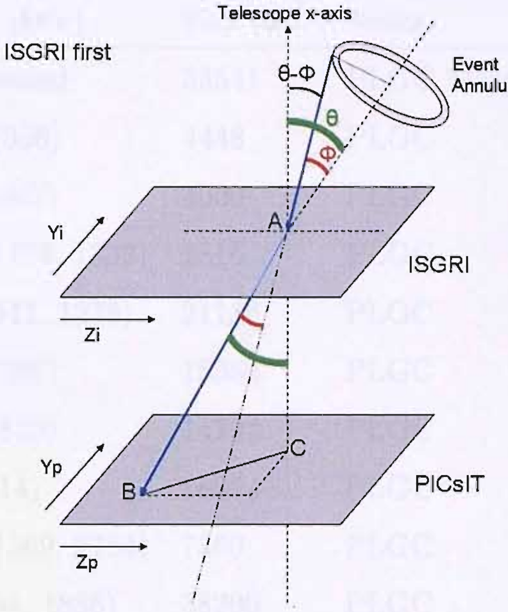

Figure 3.2: Compton kinematics for forward scattering showing Compton scattering angle ϕ, geometrical scattering angle θ. (Y_i, Z_i) and (Y_p, Z_p) define the ISGRI and PICsIT detector planes. A and B mark the first and second sites of interaction, with BC measuring the horizontal distance between the two sites.

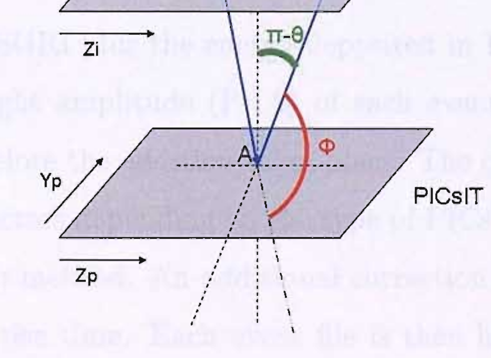

Figure 3.3: Compton kinematics for back scattering.

Run id	Source (keV)	Exp (sec)	Notes
8888	Background	33541	PLGC Merged spectrum
4758	^{133}Ba (356)	4448	PLGC
4760	^{137}Cs (662)	4000	PLGC
4763	^{60}Co (1175, 1332)	2816	PLGC
4767	^{22}Na (511, 1275)	21136	PLGC
4785	^{113}Sn (392)	18384	PLGC
4791	^{54}Mn (835)	14704	PLGC
4818	^{85}Sr (514)	18024	PLGC
4834	^{24}Na (1369, 2754)	7360	PLGC
4851	^{88}Y (898, 1836)	38200	PLGC
4859	^{65}Zn (1100)	25552	PLGC
4319	^{88}Y (898, 1836)	7163	Laben E_{sel} = 1.3 MeV, $\Phi = 5°$
4320	^{88}Y (898, 1836)	7200	Laben E_{sel}= 1.3 MeV, $\Phi = 15°$

Table 3.1: Selection of PLGC-ESTEC and Instrument-Laben calibration runs used in the calibration of the Compton mode. Laben runs include specific Compton selection angle, Φ and Compton selection energy, E_{sel} configurations. The PLGC runs used the default Compton selection parameters, E_{sel}=10 MeV and Φ=9.5° .

energy deposited in ISGRI plus the energy deposited in PICsIT. Detector software records the pulse height amplitude (PHA) of each event which is then converted into photon energy before the addition takes place. The conversion code selects the appropriate scaling factors depending on the type of PICsIT event (single/multiple) and data transmission method. An additional correction is applied to ISGRI-PHA values dependent on rise time. Each event file is then histogrammed and divided by the exposure to produce a time scaled spectrum (counts/sec). Finally, the background spectrum is subtracted from each source spectra.

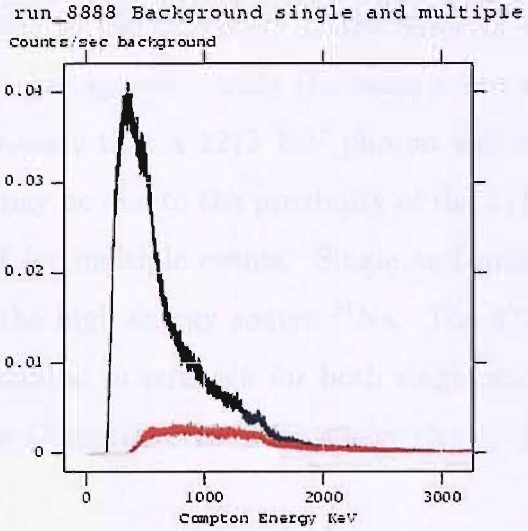

Figure 3.4: Compton Energy Spectra for PLGC background events. Black=single events, red=multiple events.

3.2.2.1 Sample Compton Event Spectra

Single and multiple Compton events from PLGC calibration data (Table 3.1) have been analysed to evaluate spectral characteristics. Figure 3.4 shows the background spectra for single and multiple Compton events. It is clear that fewer multiple events occur compared to single events by a factor of ~10. These spectra also illustrate the detector cut-off energies for each type of event; ~200 keV for single and ~500 keV for multiple. The feature at 1.4 MeV is attributed to the radioactive decay of ^{40}K in the surrounding concrete walls of the calibration site which was clearly seen in the PICsIT background.

Figure 3.5 shows single and multiple Compton spectra for ^{22}Na (background subtracted). Clear photopeaks are seen at 511 keV and 1275 keV where full photon absorption has occured. The lower energy components can be interpreted as blurring of the Compton continuum and edge (maximum energy transfer via Compton scattering, ~250 keV below photopeak) for the higher energy line, and continuum noise below 511 keV due to the proximity of the detector cut-off. The 1275 keV line for multiple events has approximately the same count rate as in single mode, suggesting equal probability that a 1275 keV photon will iteract as a multiple or single event. but this may be due to the proximity of the 511 keV line to the higher energy detector cut-off for multiple events. Single and multiple event spectra are shown in Fig. 3.6 for the high energy source ^{24}Na. The 2754 keV line has a very low count rate but is similar in strength for both single and multiple events. The 1369 keV line for single Compton events has a very clearly defined Compton edge.

3.2.3 Compton Energy Resolution

The energy resolution of the ISGRI and PICsIT detectors has been determined (Bird et al. 2003). A simple empirical model provides an adequate description for ISGRI at low energies:

$$\frac{\Delta E_i}{E_i} = 200 \times E_i^{-0.7} \tag{3.7}$$

where E_i is the energy deposit in ISGRI in keV. While, for PICsIT single events a physical model is used:

$$\frac{\Delta E_p}{E_p} = 2.35 \times \frac{\sqrt{nE + N^2}}{nE_p} + k \tag{3.8}$$

where n is the number of electrons/keV created in the CsI scintillator (~29.1), E_p is the energy deposit in PICsIT in keV, N is the electronic noise (~950 electrons rms) and k is an intrinsic resolution term (typically 1.7%) (Bird et al. 2003). Both models determine the energy resolution as a percentage at FWHM and are shown in Fig. 3.9.

A model for the energy resolution of Compton events (ISGRI event and PICsIT

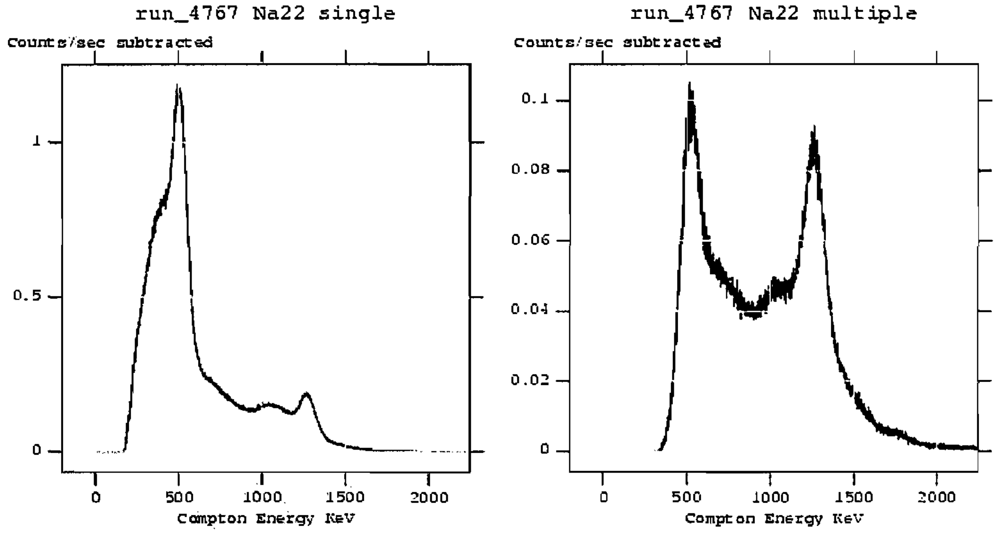

Figure 3.5: Compton Single and Multiple spectra for ^{22}Na source

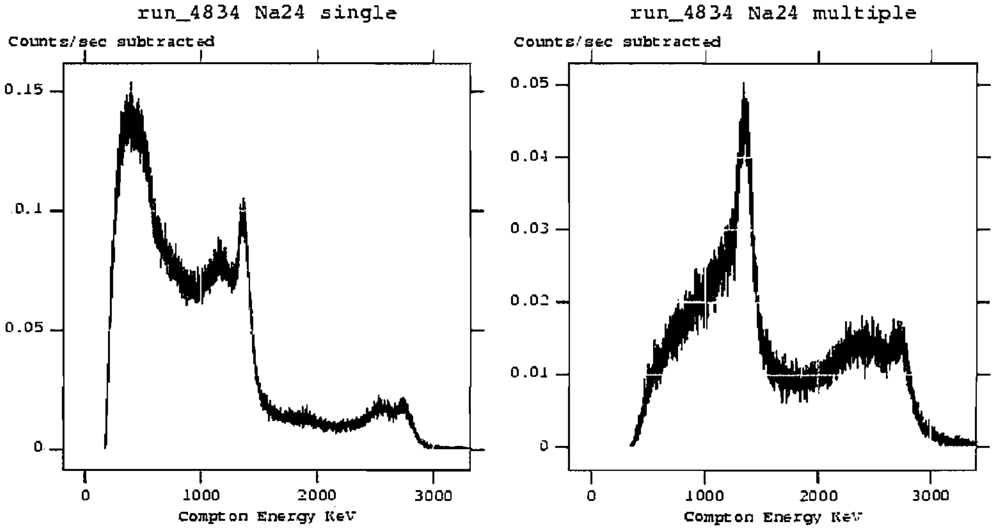

Figure 3.6: Compton Single and Multiple spectra for ^{24}Na source

Source	E_c (keV)	Mean E_i (keV)	E_i (% of E_c)	E_p (% of E_c)
^{133}Ba	356	87.1	24.5	75.5
^{113}Sn	392	114.7	29.3	70.7
^{22}Na	511	155.4	30.4	69.6
^{85}Sr	514	163.8	31.7	68.3
^{137}Cs	662	205.5	31.1	68.9
^{54}Mn	835	281.7	33.8	66.2
^{88}Y	898	316.6	35.3	64.7
^{65}Zn	1100	379.8	34.5	65.5
^{60}Co	1175	361.1	30.7	69.3
^{60}Co	1332	412.5	30.9	69.1
^{22}Na	1275	399.6	31.3	68.7
^{24}Na	1369	427.3	31.2	68.8
^{88}Y	1836	423.9	23.1	76.9
^{24}Na	2754	311.9	11.3	88.7

Table 3.2: Relative energy deposits in ISGRI and PICsIT for a range of Compton event energies. E_i and E_p are estimated to have an error of ±1%.

single event) can therefore be derived by combining these models according to the fraction of total Compton energy deposited in ISGRI and PICsIT. The mean energy deposited in ISGRI, E_i, for a given photon has been determined by analysing the calibration runs for a selection of sources/energies. For a particular source run, events were selected only when the total Compton energy, E_c, was near (±10 keV) to the expected photopeak energy. Figure 3.7 plots the percentage of Compton event energy deposited in ISGRI. The PICsIT energy, E_p, is simply E_c-E_i. The mean ISGRI energy share as determined by this method is listed in Table 3.2 for a range of energies, together with the energy share expressed as a percentage of E_c for both ISGRI and PICsIT.

The relative energy deposits in ISGRI and PICsIT are found to be approximately 30% and 70% of the Compton energy respectively over the calibrated energy range. The Compton energy resolution (if assumed to be purely statistical) can be modelled by adding the relative detector energy resolutions (Equations 3.7 and 3.8) in quadrature, thus:

$$\Delta E_c = \surd[(\Delta E_i)^2 + \Delta E_p)^2] \tag{3.9}$$

where ΔE_i is the ISGRI energy resolution for E=0.3E$_c$ and ΔE_p is the PICsIT energy resolution for with E=0.7E$_c$

As an alternative method, FWHM measurements were taken for a selection of Compton energy spectra. To improve accuracy, only the higher energy half of the photopeak was measured and then the width was doubled. This leading edge is less likely to be altered by additional line features and continuum. Figure 3.8 displays the measured Compton energy resolution for single events for the two methods. The energy resolution derived from assuming a 30%:70% energy deposit in the detectors is systematically lower than the measured FWHM values. This discrepency is not fully understood. Differences will arise due to the mean value (used to determine the ISGRI:PICsIT energy split) not being a true representation of the average energy deposited in the detector for a particular energy. Additionally, the distribution of the scattering angles has not been considered. At low energies, where photons are more likely to interact with ISGRI first, smaller deposits in ISGRI will preferentially result in a forward scatter and therefore a detected Compton event. Meanwhile, at higher energies, back scattering will dominate. This could explain the shape of Fig 3.7. The Compton energy resolution as measured by the FWHM, can be compared with the other IBIS detection modes in Fig. 3.9 and lies between the energy resolution for PICsIT single and PICsIT multiple events.

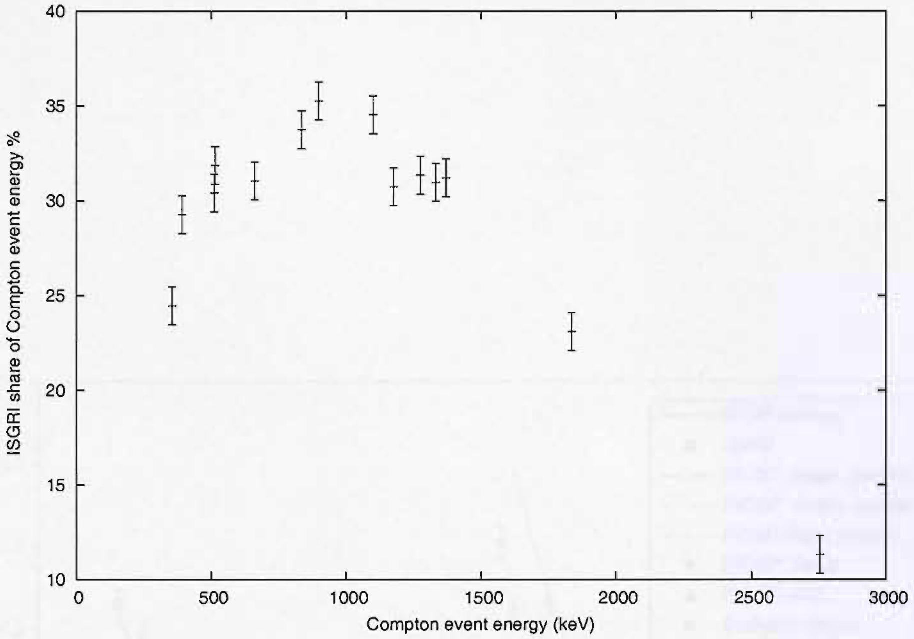

Figure 3.7: The ISGRI energy share E_i as a function of Compton event energy. Over the calibrated energy range (<2 MeV) E_i ~30%.

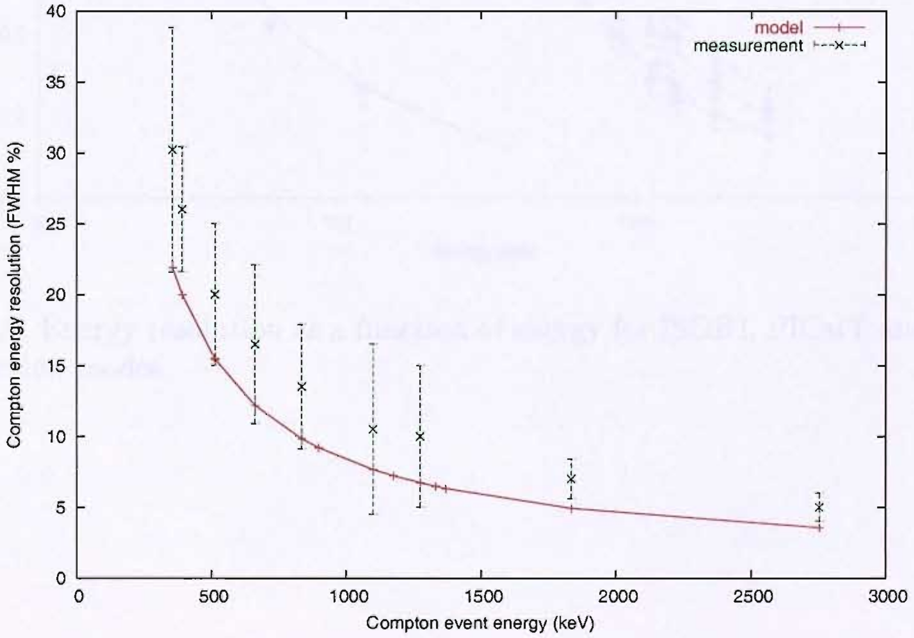

Figure 3.8: Energy resolution for Compton single events via direct FWHM measurement and a model determined from the mean ISGRI/PICsIT energy share.

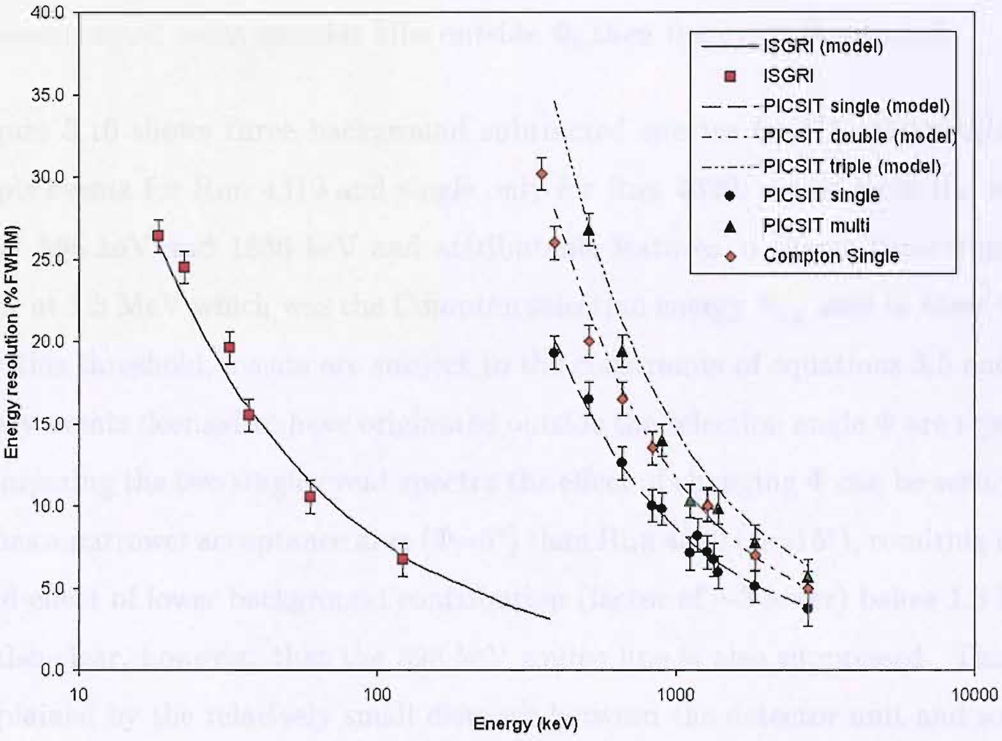

Figure 3.9: Energy resolution as a function of energy for ISGRI, PICsIT and Compton detection modes.

3.2.4 The Compton Selection function

The Laben calibration campaign included acquisitions to test the Compton selection algorithm (see Table 3.1). As explained in Section 3.2, the on-board selection algorithm is available to reduce background by only allowing those events inside a specified field of view to be transmitted. The field of view is described by the Compton selection angle Φ and the selection is applied below some energy E_{sel}. If the reconstructed event annulus falls outside Φ, then the event is rejected.

Figure 3.10 shows three background subtracted spectra for ^{88}Y, the single and multiple events for Run 4319 and single only for Run 4320. Apart from the source lines at 898 keV and 1836 keV and attributable features, a sharp discontinuity is present at 1.3 MeV which was the Compton selection energy E_{sel} used in these tests. Below this threshold, events are subject to the constraints of equations 3.5 and 3.6, whereby events deemed to have originated outside the selection angle Φ are rejected. By comparing the two single event spectra the effect of changing Φ can be seen. Run 4319 has a narrower acceptance area (Φ=5°) than Run 4320 (Φ=15°), resulting in the desired effect of lower background contribution (factor of ~3 lower) below 1.3 MeV. It is also clear, however, that the 898 keV source line is also suppressed. This can be explained by the relatively small distance between the detector unit and source, whereby the source appears off-axis for which the algorithm is not optimised (Bird et al. 2003). Image analysis (Fig. 3.11) confirms the increased collimation for Run 4319. The histograms to the right show counts per pixel though a cross-section of the source image. The source profile is stronger and wider for Run 4320 with Φ=15°. It has therefore been shown that the Compton selection algorithm reduces the background count rate by limiting the number of events flagged as Compton interactions without significantly degrading the detection of the source.

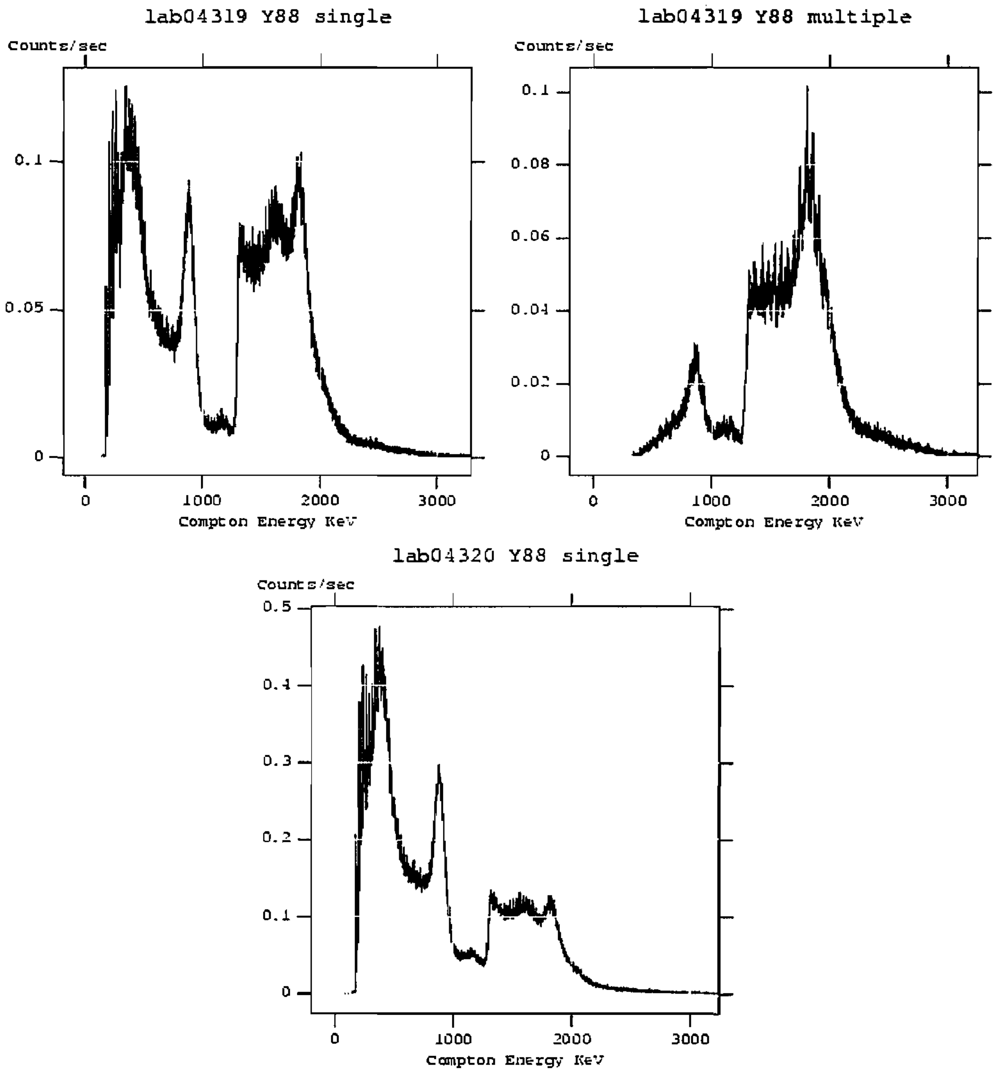

Figure 3.10: ^{88}Y Compton spectra. The Compton selection angle Φ is 5° and 15° for Runs 4319 and 4320 respectively. The selection energy, E_{sel}, is 1.3 MeV in both cases.

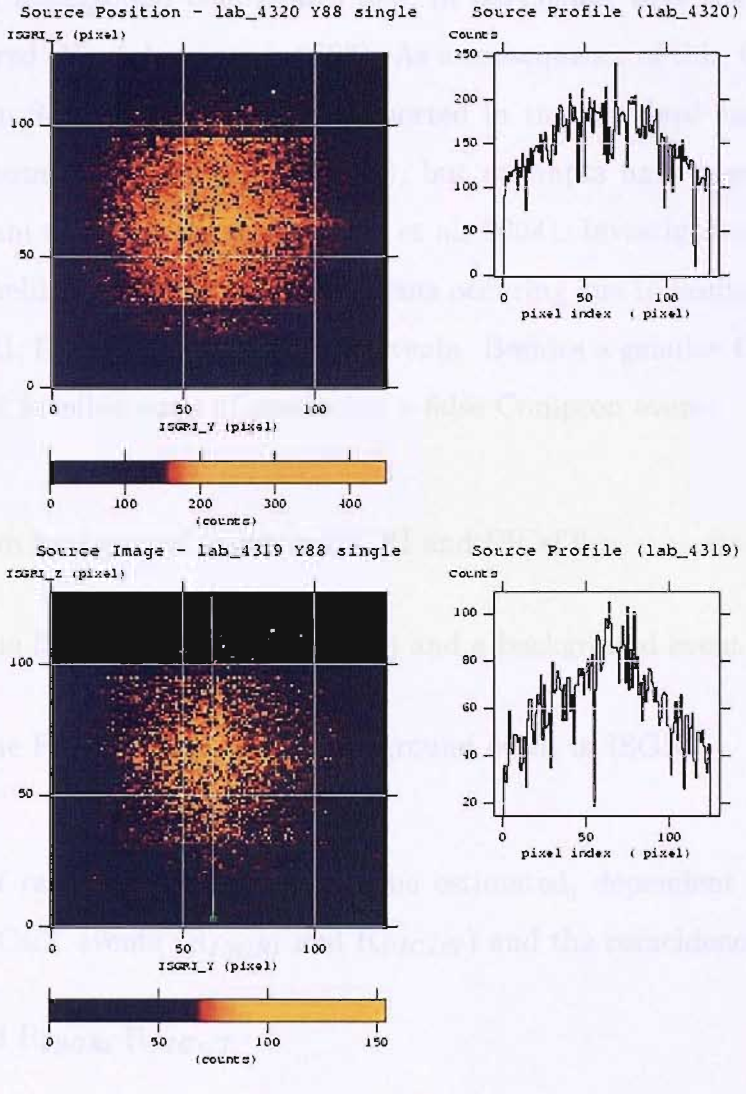

Figure 3.11: ^{88}Y image and slice for Compton Single events. Top panel: run 4320 with Φ=15°, bottom panel: run 4319 with Φ=5°.

3.3 In-flight Performance of Compton Mode

In-flight calibration of PICsIT has concluded that the detector is experiencing higher than expected background count rates and, in particular, that the background is highly structured (Nantalucci et al. 2003). As a consequence of this, Compton Mode as explained in Sec. 3.2 is not being supported in the standard analysis package, OSA (Goldwurm et al. 200; ISDC 2005), but attempts have been made by the instrument team to utilise the data (Forot et al. 2004). Investigation has also been made of the likelihood of false Compton events occuring due to random coincidences of either ISGRI, PICsIT and background events. Besides a genuine Compton event, there are three possible ways of producing a false Compton event:

- A random background event in ISGRI and PICsIT
- A genuine ISGRI event (from source) and a background event in PICsIT
- A genuine PICsIT event and a background event in ISGRI

The rate of random coincidences can be estimated, dependent on the rate of ISGRI and PICsIT events (R_{ISGRI} and R_{PICsIT}) and the coincidence window, τ:

$$R_{random} = 2\ R_{ISGRI} \cdot R_{PICsIT} \cdot \tau$$

The coincidence window τ is the maximum delay between two events for them to be considered as a Compton Event and is set between ~1 and 5μs. It has been proposed that the recorded IBIS Compton Data is severly contaminated by false events which need to be subtracted before any meaningful results can be extracted (Segreto 2003; Forot at al. 2004). Unfortuntely, as a result of these contaminations, it is unlikely that this mode will be used as originally intended.

Attempts have been made to use IBIS as a true Compton telescope (see Chapter 2) including high energy images of the Crab and sources outside the detector field of view as seen through the mask (>29°). Marcinkowski et al. (2004) have had some success in imaging a Gamma-ray burst (GRB–030406) detected 36° off-axis.

This work on Compton Mode stresses the importance of both ground and in-flight calibration. In particular, in-flight calibration is required to confirm or, if necessary, re-evaluate the performance of the telescope determined during the ground calibration campaign. The next Chapter will describe one aspect of in-flight calibration performed to correct the reconstructed flux of sources detected with the IBIS/ISGRI telescope.

Chapter 4

Calibrating the Off-axis Response of the IBIS/ISGRI Telescope

4.1 Introduction

This Chapter describes the calibration work undertaken post-launch to correct the reconstructed source flux detected by the IBIS/ISGRI telescope for the effects of the coded mask support structure. Due to poor in-flight performance of the PICsIT detector, the work described here consists solely of IBIS/ISGRI observations.

As described in Chapter 2, the IBIS telescope views the sky through a coded mask imaging device. The coded mask and detector are in a cyclic configuration where the mask is larger than the detector plane. The advantage of this over a box configuration (detector plane and mask are same size) is that the fully coded field of view (FCFOV) is larger ($\sim 9^\circ \times 9^\circ$ for IBIS). A source is said to be fully coded when the shadow created through the mask by the source photons falls entirely onto the detector plane (all sources photons falling on the detector have passed throught the mask). In a box configuration, only on-axis sources are fully coded. For IBIS, sources with an off-axis angle of ~4.5° are fully coded. The partially coded field of view (PCFOV) for IBIS extends to ~ 29° × 29° corresponding to source off-axis angles >15° (see Fig. 4.1). The sensitivity of the instrument will decrease from a constant value in the FCFOV to the edge of the telescope field of view. This is a simple geometrical effect and a correction is applied in software.

It has been discovered that there is an additional effect, linked to off-axis angle, that has a detrimental effect on the imaging efficiency. Figure 4.2 displays the reconstructed source flux processed with OSA v.3.0 for one orbit (revolution 45) of Crab observations. Each data point is a pointing (or Science Window, ScW) of ~1500 s. It can be seen clearly that the variation in flux is linked to the off-axis angle, θ, of the source. The lowest flux is when the source is on the edge of the field of view and at a maximum when on-axis. This off-axis response has been attributed to the absorption of flux by a NOMEX-honeycomb support structure attached to the IBIS coded mask. Source photons striking the mask support will travel though a greater amount of material as the off-axis angle of the source increases. An additional effect occurs when the azimuth angle, ϕ, of the source is considered. This is the possible origin of the spread in source flux, independent of off-axis angle, where flux is seen to vary by ~10% for θ=4° in the 20–25 keV energy band (as described in Section 4.3.2). Both effects are seen to vary with photon energy. The off-axis response of the NOMEX is reduced as energy increases (see Fig. 4.4) and can be considered a negligible effect above 120 keV. Similarly, the azimuth variation deteriorates as energy increases, the effect being most pronounced at energies below 40 keV, the range at which the ISGRI detector is at its most sensitive.

Both the azimuth and off-axis angle effects will particularly affect the IBIS survey work described later in this thesis, which aims to create large sky maps by mosaicing together the entire ~ 29° × 29° area of individual observations. To gain accurate

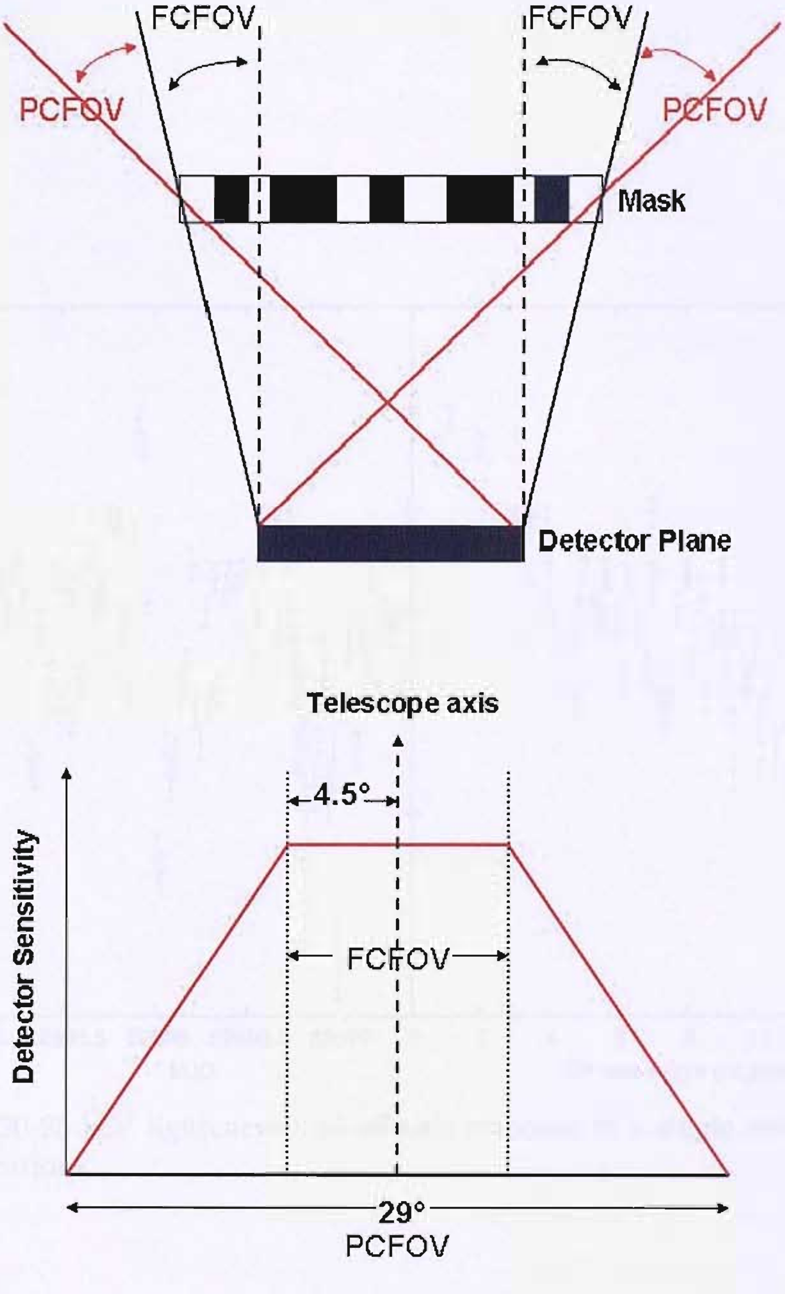

Figure 4.1: The fully-coded (FCFOV) and partially-coded (PCFOV) of the IBIS telescope. The diagrams are not to scale.

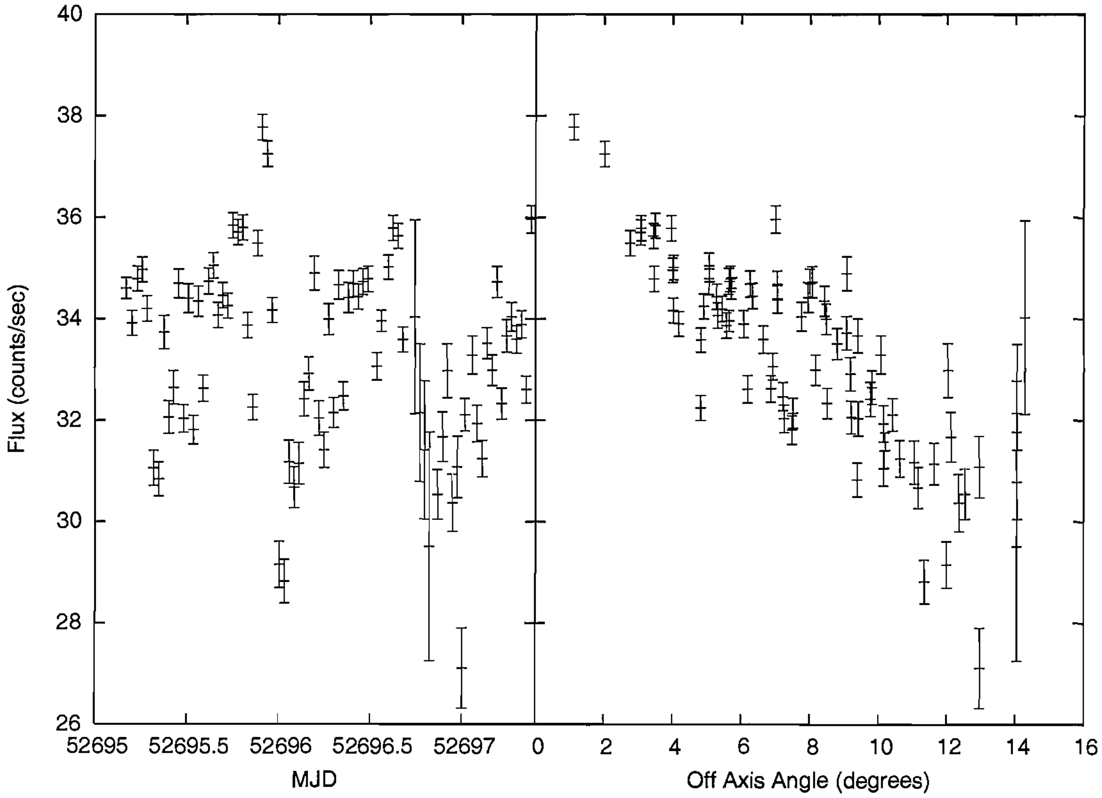

Figure 4.2: 20-25 keV lightcurve and off-axis response of a single revolution (45) of Crab observations.

and realistic reconstructed fluxes from sources in the survey mosaics (and off-axis serendipitous detections in pointed observations), one must correct for this effect. A correction for these effects has not been included in the instrument response matrices or previous versions of the *INTEGRAL* data processing software "OFFLINE STANDARD ANALYSIS" (OSA; Goldwurm et al. 2003) and it is therefore the aim of this chapter to present an additional correction.

An off-axis correction model, based on calibration observations of the Crab and averaged over azimuth angle, has been formulated and is presented in Sec. 4.3. This correction has been included in OSA v.4.0 and, as such, is available to all users of IBIS data and significantly improves the quality of the data products (imaging, spectral and timing) compared to data processed with previous versions of the software. Furthermore, Section 4.4 endeavours to model the azimuth dependancy of the telescope so as to produce a complete correction model for the azimuth and off-axis response of the telescope.

4.2 Calibration Data Set

The Crab has been established as a reliable calibration source in X-ray and gamma-ray energies on account of the strong, stable emission from the rapidly spinning pulsar and associated pulsar wind nebula (*e.g.* Kirch et al. 2005 and references therein). Due to the orbit of the *INTEGRAL* satellite, the Crab was first observed by the IBIS telescope in February 2003 and continues to be observed approximately every six months. The observed IBIS/ISGRI spectrum agrees well with published values (Di Coco et al. 2004; Zombeck 1990). The initial off-axis correction model (Sec. 4.3) utilises the early observations (revolutions 43–170) while the data set used for Correction 2 (Sec 4.4) consists of revolutions 102, 170, 239 and 300 only.

Information available from processed data includes flux, flux error, (RA, Dec) for the source and pointing (i.e. the telescope on-axis coordinates) and (Y, Z) of pointing and source position on detector plane (i.e. pixel coordinates) from which the azimuth and off-axis angles can be calculated. Care must be taken when calculating the off-axis angles to make sure the projection onto a spherical sky is taken into account.

Off axis angle $\theta=$

$$\cos^{-1}\Big(\cos(90^\circ-\delta_p)\cos(90^\circ-\delta_s)+\sin(90^\circ-\delta_p)\sin(90^\circ-\delta_s)\cos(\alpha_p-\alpha_s)\Big) \quad (4.1)$$

in degrees, where (α_p, δ_p) are the pointing coordinates and (α_s, δ_s) are the source coordinates.

Or alternatively:

$$\theta = P \cdot \sqrt{(Y_p - Y_s)^2 + (Z_p - Z_s)^2} \quad (4.2)$$

where Y_p, Z_p are the pointing pixel coordinates and Y_s, Z_s are the source pixels. To convert from pixels to degrees use conversion factor P=0.08228. This method has good agreement with the spherical distance method for small off-axis angles but due to tangent plane projection, pixels cover a smaller area of sky at larger off axis angles.

Azimuthal angle ϕ, in degrees:

$$\phi = \tan^{-1}\left(\frac{Y_s}{Z_s}\right) \quad (4.3)$$

It is important to use the detector (Y, Z) coordinate system to calculate the azimuth position of the source, as the roll angle (pointing of telescope axis with respect to the sky) of the telescope can change between revolutions.

Revolution	Type	Number of ScW
43-45	Near-axis 5x5 dithers and various off-axis	247
102	5x5 dither, on-axis staring (0.27°)	36
170	θ=0.27° -19°	70
239	fine and normal 5x5 dither, half circle at θ=4°	93
300	full circle at θ=10° , 5x5 dither	72

Table 4.1: Calibration data set of Crab observations. The effective exposure is approximately 1500 s per Science Window (ScW).

4.3 Correction 1 : Average Off-axis Response

This section will describe the 'average' off-axis angle correction models delivered with OSA v.4.0. There has been no consideration of the physical reason for the shape of the response or of any azimuthal effects. What follows is simply a method to improve the imaging efficiency by correcting the Crab light-curve for the off-axis dependent effect. Revolutions 43-45, 102 and 170 have been processed with OSA v.3.0 in seven energy bands: 15–20, 20–25, 30–35, 35–40, 40–60 and 60–120 keV. Figure 4.3 illustrates clearly the shape of the off-axis response for Rev 170 in the 20–25 keV energy band. The response is not smooth; it can be seen to fall off steeply between θ ~0° -2° , then appears flat between θ ~4.5° -10° (between the FCFOV and PCFOV at 50% response). Data at very large off-axis angles have large error bars as a consequence of being on the very edge of the PCFOV, where the detector is less sensitive. Figure 4.4 shows the off-axis dependency of the reconstructed Crab flux for all seven energy bands. As energy increases the change in response is not as pronounced.

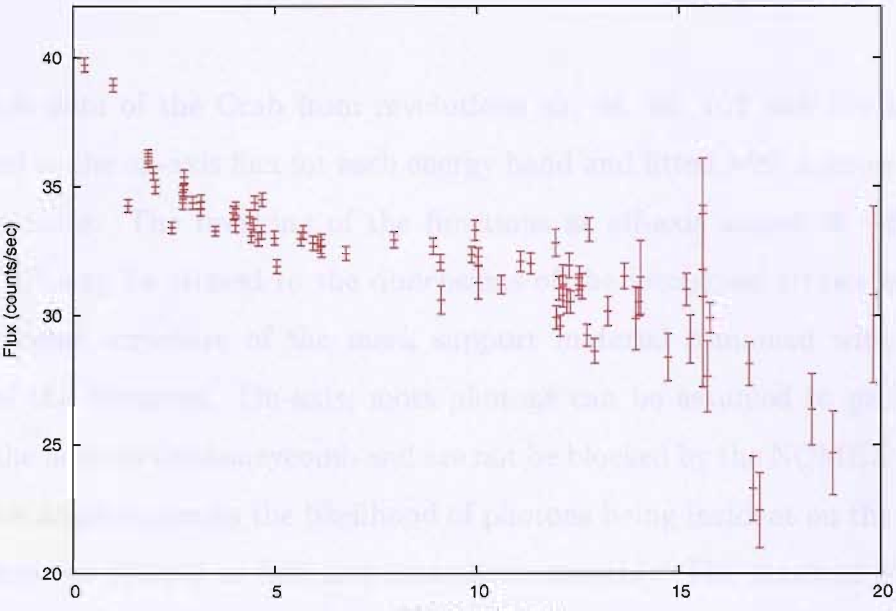

Figure 4.3: Off-axis response for revolution 170, 20–25 keV energy band. Each point is one ScW (~2000 s)

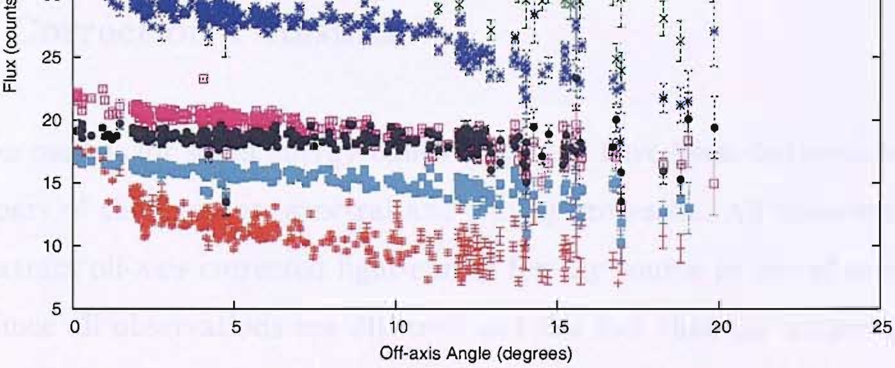

Figure 4.4: Off-axis response of revolutions 43, 44, 45, 102 and 170 for all seven energy bands. Note the flatter response at higher energies.

4.3.1 The Off-axis Correction

Calibration data of the Crab from revolutions 43, 44, 45, 102 and 170 have been normalised to the on-axis flux for each energy band and fitted with a series of simple linear functions. The breaking of the functions at off-axis angles of ~2°, 4° and possibly 10° may be related to the dimensions of the hexagonal straws making up the honeycomb structure of the mask support material combined with the field of view of the telescope. On-axis, most photons can be assumed to pass straight through the holes of the honeycomb and are not be blocked by the NOMEX walls. As the off-axis angle increases the likelihood of photons being incident on the NOMEX straws increases sharply at first and then more smoothly. The break at 4° possibly corresponds to when the source leaves the FCFOV, whereby not all of the photons will encounter the mask support. The resulting correction models are illustrated in Fig. 4.5. The correction functions for 35–40 keV and 40–60 keV are seen to cross at ~6° off-axis. This is attributed to the large spread in the observed response of the data. Above 120 keV the response is considered flat. From these models, efficiency maps have been created to be included in OSA v.4.0 light-curve software (see Fig. 4.6).

4.3.2 Correction 1 Results

Correction models for seven energy bands (Fig. 4.6) have been delivered with OSA v.4.0 as part of the imaging, spectral and timing processes. All observers are now able to extract off-axis corrected light-curves for any source in one of seven energy bands. Since all observations are dithered and the fact that the majority (>80%) of photons are detected below 30 keV, these corrections provide a real improvement to the off-axis response of the reconstructed source flux, which would otherwise introduce large systematic variations. To illustrate this, Fig. 4.7 displays the off-axis

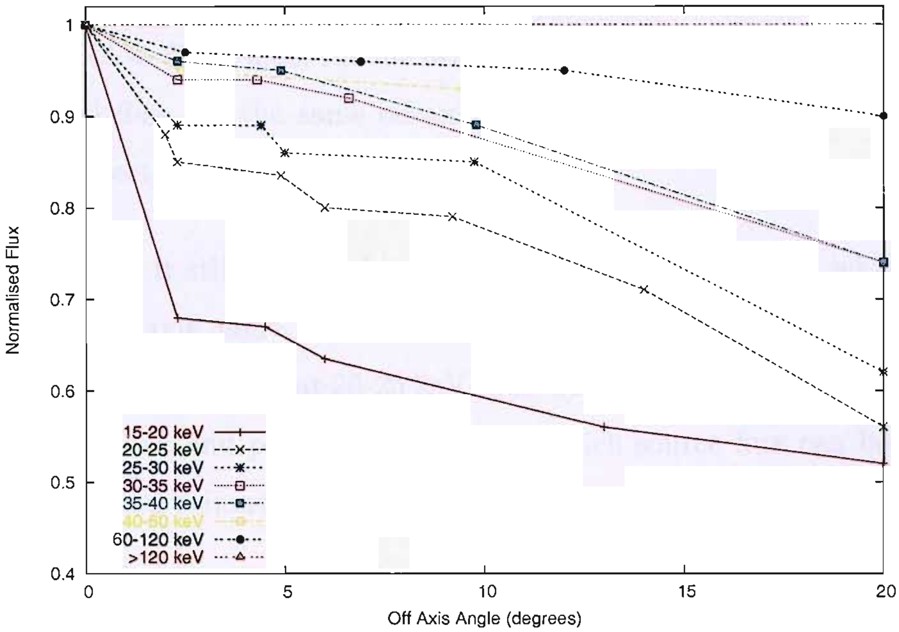

Figure 4.5: Correction models for the off-axis angle response for seven energy bands.

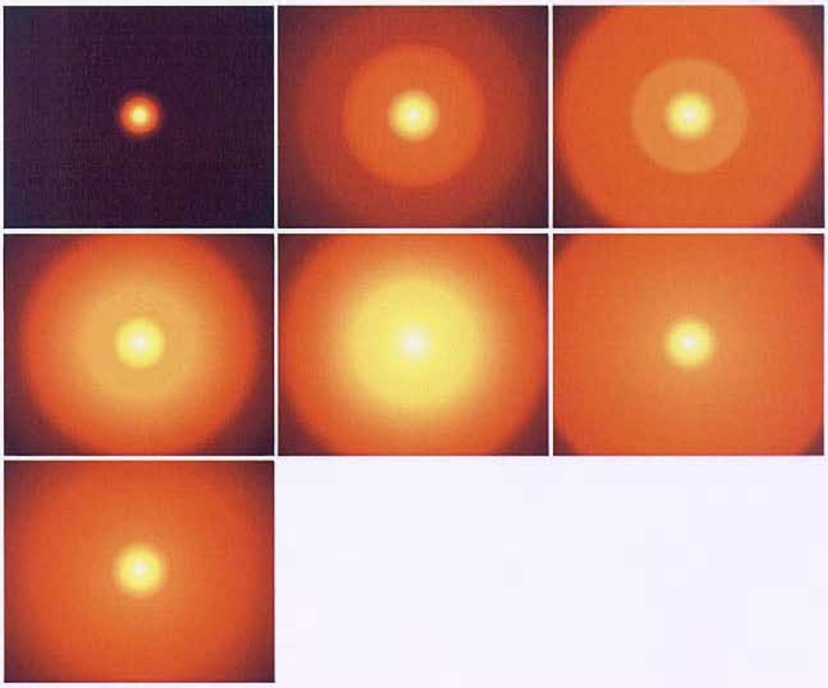

Figure 4.6: Efficiency maps delivered with OSA v.4.0 to correct for θ. First row from top: 15-20, 20-25, 25-30 keV, second row: 30-35, 35-40, 40-60 keV, third row: 60-120 keV.

corrected Crab flux compared to the uncorrected flux for Rev 170 in the 20–25 keV energy band. Below 5° off-axis, the uncorrected flux varies by $>20\%$. The variation in the corrected flux, for the same off-axis range, is reduced to $<10\%$ as a direct result of the correction model for this energy band.

Nethertheless, is it still undesirable to have such a spread in data which appears independent of off-axis angle. At 4° off-axis, the reconstructed source flux for the Crab is seen to vary by $\sim10\%$ at 20-25 keV. The next section investigates the source of this spread in flux and provides a model by which source flux can be corrected for both off-axis and azimuth effects.

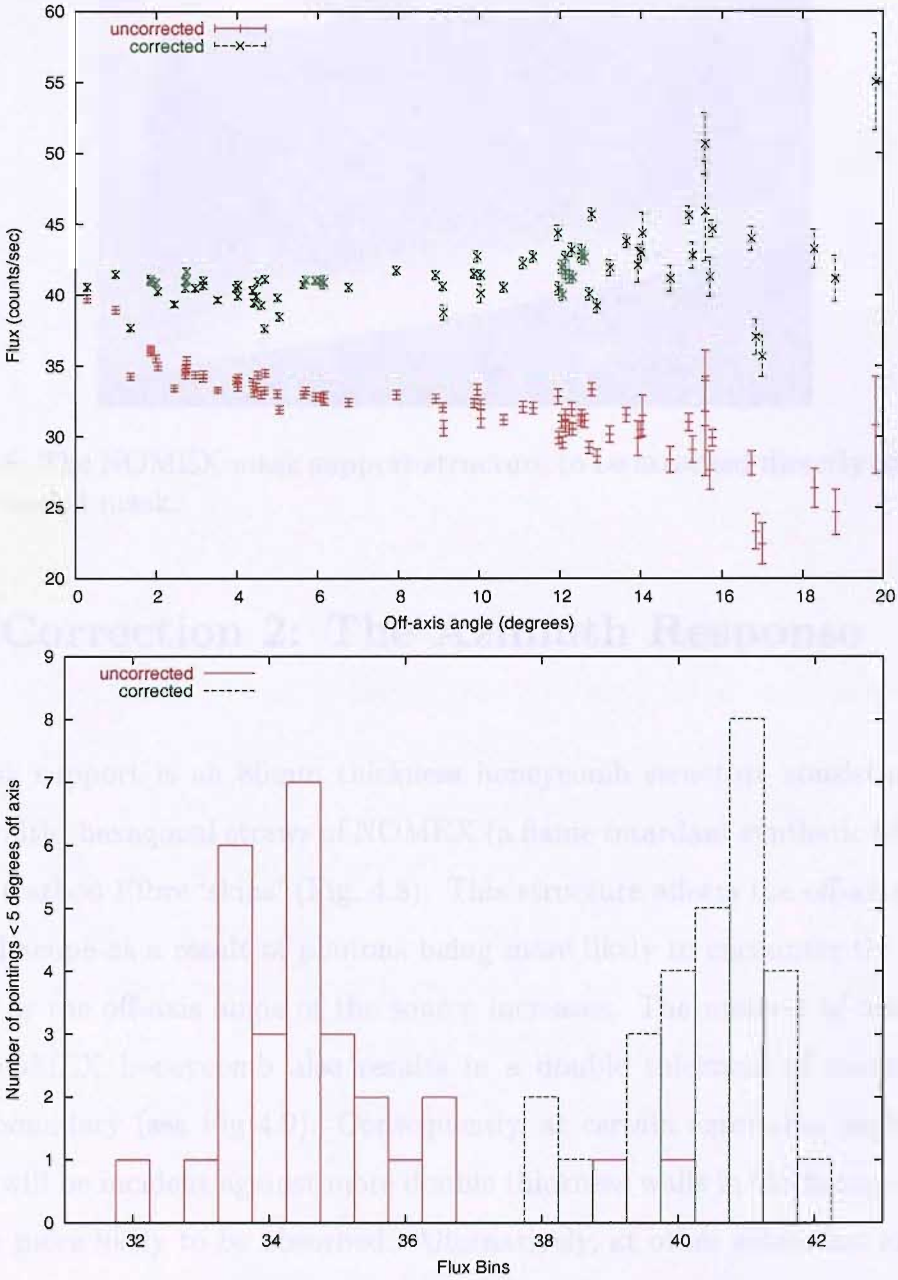

Figure 4.7: Revolution 170 before and after correction. The histogram shows the reduced flux dispersion for pointings where off-axis angle $\theta < 5°$.

Figure 4.8: The NOMEX mask support structure to be attached directly underneath the IBIS coded mask.

4.4 Correction 2: The Azimuth Response

The mask support is an 80mm thickness honeycomb structure consisting of thin (~mm width) hexagonal straws of NOMEX (a flame retardant synthetic fibre) glued between Carbon Fibre 'skins' (Fig. 4.8). This structure affects the off-axis response of the telescope as a result of photons being more likely to encounter the NOMEX material as the off-axis angle of the source increases. The method of manufacture of the NOMEX honeycomb also results in a double thickness of material along the ±y boundary (see Fig 4.9). Consequently, at certain azimuthal angles, source photons will be incident against more double thickness walls in the honeycomb, and therefore more likely to be absorbed. Alternatively, at other azimuthal angles, the photon will be incident upon only single thickness walls, or a combination of single and double. This, combined with the off-axis related effect, is most likely the source of the variation in reconstructed source flux.

This section will detail the strategy to correct for both off-axis and azimuth ef-

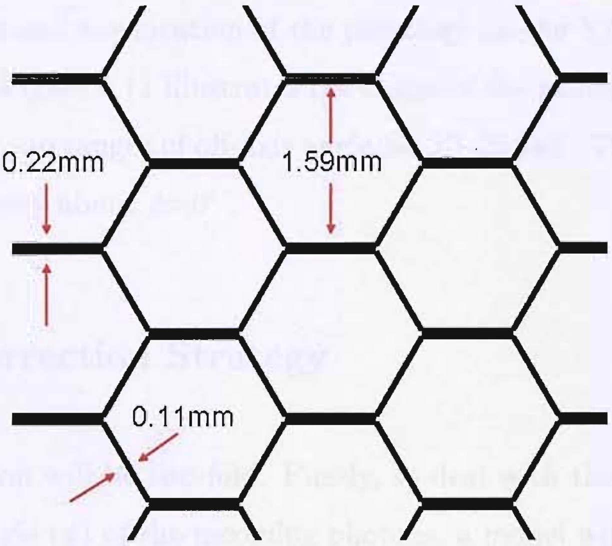

Figure 4.9: Schematic of the NOMEX honeycomb structure, highlighting the double thickness.

fects. In the first instance, a mass model of the support structure has been employed to fit the calibration data. More succesful is an empirical model based on the features seen in both the mass model results and observed Crab data set. The calibration observations of the Crab used in this section were collected between September 2003 and March 2005 and consist of revolutions 102, 170, 239 and 300. The data have been processed using OSA v.5.0 in seven energy bands as in Sec. 4.3 and observations where the instrument was known to be in a different configuration have been discarded (hence the absence of the early revolutions 43-45). Revolutions 239 and 300 include dedicated azimuth observations: a half circle of pointings every 4° in azimuth at an off-axis angle of 4°, and a full circle every 8° in azimuth at 10° off axis. These pointings were deliberately chosen to try to pin-point the location and amplitude of the features seen in the mass model and hinted at in previous observations. Only a limited exposure time was available for these calibration observations, so a compromise had to be made between the spacing of the pointings and the individual exposures. Consequently, features at an off-axis angle of 4° and 10° can be modelled better than for extreme on- and off-axis positions. Figure 4.10 displays the off-axis response and the location of the pointings on the YZ detector plane for the entire data set. Figure 4.11 illustrates the shape of the azimuth response for the whole data set split into ranges of off-axis angle for 20–25 keV. There is a suggestion of azimuthal symmetry about ϕ=0° .

4.4.1 The Correction Strategy

A complete correction will be two-fold. Firstly, to deal with the spread of flux due to the azimuthal angle (ϕ) of the incoming photons, a model will be produced that describes how flux varies with this angle. The azimuthal correction, ϕ_{Corr} will vary between 0 and 1 (i.e. no correction at maximum flux) and will include an off-axis angle (θ) dependent term. Once the azimuth-dependent effect has been described and corrected for all values of θ and ϕ, what remains is simply the response of the ϕ corrected flux as a function of off-axis angle. This response can be described by a second θ-dependent function (θ_{Corr}) with respect to the on-axis flux which can be considered as maximum and therefore has a correction factor of 1. The source flux can therefore be corrected as follows:

$$\text{Corrected Flux} = \frac{\text{Original Flux}}{(\theta_{Corr} \times \phi_{Corr})} \tag{4.4}$$

4.4.2 The Mask Mass Model

The Mask Mass Model (MMM) has been developed to simulate how photons will be affected by the NOMEX mask support structure. A virtual model of the mask support is created: 2400 x 2400 x 80 mm total size of 1400 hexagonal straws (density 1.531 gcm^{-3}, wall thickness 0.11 mm, hexagon width 1.59 mm) with double thickness at ±y boundaries. Virtual photons (a minimum of 10000 are needed for good statistics) with a given range of energies are fired into the mass model with

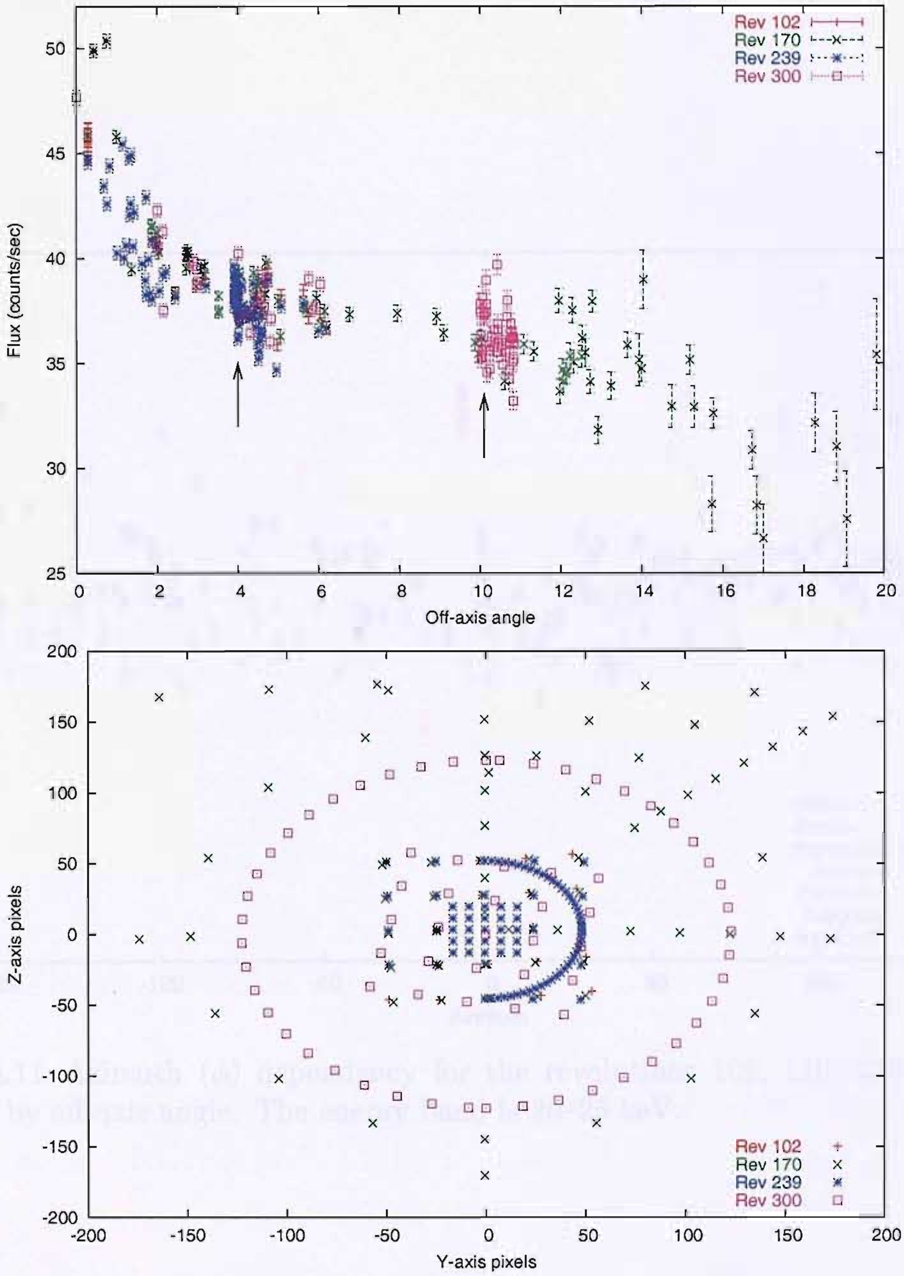

Figure 4.10: Data set used for the azimuth correction. The arrows mark the half circle at 4° off-axis and the full circle at 10° off-axis.

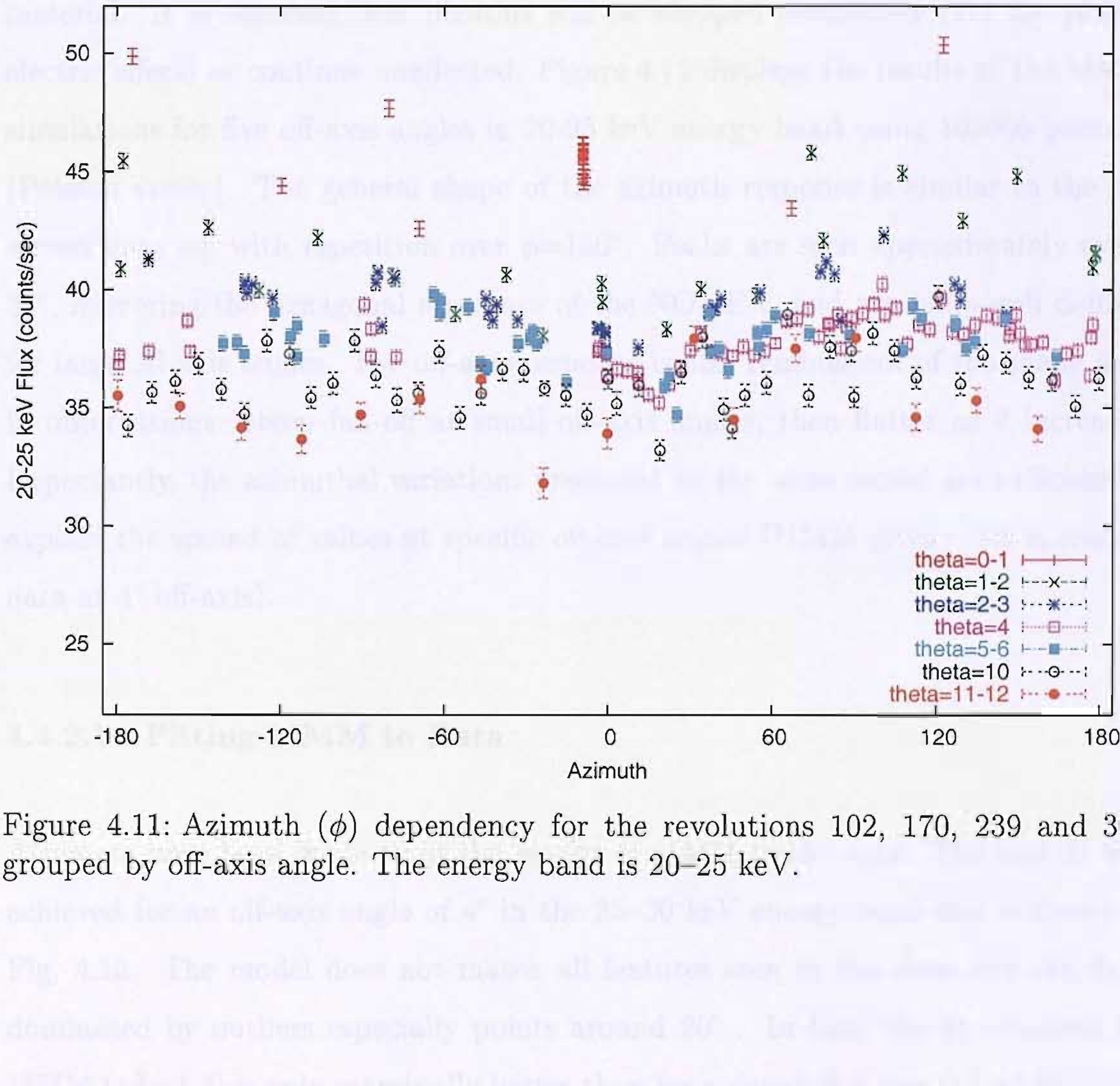

Figure 4.11: Azimuth (ϕ) dependency for the revolutions 102, 170, 239 and 300 grouped by off-axis angle. The energy band is 20–25 keV.

specified off-axis and azimuth angles. The distribution of photon energies has been set to follow a Crab-like spectrum, where:

$$f(E) = A \cdot E^{-2.05} \tag{4.5}$$

(Zombeck 1990).

The model output gives the number of photons that remain unattenuated by the material. It is assumed that photons will be stopped completely (via the photoelectric effect) or continue unaffected. Figure 4.12 displays the results of the MMM simulations for five off-axis angles in 20-25 keV energy band using 100000 photons (Poisson errors). The general shape of the azimuth response is similar to the observed data set with repetition over ϕ=180°. Peaks are seen approximately every 30°, mirroring the hexagonal structure of the NOMEX, and are more well defined for large off-axis angles. The off-axis response is also reminiscent of the shape seen in observations: steep fall-off at small off-axis angles, then flatter as θ increases. Importantly, the azimuthal variations predicted by the mass model are sufficient to explain the spread of values at specific off-axis angles (MMM gives ~8% spread in data at 4° off-axis).

4.4.2.1 Fitting MMM to Data

Attempts have been made to fit the results of MMM to the data. The best fit was achieved for an off-axis angle of 4° in the 25–30 keV energy band and is shown in Fig. 4.13. The model does not match all features seen in the data and the fit is dominated by outliers especially points around 20° . In fact, the fit obtained for MMM (χ^2_ν=4.2) is only marginally better than for a simple flat line (χ^2_ν=4.95). It is therefore concluded that the raw MMM results cannot be adequately fitted to the measured data, and either the MMM must be altered, perhaps by smoothing, or an alternative empirical mode must be used.

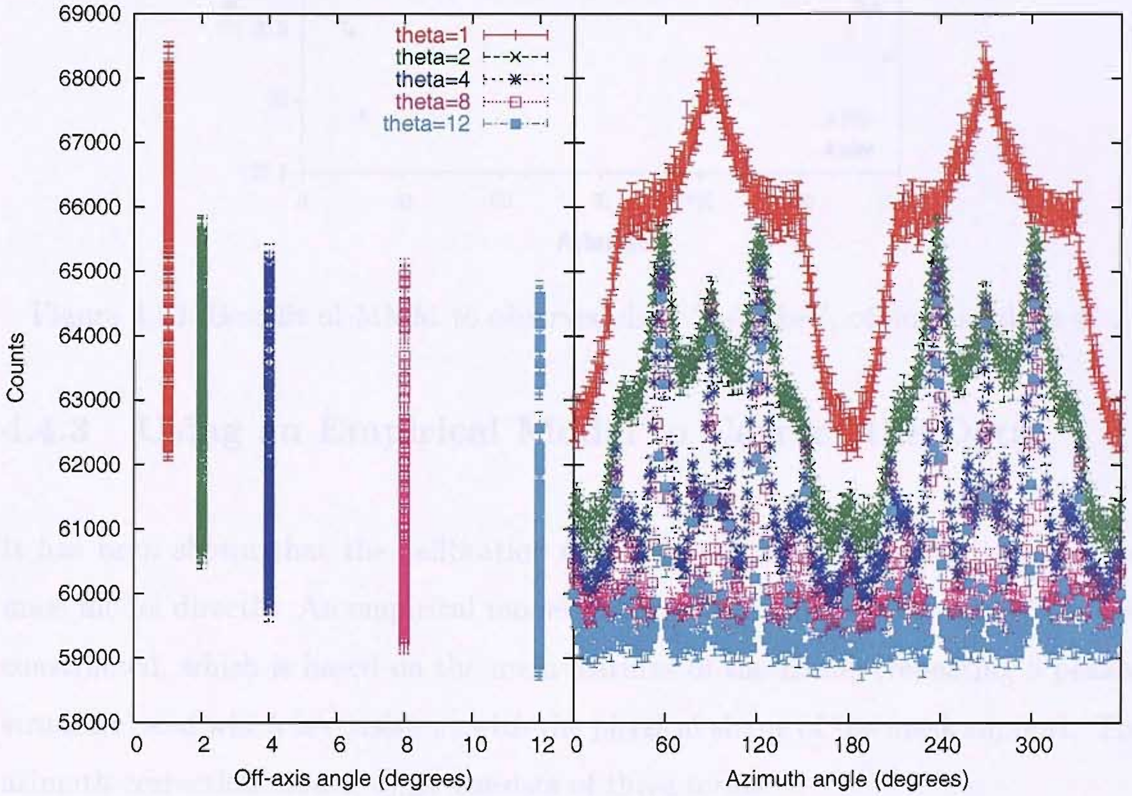

Figure 4.12: Mask Mass Model results for 5 different off-axis angles (θ) in the 20–25 keV energy band. The plot on the right shows azimuth (ϕ) dependency while the plot on the left illustrates how flux decreases with off-axis angle.

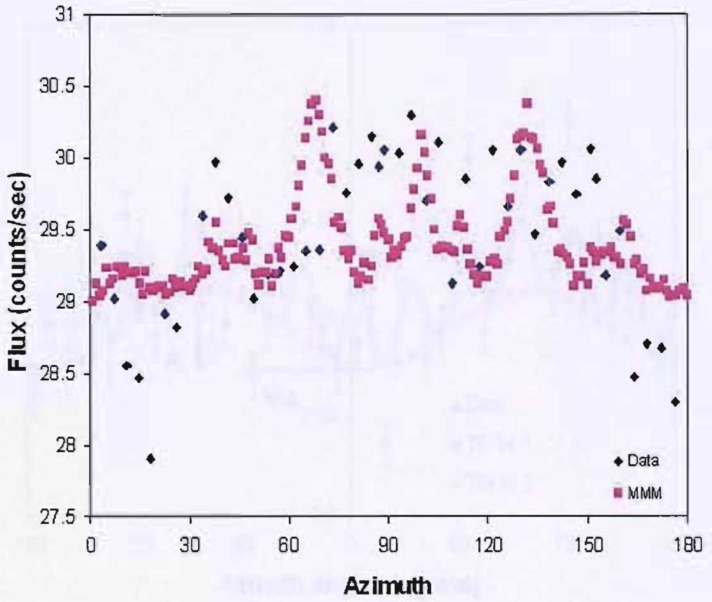

Figure 4.13: Best fit of MMM to observed data 25-30 keV, off-axis angle is 4° .

4.4.3 Using an Empirical Model to Correct the Data

It has been shown that the calibration data cannot be fit satisfactorily using the mass model directly. An empirical model to correct for azimuth has therefore been constructed, which is based on the main features of the model (repeating 6 peaked structure) and which is consistent with the physical shape of the mask support. The azimuth correction model, ϕ_{Corr} consists of three terms:

$$\phi_{Corr} = \underbrace{A\cos^2(\phi+\psi_A)}_{Term\ 1} + \underbrace{B\cos^2(C(\phi+\psi_B))}_{Term\ 2} + \underbrace{(1-(A+B))}_{Term\ 3} \tag{4.6}$$

The first term describes the large scale shape of the response repeated over 180° in azimuth. To account for the variation between the orientation of the mask structure and the theoretical ϕ=0° (as determined by Equ. 4.3), a phase is introduced, ψ_A, which shifts the model along the azimuth scale. The amplitude of Term 1 is varied by A. Similarly, B and ψ_B are the amplitude and phase for Term 2, which mimics the finer 6 peaked structure (where C=6). The correction is performed on normalised

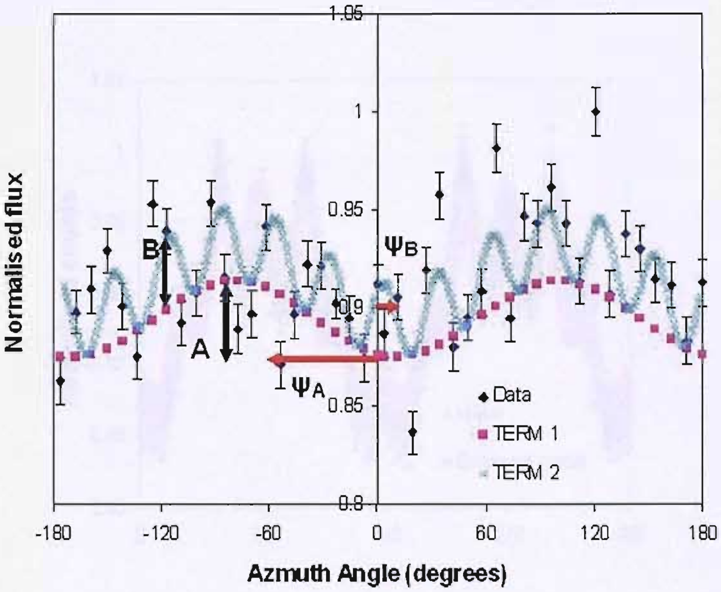

Figure 4.14: Illustrating the parameters used in ϕ_{Corr}. Term 1=$A\cos^2(\phi + \psi_A$ and Term 2=$B\cos^2 C(\phi+\psi_B)$ where C=6. Data is revolution 300; full circle observations for θ=10° for 20-25 keV.

data, hence the final term. A pictorial representation of these parameters is shown in Fig. 4.14.

Figure. 4.15 compares the empirical azimuth correction model (ϕ_{Corr}) to the mass model for 25-30 keV and θ=2° . It can be seen that this simple emprical model is able to approximate most of the features predicted by the mass model, but allows more flexibilty in use, in that interpolation is possible and computation is fast.

The phases, ψ_A and ψ_B, act independently of each other and are constant in all data sets. They have been determined by peforming a simultaneous fit between model and data for off-axis angles of θ=4° and θ=10° for all energy bands with A and B as free parameters. Values are found to be ψ_A=79° , ψ_B=-23° . The amplitudes, A and B, are energy and off-axis angle dependent and are determined by minimising the model fit to data at off-axis angles of 4° and 10° for each energy band separately. Fit results for θ=10° for all energy bands are shown in Fig. 4.16. Fits were also

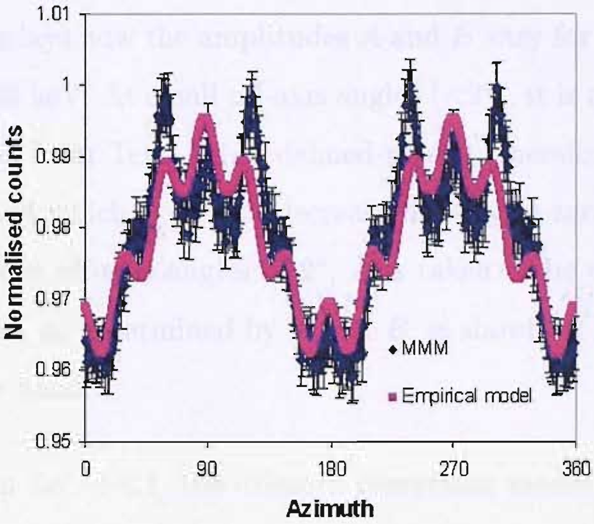

Figure 4.15: Comparing the empirical azimuth correction model to the mask mass model for θ=2° in the 25-30 keV energy band.

attempted for data at small and large off-axis angles. Model parameters could not be constrained well, but give a suggestion of behaviour which can be matched to the shape predicted by MMM (broader overall features at small off-axis angles, and sharper, more definied peaks further off-axis). The best model fit for the half circle of data at 4° was obtained in the 25–30 keV energy band ($\chi^2_\nu \sim 1.9$, 43 d.o.f.). Figure 4.17 shows the model fit and a histogram comparing the spread of flux in 0.2 counts/sec bins between uncorrected data, empirical model (ϕ_{Corr}) corrected data and data corrected with a simple straight line fit. The FWHM of the ϕ_{Corr} distribution is 2.6% which provides a real improvement on both the uncorrected (~4%) and line corrected (3.8%) data. The energy dependency of A and B could not be well understood as a result of this fitting and subsequent corrections are based on 25–30 keV data only. Although better χ^2_ν fits were obtained for higher energy bands, the features to be modelled are not as defined so it is easier to get a better fit. ISGRI is most sensitive below 40 keV and therefore it is most important to understand the azimuth effects in this lower energy range.

Figure 4.18 displays how the amplitudes A and B vary for positions on the detector plane for 25–30 keV. At small off-axis angles (<2°), it is assumed that there will be no contribution from Term 2 (no defined peaks), therefore B=0 and the model depends solely on A which is seen to decrease linearly to zero on-axis (no spread in data points). Above off-axis angles of 2°, A is taken to be constant. The azimuth correction function, as determined by A and B, is shown in Fig. 4.19, again for the 25–30 keV energy band.

As explained in Sec. 4.4.1, the azimuth correcting model ϕ_{Corr} does not correct for the off-axis response. The azimuth corrected data must now be corrected for off-axis angle using a similar set of linear functions as described in Sec. 4.3. The off-axis correction function θ_{Corr} is described in Fig. 4.20 for the 25–30 keV energy band. Data can now be simultaneously corrected for both responses using the final correction $\theta_{Corr} \times \phi_{Corr}$ illustrated in Fig. 4.20.

4.4.4 Correction 2 Results

Using an empirical model constructed to correct for off-axis and azimuth effects (Fig. 4.20), Crab calibration data in the 25–30 keV energy band has been corrected and is presented in Fig. 4.21 compared to the uncorrected flux and data corrected with a simple off-axis only model. By fitting a straight line at the value of the on-axis flux through the corrected data, a measure can be made of how well the azimuth effect has been corrected for in comparison to correcting for off-axis alone. For the entire data set, the fit is only marginally better for the azimuth corrected data (χ^2_ν=7.7 and 8.1 respectively, 258 d.o.f.), decreased to 6.8 and 6.5 if the two outliers with fluxes ~35 counts/sec are removed). For the data at 4° off-axis however, the

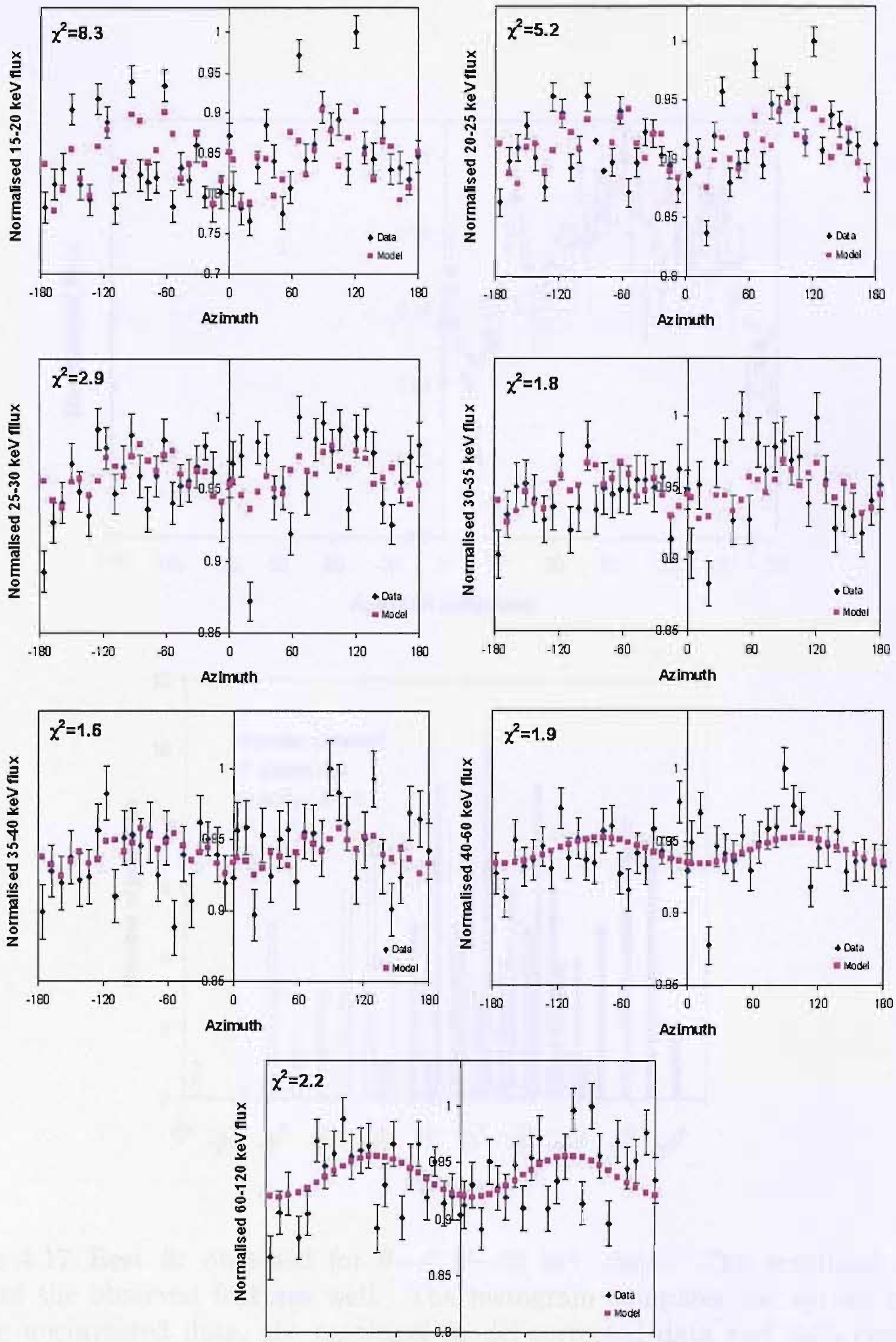

Figure 4.16: Normalised data and the ϕ_{Corr} model fits for all energy bands for θ=10° . χ^2 quoted is the reduced value with 44 degrees of freedom.

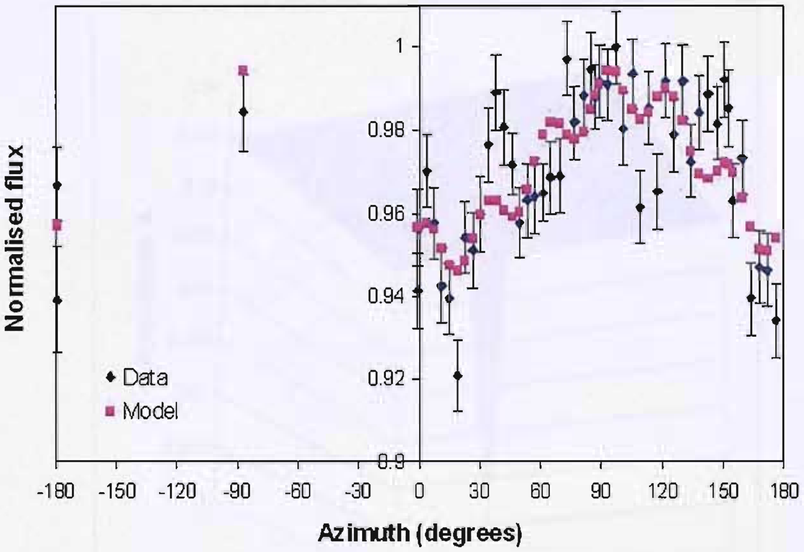

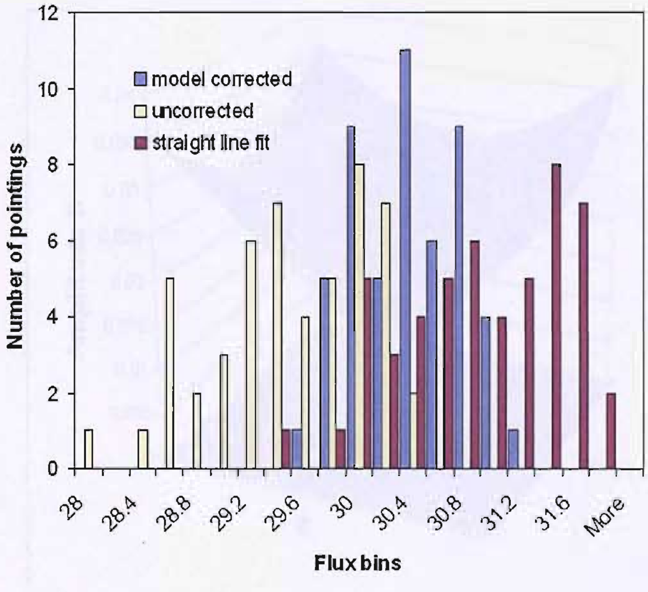

Figure 4.17: Best fit obtained for θ=4° 25–30 keV data. The empirical model matches the observed features well. The histogram compares the spread of flux for the uncorrected data, the empirical model-corrected data and data corrected with a simple straight line fit.

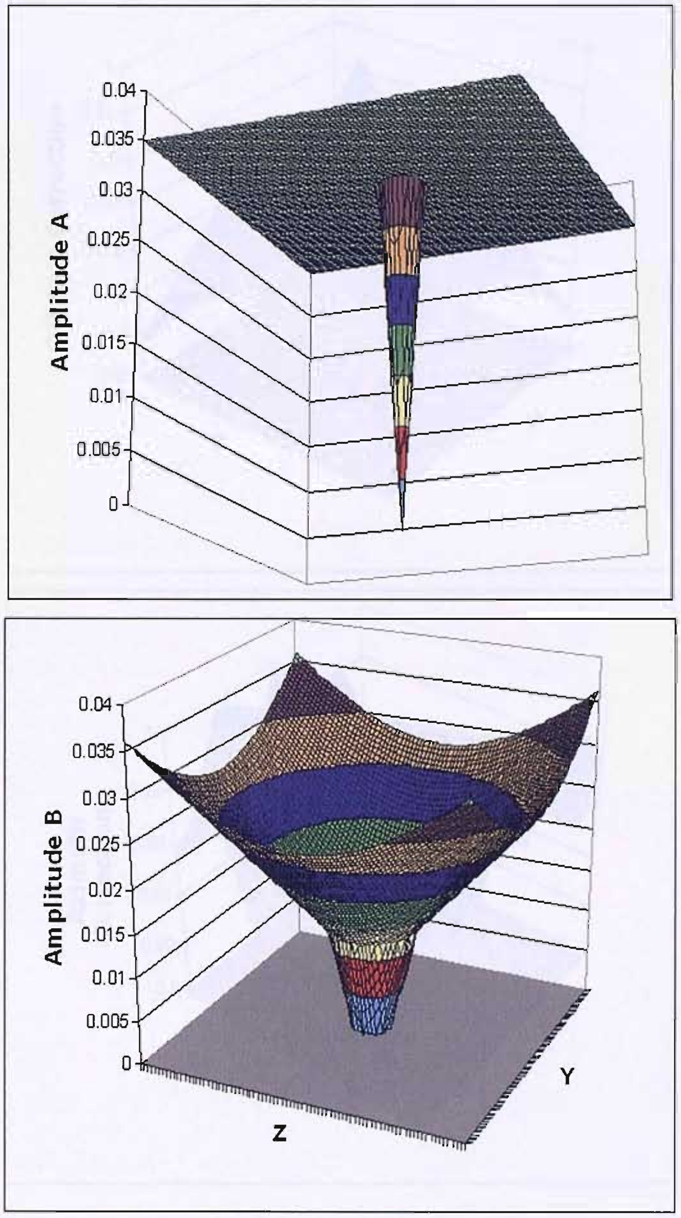

Figure 4.18: Variation of the ϕ_{Corr} amplitudes A and B for off-axis positions in the 25–30 keV energy band. The Y and Z planes represent the detector plane (200 x 200 pixels) and for clarity have not been labelled in the Amplitude A plot.

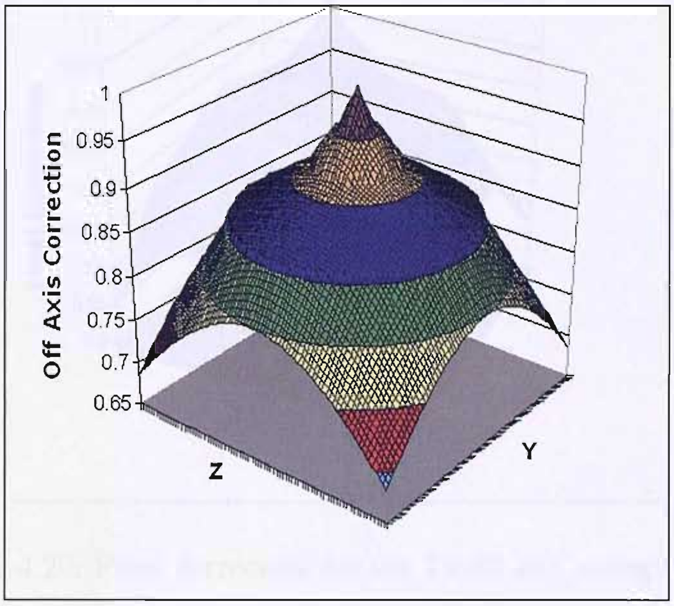

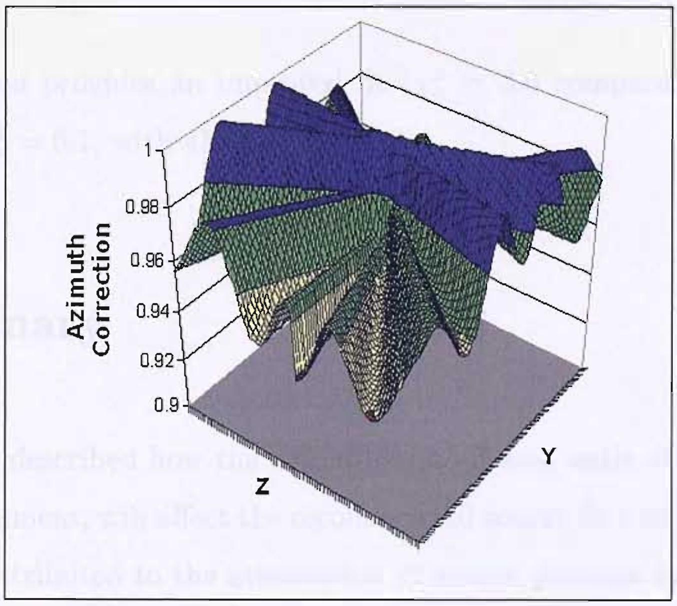

Figure 4.19: How the azimuth and off-axis correction terms vary over the detector plane for the 25–30 keV energy band. The azimuth correction, ϕ_{Corr}, is dependent on Amplitudes A and B (see Fig. 4.18). The final correction shown in Fig. 4.20 is the product of the azimuth and off-axis corrections ($\phi_{Corr} \times \theta_{Corr}$)

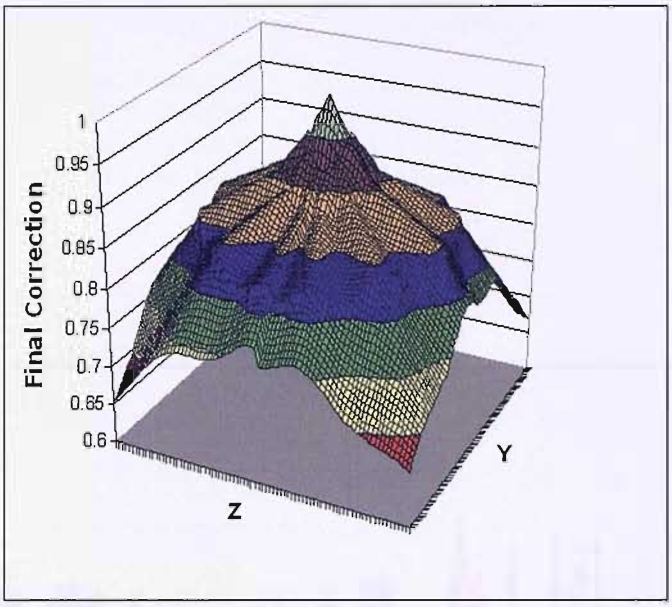

Figure 4.20: Final correction for the 25–30 keV energy band.

azimuth correction provides an improved fit (χ^2_ν = 3.6 compared to off-axis only corrected data $\chi^2_\nu = 6.1$, with 43 d.o.f.).

4.5 Summary

This chapter has described how the azimuth and off-axis angle of a source, as seen by the IBIS instrument, will affect the reconstructed source flux below 120 keV. This effect has been attributed to the attenuation of source photons by the coded mask support structure. A preliminary correction, for off-axis effects alone, has been produced and is now successfully included in the standard light curve software (OSA v.4). A major impact of this correction can be illustrated by the flux extraction process in the IBIS/ISGRI survey (see Chapter 5). For the first catalogue, fluxes were extracted from mosaics which are the result of combining multiple pointings at various off-axis angles using OSA v.3.0. The lack of off-axis corrections in this soft-

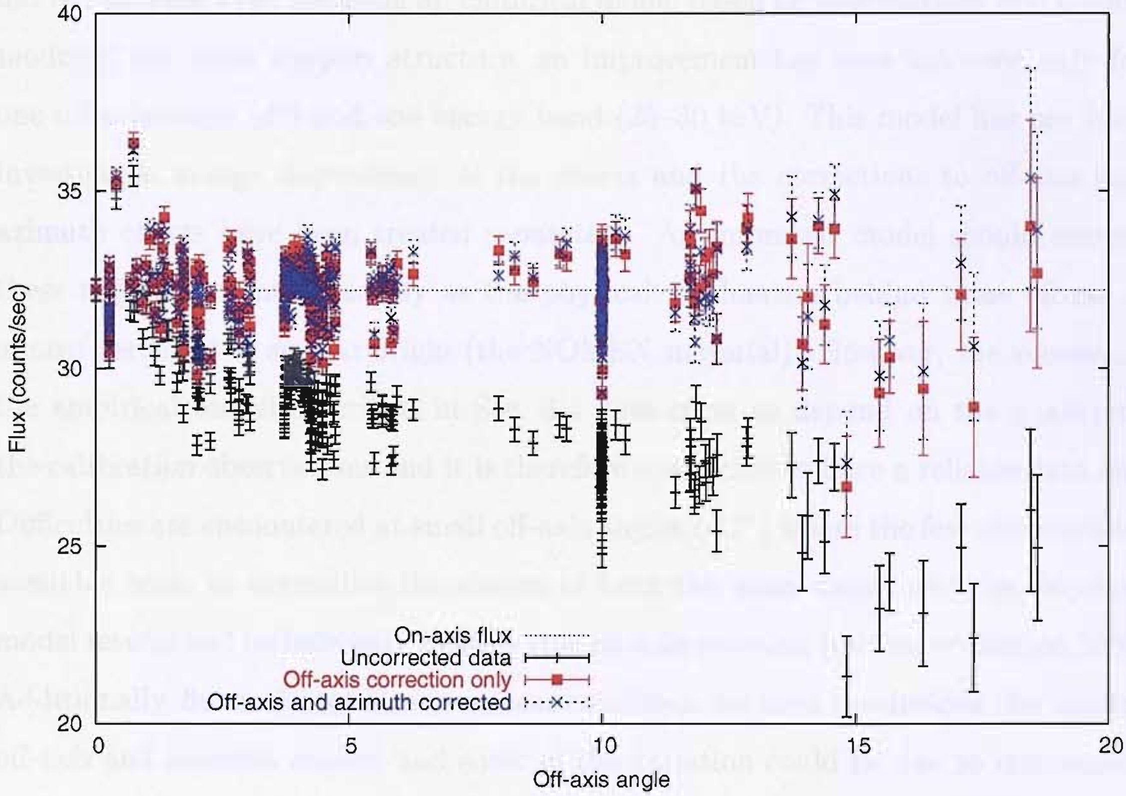

Figure 4.21: Comparing the azimuth and off-axis model corrected data with the original uncorrected data and a simple off-axis correction for 25–30 keV. The dotted line represents the value of the on-axis source flux.

ware version will have created a systematic underestimate of fluxes. This situation has been improved in the second catalogue through the use of OSA v.4.1.

Although correcting for the average off-axis angle response of the IBIS telescope has proved successful, attempts to correct for the azimuth-related spread in flux have not yet produced a satisfactory result. A mass model of the support structure did not fit data well. By using an empirical model based on observations and a mass model of the mask support structure, an improvement has been achieved only for one off-axis angle (4°) and one energy band (25–30 keV). This model has not fully investigated energy dependency of the effects and the corrections to off-axis and azimuth effects have been treated separately. An improved model should correct these responses simultaneously as the physical mechanism behind these effects is almost certainly of similar origin (the NOMEX material). However, the success of the empirical model described in Sec. 4.4 does seem to depend on the quality of the calibration observations and it is therefore important to have a reliable data set. Difficulties are encountered at small off-axis angles (<2°) where the few observations available seem to contradict the shapes of both the mass model and the emprical model results and include only a single true on-axis pointing (during revolution 300). Additionally, fluxes do not always appear consistent between revolutions (for similar off-axis and azimuth angles) and some of the variation could be due to instrument configuration changes.

To be able to construct a successful correction model, it is clear that more Crab calibration observations are needed. Future observations have been proposed which include smaller, finer spacing arcs in azimuth for various off-axis angles and at higher exposures to improve the statistics of each data point. Most important are a set of observations at off-axis angles <2° to determine whether the model does break down here, together with contiguous on-axis pointings to ensure no configuration changes occur mid-revolution and to obtain an accurate measure of the on-axis flux.

An alternative strategy to the empirical model is to modify the mass model (MMM) to account for the random orientation of the NOMEX straws within the support structure which would distort the hexagonal symmetry of the honeycomb. Any modification based on the actual structure is hindered by the lack of any detailed technical documents regarding the design and placement of the mask support. Simple smoothing of MMM results alone does not improve the fit with observations and, in fact, contradicts the observed pattern of increased amplitude of azimuth response at larger off-axis angles. Similar work has been undertaken by the *INTEGRAL* Science Data Centre (Lubinski et al. 2005), introducing a function to describe the 'tilt' of the NOMEX straws. Comparable results have been obtained, which underlines the importance of further investigation into these effects.

In summary, this work has been successful in significantly improving the systematic variation of the IBIS reconstructed source flux caused by off-axis related effects. Whereas OSA v.3.0 does not correct for these effects and flux variations of up to 40% exist, corrections applied with OSA v4.0 reduce this by half. A subsequent release of OSA v.5.X will additionally correct for the azimuth effect and will lower the overall spread in flux to ~10%.

Chapter 5

The IBIS/ISGRI Survey of the Soft Gamma-ray Sky

5.1 Introduction

The IBIS/ISGRI survey forms one of the main objectives of the *INTEGRAL* mission by exploiting the unprecedented imaging capability of the IBIS instrument in the >20 keV energy regime. The role of the survey is to expand the current knowledge of the soft gamma-ray sky by documenting the number, distribution and behaviour of the different types of high energy emitters detected in all-sky images created from guaranteed Core Programme obervations. The IBIS telescope (see Chapter 2 for review of instrument characteristics) is the first instrument capable of achieving these scientific goals Due to its unprecedented sensitivity of ~1 mCrab in the 20–100 keV energy band, wide field of view (FOV= 29°×29°) and typical source positional accuracy between ~1–3′, the IBIS telescope is the first instrument capable of achieving these scientific goals(see Chapter 2 for review of instrument characteristics).

Prior to IBIS, all-sky surveys in the 20–100 keV range have been produced by the *HEAO-1* A4 experiment (Levine et al. 1984) and the BATSE instrument on-board *CGRO* (Shaw et al. 2004); however, the *HEAO-1* satellite took ~6 months to scan the entire sky, thereby reducing the transient detection rate and was over an order of magnitude less sensitive than IBIS, while the BATSE survey suffered from limited angular resolution of the order of a degree, largely because BATSE was not initally developed as a survey instrument, but used the earth occultation technique. Nethertheless, these surveys presented an important insight into the range of objects emitting in this energy range and gave incentive to study this energy range further with improved imaging techniques. *GRANAT*/SIGMA, the first coded mask telescope, detected a number of sources in the Galactic centre region between 40–800 keV with a limiting sensitivity of 30 mCrab (Vargas et al. 1996). The WFC coded mask instruments on board *BeppoSAX* had an improved sensitivity of ~2 mCrab and a wide field of view making it particularly suitable for detecting transients, but had an upper energy range of 30 keV (in't Zand et al. 2004). Therefore, the IBIS imager on-board the *INTEGRAL* satellite represents the best opportunity to date to obtain an accurate picture of the sky between 20–100 keV. Table 5.1 compares the number of sources detected and relative flux sensitivity of previous surveys ≥20 keV.

Initially, the IBIS survey exposure was concentrated along Galactic plane (Catalogue 1). More recently, guest observer have become available, filling in other areas of the sky (Catalogue 2 exposure covers >50% of the sky), aiming towards a truly all-sky coverage. Not only does the survey create all-sky images, but it provides long-term spectral and timing information for the detected sources. Supplementing this survey work is a separate high energy catalogue (100–300 keV; Bazzano et al. 2006) and an AGN catalogue (Bassani et al. 2006).

This chapter describes the techniques involved in producing the first and sec-

Mission (Instrument)	Energy Range (keV)	Number of sources and flux sensitivity
HEAO-1 (A4)	13–180	72 sources (all sky), 14 mCrab [1]
GRANAT (SIGMA)	40–800	15 GC sources, 30 mCrab [2]
BeppoSAX (WFC)	2.8–30	76 transient sources in GC and GP, ~2 mCrab [3]
CGRO (BATSE)	25–160	25 sources (all sky), ~3 mCrab [4]
INTEGRAL (IBIS)	20–100	200+ sources (all sky), ~1 mCrab [5]

Table 5.1: Results of hard X-ray/soft gamma-ray surveys. GC=Galactic centre, GP=Galactic plane. References: [1]Levine et al. 1984; [2]Vargas et al. 1996; [3]in't Zand et al. 2004; [4]Shaw et al. 2004; [5]Bird et al. 2004, 2006.

ond IBIS/ISGRI catalogues obtained from the first two years of *INTEGRAL* observations. The following section summarises the first IBIS/ISGRI catalogue which presents the locations and fluxes of 123 sources in the 20–100 keV energy band, of which 28 were of an unclassified nature. The second catalogue (Sec. 5.3) benefited from an improved data set and analysis techniques and lists 209 sources in the same energy range, of which 56 are unclassified. Section 5.3.5 presents average spectral analysis of the sources in the second catalogue.

5.2 The First IBIS/ISGRI Catalogue

Each orbit (or revolution) of the *INTEGRAL* satellite takes approximately 3 days, and consists of individual IBIS/ISGRI pointings (or Science Windows, ScW) of typically ~2000 s. As part of the Core Programme (CP), regular scans of the Galactic plane are performed, together with deep exposures of the Galactic centre (GPS and GCDE observations respectively). The data used in the first catalogue consists exclusively of CP data, totalling 2529 ScW between revolutions 46 (27th February 2003) and 120 (10th October 2003), with a total exposure exceeding 5 Ms (Fig. 5.1). Observations prior to revolution 46 are part of the performance verification phase of

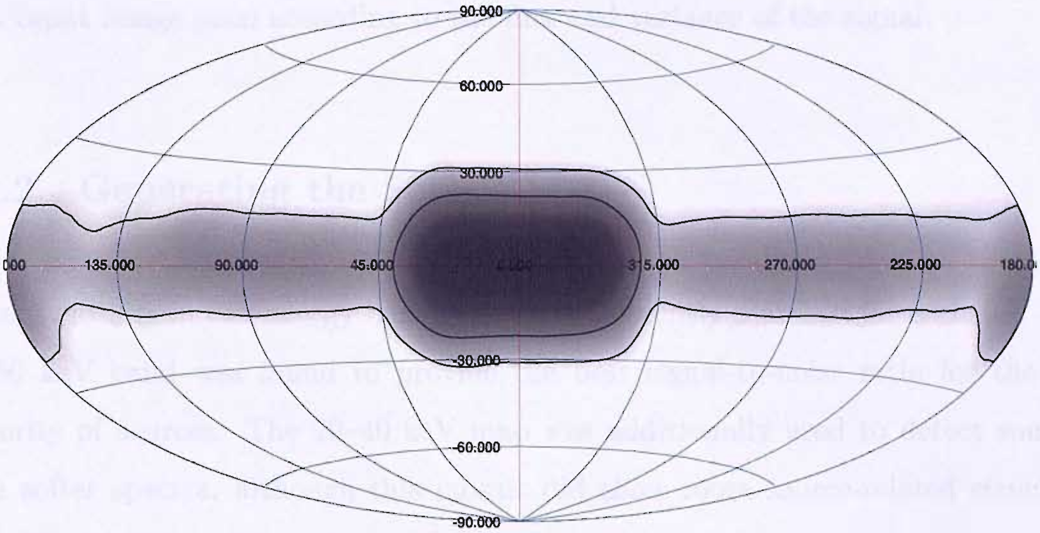

Figure 5.1: The first *INTEGRAL* catalogue exposure map, consisting of the CP Galactic centre deep exposures (GCDE) and Galactic plane scans (GPS). Contours mark 10 and 100 ks.

the instrument and are not suitable for survey work. This first catalogue presents the location of 123 sources detected in the all-sky maps, together with source fluxes in the 20–40 and 40–100 keV energy bands.

5.2.1 Preparing the data

The Offline Standard Analysis (OSA) software v.3.0 (Goldwurm et al. 2003) was used to generate images in flux, variance and significance for each ISGRI ScW. Ghost sources (a consequence of coded-mask image deconvolution) are removed from the individual ScW images prior to the mosaicing process, using a cleaning catalogue consisting of the sources significantly detected in each ScW. Ghost sources, therefore, may be missed if a source is only significant in the final mosaiced image. All-sky mosaics are then created in energy bands of 20–40 keV and 30–50 keV by combining the individual images in Aitoff coordinates by weighting the individual events from each input image pixel according to the flux and variance of the signal.

5.2.2 Generating the Source List

All-sky mosaics in two energy bands were independently searched for excesses. The 30–50 keV band was found to provide the best signal-to-noise ratio for the the majority of sources. The 20–40 keV map was additionally used to detect sources with softer spectra, although this mosaic did show more source-related structure than the 30–50 keV band. The SExtractor search tool (Bertin & Arnouts 1996) provided a list of excesses using a simple Gaussian point-spread function (PSF) filter which was cross-checked using a simple search for excesses (above a certain significance threshold). Positions were determined from the centroid of the source profile. A preliminary source list was created by combining the separate lists of excesses. Finally, ambiguous sources were checked visually, noting, for example, the location with respect to areas of structure around bright sources such as the Crab and Sco X-1. False detections are quantified and minimised by fitting plots of the number of excesses above a certain significance as a function of significance (log N–log S) for the 20–40 and 30–50 keV mosaics. From this log N–log S analysis, sources below 6σ for the 30–50 keV band or 7σ in the 20–40 keV band were not included in the catalogue (Bird et al. 2004). Above these levels, it is expected that at least 99% of the excesses are true sources. This method of searching for sources in the final mosaic is ideal for detecting bright persistent sources but as a consequence will not find transient sources whose significance averaged over the survey time period is below the cut-off.

Fluxes are determined from the total accumulated source flux averaged over the period of the exposure for that region of sky. The fluxes and associated uncertainties are extracted from the position of maximum significance for each source in the flux and variance maps (20–40 and 40–100 keV energy bands). The off-axis response of IBIS (see Chapter 4) was not yet fully calibrated and therefore the fluxes include a systematic uncertainty related to the source location in each pointing ($\sim$10% for sources $>20\sigma$). Fluxes from low significance ($< 6\sigma$) sources are quoted as 2σ upper limits.

The classification of known sources was obtained by cross-correlation with the SIMBAD[1] and NED[2] online databases using a nominal $3'$ error circle. Sources are designated as *INTEGRAL* Gamma-ray (IGR) sources if they have not been previously detected in X-ray or higher energies (*ROSAT* associations excepted).

5.2.2.1 ROSAT Counterparts

A detailed correlation was performed between the first catalogue sources and the *ROSAT* All Sky Survey Bright Source Catalogue (Stephen et al. 2005). It was found that 75 sources ($\sim$60%), including 10 unclassified objects, are coincident with the location of a *ROSAT* source. IBIS survey sources have a nominal error circle of $3'$ (Gros et al. 2003) which makes searching for longer wavelength counterparts unfeasible, therefore, the main advantage of finding a *ROSAT* counterpart is the possibility of greatly reducing the error circle of the *INTEGRAL* source to $\sim 10''$ if the association is real.

One such correlation with an unclassified *INTEGRAL* source is between IGR J15479–4529 and 1RXS J154814.5–452845. First discovered serendipitously, the centroid position of IGR J15479–4529 was $3.6'$ from the location of the *ROSAT* source (Tomsick et al. 2004). As a result of the IBIS survey observations, a more accurate position could be obtained, being only $0.7'$ from the *ROSAT* source (Stephen et al. 2005;

---

[1] `http://simbad.u-strasbg.fr/`

[2] `http://nedwww.ipac.caltech.edu/`

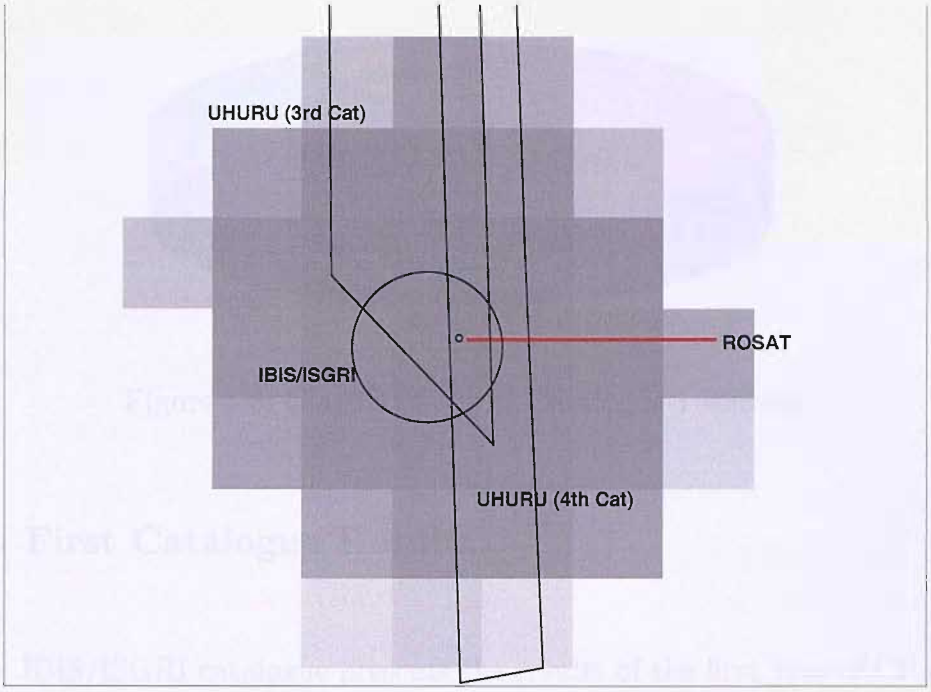

Figure 5.2: Redefining the position of 4U1705-32. UHURU error boxes come from Giacconi et al.(1974); Forman et al.(1978). IBIS error circle is 3′ and ROSAT error cirle is 8″.

Bird et al. 2004). *XMM-Newton* observations of the *ROSAT* object indicate that the source is an Intermediate Polar cataclysmic variable (CV) (Haberl et al. 2002).

Correlations can also be used to validate previous tentative associations between high energy sources and *ROSAT* sources. For example, the large error box of *UHURU* source 4U1705-32 makes the association with the *ROSAT* source 1RXS J170854.4–321857 unclear (see Fig. 5.2). The IBIS detection helps to confirm this association and redefines the IBIS error circle to 8″. Subsequent analysis of *BeppoSAX* observations of this source reveal the detection of a single Type-I X-ray burst, characteristic of a neutron star low-mass X-ray binary system (in't Zand et al. 2005). IBIS observations are important in understanding if this source is transient or simple a low-luminosity persistent system.

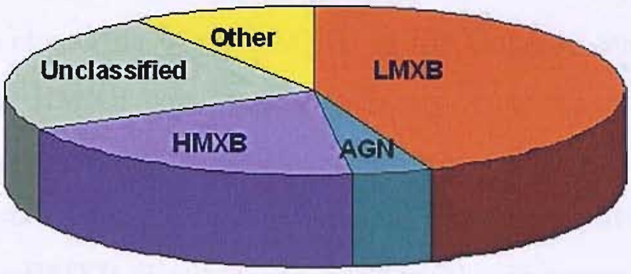

Figure 5.3: Classifications of Catalogue 1 sources.

5.2.3 First Catalogue Results

The first IBIS/ISGRI catalogue presents the results of the first year of CP observations (Bird et al. 2004). 123 sources have been detected in the 20–100 keV energy band with a limiting sensitivity of 1 mCrab. It has since been discovered that one catalogued source (IGR J17460–3047) is not real and can be attributed to an artifact of the imaging process. This is consistent with the false detection estimate of 1% as described in Sec. 5.2.2. Figure 5.3 illustrates the proportion of source types detected by the survey. A significant proportion of the sources are Galactic X-ray binaries (~60%), the majority (54 sources) being low-mass X-ray binary (LMXB) systems. Additionally, 5 AGN are detected along with 12 "other" sources (including supernovae remnants and CVs). The lack of extra-galactic sources is partially a consequence of the exposure bias along the Galactic plane. The remaining 28 sources are unclassified, around one quarter of the total sample, of which 24 are entirely new detections (IGRs). The remaining 3 IGRs are catalogued as a CV (IGR J15479–4529; Stephen et al. 2005), an HMXB (IGR J16318-4848; Walter et al. 2003) and an LMXB harbouring a BHC (IGR J17474–3212; Markwardt et al. 2003c).

It is interesting to look at the relative location of the Galactic binaries with respect to the unclassified sources. Dean et al. (2005) found, as expected, that the high-mass X-ray binaries (HMXB) are distributed along the Galactic plane in marked constrast with the clustering of the LMXBs in the Galactic centre region. This is probably due to the HMXB being young stellar systems, expected to be located in recent star forming regions, such as the spiral arms. The angular distribution of the unclassified systems away from the Galactic plane does not conform exactly to either the LMXB or HMXB distributions, but does show a narrower range of angular separations, more similar to the HMXBs. Furthermore, log N–log S analysis of the luminosity functions according to the nature of the donor star and compact object, find that the unclassified sources tend towards the luminosity functions of HMXB containing a neutron star, assuming location near to the Galactic Centre.

From independent observations of *INTEGRAL* sources, a new class of objects has been proposed characterised by a high degree of photoelectric-absorption, exceeding that expected from the interstellar medium by large quantities – more than a factor of 100 in the case of IGR J16318–4848 (Walter et al. 2004a; Lutovinov et al. 2005). Further analysis has shown that these systems are likely to be HMXB, with a high degree of intrinsic absorption below 10 keV. Therefore, the *INTEGRAL* survey is vital in order to identify the true number of HMXBs in our Galaxy and it is expected that a high proportion of the currently unclassified IBIS survey sources are highly absorbed HMXB.

5.3 The Second IBIS/ISGRI Catalogue

A second catalogue has been compiled using ~4000 additional ScW, as a result of continuing dedicated CP observations and proprietary data becoming public, enabling 'gaps' in the year and a half of obeservations to be filled. The data-set consists of 164 uninterrupted revolutions between 27th February 2003 (Rev 46) and

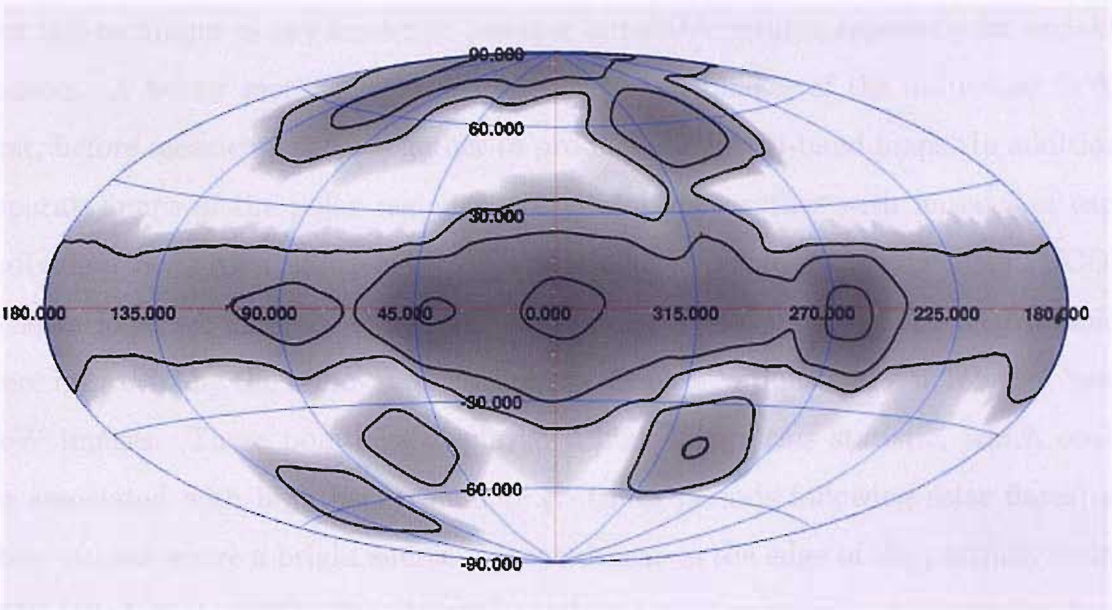

Figure 5.4: Second catalogue exposure map. Contours mark 10, 100 and 1000 ks.

29th June 2004 (Rev 209), with total exposure of >10Msec unveiling 209 sources, almost double that of the first catalogue. The increase in observations helps to expand the IBIS/ISGRI survey from a Galactic plane study to an all-sky monitoring programme and to provide a deeper look into the central regions of the Galaxy. The exposure map of the second catalogue illustrates that ~50% of the sky is now observed with an exposure of at least 10 ksec (Fig. 5.4).

5.3.1 Improvements to the Data Set

Individual images were mosaiced together to form final all-sky maps in ten energy bands (15–20, 20–30, 30–40, 40–60, 60–80, 80–100, 100–150, 150–300, 300–500 keV) using a later version of the analysis software (OSA v.4.1) which includes a correction for the off-axis response of the instrument (see Chapter 4). Mosaics of consecutive energy bands are then combined to create broad-band maps, *e.g.* 20–40, 20–100 keV, but this technique is now known to produce unreliable results, especially for variable sources. A better method is to create broad-band images of the individual ScWs first, before mosaicing them together to produce the broad-band maps. In addition, separate maps of the polar regions were produced, together with mosaics of each individual revolution and for 4 groups of Galactic centre deep exposures (GCDE observations, see Chapter 6, Sec. 6.2 for details). The quality of the final mosaics were improved by the removal of 'staring' mode observations and a number of 'bad' ScW images. These pointings displayed a high image rms statistic, which could be associated with high background (*e.g.* times periods following solar flares) or observations where a bright source is located near to the edge of the partially coded FOV (Bird et al. 2006). The cleaning catalogue used to remove ghost sources from the images additionally included all sources in the first catalogue, sources (>4.5σ) obtained from a preliminary search of OSA v.4.0 mosaics (including ScW images for transients) and any additional IGR sources not detected in the survey mosaics, but previously published.

5.3.2 Improvements to the Source Selection Procedure

Apart from the increase in exposure time, a greater number of mosaics were employed in the search for sources for the second catalogue:-

- 20–40 keV and 30–60 keV all sky images used as primary search maps as in first catalogue;
- additional all sky map in the 20–100 keV band, more suited in the search for extra-galactic objects;
- individual 20–40 keV revolution maps and 20–100 keV GCDE maps searched for transient objects that would otherwise be missed in the final mosaics due

to average detection significance falling below selected threshold;

- separate maps of the polar regions enable more effective searching at high latitudes as Aitoff projection maps produce heavy distortion to the PSF of sources with |b|>60° .

As in the first catalogue, the SExtractor search tool was used to create a list of excesses, but this time an additional filter (`mexhat`) was included to minimise source confusion in crowded regions of the sky –see Bird et al. (2006) for details. Log N–log S analysis was re-performed and derived lower significance thresholds of 5.5σ in the 20–40 keV band, 5σ in the 30–60 keV and 20–100 keV bands and 6σ for the individual revolution mosaics (20–40 keV), as a result of the better quality maps. Sources located in areas of structure were required to have a significance of at least 3σ above any non-statistical background features within a few degrees radius.

The positional error of the sources is dependent on the source significance and can be determined using the following model:

$$\delta x = 11.6\ S^{-1.36} + 0.51 \tag{5.1}$$

where δx is the point source location error in arcminutes and S is the source significance (modified from Gros et al. 2003). The model parameters have been determined by calculating the angular distance between the IBIS and SIMBAD position for 179 well defined IBIS catalogue sources, plotting these distances as a function of source significance and performing a fit. From Eqn. 5.1, sources with a significance $>10\sigma$ have an positional error $<1'$.

5.3.2.1 The Galactic Centre

The final survey images used for the second catalogue are mosaics of revolutions 46 to 209 and as such give an 'averaged' view, not truly representing all of the sources the IBIS/ISGRI instrument has detected. In particular the Galactic Centre Region (GCR) contains many highly variable sources in a small area of sky (~2° x 2°), leading to a high degree of source confusion and positional uncertainty. The Galactic Centre was observed in 33 revolutions of the survey data used for the second catalogue. In the final mosaic, the GCR appears as a blend of sources, impossible to resolve into its constituents. However, the GCR sources are seen to vary in brightness from revolution to revolution (see Fig. 5.5). By exploiting this variability, most sources can be de-blended by analysing the individual revolution (~3 day) mosaics. For example, SLX 1744–299 was present in all but 9 of the 33 revolutions, while SAX J1747.0-2853 appears only in revolution 175.

Bélanger et al. (2004) reports the positions of 6 sources located in the central 2° x 2° region of the Galaxy, as seen with ISGRI during April/May 2003 and determined from 20–40 keV and 40–100 keV mosaics of 850 ksec total effective exposure, using a simultaneous PSF fit of all sources in the GCR. This, combined with the more isolated sources seen in the second catalogue survey mosaics, represents the best prior knowledge of the hard X-ray emitters in the Galactic Centre. The *INTEGRAL* source IGR J17456–2901 is presented as being coincident to within 1′ with Sgr A*, the supermassive black hole at the centre of the Galaxy (Bélanger et al. 2004; 2005).

To localise the survey sources in this region, each revolution mosaic (20–40 keV band) covering the GCR was visually inspected in turn, noting the coordinates of any excesses. By combining the positions obtained this way, ten distinct sources could be identified, including all 6 sources detected by Belanger et al.(2004) (see Fig. 5.6). Table 5.2 illustrates the variability of the ten sources by identifying which

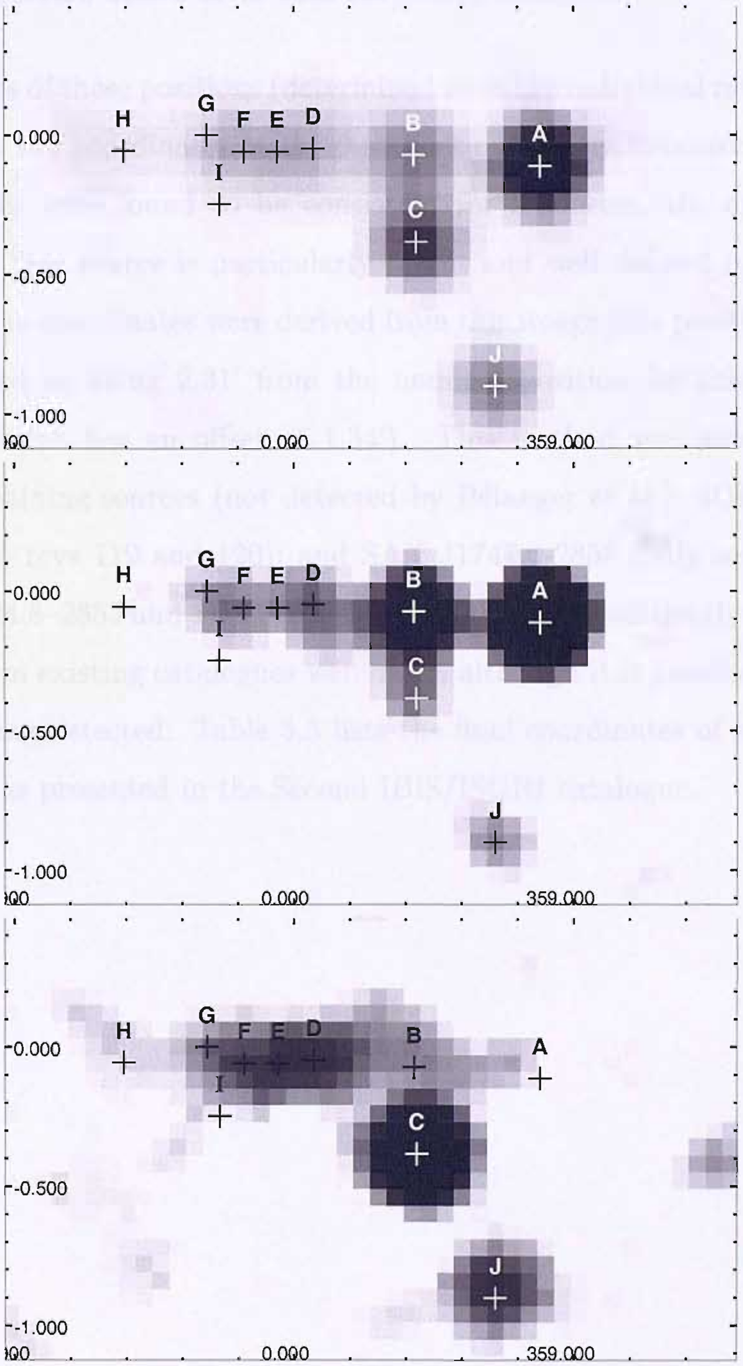

Figure 5.5: Final survey mosaic (top) showing the blending of the sources. Individual revolution mosaics (middle - rev 53; bottom - rev183) illustrating the variability of the Galactic centre. All mosaics are in the 20–40 keV band. See Table 5.3 for key to sources.

sources were detected above 4σ in each revolution searched.

The centroids of these positions (determined from the individual revolutions) were compared with the coordinates of the 6 sources quoted by Bélanger et al. (2004). The coordinates were found to be consistent for 5 sources, the exception being KS 1741-293. This source is particularly bright and well defined in revolution 53 and therefore the coordinates were derived from this image (the position in Belanger et al. is quoted as being $2.31'$ from the nominal position for this source, while the survey position has an offset of $1.34'$). This method was also employed for two of the remaining sources (not detected by Bélanger et al.): IGR J17475–2822 (well defined in revs 119 and 120); and SAX J1747.0-2853 (only seen in rev 175). Finally, 1E 1724.8–2853 and 1E 1742.9–2849 could not be sufficiently de-blended, so coordinates from existing catalogues were used, although it is possible these are not the sources being detected. Table 5.3 lists the final coordinates of the 10 Galactic centre sources as presented in the Second IBIS/ISGRI catalogue.

Revolution	A	B	C	D	E	F	G	H	I	J
51	√	×	×	×	×	×	×	×	×	√
52	√	√	×	×	×	×	×	√	×	√
53	√	√	√	√	×	√	×	×	×	√
54	√	√	×	×	×	×	×	×	×	×
55	√	×	×	×	×	×	×	×	×	×
56	√	√	×	×	×	×	√	×	×	√
57	√	×	×	×	×	×	×	×	×	×
58	√	√	√	√	√	×	×	×	×	√
59	√	√	×	×	×	×	×	×	×	√
61	√	√	√	√	×	×	√	√	√	√
62	√	√	√	×	√	√	×	√	√	√
63	√	√	×	√	√	×	√	×	√	√
64	√	√	×	×	×	×	×	×	×	√
116	√	×	×	×	×	√	×	×	×	√
117	×	×	×	×	×	×	×	×	×	×
118	√	×	×	×	√	×	×	×	×	√
119	√	×	√	×	√	×	×	√	×	√
120	√	×	√	√	√	√	×	√	×	√
121	√	×	×	×	√	×	×	×	×	√
164	√	×	√	×	√	√	×	×	×	√
165	√	√	√	×	×	√	×	√	×	√
167	×	√	√	×	√	×	×	×	×	√
168	×	√	×	√	√	×	×	×	×	√
169	√	√	×	×	√	√	×	×	×	√
171	×	√	√	×	√	×	×	×	×	√
175	×	√	√	×	×	×	×	×	√	√
179	×	√	√	√	×	×	√	×	×	√
181	√	√	√	×	×	×	×	×	×	√
183	×	×	√	√	√	×	×	×	×	√

Table 5.2: Results of searching individual revolution mosaics for the Galactic centre sources, $\times$=source not detected above $>4\sigma$. For a key to the sources see Table 5.3.

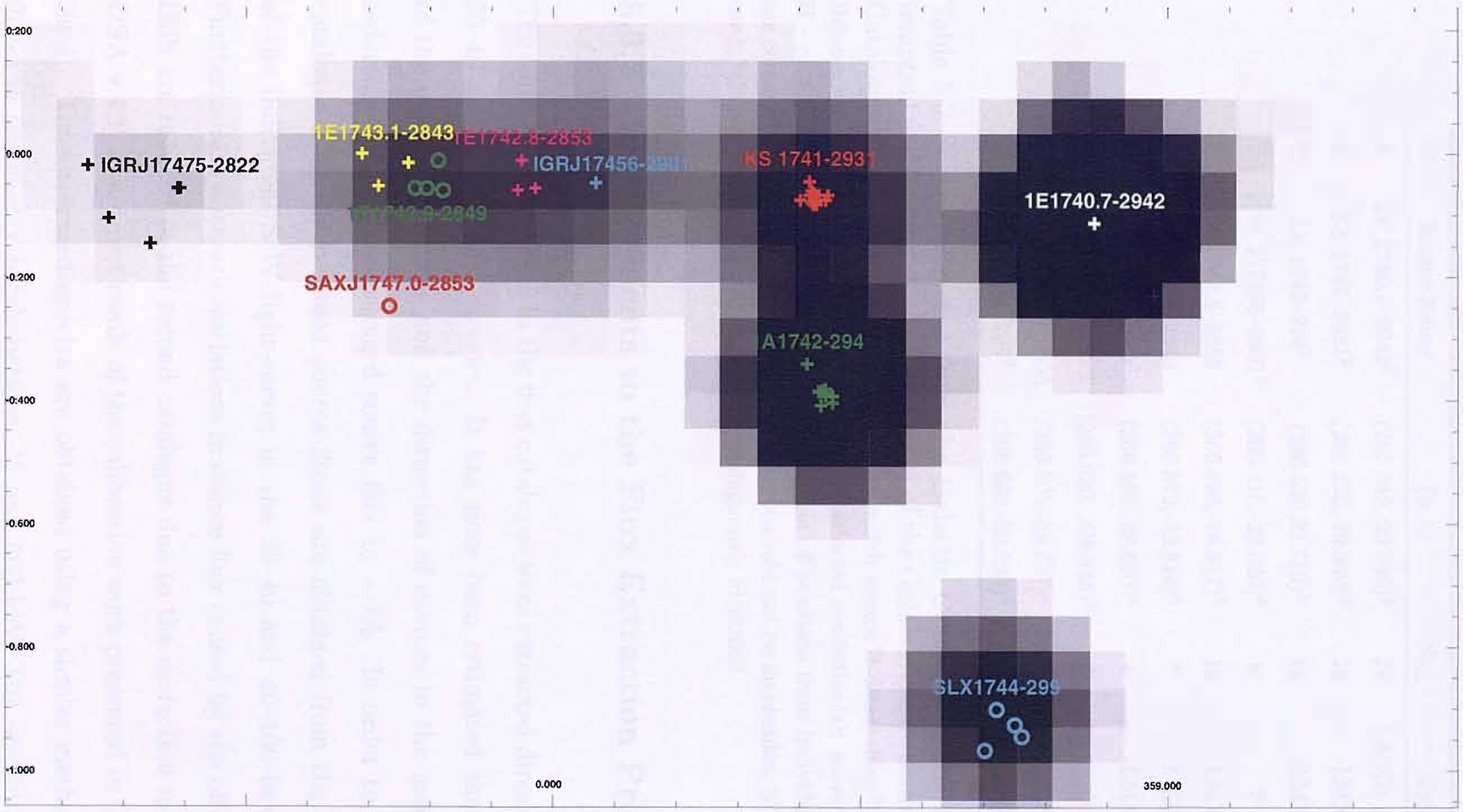

Figure 5.6: Results of searching each revolution mosaic for Galactic centre sources, overlaid on a final mosaic image. Each point is a detection in an individual revolution with coordinates taken from the brightest pixel.

ID	Source Name	(α,δ)	N_{rev}[1]	Type
A	1E 1740.7–2942[2]	(265.988,-29.745)[4]	21	LMXB (BHC)
B	KS 1741–2931[2]	(266.220,-29.340)[3]	19	LMXB
C	1A 1742–294[2]	(266.520,29.510)[4]	18	LMXB
D	IGR J17456-2901[2]	(266.410,-29.020)[4]	9	?[6]
E	1E 1742.8–2853	(266.498,-28.917)[5]	13	LMXB
F	1E 1742.9–2849	(266.570,-28.814)[5]	7	LMXB
G	1E 1743.1–2843[2]	(266.590,-28.670)[4]	4	LMXB
H	IGR J17475–2822	(266.820,-228.445)[3]	6	?
I	SAX J1747.0–2853	(266.805,-28.837)[3]	1	LMXB
J	SLX 1744–299[2]	(266.860,-30.020)[4]	29	LMXB

Table 5.3: Source extracted from the Galactic Centre as a result of spatial and temporal de-blending. Final coordinates of the Galactic centre sources in the Second Catalogue. Notes: [1]Number of revolutions in which source is detectable; [2]Source presented in Bélanger et al. (2004); [3]Coordinates taken from selected revolution(s): source B - rev 53; source H - revs 119 & 120; source I - rev 175; [4]Centroid of positions from individual revolutions that are consistent with Bélanger et al. (2004); [5]Source could not be de-blended, SIMBAD coordinates used; [6]Coincident with Sgr A*, but not unambiguously identified.

5.3.3 Improvements to the Flux Extraction Process

The source fluxes quoted in the first catalogue were extracted directly from the final 20–40 and 40–100 keV mosaics. It has since been estimated that a combination of the mosaicing process and the distortion of sources in the mosaic can cause a reduction of the time-averaged source flux by ~5%. In order to correct for this, catalogue 2 survey-averaged source fluxes are obtained from the weighted means of the individual ScW light-curves in the 20–40 and 40–100 keV energy bands. Furthermore, systematic variations in source flux caused by the off-axis response of IBIS are reduced in the second catalogue due to the correction model included in OSA v.4.1, as a direct result of the calibration work presented in Chapter 4 of this thesis. Time-averaged spectra are obtained using a similar method by extracting fluxes in ten energy bands between 15 and 500 keV. The second catalogue fluxes (assuming a Crab-like spectrum) are expressed in mCrab; appropriate conversion factors are:

20-40 keV, 10 mCrab = 7.57×10^{-11} erg cm^{-2} s^{-1} = 1.71×10^{-3} ph cm^{-2} s^{-1}

40-100 keV, 10 mCrab = 9.42×10^{-11} erg cm^{-2} s^{-1} = 9.67×10^{-3} ph cm^{-2} s^{-1}

5.3.4 Second Catalogue Results and Comparison to the First Catalogue

Improvements in both exposure and methods for detection of sources have nearly doubled the number of sources found in the second catalogue, a total of 209 objects in the 20–100 keV band (Table 5.4). Example significance maps are displayed in Fig. 5.9. Additionally, corrections to the off-axis behaviour of the instrument (see Chapter 4) and an improved flux extraction technique have produced more reliable time-averaged source fluxes. An extensive literature search has been performed to provide references for all source classifications. Where possible, existing catalogues have been referenced (Liu et al. 2000; 2001 for X-ray binaries, Downes et al. 2001 for CVs and Veron-Cetty & Veron 2003 for AGN). In other cases, the first published high energy (>10 keV) detection has been used. All sub-classifications and tentative associations are accounted for using Astronomer's Telegrams and unpublished but accepted papers where necessary.

Four sources are included as a result of searching the individual mosaics, which would have otherwise not been significantly detected in the final all-sky maps. Of these sources, two are Be X-ray binaries (GRO J1008-57, 11σ in revolution 203 and XTE J1858+034, briefly detected during revolution 139 at nearly 50σ) and two are LMXB (XTE J1709-267 detected at nearly 20σ during revolution 171 and XTE J1739-285 detected in revolution 120 with 8σ). Similarly, the transient nature of IGR J17285-2922 prevented the source's acceptance in the first catalogue ($<6\sigma$ in

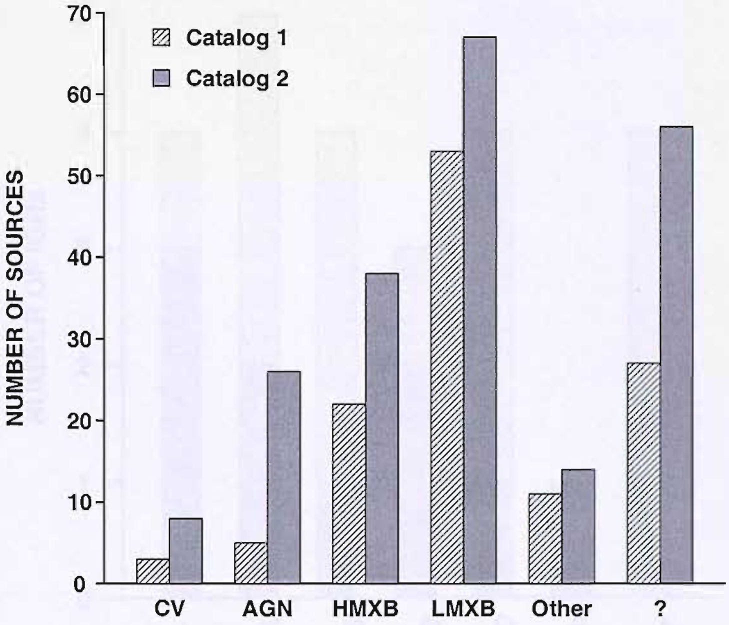

Figure 5.7: Numbers of sources in the 1st and 2nd IBIS/ISGRI Catalogues, classified by type.

the final map), but has been included in the second catalogue (7.3σ in 20–100 keV all-sky map) as a result of better mosaic quality and improved source searching techniques. Further analysis of this source is detailed in Chapter 6.

A breakdown by source type of the 209 sources presented in the second catalogue, and how this compares to the first catalogue, is shown in Fig. 5.7. The source list remains dominated by Galactic accreting binaries: a total of 113 objects, represented by 38 HMXB and 67 LMXB, but also a small population of CVs. In most cases, the compact object is a NS (79 confirmed cases, 32 in HMXB, 47 in LMXB) but the sample also contains 4 confirmed BH (1 in HMXB, 3 in LMXB) and 6 LMXB BH candidates (BHC). There are an additional 4 associations with BHCs, based on the spectral and temporal characteristics of the sources. Also worthy of note is the detection of IGR J1745.6-2901, shown to be coincident with the supermassive BHC Sgr A* (Bélanger et al. 2004, 2005). The Galactic sample also includes 4 isolated pulsars (one of which is an AXP), 4 SNR (of which 2 are associated with AXP) and

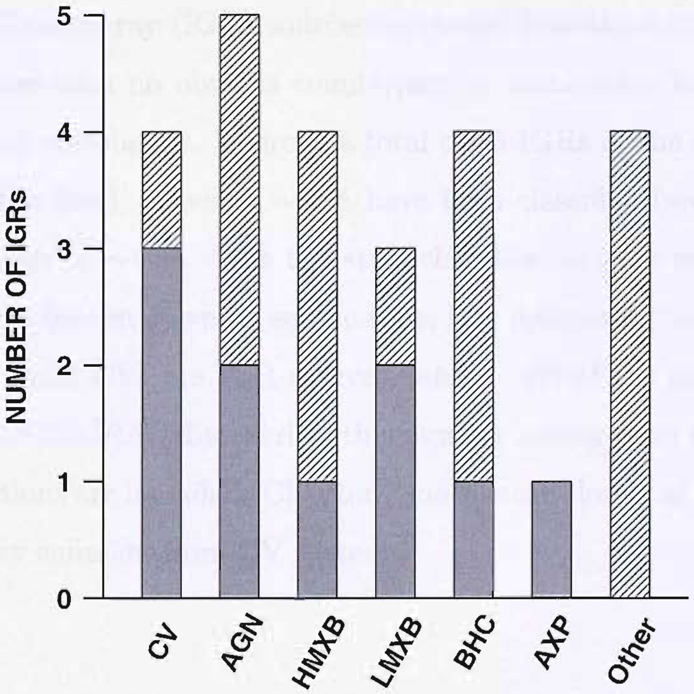

Figure 5.8: Classifications of IGR sources. Solid bars indicate numbers of IGRs with firm classifications (sources can be in more than one category), hatched bars show tentative classifications.

two associations with molecular clouds (Bassani et al. 2006). Compared to the first catalogue, there has been a five-fold increase in detections of AGN, which can be directly attributed to the wider and deeper sky coverage.

Catalogue 2 contains roughly twice the number of detections without a firm classification than contained in catalogue 1, but this represents a similar proportion of the total number of sources in the catalogues (~25%). Of the unclassified sources, 39 are of an unknown nature, while the remaining 17 have unconfirmed classifications. Approximately one quarter of the source catalogued as unclassified in the first catalogue have now been classified - 3 HMXB, 1 LMXB, 1 CV and 2 AGN – with many more tentative associations. The majority (~80%) of the remaining and new unclassified sources are *INTEGRAL* discoveries (IGR sources).

INTEGRAL Gamma-ray (IGR) sources represent detections that are either entirely new or those with no obvious counterpart or association in the hard X-ray and/or gamma-ray wavebands. There is a total of 56 IGRs in the second catalogue (double that of the first), of which ~20% have been classified (see Fig. 5.8). This percentage increases to ~40% if the tentative classifications are included. Looking at the IGR sources broken down by source type, it is interesting to note that nearly half of the catalogued CVs are IGR sources, while <5% of the catalogued LMXB and HMXB are *INTEGRAL* discoveries; this number increases to nearly 10% if the tentative associations are included. Chapter 7 looks more closely at the phenomenon of soft gamma-ray emission from CV systems.

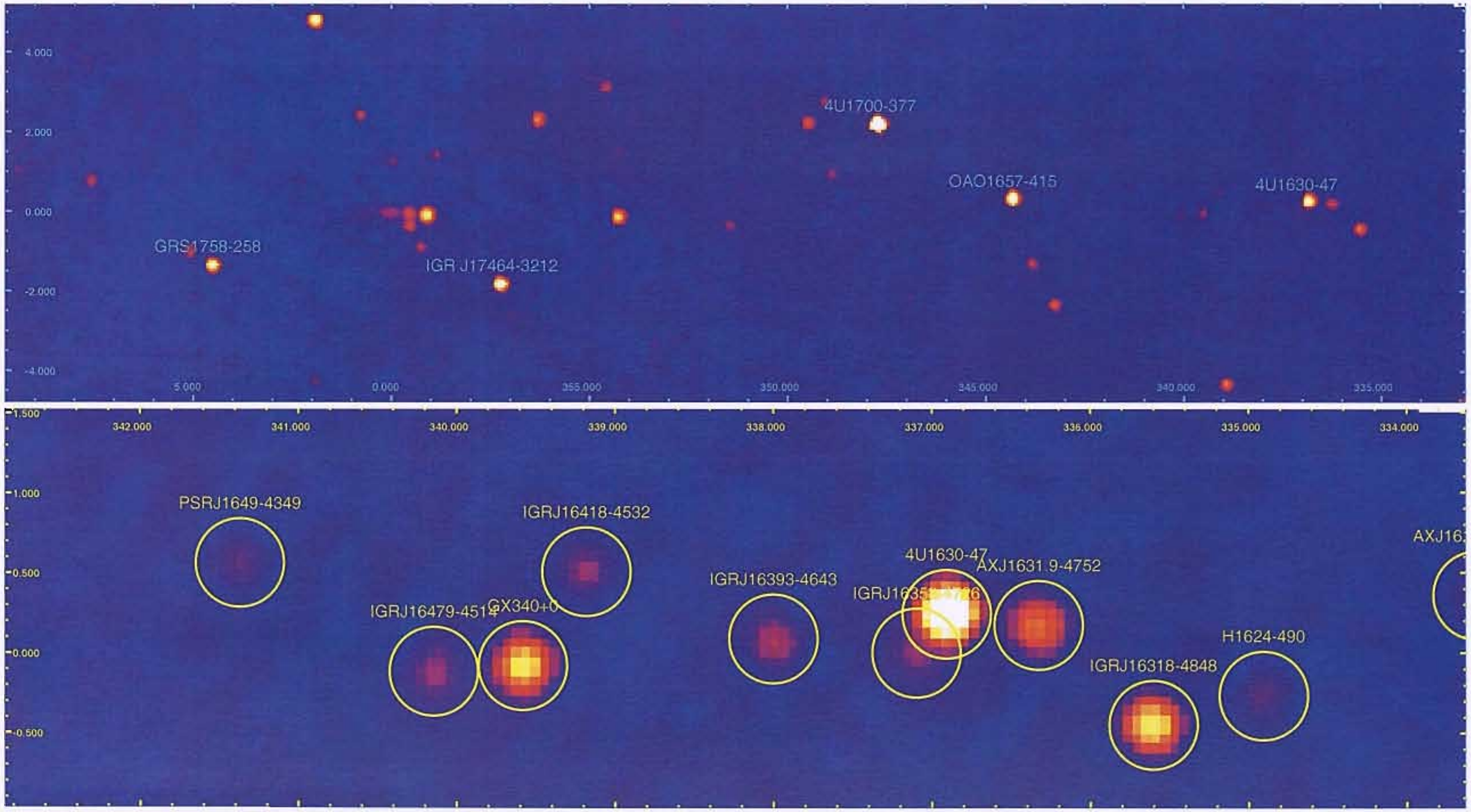

Figure 5.9: Second catalogue significance maps. Top: 30–60 keV map with a selection of bright sources labelled. Bottom: 20–100 keV map zoomed in on the Norma arm region of the Galaxy; all sources labelled are in the second catalogue.

Table 5.4: The Second IBIS/ISGRI Catalogue : 20–100 keV

Name[1]	**RA** (deg)	**Dec.** (deg)	**Err**[2] (arc min)	F_{20-40}[3] (mCrab)	F_{40-100}[3] (mCrab)	**Sig**[4]	**Exp**[5] (ks)	**Type**[6]	**Refs**[7]
V709 Cas	7.252	59.317	1.3	4.1±0.5	<2.9	6.9*	79	CV	1
RX J0053.8-7226	13.531	-72.426	1.2	3.3±0.4	<2.3	7.6*	106	HMXB, XP, T, Be	2 , 3
gam Cas	14.126	60.702	1.1	5.2±0.5	<2.9	8.8*	77	HMXB, Be	2 , 3
SMC X-1	19.324	-73.444	0.5	39.6±0.4	9.2±0.8	86.7*	106	HMXB, XP	2
1A 0114+650	19.511	65.288	0.7	10.3±0.5	5.3±1.0	17.5*	78	HMXB, XP	2
QSO B0241+62	41.184	62.510	1.4	3.7±0.7	5.8±1.2	6.4**	51	AGN,Sy1.2	4
X Per	58.842	31.036	0.9	50.1±4.8	51.0±7.5	11.2**	2	HMXB, XP, Be	2 , 3
LMC X-4	83.221	-66.365	0.6	50.3±1.5	12.0±2.5	33.5*	23	HMXB, XP	2
Crab	83.628	22.020	0.5	1000.0	1000.0	1691.0**	97	PWN, PSR	5
MCG+08-11-011	88.745	46.454	1.4	6.1±1.0	<5.5	6.2*	23	AGN, Sy1.5	4
4U 0614+091	94.270	9.145	0.6	24.7±0.8	22.8±1.4	29.5**	46	LMXB, B, A	6
IGR J07506-1547	117.647	-15.788	1.7	2.2±0.6	4.2±1.1	5.3**	64	?	
IGR J07565-4139	119.123	-41.642	1.3	1.0±0.2	<0.8	6.8*	949	?	
IGR J07597-3842	119.930	-38.730	0.9	2.3±0.2	1.9±0.3	11.4**	774	AGN?	7
ESO 209-12	120.483	-49.738	0.9	1.4±0.2	1.8±0.3	11.3**	939	AGN, Sy1.5	4
Vela Pulsar	128.816	-45.184	0.5	6.9±0.1	8.2±0.2	64.8**	1450	PWN, PSR	5
4U 0836-429	129.338	-42.893	0.5	36.6±0.1	31.1±0.2	240.9**	1400	LMXB, T, B	6
FRL 1146	129.633	-36.008	1.2	1.3±0.2	0.9±0.3	7.9*	881	AGN, Sy1	4
Vela X-1	135.512	-40.557	0.5	216.9±0.1	48.1±0.2	1440.1*	1220	HMXB, XP	2
IGR J09026-4812	135.638	-48.196	1.1	0.9±0.1	0.9±0.2	8.5*	1350	?	
4U0919-54	140.050	-55.187	0.7	3.6±0.2	2.6±0.4	16.1**	602	LMXB	6
EXMS B0918-549E	140.022	-55.143	0.9	-	-	12.0*	602	?,T	
MCG-05-23-016	146.869	-30.930	1.0	10.2±1.4	8.4±2.0	9.9**	27	AGN, Sy1i	4

Table 5.4 – Continued

Name	RA	Dec.	Err	F_{20-40}	F_{40-100}	Sig	Exp	Type	Refs
GRO J1008-57	152.396	-58.294	0.9	<1.3	<2.2	11.6	130	HMXB, XP, Be, T	2 , 3
IGR J10404-4625	160.095	-46.416	1.5	2.9±0.7	5.9±1.1	5.7**	102	AGN?	8
IGR J11114-6723	167.854	-67.392	1.7	1.7±0.4	2.3±0.7	5.1**	199	?	
Cen X-3	170.300	-60.638	0.5	27.4±0.4	3.6±0.6	71.9*	209	HMXB, XP	2
1E 1145.1-6141	176.866	-61.957	0.5	30.1±0.3	17.5±0.5	83.4**	269	HMXB, XP	2
2E 1145.5-6155	177.016	-62.199	0.7	7.9±0.3	4.6±0.5	17.5*	274	HMXB, XP, Be, T	2 , 3
NGC 4151	182.640	39.401	0.5	32.7±0.6	40.0±1.0	42.4**	56	AGN, Sy1.5	4
4C 04.42	185.606	4.239	1.4	1.4±0.4	3.9±0.6	6.5**	213	AGN, QSO	4
NGC 4388	186.446	12.637	0.6	15.4±0.9	16.7±1.4	21.0**	62	AGN, Sy1h	4
GX 301-2	186.653	-62.776	0.5	112.8±0.3	14.4±0.4	401.1*	406	HMXB, XP, T	2
3C 273	187.293	2.027	0.6	7.5±0.3	8.5±0.5	28.2**	279	AGN, QSO	4
IGR J12349-6433	188.709	-64.570	0.7	4.5±0.3	2.8±0.4	16.8*	437	Symb	9
NGC 4507	188.912	-39.903	0.7	10.7±0.7	12.2±1.1	17.5**	63	AGN, Sy1h	4
LEDA 170194	189.796	-16.182	1.2	2.6±0.5	5.6±0.9	7.6**	111	AGN?	8
NGC 4593	189.927	-5.353	0.7	4.1±0.3	4.0±0.5	16.2**	349	AGN, Sy1	4
4U 1246-588	192.351	-59.091	1.1	2.0±0.3	2.0±0.4	8.3**	436	HMXB, T	2
3C 279	194.038	-5.781	1.2	1.9±0.3	2.2±0.5	7.5**	326	Blazar	4
1H 1254-690	194.361	-69.305	1.2	2.5±0.3	<1.4	7.7*	369	LMXB, B, D	6
Coma cluster	194.880	27.961	1.3	1.9±0.3	<1.5	7*	251	Cluster	5
IGR J13020-6359	195.541	-63.925	1.1	2.1±0.2	1.3±0.4	8.4*	501	?	
NGC 4945	196.362	-49.476	0.5	11.4±0.4	18.5±0.7	38.2**	226	AGN, Sy2	10
Cen A	201.364	-43.021	0.5	49.7±0.4	63.8±0.8	129.2**	112	AGN, Sy2	11
4U 1323-62	201.650	-62.126	0.7	3.8±0.2	2.4±0.4	16.9*	535	LMXB, B, D	6
4U 1344-60	206.872	-60.604	0.7	3.9±0.2	4.7±0.4	19.9**	526	AGN?	8
IC 4329A	207.348	-30.323	1.1	10.0±1.1	8.1±1.8	8.6**	29	AGN, Sy1.2	4
Circinus Galaxy	213.274	-65.343	0.5	14.0±0.2	11.5±0.4	62.3*	487	AGN, Sy1h	4

Table 5.4 – Continued

Name	RA	Dec.	Err	F_{20-40}	F_{40-100}	Sig	Exp	Type	Refs
IGR J14492-5535	222.305	-55.579	1.5	1.5±0.2	<1.2	5.7*	520	?	
PSR B1509-58	228.466	-59.147	0.5	8.6±0.2	11.0±0.4	44.4**	509	PSR	12
Cir X-1	230.178	-57.174	0.5	15.6±0.2	<1.2	59.6*	512	LMXB, T, B, A	6
IGR J15359-5750	233.965	-57.832	1.3	1.2±0.2	2.0±0.4	7.0**	505	?	
4U 1538-522	235.600	-52.378	0.5	22.6±0.2	3.0±0.4	91.9*	553	HMXB, XP	2
4U 1543-624	236.947	-62.577	0.9	2.9±0.3	<1.4	10.8*	386	LMXB	6
IGR J15479-4529	237.033	-45.484	0.6	5.4±0.2	2.4±0.4	20.9*	544	CV	13 , 14
XTE J1550-564	237.746	-56.482	0.5	115.1±0.2	176.5±0.4	628.1**	525	LMXB, T, BH	6 , 15
4U 1608-522	243.175	-52.434	0.5	14.8±0.2	11.9±0.3	68.4**	648	LMXB, T, B, A	6
IGR J16167-4957	244.139	-49.985	1.0	2.1±0.2	<1.0	9.3*	682	?	
IGR J16194-2810	244.858	-28.160	1.5	2.2±0.3	<1.5	6.0*	349	?	16
AX J161929-4945	244.865	-49.727	0.9	2.2±0.2	1.9±0.3	10.5**	690	HMXB, NS?	17
Sco X-1	244.988	-15.648	0.5	716.9±0.6	16.3±0.9	1060.0*	110	LMXB, Z	6
IGR J16207-5129	245.195	-51.504	0.8	3.3±0.2	2.4±0.3	14.9**	676	?	
4U 1624-490	247.012	-49.204	0.7	4.2±0.2	<1.0	18.7*	715	LMXB, D	6
IGR J16318-4848	247.942	-48.824	0.5	29.3±0.2	14.4±0.3	129.1*	724	HMXB, T	18
AX J1631.9-4752	248.006	-47.870	0.5	17.1±0.2	6.6±0.3	78.3*	737	HMXB, T, XP	19 , 20
4U 1626-67	248.098	-67.456	0.6	16.1±0.5	<2.3	31.0*	181	LMXB, XP	6
4U 1630-47	248.517	-47.398	0.5	63.5±0.2	44.9±0.3	290.5**	742	LMXB, T, U, D, BHC	6
IGR J16358-4726	248.970	-47.421	0.7	4.3±0.2	2.4±0.3	19.7*	747	LMXB?, T	21
IGR J16377-6423	249.420	-64.382	1.6	2.2±0.4	<1.8	5.6*	235	Cluster?	22 , 16
AX J163904-4642	249.763	-46.693	0.6	6.9±0.2	<1.0	32.9*	760	HMXB?, T, XP	23 , 24 , 25
4U 1636-536	250.222	-53.755	0.5	24.2±0.2	13.4±0.4	106.5*	641	LMXB, B, A	6
IGR J16418-4532	250.440	-45.532	0.6	5.2±0.2	1.3±0.3	23.0*	784	?	
GX 340+0	251.447	-45.612	0.5	34.9±0.2	2.1±0.3	158.7*	794	LMXB, Z	6
IGR J16479-4514	252.004	-45.207	0.7	3.9±0.2	2.7±0.3	18.2*	805	HMXB?	26

Table 5.4 – Continued

Name	RA	Dec.	Err	F_{20-40}	F_{40-100}	Sig	Exp	Type	Refs
IGR J16482-3036	252.040	-30.593	1.1	1.6±0.2	1.6±0.3	8.4**	857	AGN?	8 , 16
IGR J16493-4348	252.381	-43.835	0.8	2.7±0.2	2.2±0.3	13.3**	847	XB?	27
IGR J16500-3307	252.505	-33.116	1.2	1.7±0.2	<0.9	7.8*	966	?	16
ESO 138-1	252.938	-59.213	1.3	1.9±0.3	1.6±0.4	6.7**	402	AGN, Sy2	4
IGR J16558-5203	254.012	-52.052	1.0	1.4±0.2	2.5±0.4	9.1**	660	?	
AX J1700.2-4220	255.073	-42.396	1.2	1.4±0.2	1.3±0.3	7.6**	946	?	
OAO 1657-415	255.206	-41.661	0.5	85.1±0.2	45.8±0.3	402.6*	980	HMXB, XP	2
GX 339-4	255.708	-48.791	0.5	22.7±0.2	28.2±0.3	126.1**	710	LMXB, T, U, BH	6 , 28
4U 1700-377	255.988	-37.849	0.5	207.3±0.2	124.6±0.3	1110.2**	1180	HMXB	2
GX 349+2	256.448	-36.419	0.5	46.0±0.2	1.6±0.3	241.5*	1220	LMXB, Z	6
4U 1702-429	256.566	-43.055	0.5	14.9±0.2	9.3±0.3	71.1*	921	LMXB, B, A	6
IGR J17088-4008	257.208	-40.142	0.9	1.1±0.2	2.2±0.3	10.3**	1110	AXP	6
4U 1705-440	257.226	-44.107	0.5	27.3±0.2	16.4±0.3	124.4*	863	LMXB, B, A	6
4U 1705-32	257.237	-32.317	0.7	2.9±0.2	3.0±0.3	19.3**	1290	LMXB, B	29
IGR J17091-3624	257.278	-36.415	0.5	10.0±0.2	13.2±0.3	71.5**	1260	BHC?	30
XTE J1709-267	257.389	-26.655	0.7	1.0±0.2	<0.8	18.4	1140	LMXB, B, T	6
XTE J1710-281	257.550	-28.140	0.6	3.0±0.2	4.1±0.3	22.0**	1210	LMXB, T, B	6
Oph Cluster	258.109	-23.363	0.6	4.9±0.2	1.7±0.3	25.6*	1020	Cluster	31
4U 1708-40	258.139	-40.850	1.3	1.2±0.2	<0.8	6.9*	1060	LMXB, B	6
SAX J1712.6-3739	258.146	-37.655	0.6	5.2±0.2	4.5±0.3	31.0**	1250	LMXB, T, B	6
V2400 Oph	258.170	-24.267	0.7	3.5±0.2	2.1±0.3	19.4*	1070	CV	1
XTE J1716-389	258.941	-38.835	1.1	1.6±0.2	1.0±0.3	8.8*	1200	?	16
NGC 6300	259.213	-62.823	1.0	4.3±0.4	3.7±0.7	10.1**	200	AGN, Sy2	4
IGR J17195-4100	259.931	-41.032	0.8	2.3±0.2	2.2±0.3	13.9**	1060	?	
XTE J1720-318	259.976	-31.749	0.5	6.1±0.2	8.1±0.2	49.4**	1410	LMXB, T, BHC	32
IGR J17200-3116	260.022	-31.290	0.7	3.0±0.2	2.3±0.2	19.4**	1430	?,T	

Table 5.4 – Continued

Name	RA	Dec.	Err	F_{20-40}	F_{40-100}	Sig	Exp	Type	Refs
IGR J17204-3554	260.104	-35.900	0.8	1.5±0.2	2.1±0.2	13.1**	1360	mol cloud?	33
EXO 1722-363	261.288	-36.277	0.5	8.9±0.2	3.2±0.2	51.8*	1360	HMXB, XP	2
IGR J17254-3257	261.350	-32.968	0.7	2.7±0.2	3.0±0.2	19.9**	1450	?	
GRS 1724-30	261.884	-30.812	0.5	18.2±0.2	16.0±0.2	125.6**	1470	LMXB, G, B, A	6
IGR J17285-2922	262.172	-29.382	1.2	0.7±0.2	1.4±0.2	7.3**	1470	BHC?, T	34
IGR J17303-0601	262.593	-6.016	0.9	3.7±0.3	2.1±0.5	11.6*	282	LMXB?,CV?	35 , 36
GX 9+9	262.927	-16.974	0.5	12.9±0.2	1.6±0.3	53.8*	722	LMXB, A	6
GX 354-0	262.988	-33.830	0.5	44.1±0.2	16.8±0.2	264.1*	1460	LMXB, B, A	6
GX 1+4	263.004	-24.752	0.5	42.5±0.2	31.0±0.2	259.2**	1330	LMXB, XP	6
4U 1730-335	263.354	-33.390	0.8	2.4±0.2	<0.7	15.0*	1470	LMXB, G, RB, T	6
GRS 1734-294	264.381	-29.136	0.6	5.4±0.1	3.9±0.2	33.5**	1510	AGN, Sy1	4
SLX 1735-269	264.567	-26.995	0.5	9.3±0.2	7.5±0.2	61.6**	1460	LMXB, B	6
4U 1735-444	264.744	-44.451	0.5	29.6±0.2	1.3±0.3	132.3*	767	LMXB, B, A	6
XTE J17391-3021	264.818	-30.347	1.1	1.3±0.1	0.9±0.2	8.5**	1510	HMXB, NS, Be?, T	2 , 37 , 3
XTE J1739-285	264.961	-28.496	1.1	<0.4	<0.7	8.4	1500	LMXB?	38
SLX 1737-282	265.191	-28.280	0.6	3.2±0.1	3.3±0.2	23.8**	1490	LMXB, B	6 , 39
2E 1739.1-1210	265.463	-12.196	1.1	2.2±0.2	1.8±0.4	8.8**	526	AGN, Sy1	40
XTE J1743-363	265.751	-36.381	0.8	2.5±0.2	1.9±0.2	14.6**	1340	?,T	
1E 1740.7-2942	265.988	-29.745	0.5	26.7±0.1	34.0±0.2	222.0**	1510	LMXB, BHC	6 , 41 , 42
IGR J17445-2747	266.132	-27.783	1.5	0.9±0.1	0.8±0.2	6.0*	1480	?	
KS 1741-293	266.220	-29.340	0.5	8.8±0.1	7.8±0.2	62.3**	1510	LMXB, T, B	6
IGR J17456-2901	266.410	-29.020	0.6	5.0±0.1	2.7±0.2	30.9*	1500	?	43
1E 1742.8-2853	266.498	-28.917	0.6	5.4±0.1	3.7±0.2	31.8*	1500	LMXB	6
1A 1742-294	266.520	-29.510	0.5	14.1±0.1	7.9±0.2	85.7*	1510	LMXB, B	6
IGR J17464-3213	266.567	-32.232	0.5	66.5±0.2	40.5±0.2	405.1*	1490	LMXB, T, BHC	6 , 44
1E 1742.9-2849	266.570	-28.814	0.6	5.4±0.1	2.8±0.2	31.6*	1500	LMXB	6

Table 5.4 – Continued

Name	RA	Dec.	Err	F_{20-40}	F_{40-100}	Sig	Exp	Type	Refs
1E 1743.1-2843	266.590	-28.670	0.8	3.8±0.1	1.6±0.2	13.5*	1500	LMXB	6
SAX J1747.0-2853	266.805	-28.837	1.1	1.4±0.1	<0.7	8.8*	1500	LMXB, B, T	6
IGR J17475-2822	266.820	-28.445	0.7	2.1±0.1	1.9±0.2	15.1**	1490	mol cloud?	45
SLX 1744-299	266.860	-30.020	0.5	8.8±0.1	5.7±0.2	56.5*	1500	LMXB, B	6
GX 3+1	266.989	-26.562	0.5	13.5±0.2	0.8±0.2	84.7*	1440	LMXB, B, A	6
1A 1744-361	267.057	-36.133	1.2	1.0±0.2	1.3±0.2	7.7**	1340	LMXB, T	6
IGR J17488-3253	267.206	-32.914	0.7	2.3±0.2	3.3±0.2	19.4**	1460	?	
4U 1745-203	267.217	-20.386	0.7	2.1±0.2	3.2±0.3	16.1**	1070	LMXB, T, G	6
4U 1746-370	267.557	-37.047	0.6	4.7±0.2	1.9±0.3	25.5*	1270	LMXB, G, B, A	6
GRS 1747-312	267.637	-31.296	1.1	1.1±0.2	1.1±0.2	8.4**	1480	LMXB, G, T	6
IGR J17513-2011	267.822	-20.188	0.8	2.0±0.2	2.5±0.3	13.4**	1060	?	16
IGR J17544-2619	268.605	-26.342	1.3	1.1±0.2	<0.7	6.7*	1410	HMXB?, T	46 , 47 , 16
IGR J17597-2201	269.939	-22.033	0.5	8.4±0.2	7.8±0.3	52.2**	1190	LMXB, B, D	48 , 37
GX 5-1	270.287	-25.079	0.5	55.3±0.2	3.2±0.2	318.9*	1340	LMXB, Z	6
GRS 1758-258	270.303	-25.749	0.5	39.5±0.2	48.1±0.2	291.9**	1350	LMXB, U, BHC	6 , 49
GX 9+1	270.388	-20.524	0.5	17.6±0.2	0.9±0.3	93.0*	1080	LMXB, A	6
IGR J18027-1455	270.690	-14.922	0.7	3.0±0.2	3.3±0.3	15.5**	766	AGN, Sy1	35
SAX J1802.7-201	270.692	-20.294	0.6	5.8±0.2	2.5±0.3	30.5*	1070	HMXB, T, XP	50 , 51
IGR J18048-1455	271.211	-14.914	1.0	1.7±0.2	2.0±0.3	9.3**	774	?	
XTE J1807-294	271.748	-29.410	0.6	3.1±0.2	3.1±0.2	21.6**	1340	LMXB, T, XP	52
SGR 1806-20	272.156	-20.423	0.6	3.4±0.2	4.7±0.3	23.7**	1060	SGR	53
IGR J18135-1751	273.363	-17.849	1.1	1.6±0.2	1.2±0.3	8.2**	916	?	54
GX 13+1	273.618	-17.146	0.5	17.5±0.2	5.0±0.3	84.5*	880	LMXB, B, A	6
M 1812-12	273.779	-12.102	0.5	25.7±0.2	25.5±0.3	137.7**	735	LMXB, B	6
GX 17+2	274.007	-14.040	0.5	58.4±0.2	3.2±0.3	263.9*	781	LMXB, B, Z	6
SAX J1818.6-1703	274.671	-17.055	1.4	1.2±0.2	1.2±0.3	6.5**	869	?,T	

Table 5.4 – Continued

Name	RA	Dec.	Err	F_{20-40}	F_{40-100}	Sig	Exp	Type	Refs
IGR J18193-2542	274.820	-25.703	1.5	0.8±0.2	1.1±0.3	5.7**	1130	?	
AX J1820.5-1434	275.133	-14.572	0.6	5.1±0.2	3.3±0.3	23.4*	794	HMXB, XP, Be	2 , 3
IGR J18214-1318	275.340	-13.308	0.9	2.1±0.2	2.0±0.3	10.8**	773	?	
4U 1820-303	275.928	-30.370	0.5	35.3±0.2	2.3±0.3	186.6*	1070	LMXB, G, B, A	6
4U 1822-000	276.335	-0.032	1.0	2.4±0.2	<1.1	9.9*	641	LMXB	6
IGR J18256-1035	276.406	-10.587	1.5	1.2±0.2	<1.0	5.9*	762	?	
3A 1822-371	276.462	-37.102	0.5	34.1±0.2	4.3±0.3	162.5*	895	LMXB, D	6
IGR J18259-0706	276.485	-7.106	1.4	1.2±0.2	1.0±0.3	6.2**	743	?	
GS 1826-24	277.367	-23.801	0.5	73.3±0.2	58.6±0.3	359.8**	942	LMXB, B	6
IGR J18325-0756	278.118	-7.940	0.7	3.9±0.2	2.2±0.3	18.2*	794	?	
SNR 021.5-00.9	278.395	-10.558	0.7	2.8±0.2	3.3±0.3	15.9**	785	SNR, PWN	55
PKS 1830-211	278.405	-21.052	0.7	3.0±0.2	3.7±0.3	17.7**	843	AGN, QSO	4
RX J1832-330	278.921	-32.989	0.5	11.6±0.2	9.9±0.3	58.6**	823	LMXB, G, B, T	6
AX J1838.0-0655	279.507	-6.904	0.8	2.1±0.2	3.1±0.3	14.1**	835	?	56
ESO 103-35	279.578	-65.431	1.4	5.9±0.9	4.5±1.5	6.2**	42	AGN, Sy1.9	4
Ser X-1	279.992	5.031	0.5	10.1±0.2	<0.9	48.7*	861	LMXB, B	6
AX J1841.0-0535	280.237	-5.602	1.5	1.0±0.2	1.1±0.3	6.0**	861	HMXB, XP, Be?	57
Kes 73	280.338	-4.949	0.7	2.0±0.2	3.8±0.3	15.1**	875	SNR, AXP	58
IGR J18450-0435	281.243	-4.602	1.8	1.0±0.2	<0.9	5.0**	907	?	
GS 1843+009	281.418	0.875	0.6	4.3±0.2	3.2±0.3	22.9**	970	HMXB, XP, Be, T	2 , 3
AX J1846.4-0258	281.622	-2.973	0.8	1.9±0.2	2.5±0.3	12.5**	940	SNR, PWN, AXP	59
IGR J18483-0311	282.064	-3.169	0.7	4.1±0.2	2.7±0.3	20.3*	945	?	
3A 1845-024	282.082	-2.424	1.3	1.3±0.2	0.9±0.3	6.7*	956	HMXB, XP, Be?, T	2 , 3
IGR J18490-0000	282.267	-0.025	1.4	1.2±0.2	0.9±0.3	6.4**	998	?	
4U 1850-087	283.266	-8.706	0.6	4.6±0.2	3.8±0.3	23.2**	804	LMXB, G, B	6
IGR J18539+0727	283.477	7.458	0.9	1.9±0.2	1.6±0.3	11.3**	1000	BHC?	30

Table 5.4 – Continued

Name	RA	Dec.	Err	F_{20-40}	F_{40-100}	Sig	Exp	Type	Refs
V1223 Sgr	283.755	-31.145	0.6	7.8±0.2	3.5±0.4	30.3*	512	CV	1
XTE J1855-026	283.877	-2.604	0.5	11.8±0.2	6.9±0.3	64.8*	969	HMXB, XP, T	2
2E 1853.7+1534	284.008	15.621	0.9	2.8±0.2	2.0±0.4	12.0**	578	AGN?	8
XTE J1858+034	284.686	3.431	0.5	0.8±0.2	<0.8	49.8	1090	HXMB, XP, Be?, T	2 , 3
XTE J1901+014	285.397	1.439	0.6	3.4±0.2	3.0±0.3	21.6**	1070	T, BHC?	60
4U 1901+03	285.913	3.205	0.5	93.8±0.2	10.5±0.3	552.3*	1090	HMXB, T, XP	2 , 61
XTE J1908+094	287.220	9.390	0.6	3.6±0.2	4.2±0.3	23.7**	998	LMXB, T, BHC	62
4U 1907+097	287.414	9.836	0.5	16.5±0.2	2.0±0.3	91.4*	980	HMXB, XP, T	2
4U 1909+07	287.701	7.602	0.5	14.4±0.2	8.7±0.3	81.6*	1060	HMXB, XP	63
Aql X-1	287.811	0.577	0.5	9.4±0.2	5.1±0.3	53.8*	1010	LMXB, B, A, T	6
SS 433	287.957	4.974	0.5	14.5±0.2	7.3±0.3	89.0*	1090	HMXB	2
IGR J19140+0951	288.525	9.872	0.5	9.5±0.2	5.7±0.3	54.7*	981	HMXB?, NS?	64 , 65
GRS 1915+105	288.798	10.940	0.5	288.1±0.2	108.8±0.3	1591.0*	926	LMXB, T, BH	6 , 66
4U 1916-053	289.697	-5.243	0.5	9.3±0.2	3.9±0.3	42.1*	682	LMXB, B, D	6
IGR J19284+0107	292.098	1.119	1.3	1.2±0.2	<0.9	6.8*	857	?	
IGR J19308+0530	292.692	5.502	1.4	0.8±0.2	1.5±0.3	6.6***	949	?	
RX J1940.1-1025	295.066	-10.408	1.1	3.0±0.3	2.1±0.6	8.1*	267	CV	1
NGC 6814	295.644	-10.332	1.0	3.1±0.3	3.9±0.6	9.9**	248	AGN, Sy1.5	4
KS 1947+300	297.396	30.210	0.5	38.4±0.6	23.9±1.0	55.6*	93	HMXB, T, XP	2 , 67 , 68
Cyg X-1	299.592	35.194	0.5	812.9±0.6	944.3±1.0	1417.3**	100	HMXB, BH, U	2
Cyg A	299.878	40.755	1.1	5.4±0.6	6.0±1.0	8.8**	91	AGN, Sy1.9	4
EXO 2030+375	308.046	37.630	0.5	38.9±0.5	20.4±0.8	74.6*	147	HMXB, XP, Be, T	2 , 3
Cyg X-3	308.108	40.953	0.5	201.1±0.4	82.2±0.7	418.4*	151	HMXB	2
SAX J2103.5+4545	315.891	45.743	0.5	33.4±0.4	18.5±0.7	78.4*	166	HMXB, XP, Be, T	2 , 3
IGR J21247+5058	321.151	50.980	0.7	5.7±0.4	8.1±0.7	16.3**	143	AGN, Sy1?	35
IGR J21335+5105	323.375	51.092	1.2	2.9±0.4	<2.1	7.8**	143	CV	1

Table 5.4 – Continued

Name	RA	Dec.	Err	F_{20-40}	F_{40-100}	Sig	Exp	Type	Refs
1H 2140+433	325.745	43.587	1.1	4.4±0.4	<2.2	8.8*	127	Dwarf nova, CV	1
Cyg X-2	326.168	38.318	0.5	26.7±0.5	<2.7	43.9*	96	LMXB, B, Z	6
4U 2206+543	331.974	54.514	0.6	12.8±0.5	9.2±0.8	24.6*	114	HMXB, NS, Be	2 , 69 , 3
Cas A	350.822	58.792	1.1	3.9±0.5	3.3±0.9	8.0**	95	SNR	5

---

[1]Names in bold face indicate new detections since first catalog; [2]Position errors are expressed as radius of 1σ error circle; [3]Fluxes are expressed in units of mCrab; appropriate conversion factors are: (20-40 keV) 10 mCrab = 7.57 x 10^{-11} erg cm^{-2} s^{-1} = 1.71 x 10^{-3} ph cm^{-2} s^{-1}; (40-100 keV) 10 mCrab = 9.42 x 10^{-11} erg cm^{-2} s^{-1} = 9.67 x 10^{-4} ph cm^{-1} s^{-1}; [4]Maximimum significance is quoted in either (*) 20–40 keV band, (**) 20–100 keV band, (***) 30–60 keV band, (no mark) significance in one revolution 20–40 keV; [5]Exposure is the corrected on-source exposure in ksec [6]Source type classifications: A=Atoll source (neutron star); AGN=Active galactic nuclei; AXP=Anomalous X-ray pulsar; B=Burster (neutron star); Be=B-type emission-line star; BH=Black hole (confirmed mass evaluation); BHC=Black hole candidate; Cluster=Cluster of galaxies; CV=Cataclysmic variable; D=Dipping source; G=Globular Cluster X-ray source; HMXB=High-mass X-ray binary; LMXB=Low-mass X-ray binary; Mol Cloud=Molecular cloud; NS=Neutron Star; PSR=Radio pulsar; PWN=Pulsar wind nebula; QSO = Quasar; SGR=Soft gamma-ray repeater; SNR=Supernova remnant; Sy=Seyfert galaxy; Symb=Symbiotic star; T=Transient source; U=Ultrasoft source; XB=Galactic X-ray binary; XP=X-ray pulsar; Z=Z-type source (neutron star) [7]References: (1) - Downes et al. 2001; (2) - Liu et al. 2000; (3) - Raguzova & Popov 2005; (4) - Veron & Veron 2003; (5) - Forman et al. 1978; (6) - Liu et al. 2001; (7) - Molina et al. 2004; (8) - Bassani et al. 2005; (9) - Masetti et al. 2005; (10) - Done et al. 1996; (11) - Dermer & Gehrels 1996; (12) - Laurent et al. 1994; (13) - Haberl et al. 2002; (14) - Stephen et al. 2005; (15) - Orosz et al. 2002; (1) - Stephen et al. 2006; (17) - Sidoli 2005; (18) - Walter et al. 2003; (19) - Rodriguez et al. 2003; (20) - Lutovinov et al. 2005a; (21) - Patel et al. 2004; (22) - Ebeling et al. 2002; (23) - Combi et al. 2004; (24) - Malizia et al. 2004; (25) - Walter et al. 2004b; (26) - Walter et al. 2004a; (27) - Grebenev et al. 2005; (28) - Cowley et al. 1987; (29) - in't Zand et al. 2005a; (30) - Lutovinov & Revnivtsev 2003; (31) - Arnaud et al. 1987; (32) - Rupen et al. 2003; (33) - Sekimoto et al. 2000; (34) - Barlow et al. 2005; (35) - Masetti et al. 2004a; (36) - Gänsicke et al. 2005a; (37) - Lutovinov et al. 2005b; (38) - Harmon et al. 2004; (39) - in't Zand et al. 2002; (40) - Torres et al. 2004; (41) - Sunyaev et al. 1991; (42) - Mirabel et al. 1992; (43) - Bélanger et al. 2004; (44) - Markwardt et al. 2003c; (45) - Revnivtsev et al. 2004; (46) - Gonzalez-Riestra et al. 2004; (47) - Revnivtsev 2003; (48) - Markwardt & Swank 2003b; (49) - Rodriguez et al. 1992; (50) - Augello et al. 2003; (51) - Hill et al. 2005; (52) - Markwardt et al. 2003a; (53) - Atteia et al. 1987; (54) - Ubertini et al. 2005; (55) - Davelaar et al. 1986; (56) - Malizia et al. 2005; (57) - Bamba et al. 2001; (58) - Vasisht & Gotthelf 1997; (59) - Gotthelf & Vashisht 1998; (60) - Remillard et al. 2002; (61) - Galloway et al. 2003; (62) - Woods et al. 2002; (63) - Levine et al. 2004; (64) - in't Zand et al. 2005b; (65) - Rodriguez et al. 2005; (66) - Mirabel & Rodriguez 1994; (67) - Swank & Morgan 2000; (68) - Negueruela et al. 2000; (69) - Masetti et al. 2004b

5.3.5 Spectral Analysis of Sources in the Second Catalogue

In the X-ray regime (~2–10 keV), colour-colour diagrams are used to track spectral shape variations of individual sources. In this section, soft gamma-ray colour-colour diagrams are used to compare the average spectral characteristics of sources in the second IBIS catalogue. These average colour-colour diagrams (Av-CD) have been derived from time-averaged fluxes in three energy bands (20–30, 30–40 and 40–100 keV) over the entire second survey set of observations in ISGRI counts/s. 'Hard' colour = 40–100/30–40 and 'Soft' colour = 30–40/20–30. The fluxes and associated errors are obtained from the weighted average of the source light-curves in the ten energy bands as described in Sec. 5.3.3, which can be combined to create the broad band values. By overlapping the colours using the 30–40 keV range, the statistics were improved over using four bands, e.g. 40–60 keV and 60–100 keV separately. Faint transient sources (*e.g.* those only detected in one revolution) were excluded from the analysis.

Figure 5.10 displays the average colours of the X-ray binaries included in the second catalogue and reveals that LMXB and HMXB largely occupy different parts of the colour-colour diagram. Also plotted are the equivalent colours for models corresponding to different spectral fits, a simple power law model with photon index, Γ, between 1 and 4 and a set of cut-off power-law models with Γ=1, 2, 3. Data-points on the cut-off power-law models correspond to the energy of the exponential roll-off E_{fold}, where:

$$A(E) = N \cdot E^{-\Gamma}\ e^{-E/E_{fold}} \tag{5.2}$$

On the whole, the location of the HMXBs is better described using the cut-off power law models, while the LMXBs are closer to the simple power law model with Γ=2–3.

To analyse the spectral characteristics of the X-ray binaries further, they have been split according to compact object (neutron star - NS, or black hole - BH).

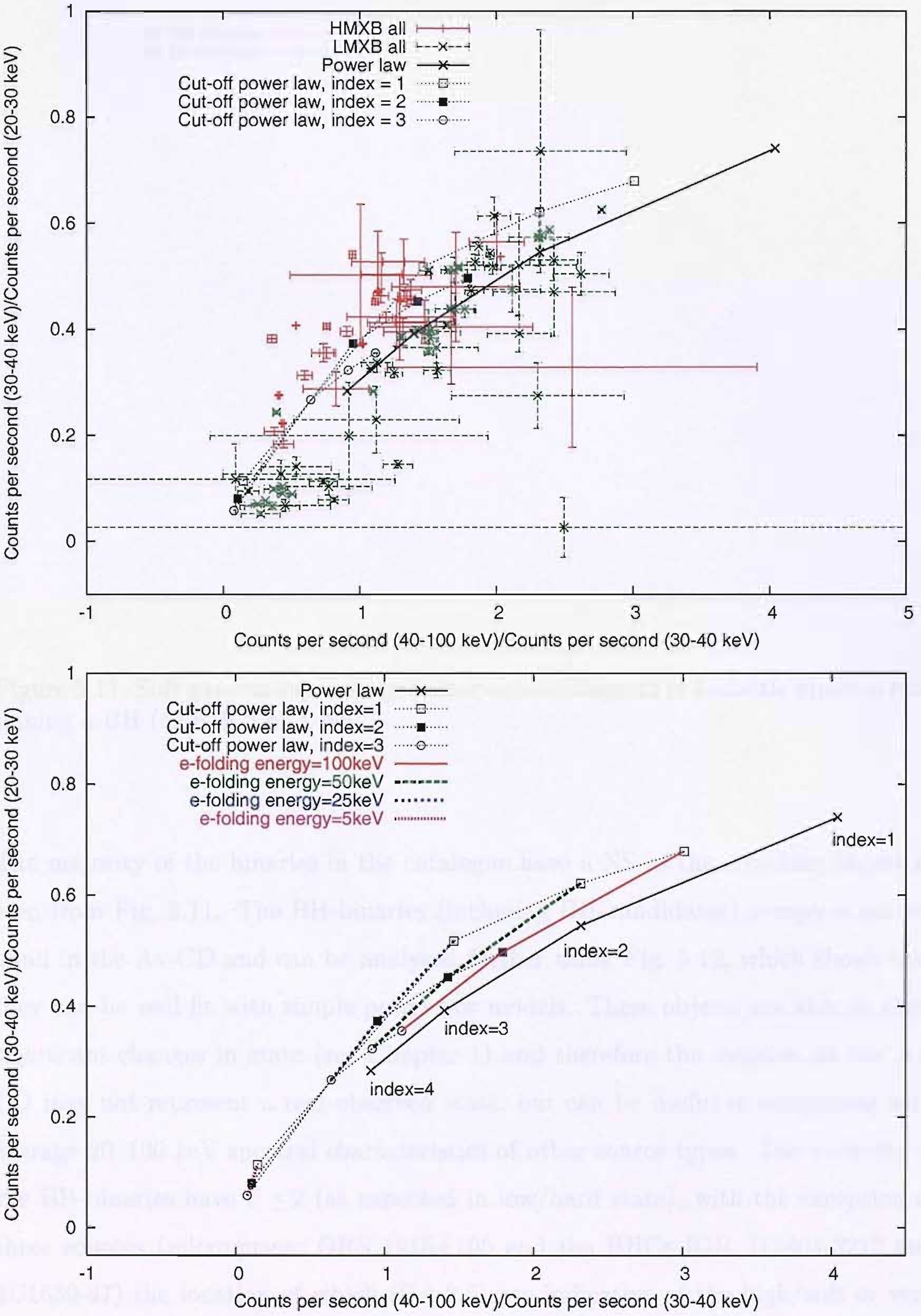

Figure 5.10: Top: Soft gamma-ray average colour-colour diagram of HMXB and LMXB. Bottom: key to spectral models.

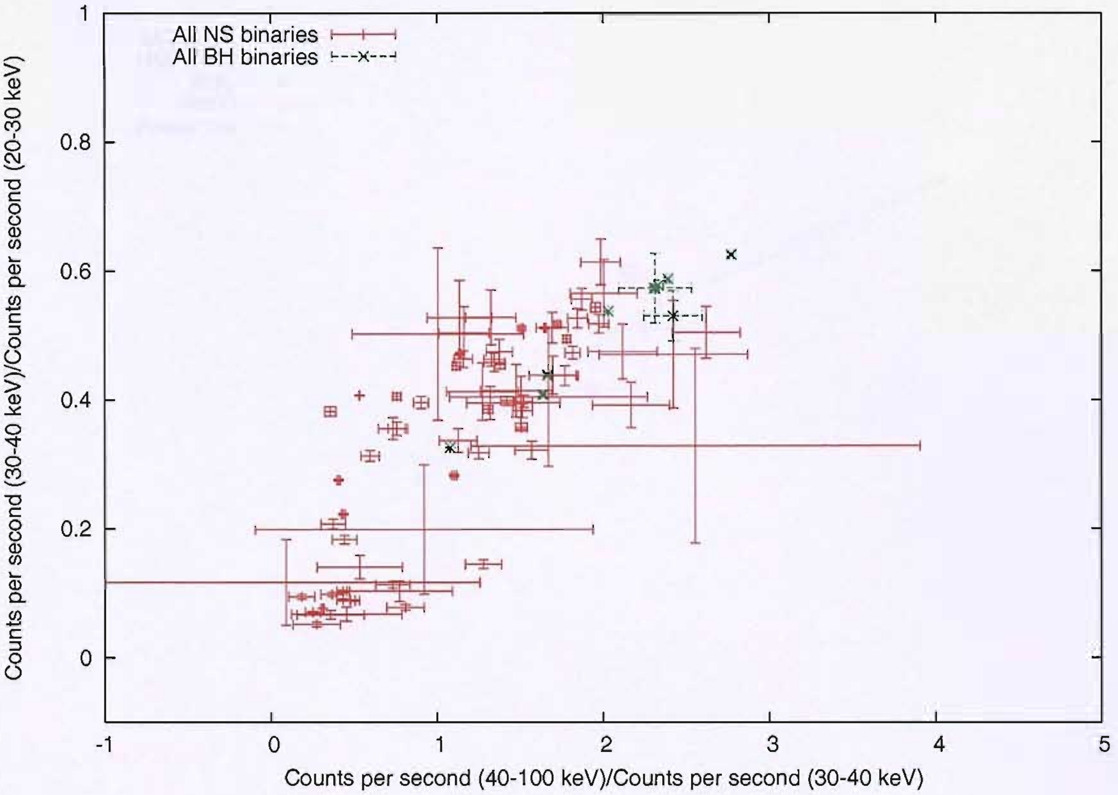

Figure 5.11: Soft gamma-ray average colour-colour diagram of Galactic binaries containing a BH (or BHC) or a NS.

The majority of the binaries in the catalogue have a NS as the accreting object as seen from Fig. 5.11. The BH-binaries (including BH candidates) occupy a narrow band in the Av-CD and can be analysed further using Fig. 5.12, which shows that they can be well fit with simple power law models. These objects are able to show significant changes in state (see Chapter 1) and therefore the location on the Av-CD may not represent a real observed state, but can be useful in comparing with average 20–100 keV spectral characteristics of other source types. The majority of the BH-binaries have $\Gamma \leq 2$ (as expected in low/hard state), with the exception of three sources (microquasar GRS 1915+105 and the BHCs IGR J17464-3212 and 4U1630-47) the location of which ($\Gamma > 2.5$) are indicative of the high/soft or very high states where $\Gamma = 2.1$–4.8 (McClintock & Remilard 2004).

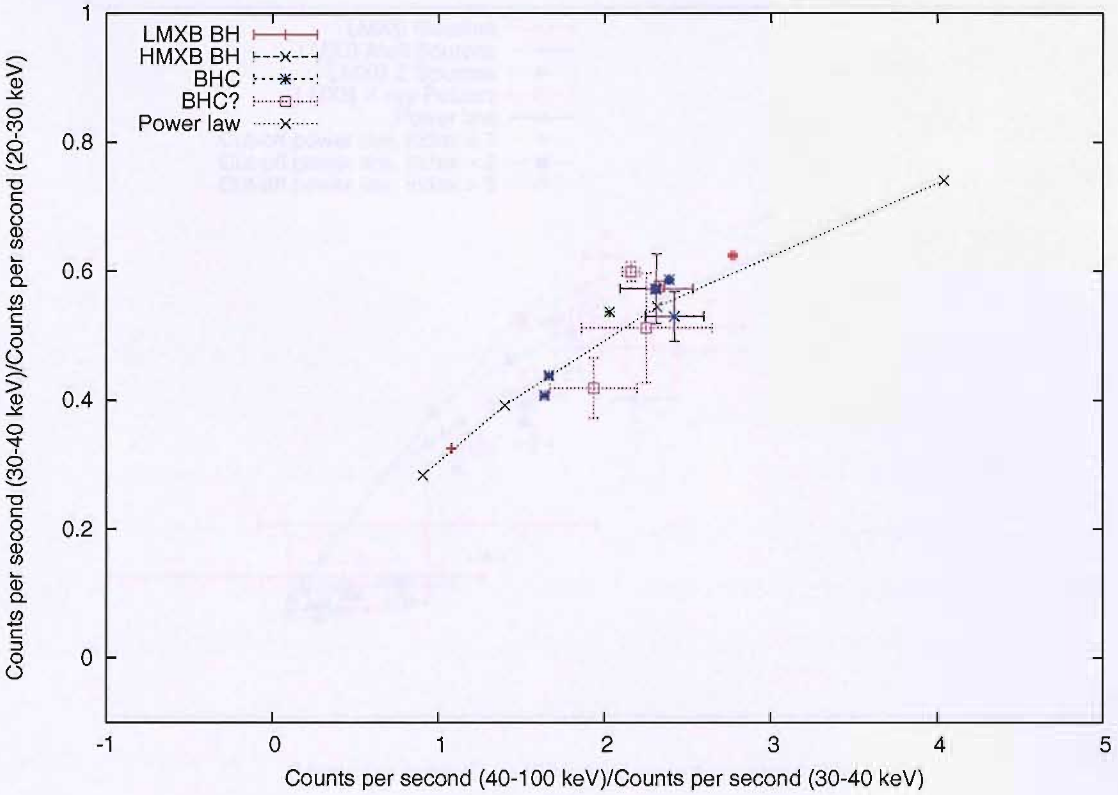

Figure 5.12: Soft gamma-ray average colour-colour diagram of Galactic binaries containing a BH or BHC. The microquasar GRS 1915+105 is the red cross near to index=4. Dotted line describes power law models with photon index between 1 (top-right data-point) and 4.

The NS-binaries are further split into sub-types: Atoll sources, Z sources and those exhibiting type I X-ray bursts (but without an atoll classification) for LMXBs (Fig. 5.13) and absorbed, Be star binaries and X-ray Pulsar systems for HMXBs (Fig. 5.14). The LMXB-NS systems are located in two distinct groups in the Av-CD (Fig. 5.13) - harder sources with 30–40/20–30 colour>0.2, 40–100/30–40 colour >1 and softer sources clustered around 30–40/20–30 colour ~0.1, 40–100/30–40 colour ~0.5. The harder group of objects consists of the majority of the Bursting sources and approximately half of the Atoll sources. These sources appear to follow the power law models with a photon index >2 and/or cut-off power law with E_{fold} between 25 and 50 keV and index 1-2. The softer group contains the remainder of

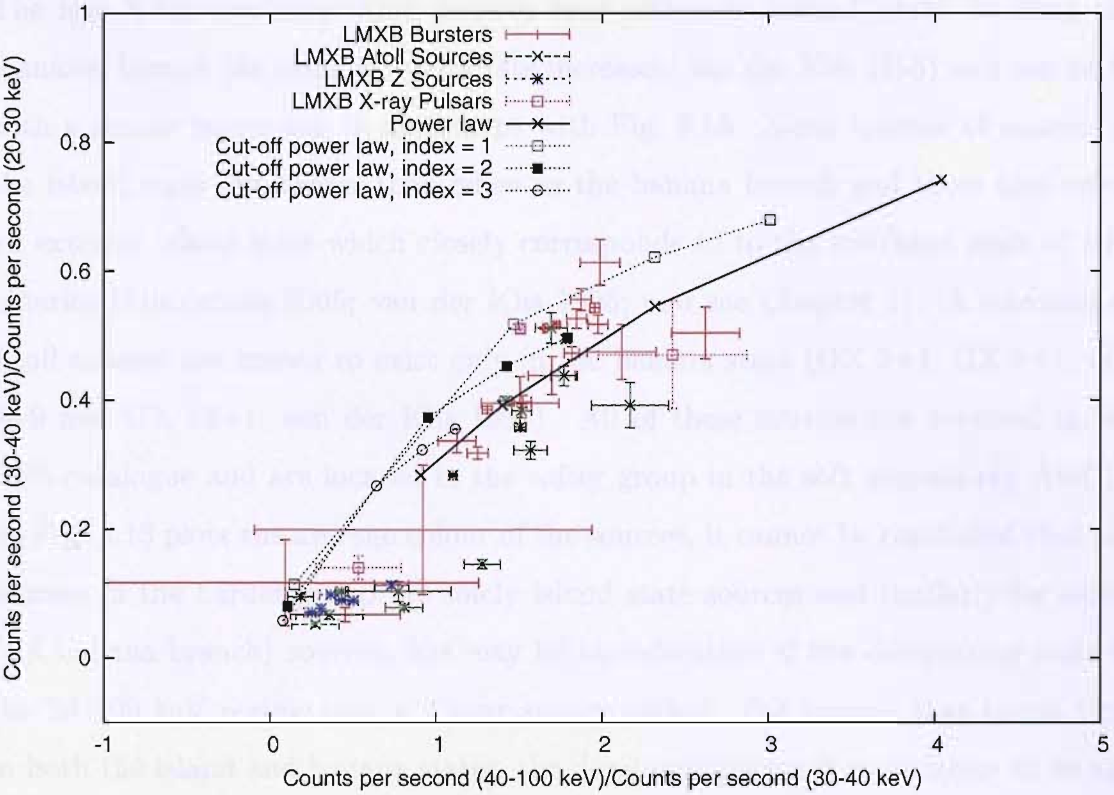

Figure 5.13: Soft gamma-ray average colour-colour diagram of LMXB containing a NS by sub-type. The solid line describes power law models with photon index between 1 (top-right data point) and 4. The dotted line/open squares represents a power law of Γ=1 cut-off with exponential roll-off energies (from top-right data point) of 100, 50, 25 and 5 keV. Similarly for Γ=2 (dotted line/filled squares) and dotted line–open circle for Γ=3 (dotted line/open circle).

the Atoll sources and the entire set of Z-type sources, together with a small number of bursters. These sources do not follow the power law or cut-off power law models.

As introduced in Chapter 1, Atoll and Z-type sources are subtypes of accreting non/low-magnetic neutron stars in LMXB systems and are defined according to their X-ray spectral and timing behaviour. Z-type sources have generally higher L_X ($>10^{37}$ erg s^{-1}) than Atoll sources and their broad-band IR–hard X-ray spectra can be best fit with thermal bremsstrahlung model (White, Nagase & Parmar 1995).

The less X-ray luminous Atoll sources exist either an 'island' state or along the 'banana' branch (as mass accretion rate increases, van der Klis 1995) and can be fit with a simple power-law in agreement with Fig. 5.13. X-ray spectra of sources in the island state are harder than when in the banana branch and there also exists an extreme island state which closely corresponds to to the low/hard state of BH-binaries (Maccarone 2005; van der Klis 1995; and see Chapter 1). A selection of Atoll sources are known to exist only in the banana state (GX 3+1, GX 9+1, GX 9+9 and GX 13+1; van der Klis 1995). All of these sources are detected in the IBIS catalogue and are located in the softer group in the soft gamma-ray Av-CD. As Fig. 5.13 plots the average colour of the sources, it cannot be concluded that the sources in the harder group are solely island state sources and similarly for softer (*c.f.* banana branch) sources, but may be an indication of the dominating state in the 20–100 keV regime over a 2 year survey period. For sources that spend time in both the island and banana states, the dominating state is more likely to be the island state as observations have shown that sources move along the banana branch on short timescales (hrs-days) compared to island states which exist on timescales of weeks to months (van der Klis 1995). Fig. 5.13 indicates a similarity between the soft gamma-ray characteristics of banana-state Atoll sources and Z-type sources and also between average BH-binary and Atoll-Island spectral states as suggested by Maccarone (2005).

HMXBs mostly follow the cut-off power law models with E_{cut}=5–25 keV – slightly lower than for the harder group of LMXB. There is a loose group of X-ray pulsars in the region soft colour$\sim$0.4, hard colour$\sim$0.5 which can be fit with bremsstrahlung model with kT$\sim$10–20 keV. Absorbed sources do not appear to cluster in any one area, indicating the soft gamma-ray emission from these sources is similar to the unabsorbed systems, but the colours appear less constrained. Example IBIS spectra of X-ray pulsars can be found in Fillipova et al. (2004).

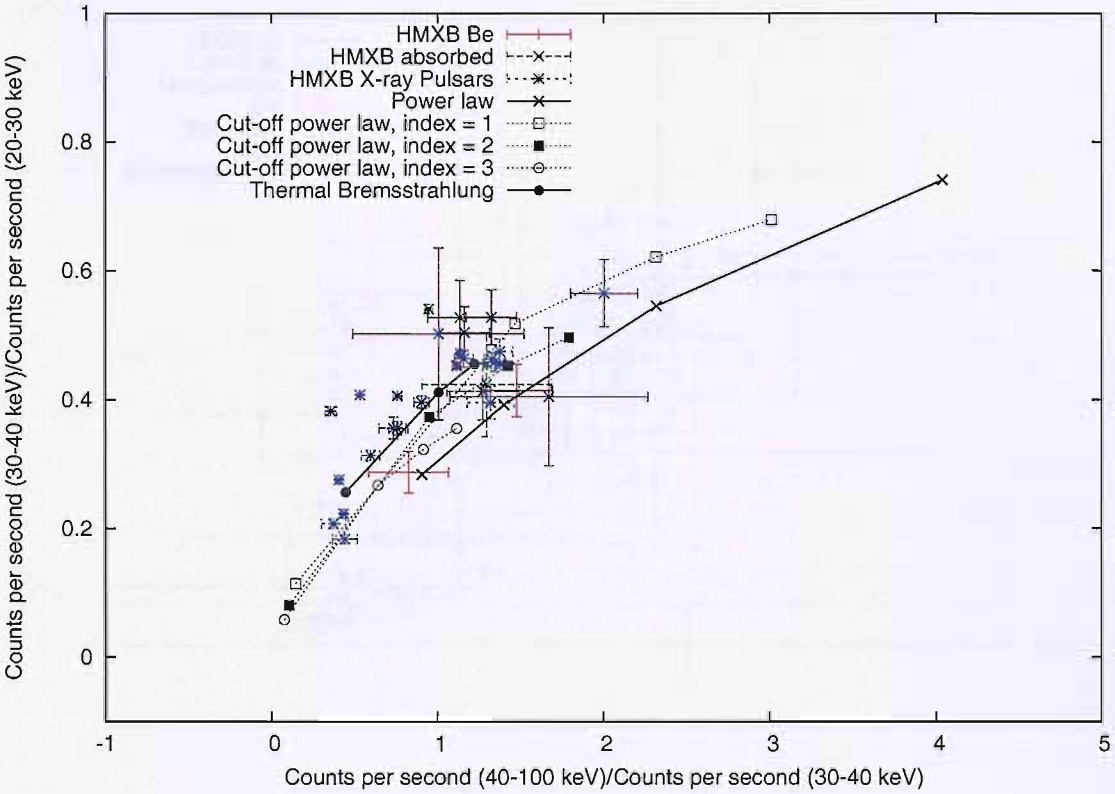

Figure 5.14: Soft gamma-ray average colour-colour diagram of HMXB containing a NS by sub-type. The solid line is power law fit with photon index between 1 (top right data point) and 4. The dotted line/open squares represents a power law of Γ=1 cut-off with exponential roll-off energies (from top-right data point) of 100, 50, 25 and 5 keV. Similarly for Γ=2 (dotted line/filled squares) and dotted line/open circle for Γ=3 (dotted line/open circle). Solid line/filled circles represents bremsstrahlung model with temperature (from bottom left data-point) kT=10, 20 and 25 keV

Fig. 5.15 displays the average colours for all sources in the second catalogue with and without error-bars to aid in the identification of any clustering. Unclassified sources appear to be fairly evenly distributed (even in the hard regions where AGN are located), except perhaps in the soft LMXB area. There does seem to be a handful of unclassified sources to the left of the HMXB area and near to the CV IGR J21335+5105, their location indicating that there is little flux above 40–100 keV. The possiblity of *INTEGRAL* sources being CV systems is investigated in Chapter 7. Analysis of the average spectral characteristics of the extra-galactic

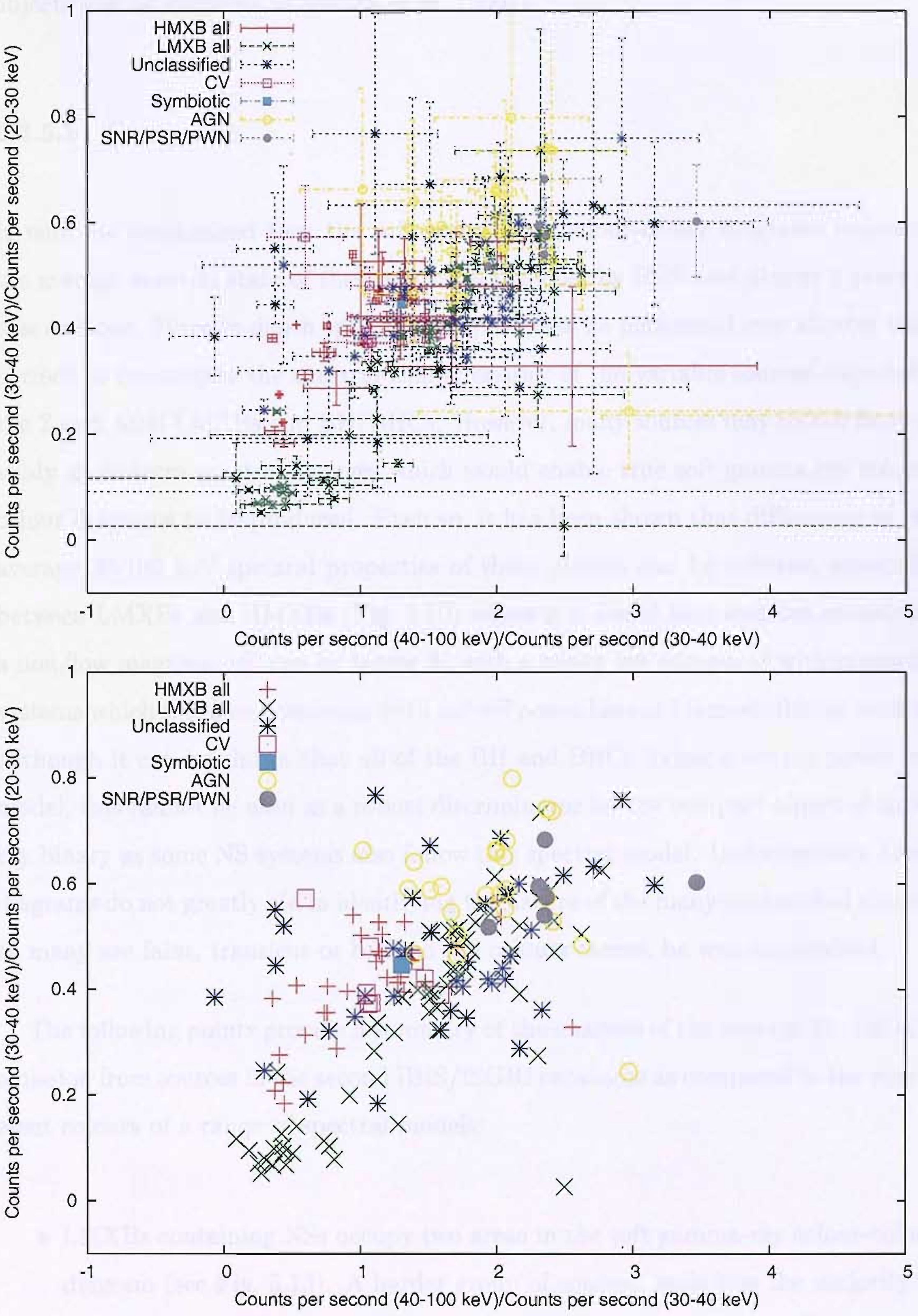

Figure 5.15: Soft gamma-ray average colour-colour diagram of all second catalogue sources.

objects will be included in Molina et al. (2006).

5.3.5.1 Summary

It must be emphasised that the soft gamma-ray colour-colour diagrams represent the average spectral state of these source as detected by IBIS over almost 2 years of observations. More in-depth spectral analysis must be performed over shorter time periods to investigate the spectral characteristics of the variable sources, especially the Z and Atoll LMXBs and BH/BHCs. However, many sources may be too faint to study short-term spectral changes which would enable true soft gamma-ray colour-colour diagrams to be produced. Even so, it has been shown that differences in the average 20-100 keV spectral properties of these objects can be inferred, especially between LMXBs and HMXBs (Fig. 5.10) where it is found that systems containing a non/low magnetic NS can be better fit with a power law compared with magnetic systems which are more consistent with cut-off power laws or bremsstrahlung models. Although it can be shown that all of the BH and BHCs follow a simple power law model, this cannot be used as a robust discriminator for the compact object of an X-ray binary as some NS systems also follow this spectral model. Unfortunately, these diagrams do not greatly aid in identifying the nature of the many unclassified sources as many are faint, transient or both so the colours cannot be well constrained.

The following points provide a summary of the analysis of the average 20–100 keV emission from sources in the second IBIS/ISGRI catalogue as compared to the equivalent colours of a range of spectral models:

- LMXBs containing NSs occupy two areas in the soft gamma-ray colour-colour diagram (see Fig. 5.13). A harder group of sources, including the majority of bursting sources and half of the Atoll sources, can be described well by a simple power-law (Γ >2) model or by a power-law with E_{fold} >50 keV. The softer group of sources which include all of the Z-type sources and the remainder of the Atoll sources cannot be well fit with a power-law model, and are better modelled with a cut-off power-law with E_{fold} <25 keV.

- HMXBs containing NSs are largely located in a different area of the soft gamma-ray colour-colour diagram from the LMXBs (Fig. 5.10). These sources, particularly those containing pulsars, can be fit with either a cut-off power-law with E_{fold} ~25 keV or a thermal bremsstrahlung model with kT=10–25 keV (Fig. 5.14).
- From comparison of the relative locations of HMXB and LMXB systems with a NS accretor, it can be shown that the average 20–100 keV emission from magnetic/young NS systems can be fit with a different spectral model than old/non-magnetic NS systems. On the whole, systems which have been observed to display Type 1 X-ray bursts (non-magnetic NSs in LMXBs) can be described well with a power-law model (perhaps with a high energy cut-off; Fig. 5.13), while pulsar systems (younger, magnetic NSs in HMXB) can be fitted better with a thermal bremsstrahlung model (Fig. 5.14).
- Binary systems containing a BH or BHC can all be well fit with a simple power-law model Γ ~2, except for GRS 1915+105 (Γ ~3.5; Fig. 5.12).
- The location of the unclassified sources does not suggest an unambiguous association with any single class of object (see Fig. 5.15).

5.4 Current Status of the IBIS/ISGRI Survey

The IBIS/ISGRI catalogue represents the most complete survey of the soft gamma-ray sky to date, in terms of the number of source detected, angular resolution

Catalogue	OSA v.	ScW	Exposure	Sources
1	3.0	2529	>5 Ms	123
2	4.1	~6300	>10 Ms	209
3	5.1	~18000	~30 Ms	~300

Table 5.5: Comparison between the IBIS/ISGRI survey catalogues. Catalogue 3 is in progress.

of the telescope and flux sensitivity in the 20–100 keV energy band. The second IBIS/ISGRI catalogue also represents a significant improvement over the first catalogue, not only in the number of source detected but in the methods used to generate the mosaics and source list. It has been successful in overcoming certain limitations of the first catalogue, namely improving exposure away from the Galactic plane, correcting for the off-axis response of the telescope and searching for transient sources. Subsequent catalogues will aim to increase the sky coverage further and to search for transients at a deeper level, enabling the IBIS/ISGRI survey to represent truly all sources seen by the instrument during the mission lifetime. Additionally, improved analysis of crowded regions will be possible as the result of mosaicing images over a finer pixel size. From conservative projections using observed log N-Log S analysis, it is estimated that at least 500 sources will be detected in the 20–100 keV band all-sky map. As of January 2006, the production of a third IBIS/ISGRI catalogue is underway which includes at least three times the number of ScWs as Catalogue 2 (see Table 5.5). The most recent version of the imaging software (OSA v.5.1) has new algorithms implemented to reduce the number of noisy detector pixels being transmitted and improve the image cleaning process, which should produce better quality maps.

The following chapter will present more detailed analysis of an unclassified IGR source (IGR J17285-2922) discovered during the survey work and Chapter 7 will describe the soft gamma-ray properties of CVs using supplementary survey data.

Chapter 6

Unclassified *INTEGRAL* Source Case Study - IGR J17285-2922

6.1 Introduction

Of the 209 sources listed in the 2nd IBIS/ISGRI catalogue, approximately 25% are currently unclassified (see Chapter 5; Bird et al. 2005). As a result of the exposure bias on the Galactic plane and especially the Galactic centre, the majority of the classified IBIS catalogue sources are Galactic X-ray binaries, further classified according to the mass of the donor star (see Chapter 1). Low-mass binaries (LMXBs) are generally located in the Galactic Bulge and high-mass binaries (HMXBs) in the Galactic Plane, following the expected distributions of their parent stellar populations; see Psaltis (2004) for a review and Dean et al. (2005). Therefore, it may be expected that most of the unidentified sources will also be X-ray binaries, including systems containing a black hole e.g. IGR J17464–3213 (Parmar et al. 2003) and a new class of highly absorbed objects characterised by an absence of soft X-ray emission, *e.g.* IGR J16318–4848 (Walter et al. 2003). As presented in Chapter 5, the second IBIS/ISGRI catalogue improves on the first catalogue due to increased exposure and due to the searching of individual revolution mosaics, revealing transient sources which do not appear in the final mosaics. As such, the IBIS survey not only provides a unique opportunity to study the long term behaviour of persistent soft gamma-ray sources, but is also able to identify faint high-energy transient objects that would have otherwise remained undiscovered.

IGR J17285–2922 was first discovered from investigation of the IBIS/ISGRI survey mosaics (Walter et al. 2004c), but was not included in the first IBIS/ISGRI catalogue as the source's detection significance (based on mean survey source flux) was below the 6σ threshold set to minimise the chance of false detections (from a systematic logN/logS analysis, Bird et al. 2004). The transient nature of IGR J17285–2922 has been unveiled during the analysis of a nearby source and is found to have a maximum 20-40 keV detection of 11σ at $(\alpha,\delta)=(17^{\rm h}28^{\rm m}41^{\rm s}, -29^{\circ}22'56'') \pm 2'$. IGR J17285–2922 is ~4° from the Galactic Centre and within 1.5° of the bright X-ray source, 4U 1724–307, associated with the globular cluster Terzan 2. A search of existing source catalogues has yielded no known X-ray counterparts within the $2'$ error circle. Although it has been found that ~60% of IBIS/ISGRI survey sources have *ROSAT* counterparts (Stephen et al. 2005), no such association has been found for this source. A search at longer wavelengths is impractical at present due to the relatively large error circle (~$2'$) and crowded region of the sky. IGR J17285–2922 appears in the 2nd IBIS Catalogue as a 7.3σ source as detected in one revolution of data. This Chapter presents an analysis of the timing and spectral characteristics of IGR J17285–2922 and discusses its possible nature as an example of one of the many unclassified sources discovered by the ISGRI/IBIS survey.

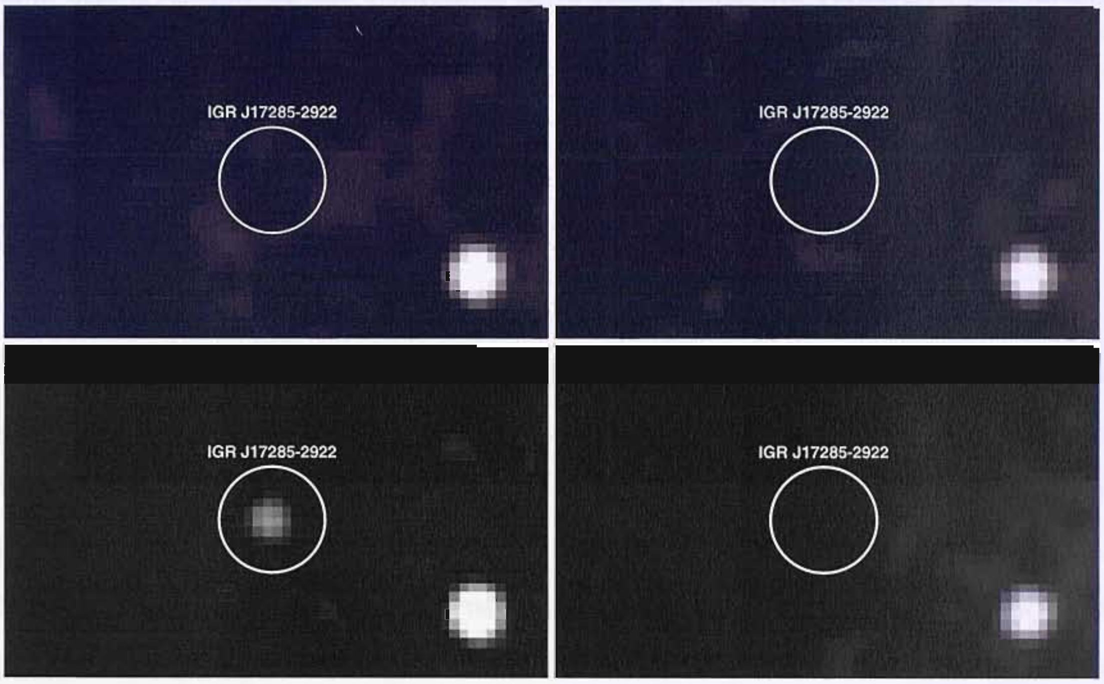

Figure 6.1: Significance mosaics (20–100 keV energy band) showing the region around IGR J17285–2922 (indicated by circle). Top left: Mar/Apr 2003 (A), top right: Aug 2003 (B), bottom left: Sep/Oct 2003 (C), bottom right: Feb–Apr 2004 (D). The bright source in the bottom right of the frame is the Terzan 2 X-ray source. For mosaic exposures see Table 6.1.

GCDE	Obs Date	Rev	IJD	$t_{\rm eff}$ (ksec)
A	27/02/03 - 04/05/03	46-67	1153.9 - 1219.6	471
B	08/08/03 - 20/08/03	100-1,103	1315.4 - 1327.3	96
C	25/09/03 - 19/10/03	116-123	1363.3 - 1387.1	191
D	12/02/04 - 24/04/04	163-186	1503.9 - 1575.6	550

Table 6.1: Overview of the Galactic Centre Deep Exposure (GCDE) observations, giving the date, revolution numbers, time in *INTEGRAL* Julian Date and on source effective exposure, $t_{\rm eff}$. IGR J17285–2922 was detected in revolutions 118-121 in Group C only. *INTEGRAL* Julian Date (IJD) = MJD - 51544.

6.2 Observations and Data Analysis

The IBIS survey utilises Core Programme data that consists of deep exposures of the Galactic Centre region and regular scans along the Galactic Plane. The Galactic Centre Deep Exposure (GCDE) is performed at ~6 month intervals (due to source visibility constraints) and consists of ~1 month of quasi-continuous observations. Table 6.1 summarises GCDE observations taken between February 2003 and April 2004. Each orbit (revolution) of GCDE data is divided into ~2000s long science windows (ScW). Data used in this Chapter has been processed using the Offline Standard Analysis, OSA v4.1 software (Goldwurm et al. 2003) available from ISDC (Courvoisier et al. 2003) which includes a correction for off-axis angle effects (see Chapter 4). ScW images can be combined together to form mosaics of the soft gamma-ray sky across time or energy bands, forming a final image of 0.06° pixels.

Separate mosaics have been made for each set of GCDE observations in energy bands of 20–40 and 20–100 keV. A zoom-in on the four mosaics (20–100 keV) centred on the location of IGR J17285-2922 is shown in Fig. 6.1, illustrating that the source is visible during observation C only with $F_{20-100keV}$=0.9 counts/sec ($\simeq$6.5 mCrab). As a consequence of this, mosaics were also produced for individual revolutions in

GCDE sets B and C in two energy bands (20–40 and 40–100 keV). Each revolution consists of approximately 100 ScW. The source is not statistically significant in individual ScW images for any of the sets of observations. Simultaneous images from the JEM-X instrument (Lund et al. 2003) were processed for revolutions 119 and 120 in the 3–20 keV energy range, but no detection was obtained. Comparing the extrapolated ISGRI power law spectrum to the JEM-X sensitivity curve, a weak detection in this energy range might be expected. However, the region around IGR J17285–2922 is heavily affected by systematic image artefacts, probably deriving from GX3+1, ∼5° away. Thus, the sensitivity attained is far poorer than the statistical limit. The 3σ upper limits for the source flux, obtained from the JEM-X observations, are consistent with this scenario and are plotted in Fig. 6.5. The angular resolution (∼degree) of the spectrometer, SPI (Vedrenne et al. 2003), is not sufficiently fine to obtain a clear detection of the source, due to close proximity of other bright sources and its location near to the Galactic centre.

Spectral and timing analysis has been performed solely on data from the GCDE C set of observations, more specifically revolutions 119 and 120 when the source was within the IBIS fully coded field of view.

6.2.1 ISGRI Timing Analysis

Figure 6.2 summarises the behaviour of IGR J17285–2922 throughout all of the GCDE observations. The source is not detected in GCDE observations A, B and D. GCDE C has been broken down into separate revolutions where the source was visible. The source undergoes an outburst that started around IJD 1365 (revolution 118), continuing for at least two weeks. Unfortunately, the source passes out of the IBIS field of view after revolution 121 and was not observed again by *INTEGRAL* until four months later, by which time the source had returned to an undetectable

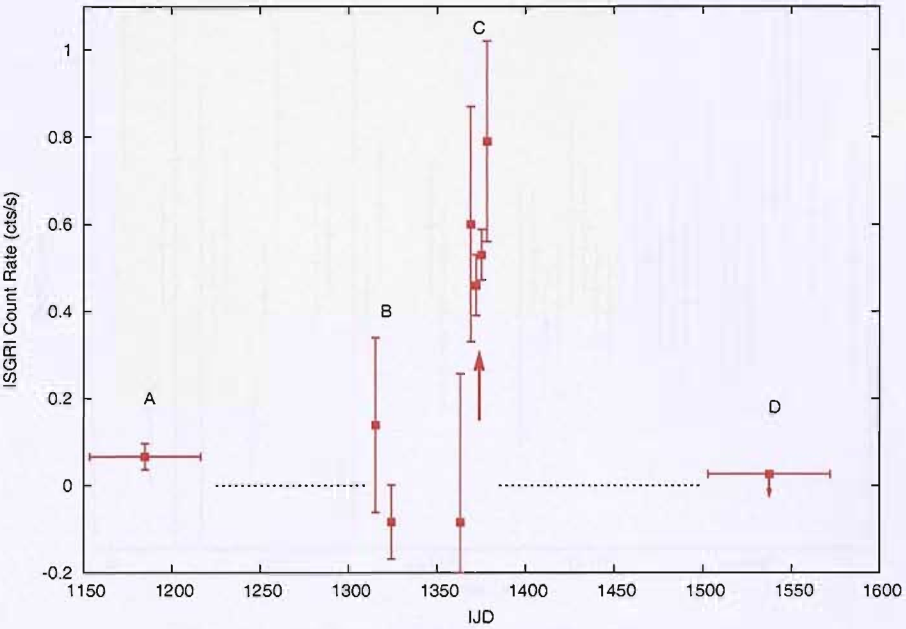

Figure 6.2: IBIS/ISGRI light curve for IGR J17285–2922 (20–40 keV energy band). Flux values are averaged over each revolution (~3 days) for observation sets B and C and averaged over the whole GCDE observation for A and D. The dashed lines represent periods when the source could not be observed by IBIS and the single arrow indicates the revolutions (119 and 120) used for timing and spectral analysis. IJD = *INTEGRAL* Julian Date = MJD - 51544.

quiescent state. The large error bars on some of the data points correspond to the source being on the edge of the partially coded field of view of the instrument.

For timing analysis, 193 ScWs from revolutions 119 and 120 were used, of total duration 347 ksec. In revolutions 118 and 121, the source was mainly on the edge of the IBIS field of view as a consequence of the dithering pattern of the telescope during the deep exposures and are not included in the analysis. Light-curve information was extracted for all bright sources in the field of view using OSA v4.1. The software enables ScW and sub-ScW fluxes to be obtained for the source using the Pixel Illumination Function (PIF). The PIF gives the relative illumination of each pixel by photons, from a given sky position, shining through the coded mask. Events were selected with PIF=1 (*i.e.* the whole pixel was open to the source position),

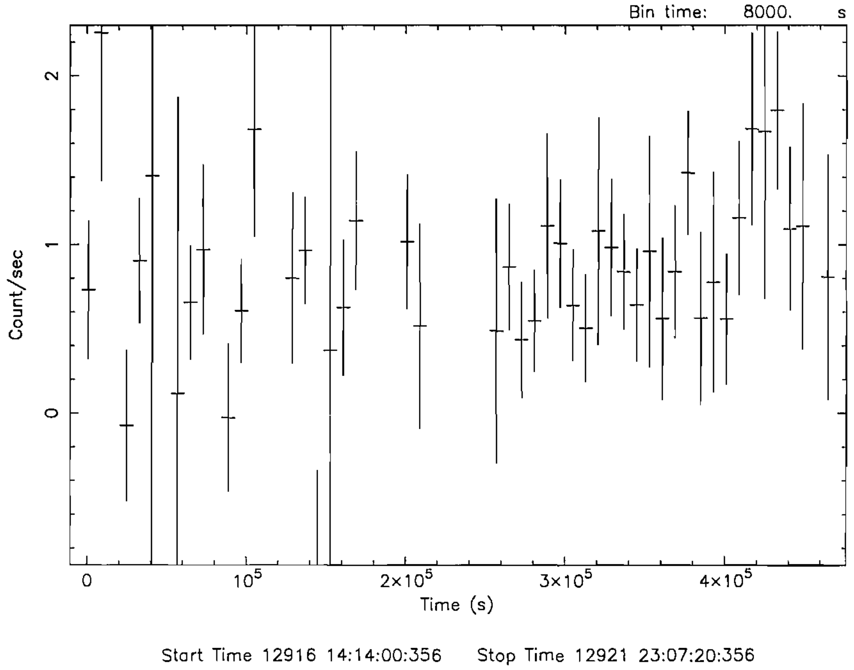

Figure 6.3: ISGRI light curve of IGR J17285–2922 for revolutions 119 and 120 binned over 8000s (20–40 keV). Time starts from the beginning of revolution 119, IJD=1372, where IJD = MJD - 51544.

thereby minimising systematic effects over the whole detector plane due to photons that could not have originated from the source. Fig. 6.3 shows the 20–40 keV light curve using 8000s bins for data when the source was within 10°off-axis to improve statistics. The source counts are seen to vary, but there are no significant bursts or flares present. The average ISGRI source flux in 20–40 keV is 0.53 counts s^{-1}. A Fast Fourier Transform was performed using the Lomb-Scargle method (Lomb 1976; Scargle 1982; Press & Rybicki 1989), searching the 20–40 keV data between frequencies of 1 and 4×10^{-6} Hz. In a Lomb-Scargle periodogram, a maximum in the power is produced at the frequency that gives the least squares fit of a sinusoidal wave to the data. Only observations where the source was within 10° off-axis were included to reduce systematic errors related to the position of the source in the partially coded FOV. No evidence of any periodicities is obtained but, being mindful of the low source counts, it is not possible to draw any conclusions from this result.

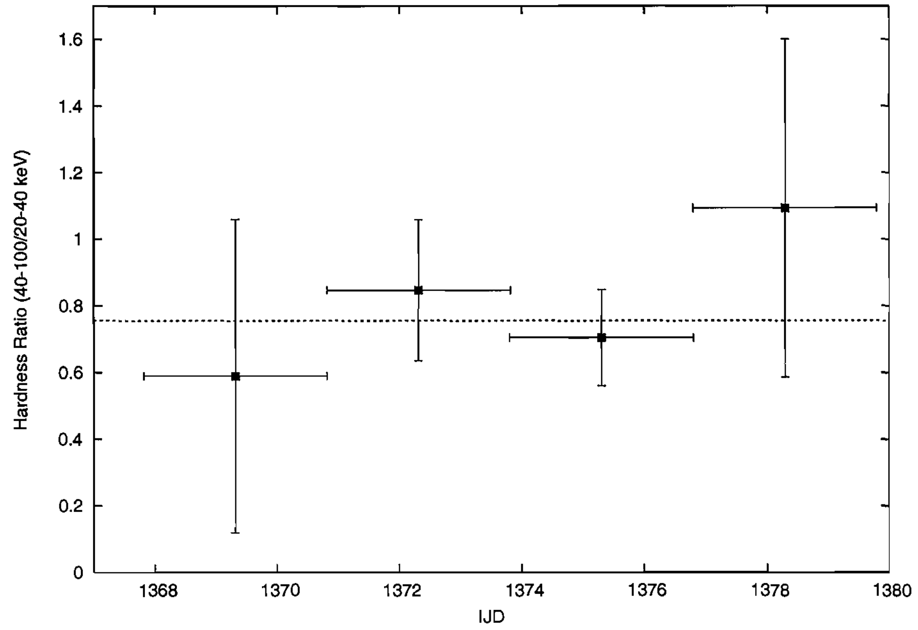

Figure 6.4: $\mathrm{Flux}_{40-100}/\mathrm{Flux}_{20-40}$ hardness ratio for revolutions 118 to 121 (bins ~3 days). Dotted line shows average hardness for GCDE C. IJD = *INTEGRAL* Julian Date = MJD - 51544.

6.2.2 ISGRI Spectral Analysis

In order to investigate if the source exhibits any spectral evolution, simple flux ratios (F_{40-100}/F_{20-40}) were calculated for the four revolutions at the start of the source activity (118–121) using fluxes extracted directly from revolution mosaics. Fig. 6.4 plots the source hardness compared to the average value from fluxes extracted from GCDE mosaic C. It is noted that the source did not show any significant change in hardness during observations.

Fluxes for spectral analysis were extracted from fine-energy band mosaics of revolutions 119 and 120 added together. Analysis was performed on 20–150 keV data in XSPEC v11.3.1 with a systematic error of 5%. A simple power law model with a photon index $\Gamma = 2.1 \pm 0.17$ gives the best fit (Fig. 6.5). The flux in the 20–150 keV energy band is 1.1×10^{-10} erg cm^{-2} s^{-1} corresponding to a luminosity estimate of

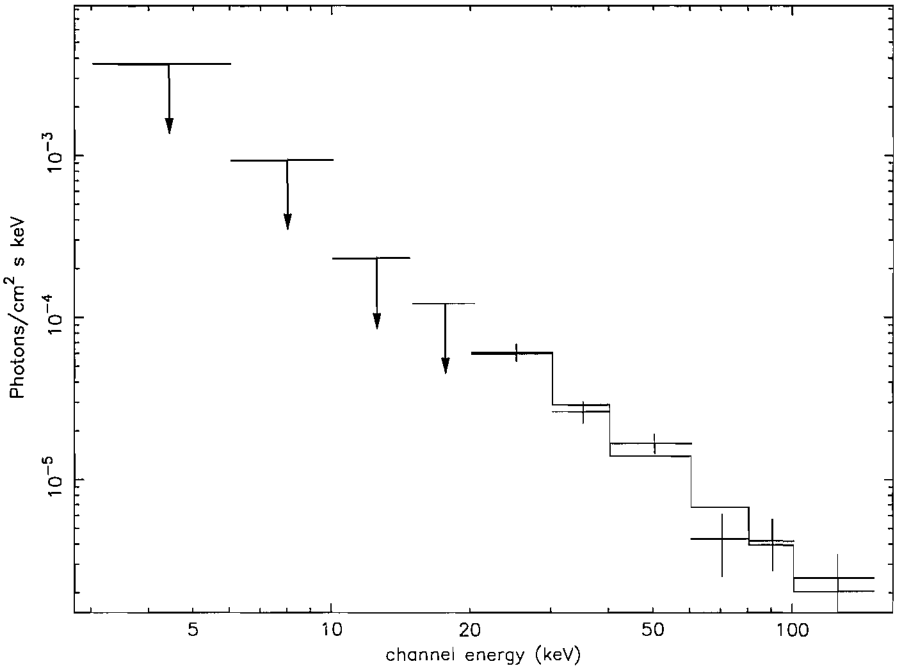

Figure 6.5: 20–150 keV IBIS/ISGRI spectrum of IGR J17285–2922 best fit with a power law Γ=2.1 and 3–20 keV JEM-X 3σ upper limits.

1×10^{36} erg s^{-1}, assuming the source is at Galactic Centre distance of 8.5 kpc, using Eqn. 6.1. Fits were also attempted with Comptonised (CompTT) and cut-off power law models (Titarchuk 1994), but statistics in the data were not good enough to constrain these models.

$$L_{20-150} = 4\pi D^2 F_{20-150} \tag{6.1}$$

6.3 Discussion

The spectral characteristics of the source and its location in the Galactic bulge are consistent with IGR J17285–2922 being a Galactic binary undergoing transient activity.

Type I X-ray bursts are observed uniquely in neutron star (NS) systems and explained as thermonuclear burning of material on the surface of the star. Burst profiles typically display short rise times ($\leq$10 s) and longer, exponential-type decays ($\geq$10 s–minutes) with spectra described by blackbody radiation with a temperature of 2–3 keV (see Lewin et al. (1993) for a review). IGR J17285–2922 has a persistent luminosity of L_{20-150} $\sim$$10^{36}$ erg s^{-1} and, if a NS system, we might expect it to display Eddington-limited bursts with a bolometric peak flux of $\sim$$10^{38}$ erg s^{-1} and exponential decay times of 100–1000 s (Bildsten 1995). The time between such bursts is related to the accretion rate and the energy released in the burst. Specifically, the expected burst rate can be calculated assuming a ratio of the total accretion energy released between bursts and burst fluence to be 100, Eqn. 6.2 (van Paradijs et al. 1988).

$$\frac{L \times \tau}{E_{burst}} = 100 \tag{6.2}$$

Assuming a typical burst fluence E_{burst} $\sim$$10^{39}$ erg gives an average time between bursts, τ=100 ksec for IGR J17285–2922 where $L = 10^{36}$ erg s^{-1}. Using Poisson statistics the probability of not observing a burst can be found (Eqn. 6.3), where $\mu = t/\tau$; t=observation time; τ=wait time.

$$P(x:\mu) = \frac{\mu^x}{x!}e^{-\mu} \tag{6.3}$$

ISGRI has on-source exposure totalling almost 350 ksec (=t), giving a $\sim$3% probability of no burst occuring during the observations, if such activity was taking place with τ=100 ksec. For JEM-X (sensitive over 3–20 keV), although more capable of detecting bursts, the probability of no bursts occuring during observations increases to 67% due to reduced source exposure (t $\sim$40 ksec) as a result of the small field of view. Therefore, it is rather likely all bursts would be missed with JEM-X. For a typical burst, we estimate that the peak luminosity should be at least 10^{37} erg s^{-1} in the 20–40 keV band. Based on ISGRI sensitivity curves, this will result in a significant ($\geq 9\sigma$) detection in the 20–40 keV band for a 100 s long burst, but a marginal ($\sim 3\sigma$) detection for shorter bursts of 10 s. Although bursts are not detected with ISGRI (Fig. 6.3) and JEM-X (see Sec. 6.2), this does not constrain the nature of the compact object. Retrospective analysis of 1.5–12 keV data between 1996-2005 from the All Sky Monitor on *RXTE* yields no significant detection of IGR J17285–2922 (Remillard 2005).

The 20–150 keV spectrum of the source is described by a power law with photon index $\Gamma = 2.1$, thus showing evidence for the hard tail exhibited by black holes (BH). For a BH in the low hard state (LHS), the spectrum is typically modelled by a power law with a high energy cut off, as a result of Comptonised emission from the inner disk (McClintock & Remillard 2004). A good fit could not be obtained for such a model. If this source is a BH in the LHS it may be that the spectral statistics are not good enough to constrain a value for the cut off, or the cut off is in excess of 100 keV. In the high soft state (HSS), emission is dominated by a thermal disk component below ~10 keV, no evidence of which is seen in JEM-X, see Sec. 6.2. The 3–20 keV upper-limits are consistent with the source either being a BH/LMXB in a LHS (McClintock & Remillard 2004), or a member of a new class of obscured objects characterised by a lack of soft X-ray emission (additionally implied by the absence of a ROSAT counterpart), interpreted as a Compton thick envelope enshrouding a HMXB (Walter et al. 2003).

The period of activity (at least 2 weeks) of IGR J17285–2922 detected by IBIS, could be the start of a stronger outburst comparable to the transient periods of X-ray Novae, lasting of order of weeks or months and recurrance times of several years, see Tanaka & Shibazaki (1996) for a full review. Historically, the vast majority of BHCs have been identified during X-ray Nova events including the *INTEGRAL* observed sources XTE 1720–318 and XTE 1550–564 (Cadolle Bel et al. 2004; Sturner & Shrader 2005). Both of these sources have been observed, at some stage, to be accreting at sub-Eddington luminosities during non-quiescent states. XTE 1720–318 was observed by *INTEGRAL* in outburst in Jan 2003 (lasting ~month) exhibiting a spectral state transition from HSS to LHS (Cadolle Bel et al. 2004). In the LHS, the 20–200 keV spectrum of XTE 1720–318 has been fit using a power law Γ=1.9, comparable with IGR J17285–2922 (Γ=2.1). Peak 20–200 keV luminosity was sub-Eddington and 7 times more luminous than the average 20–150 keV luminosity of IGR J17285–2922. Although Fig. 6.4 does not imply any spectral evolution during the observation of IGR J17285–2922, the source is showing a similar relative hardness as XTE 1720–318 at the start of its state transition.

6.4 Summary

At present, it is not possible to constrain the nature of IGR J17285–2922 from IBIS/ISGRI data alone. As with many newly discovered IGRs, IBIS data presents intriguing source activity without the statistics to fully classify the object. Although the luminosity is more consistent with NS systems, [Dean et al. (2005) finds that the 20–100 keV luminosity of NS systems in the first IBIS Catalogue ~10^{36} erg s^{-1} compared to ~10^{37} erg s^{-1} for BH systems] the lack of Type I X-ray bursts and the relative hardness of the spectrum suggests that the system may be harbouring a BH. From analysis of the average spectral characteristics of the IBIS survey sources, LMXBs containing BHs are observed to be harder than NS-LMXBs (power-law photon index Γ ~2 and >2 respectively, see Chapter 5). If the source outbursts again, a detection with *XMM-Newton* or *Chandra* would help improve the accuracy of the source location, crucial in the search for longer wavelength counterparts. A detection in quiescence would point to the system containing a NS, as BH systems in quiescence are extremely faint, $\sim 10^{31}$ erg s^{-1} (McClintock & Remillard 2004). Hopefully, the continuing survey campaign of *INTEGRAL* will enable more observations of this system to be made.

Chapter 7

Cataclysmic Variables and the *INTEGRAL*/IBIS Survey

7.1 Introduction

Cataclysmic Variables (CVs) are close binary systems (a_{binary} ~R_{sun}; P_{orb} ~hrs) consisting of a white dwarf (WD) and typically a main sequence (MS) donor star. The companion star is filling its Roche lobe and transferring mass to the WD. The classification of CVs is based largely on their long-term photometric behaviour. Some CVs are observed to undergo a optically bright nova eruption as the result of the build up of Hydrogen-rich material on the surface of the WD, which can be considered lower energy (*i.e.* longer wavelength) analogues to Type 1 X-ray bursts (see Chapter 1). CVs observed in nova eruption are termed classical novae and are designated 'fast' or 'slow' depending on the timescale of their return to quiescence (months–years). Classical novae that have been observed in nova outburst more than once are classed as recurrent nova. The behaviour of the different sub-types of CVs can be explained, in part, by the strength of the magnetic field of the WD. CVs with a WD magnetic field $<10^4$ G are considered non-magnetic and are controlled by disk accretion (see Fig. 7.1, top panel). Dwarf novae (DN) are non-magnetic systems that are observed to undergo a temporary increase in brightness due to a thermal-viscous instability in the accretion disk (Osaki 1974). As the name implies, DN outbursts are not as powerful as nova eruptions, with typical increases in brightness of 2–5 mag, and shorter recurrence times (days to weeks to years). Non-magnetic nova-like systems have high mass transfer rates and are affectively caught in permanent outburst (although low states are observed in some).

Magnetic WDs are further subdivided into polars and intermediate polars (IP). Polars (named thus due to strong polarisation of their optical flux) have magnetic fields sufficiently strong ($>10^6$G) to synchronise the spin of the WD with the orbital period of the binary ($P_{orb} \simeq P_{spin}$). The high magnetic field also prevents the formation of a disk and material is transfered directly to the WD via an accretion stream drawn along the magnetic field lines (see Fig. 7.1, bottom panel). However, there is a very small sample of polars ($\leq$5 objects) where the WD is out of synchronisation with the orbital period by a few percent, thus called asynchronous polars, and it has been suggested that matter is accreted via an extended curtain instead of a direct stream (Schwarz et al. 2005). In IPs, the magnetic field is generally not strong enough to disrupt disc formation entirely and simply truncates the inner disk resulting in an accretion flow that is channelled down towards the magnetic poles and onto the WD surface (see Fig. 7.1, middle panel). The magnetic field of IPs is also not strong enough to enforce synchronicity between the orbits, and typically $P_{spin} \sim 0.1P_{orb}$. IP nature is confirmed by the detection of coherent variability associated with the rotation of the WD and the binary period and aided by the X-ray detections of P_{spin}.

CVs are very well studied in the optical, but are not particularly well known as high-energy emitters. Nethertheless, it has long been observed with observatories such as *Einstein* and *EXOSAT* that CVs, especially the magnetic systems, can be strong X-ray emitters (for reviews see Cordova 1995; Kuulkers et al. 2003 and references therein). The first detections of hard X-ray emission from CVs occured in the late 1970's, most notably the *Astronomische Nederlandse Satelliet, (ANS)* detection of SS Cyg in the 1–7 keV energy band (Heise et al 1978) and the detection of the interesting IP, GK Per, by *Ariel V* (2–18 keV energy band; King et al. 1979). Furthermore, prior to *INTEGRAL*, there have been two recent missions that have detected CVs above 20 keV. Suleimanov et al. (2005) present the 3–100 keV spectra of 14 IPs obtained with RXTE and de Martino et al. (2003) describes the spectral and temporal properties of 4 IPs based on simultaneous soft and hard X-ray (0.1–90 keV) observations with BeppoSAX.

This chapter presents the detection of 16 CVs by IBIS in the 20–100 keV energy band. Of these objects, 8 are included in the recently published second IBIS catalogue (IBIS2, Bird et al. 2005), while a further 8 matches have been discovered by correlating an improved IBIS data set with an existing CV catalogue (Downes et al. 2001). As with past high-energy detections of CVs, it is found that the data set mainly consists of IPs with a handful of polars and at least one DN. Analysis of long term light-curves generally yields faint persistent soft gamma-ray fluxes, with two exceptions. Firstly, the bright DN SS Cyg is seen to decrease in 20-100 keV flux during optical outbursts. Secondly, evidence is obtained of an unusual short-timescale ($\sim$4hrs) outburst from an IP, V1223 Sgr, the first such detection from this type of object in the high-energy regime. These findings are discussed in Sec. 7.3.1.2 and 7.3.1.3. Light-curves folded on P_{orb} have not conclusively revealed modulated signals (apart from V834 Cen, Sec. 7.3.1.1) probably due to the limited signal-to-noise of the data set. The general spectral characteristics of all the IBIS CVs are presented and it is shown that the 20–100 keV spectra can be equally well fit with a power law or bremsstrahlung model. A comparison of the relative soft-gamma ray ‘colour’ is given with the aim to differentiate between the different classes of CVs. Finally, analysis of the location of these objects compared to the exposure bias of the IBIS survey campaign leads to the conclusion that IBIS is especially suitable for the detection of IPs. As a group, IPs constitute only about 2% of the total number of catalogued CVs, but from the results of recent searches, which have targeted X-ray emiting objects, it is likely that this number will grow (Gänsicke et al. 2005b). It can be expected that with more comprehensive sky coverage/exposure, the number of CVs (most likely more IPs) detected by IBIS will increase and that follow-ups of unclassified *INTEGRAL* sources may lead to the discovery of new IPs.

A description of our current understanding of the origin of hard X-ray/soft gamma-ray emission for certain types of CVs is given in the following sections. For a thorough review of CVs see Warner (1995). For an excellent overview of IPs see Patterson (1994).

7.1.1 High Energy Emission from Dwarf Novae

Hard X-ray/soft gamma-ray emission from DNe is generally thought to originate from the boundary layer between the accretion disk and the WD surface and is related to the mass accretion rate of the disk, $\dot{M}_{acc}$ (Pringle & Savonije 1979). At this boundary layer, accreted material releases approximately half of its accretion energy as it is decelerated onto the WD surface. Narayan & Popham (1993) find that at high accretion rates, the layer is optically thick with a temperature that decreases with decreasing $\dot{M}_{acc}$. Below a critical rate, $\dot{M}_{crit}$ ~10^{16} g s^{-1}, however, the boundary layer becomes optically thin and its width and temperature increases dramatically. Hence, during DN outbursts when there is an increase in $\dot{M}_{acc}$, the hard X-ray emission will likely be suppressed (Pringle & Savonije 1979). This has indeed been observed in the bright DN SS Cyg with *RXTE/PCA* in the 3–12 keV band (*e.g.* Wheatley, Mauche & Mattei 2003) and in the 20–100 keV *INTEGRAL* data presented in this chapter. During the periods where $\dot{M}_{acc} < \dot{M}_{crit}$, the expanded BL can also form a hot (T$\sim 10^8$K) extended corona, part of which may remain in the high accretion state, providing a source of high energy emission during outbursts (McGowan et al. 2004).

7.1.2 High Energy Emission from magnetic CVs

Magnetic CVs fall into two categories: Polars (or AM Her type) and Intermediate Polars (DQ Her type).

In the IP systems, material is accreted from the truncated disk and onto the WD poles via accretion columns, whereas for polars, the radius of the magnetosphere is large enough to prevent the formation of any accretion disk and the infalling material is 'threaded' onto the magnetic field lines creating one or two accretion regions depending on the inclination of the magnetic field with respect to the binary plane. In a simple model of a column of gas impacting the atmosphere of the WD, a shock will form and hard X-ray to soft gamma-ray emission will result from bremsstrahlung cooling by free electrons in the hot post-shock region with kT$\sim$10's of keV. Softer X-ray (and EUV, <1 keV) emission is produced from the absorption and reprocessing of these photons in the WD photosphere. Reflection of the bremsstrahlung photons also contributes to the hard X-ray spectrum (van Teeseling, Kaastra & Heise 1996). As a result, both polars and IPs should be expected to emit a hard spectrum. In fact, in polars, the ratio of soft to hard X-ray leads to an observed excess of soft X-rays (Lamb 1985). Chanmugam, Ray & Singh (1991) report that the typical X-ray (2–10 keV) luminosity for IPs is greater than that for polars by a factor of ~ 10. To account for this problem, it is proposed that the high magnetic field in polars induces a 'blobby' flow (magnetic pressure increases faster than the accretion material can

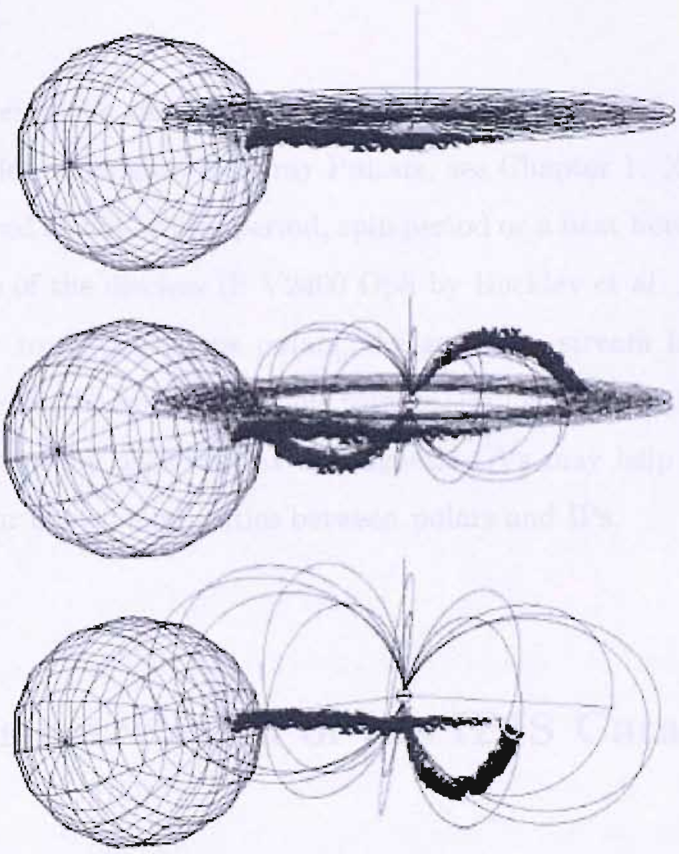

Figure 7.1: Diagrams of the accretion flow between the secondary star and the WD in three different sub-types of CVs. Top: non-magnetic system controlled by disk accretion; Middle: Intermediate Polar system with a partial disk, accretion onto WD is via magnetic poles; Bottom: Polar system where no disk forms and single accretion stream is channelled down magnetic field lines of the WD. (Courtesy of M. Cropper, MSSL.)

adjust, as it accelerates along the field lines; Warner 1995) which bypasses the shock and falls straight onto the WD surface (Kuijpers & Pringle 1982). Alternatively, for high magnetic fields and low $\dot{M}$, cyclotron cooling from fast electrons spiralling around the magnetic field lines could dominate the bremsstrahlung processes (Lamb & Masters 1979).

Pulsed X-ray emission can be observed from IPs as a result of radial accretion at the magnetic poles, analogous to X-ray Pulsars, see Chapter 1. X-ray modulations have been observed at the orbital period, spin period or a beat between the two (see, *e.g.* observations of the discless IP V2400 Oph by Buckley et al. 1995). In discless IP's, in contrast to asynchronous polars, the accretion stream is expected to flip between the poles as the magnetic dipole rotates (Hellier 1991; Hellier & Beardmore 2002). Soft gamma-ray observations of magnetic CVs may help in understanding the differences, or indeed similarities between polars and IPs.

7.2 Cross-correlation of the IBIS Catalogue

The IBIS survey data set consists of dedicated observations along the Galactic plane and around the Galactic centre. A combination of pointed and deep exposure observations taken in different parts of the sky can be added to this data set once available to the public (one year after observation date), eventually resulting in an all-sky survey. The first IBIS catalogue (IBIS1; Bird et al. 2004) consists of ~2500 separate observations (or science windows, ScW), while the second catalogue (IBIS2; Bird et al. 2005) uses ~6000. As the exposure of the data set increases, so does the number of sources detected (122 in IBIS1, 209 in IBIS2). One method of identifying newly detected IBIS sources is to perform a correlation exercise with previously published source catalogues (*e.g.* *ROSAT*, see Chapter 5). This section will describe the source correlation performed between a preliminary third IBIS catalogue data set (IBIS3pre) and a catalogue of CVs (Downes et al. 2005).

7.2.1 The Catalogues

The second IBIS catalogue (IBIS2) was accepted for publication in August 2005 and contains 209 source of which 8 were identified as CVs (see Chapter 5, Table 5.4 for the full source list). This catalogue includes all available data between revolutions 46 and 209 ($\sim$6000 ScW) and provides a significant improvement on the first IBIS Catalogue in both increased exposure, sky coverage and analysis techniques. A preliminary third catalogue (IBIS3pre) has been prepared based on additional 5000 ScW of observations, almost doubling the exposure to $\sim$20 Msec and further increasing the sky coverage. A provisional source list has been extracted from the 20–100 keV map using standard SExtractor technique (see Chapter 5, Sec. 5.2.2) and consists of 2031 excesses with a minumum significance 4.5σ. These excesses are unchecked and may include false detections associated with image artefacts and /or noise.

The Catalog and Atlas of Catalysmic Variables was originally published by Downes & Shara (1993). It has since been superceded by an electronically available edition which is regularly updated (Downes et al. 2005). As of September 2005, the catalogue contains 1740 sources, listed with their location, limited spectral informaton and subtype (including those of an unconfirmed nature and non-CVs). Less than 10% of the total number of CVs catalogued are classed as magnetic systems (included in Downes as either DQ Her or AM Her type variability), of which less than 2% are IPs.

7.2.2 Correlation Method

A correlation was performed between the IBIS3pre list of excesses and the entire Downes catalogue. A search radius was defined by the radius of the error circle around the IBIS coordinates. If a Downes source is found within this search radius it is flagged as a possible match. The correlation was performed for search radii between 0.1′ and 30′. The number of matches is the number of IBIS sources for which there is a Downes association within the specified radius. A further correlation was performed between the Downes catalogue and a fake IBIS catalogue created by adding 1° from the original IBIS3pre coordinates. See Stephen et al. (2005; 2006) for a similar approach in correlating *ROSAT* sources to IBIS survey sources.

7.2.3 Correlation Results

Figure 7.2 displays the results of the cross-correlations. For a search radius of 5°, 27 matches were obtained between Downes and the real IBIS3pre catlogue, with an expectation of 9±3 false matches from the fake IBIS3pre catalogue. A search radius of 3′ is a reasonable estimate of the IBIS source location accuracy in the 20–40 keV energy band and 20 matches are obtained with only 3±1 false matches expected. However, the matches obtained for the 5′ correlation are used for further analysis (*i.e.* the IBIS error circle has been exaggerated) due to the preliminary nature of the source list; excesses have not been checked. Additionally, excesses in 20–100 keV band may have larger positional errors compared to the main detection bands.

The 27 matches obtained using a search radius of 5′ are listed in Table 7.1. Each match has been inspected in the 20-40keV and 20-100 keV IBIS maps to check for spurious associations. Five matches were rejected as noise structure from the shape and location of the excesses (matches 23-27) and one flagged as possible noise

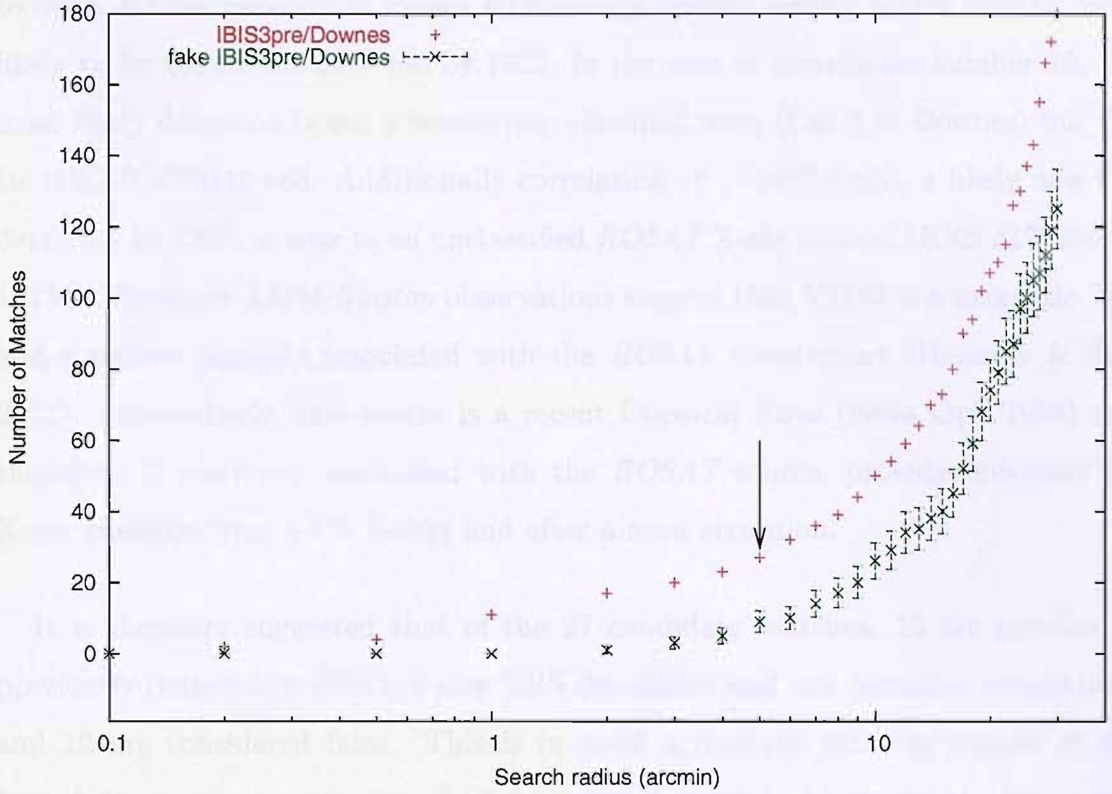

Figure 7.2: The number of matches as a function of search radius between the Downes catalogue and the IBIS3pre source list and a fake IBIS source list. The arrow marks search radius=5′ with 27 matches.

structure (match 20). Of the 22 remaining detections, 8 were previously identified CVs presented in IBIS2 (matches 7–13) and 6 were also in IBIS2 but classified as other source types, mainly X-ray binaries (matches 1–6). In four cases the IBIS2 objects are classified as LMXB in Globular Clusters, and the Downes association has only a tentative CV classification. It is important to note that working at the IBIS/ISGRI angular resolution, it is very difficult to associate a detection with an optical counterpart, especially in a crowded area of the sky such as a Globular Cluster. Therefore, it was decided to uphold the initial IBIS2 classifications for these sources.

For each of the 8 remaining new detections, a SIMBAD search was performed to check for the presence of known high energy sources nearby, which may be more likely to be the object detected by IBIS. In the case of correlation number 10, the most likely detection is not a tentatively classified nova (Cas 3 in Downes) but the Be-HMXB 4U0115+63. Additionally correlation 18 (V2487 Oph), a likely new CV detection by IBIS, is near to an unclassified *ROSAT* X-ray source, 1RXS J173200.0-191349. Previous *XMM-Newton* observations suggest that V2487 is a magnetic WD and therefore possibly associated with the *ROSAT* counterpart (Hernanz & Sala 2002). Interestingly, this source is a recent Classical Nova (Nova Oph 1998) and therefore, if positively associated with the *ROSAT* source, provides evidence for X-ray emission from a CV before and after a nova erruption.

It is therefore suggested that of the 27 candidate matches, 15 are genuine (8 previously detected in IBIS2, 6 new IBIS detections and one tentative association) and 12 are considered false. This is in good agreement with the results of the fake data, which suggests that 9±3 false matches are to be expected. Inspection of the sources correlated with an offset angle of $6'$ has led to the identification of an additional two sources in the IBIS maps: BY Cam and GK Per. These sources are on the edge of the maps and as such appear distorted, a possible reason why the IBIS3pre coordinates are not within $5'$ of the published location. They are of low significance in the 20–100 keV band ($< 5\sigma$) as a result of the low exposure in these areas of sky but are well known magnetic CV systems and have therefore been included in the subsequent spectral and timing analysis.

	l[1]	b	Offset[2]	Sig[3]	Downes Name	Downes Type	IBIS Cat 2 Name	IBIS Cat2 Type	comments
1	2.78	-7.91	0.288	192	Sgr	CV?	4U1820-303	Glob. Cluster LMXB	IBIS cat2 source
2	1.52	-11.36	0.598	85	V3616Sgr	CV?	RX1832-330	Glob. Cluster LMXB	IBIS cat2 source
3	311.31	-3.81	0.762	67	CG X-1	Polar?, ULX?	Cir Galaxy	AGN Sey 2	IBIS cat2 source
4	31.35	-8.46	1.3	35	V1336 Aql	mira variable?	4U1916-053	LMXB	IBIS cat2 source
5	4.96	-14.35	0.383	33	V1223 Sgr	IP	V1223 Sgr	CV, IP	IBIS cat2 CV
6	25.35	-4.32	0.2	26	Sct	CV?	4U1850-087	Glob. Cluster LMXB	IBIS cat2 source
7	332.43	7.02	0.184	26	Lup	IP	IGR J15479–4529	CV, IP	IBIS cat2 CV
8	359.85	8.72	1.137	25	V2400 Oph	IP	V2400 Oph	CV, IP	IBIS cat2 CV
9	120.03	-3.44	0.476	20	V709 Cas	IP	V709 Cas	CV, IP	IBIS cat2 CV
10	125.90	1.03	3.184	15	Cas3	Nova?	-	-	New IBIS source[4]
11	17.92	15.01	0.129	12	Oph	IP	IGR J17303–6016	CV, IP	IBIS cat2 CV
12	90.56	-7.12	0.79	11	SS Cyg	DN	1H2140+433	CV, DN	IBIS cat2 CV
13	94.45	-0.48	0.522	11	Cyg	CV	IGR J21335+5105	CV, IP	IBIS cat2 CV
14	4.50	-9.14	2.503	9	V1017 Sgr	Nova Slow, DN?	-	-	New IBIS CV
15	5.69	-7.57	1.099	8	V1988 Sgr	?	-	-	New IBIS CV
16	28.97	-15.52	1.543	7.5	V1432 Aql	Polar	RX J1940.1–1025	CV, P	IBIS cat2 CV
17	353.40	-5.37	4.653	7.5	V697 Sco	Nova Fast, IP?	-	-	New IBIS CV
18	6.61	7.80	1.744	6.85	V2487 Oph	Nova Fast	-	-	New IBIS CV
19	87.15	-5.70	2.411	5.8	V2069 Cyg	IP?	-	-	New IBIS CV
20	358.72	-3.45	3.046	5.7	V960 Sco	Nova	-	-	New IBIS CV/Structure?
21	7.70	3.78	1.527	5	Sgr	CV?,LMXB?	4U1745–203	Glob. Cluster LMXB	IBIS cat2 source
22	317.01	15.51	4.321	5	V834 Cen	Polar	-	-	New IBIS CV
23	184.00	14.77	3.887	-	DN Gem	Nova Fast	-	-	structure
24	71.40	4.00	2.481	-	V1819 Cyg	Nova Slow	-	-	structure
25	359.33	-3.08	0.831	-	Sco	DN	-	-	structure
26	0.84	-7.20	4.762	-	V2839 Sgr	DN	-	-	structure
27	4.88	-3.02	4.735	-	Sgr	DN	-	-	structure

Table 7.1: Results of the Downes–IBIS3pre correlation.

---

[1] l,b coordinates from IBIS3pre. [2] Offset is the distance between Downes catalogue coordinates and the IBIS3pre coordinates. [3] Significance is from 20–40 keV IBIS3pre maps. [4] Cas3 is listed in Downes as an 'uncertain' detection, source is more likely to be 4U0115+63, 1.3′ from IBIS3pre coordinates.

7.2.4 Summary

The Downes catalogue of CVs has been used to identify 6 certain new associations and 1 additional tentative association between IBIS survey sources and CVs. Together with the 8 CVs previously identified in the second catalogue and 2 additional low significance sources (BY Cam and GK Per), this increases the number of CVs seen by IBIS to 16 plus one tentative identification (V960 Sco).

7.3 Properties of *INTEGRAL* CVs

Table 7.2 presents the characteristics of the 17 CVs detected by *INTEGRAL* as a result of the cross-correlation with the Downes catalogue. Fluxes and associated errors are in IBIS/ISGRI counts/s as detected in the all-sky 20–40 keV flux and variance IBIS3pre mosaics and are therefore an time-averaged value over ~600 days. Values for P_{orb}, P_{spin} have been obtained from literature and are referenced accordingly. A selection of sources also have distance estimates.

The majority of the CVs detected by *INTEGRAL* are intermediate polars (IPs) with 3 polars and at least one Dwarf Nova (DN). Interestingly, 2 of the 3 polars are classed as asynchronous which represents half of the confirmed cases of this rare class of object. Three CVs have unconfirmed classifications (V1017 Sgr, V697 Sco and V2069 Cyg) and an additional three are as yet unclassified. All new identifications have been previously detected in the X-ray regime apart from V960 Sco and V1988 Sgr. Subsequently, analysis has indicated that the correlation with V960 Sco is probably not real and that the *INTEGRAL* detection is in fact image structure. 20–100 keV IBIS3pre data has been analysed to provide an overview of the spectral and timing properties of these CVs.

Name	Type[1]	F_{20-40} (IBIS/ISGRI counts/s)	P_{orb} (min)	P_{spin} (s)	d (pc)	Alt. Name/Notes
V709 Cas	IP	0.42 ±0.02	320.4[4]	312.77[13]	-	RX J0028.8+5917
IGR J15479-4529	IP	0.52 ±0.02	562[5]	693[5]	-	1RXS J15481.5–452845
V2400 Oph	IP	0.36 ±0.01	205.2[6]	927[6]	-	RX J1712.6-2414; discless IP[6]
IGR J17303-0601	IP	0.39 ±0.03	925.27[7]	128[7]	-	1RXS J173021.5–055933
V1223 Sgr	IP	0.84 ±0.02	201.951[8]	745.63[8]	600[15]	
RX J1940.1–1025	P	0.31 ±0.04	201.938[9]	12150.4[14]	230[9]	V1432 Aql; asynchronous; eclipsing
IGR J21335+5105	IP	0.34 ±0.03	431.58[10]	570.823[10]	-	RX J2133.7+5107
SS Cyg	DN	0.33 ±0.02	396.187[11]	-	166[16]	1H 2140+433 in Cat2
V1017 Sgr	DN?[2]	0.13 ±0.01	8228.16[8]	-	-	RN[2] nova outbursts in 1901, 1919, 1973; P_{orb} ~6 d
V1988 Sgr	?	0.11 ±0.01	-	-	-	Symbiotic?
V697 Sco	IP?[3]	0.09 ±0.01	270[3]	12600[3]	-	Nova Scorpii 1941; diskless IP?[3]
V2487 Oph	?	0.09 ±0.01	-	-	-	0.125′ from 1RXS J173200-191349[20]
V960 Sco	?	0.06 ±0.01	-	-	-	nova outburst in 1985; structure?
V834 Cen	P	0.13 ±0.02	101.4[8]	-	86[17]	
V2069 Cyg	IP?	0.12 ±0.02	448.8[12]	-	-	RX J2123.7+4217
GK Per	IP	0.22 ±0.05	2875.2[8]	351.34[8]	340[18]	nova outburst in 1901; DN outbursts; P_{orb} ~2 d
BY Cam	P	0.34 ±0.06	201.298[8]	11846.4[8]	190[19]	asynchronous

Table 7.2: Table of characteristics of the CVs seen by IBIS.

---

[1] Types without reference are from Downes et al. 2001.[2]Sekiguchi et al. 1992; [3]Warner & Woudt 2002; [4]Bonnet-Bidaud et al. 2001; [5]Haberl et al.2002; [6]Buckley et al. 1995; [7]Gänsicke et al. 2005b; [8]Ritter & Kolb 1998; [9]Watson et al.1995; [10]Bonnet-Bidaud et al. 2005; [11]Friend et al. 1990; [12]Thorstensen & Taylor 2001; [13]de Martino et al. 2001; [14]Geckeler & Staubert 1997; [15]Bonnet-Bidaud et al. 1982; [16]Harrison et al. 1999; [17]Cropper 1990; [18]Zuckerman et al.1992; [19]Warner 1995; [20]Hernanz & Sala 2002

7.3.1 Timing Analysis

Figures 7.3 and 7.4 show the long-term survey light-curves of the CVs detected by IBIS. Each data point corresponds to one ScW (~2000 s) in the 20–30 keV energy band. Data points were excluded when the source is >7° off-axis to improve the statistical quality of the data when searching for variations, except for BY Cam (<10° off-axis) as the source has only been detected on the edge of the field of view. The sources with more coverage are located around the Galactic centre and close to the Galactic plane where the exposure is greatest. Most of the light-curves show very little variability and reveal no long-term modulations when compared to a flat line or when folded on the known P_{orb} of the system. 20–30 keV lightcurves were searched for periodicities using the Lomb-Scargle periodogram procedure (Press & Rybicki 1989), but no significant periods were found. This result may be influenced by the bin size of the data points (~30 min) being similar to the P_{orb} of the CVs (smaller binning can only be achieved at present for short periods of data and would be very noisy) and the low signal-to-noise ratio of data. However, in 3 cases significant variability was observed which are discussed in the following sections.

7.3.1.1 V834 Cen

V834 Cen is a polar system that has been well studied in the X-ray regime, where it exhibits variable absorption with orbital phase and epoch, interpreted as photo-electric absorption in the pre-shock accretion column (Sambruna et al. 1994; Ishida & Fujimoto 1999). The 20–30 keV IBIS light-curve folded over P_{orb}=101.4 min (Fig. 7.5, arbitrary phase) shows evidence for a phase-related flux modulation, which has been indicated in 7.2–10 keV ASCA observations (Ishida & Fujimoto 1999). The power of the frequency associated with P_{orb} is not significant as analysed by a Lomb-Scargle periodogram. The 2–10 keV best fit bremsstrahlung temperature

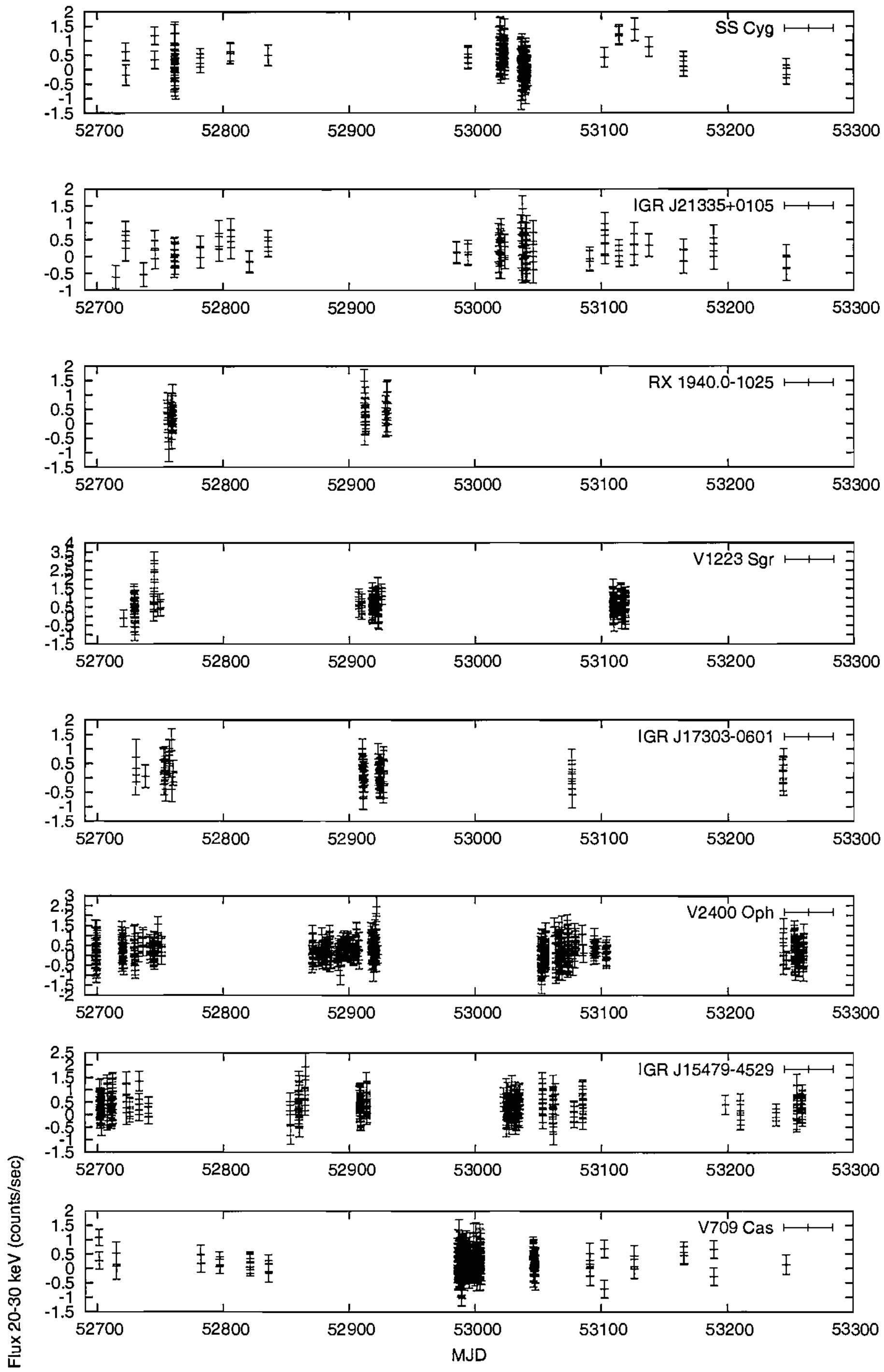

Figure 7.3: Light-curves of CVs presented in the second IBIS/ISGRI catalogue.

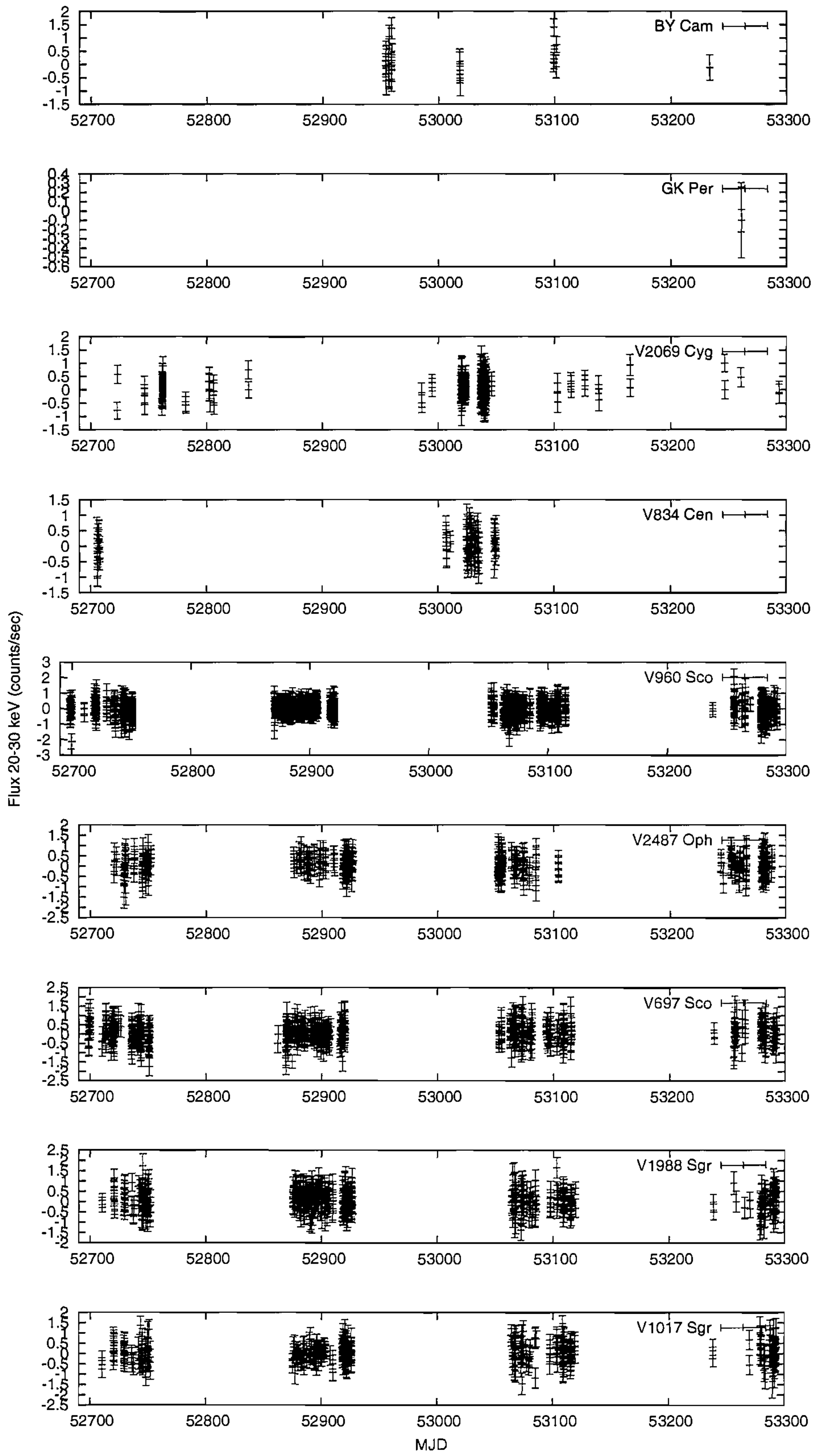

Figure 7.4: Light-curves of CVs detected using the Downes correlation for sources $< 7°$ off-axis, except for BY Cam ($10°$).

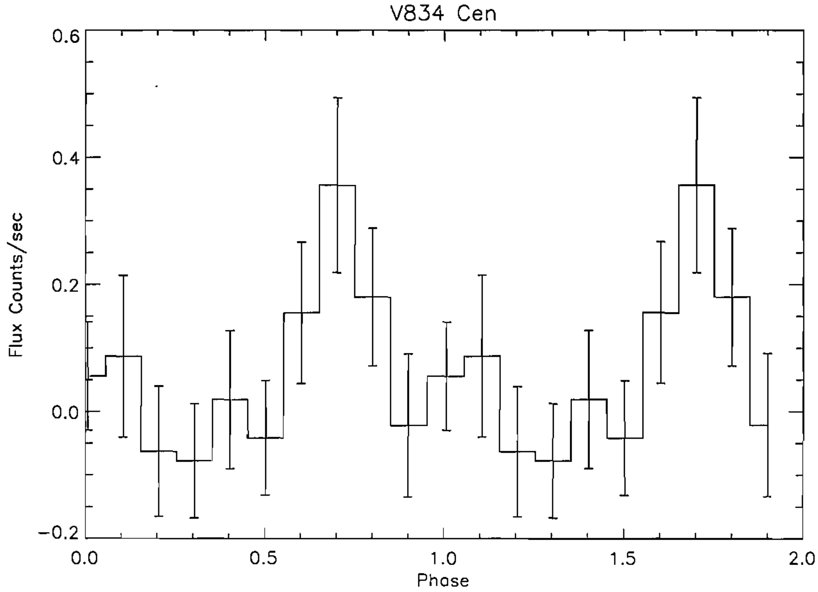

Figure 7.5: 20–30 keV light-curve of V834 Cen folded over P_{orb}=101.4 min (arbitrary phase).

kT=11.8±1.0 keV (Imamura et al. 2000) is consistent with IBIS 20–100 keV fit of 19.53±7.79 keV (see Table 7.3). Further analysis of the 20–100 keV IBIS data may aid understanding of the high energy emission regions of this system and other polars.

7.3.1.2 V1223 Sgr

The IP system V1223 Sgr is the brightest CV observed by IBIS, with a significance of 30σ in the 20–40 keV survey mosaic. This system has also been detected by RXTE during the period 1996–2000, and the broadband spectrum (*RXTE*/HEXTE+ *INTEGRAL*/IBIS, 3–100 keV, Fig. 7.6) provides an estimate of the post-shock temperature of kT=29±2 keV when fit by a bremsstrahlung model with reflection from an optically thick cold medium plus neutral absorption (n_H=3.3×10^{22} cm^{-2}) and iron line at ~6.5 keV (Revnivstev et al. 2004b). Further to this, additional system parameters including M_{WD}, $\dot{M}_{acc}$ and inclination i=22° ± 5° have been calculated (Revnivstev et al. 2004b).

Interestingly, inspection of the 20–30 keV IBIS survey lightcurve yields an episode of intense brightening of the source lasting for ~3.5 hrs during revolution 61, MJD 52743 (see Fig. 7.3). The source is clearly visible in a single ScW with a significance of up to 6.5σ and peak flux approximately three times that of the average (see Fig. 7.7). A sub-ScW light-curve has been produced for the 7 ScW in which the burst occured, shown in Fig. 7.8. It is noted that the burst timescale is almost identical to the orbit of the binary (P_{orb}=3.36 hr). A burst spectrum has been extracted from ScW 98 and 99 in revolution 61 and is compared to the average survey spectrum in Fig. 7.9. The best fit bremsstrahlung temperature of the burst in the 20–100 keV energy band is better constrained and only marginally cooler compared to the average survey spectrum (13.78±2.50 keV and 18.77±1.20 keV, respectively, as shown in Table 7.3). Noticably, this is significantly cooler than the temperature estimated by Revnivtsev et al. (2004b), kT=29 keV, derived from 3 100 keV spectrum. A finer binned 20–40keV IBIS/ISGRI burst spectrum can also be fit with a thermal bremsstrahlung model with kT=5.33±0.64 keV (χ^2_ν=1.8). The 20–100 keV luminosity (using a distance estimate of 600pc; Bonnet-Bidaud et al. 1982) has been calculated and is seen to increase from ~ 10^{33} erg s^{-1} as measured from the average 2 year flux, to ~ 10^{34} erg s^{-1} over the 3.5 hr burst period (see Table 7.5).

Such behaviour is previously unreported in the high-energy regime for magnetic CVs. However, an unusual short-term burst has also been detected from this system in the optical by van Amerongen & van Paradjis (1989). The single optical outburst lasted between 6 and 24 hr and resulted in an increase in flux by a factor of 3. They suggest that the outburst could be comparable to a DN outburst but is made shorter by the absence of the inner part of the accretion disk as seen in moderately magnetic

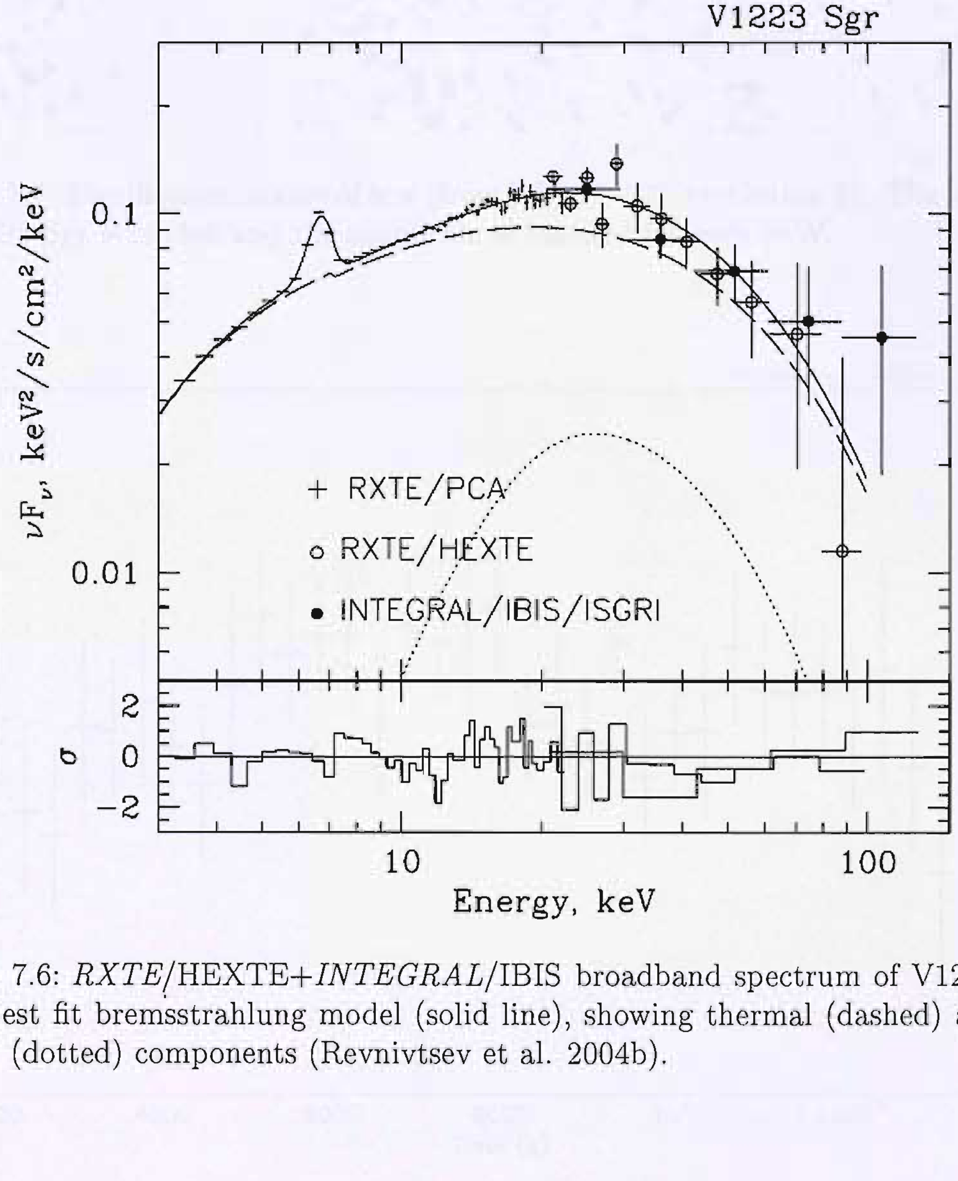

Figure 7.6: *RXTE*/HEXTE+*INTEGRAL*/IBIS broadband spectrum of V1223 Sgr with best fit bremsstrahlung model (solid line), showing thermal (dashed) and reflected (dotted) components (Revnivtsev et al. 2004b).

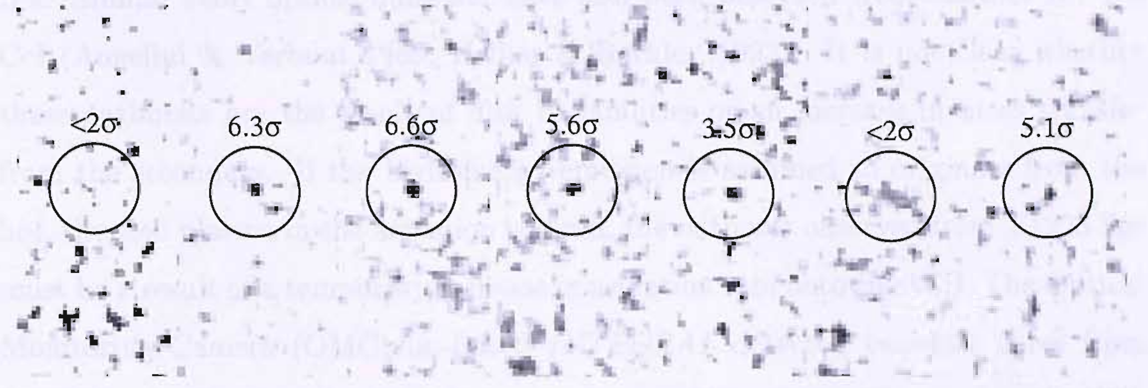

Figure 7.7: Significance images of scw (from left) 97–103, revolution 61. The location of V1223 Sgr is circled and the significances labelled for each ScW.

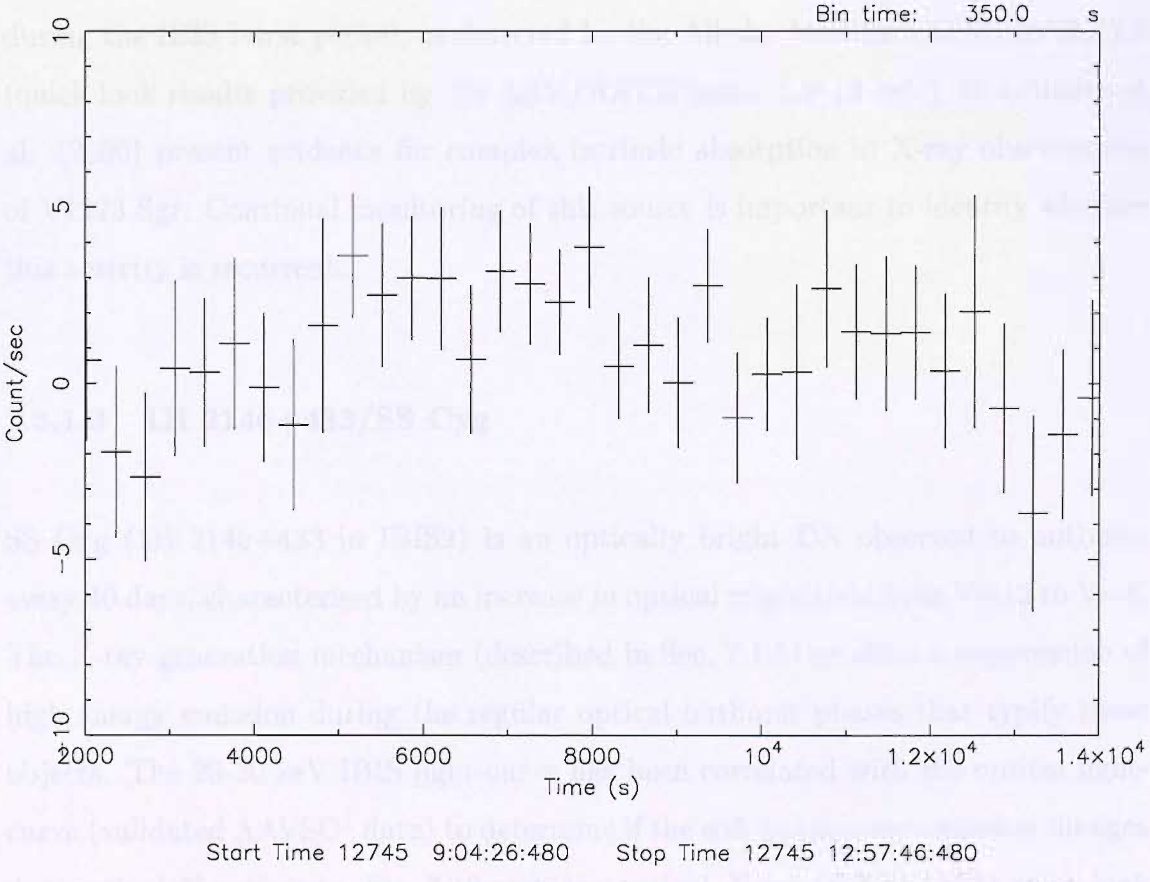

Figure 7.8: Sub-ScW light-curve of V1223 Sgr for revolution 61, ScW 97–103 binned over 350 s.

IPs. Similar short optical oubursts have also been observed from another IP, TV Col (Angelini & Verbunt 1989; Hellier & Buckley 1993). It is not clear whether these outbursts are the result of disk instabilities or an increase in mass transfer from the secondary. If the high energy emission is assumed to originate from the hot, shocked plasma in the accretion column, the outburst observed from V1223 Sgr must be a result of a temporary increase in accretion rate onto the WD. The Optical Monitoring Camera (OMC) on-board *INTEGRAL* detected two fast flares from V1223 Sgr (~15 min and ~2.5 hr) one year later (MJD=53110; 53116) than the IBIS burst (Šimon et al. 2005). Contemporaneous IBIS observations yield no increase in flux at ScW level at these times. No OMC detected flares are reported during the epoch of the IBIS burst and no significant increase in X-ray emission is seen during the IBIS burst period, as detected by the All-sky Monitor (ASM) on *RXTE* (quick-look results provided by the ASM/*RXTE* team, 1.5–12 keV). Beardmore et al. (2000) present evidence for complex intrinsic absorption in X-ray observations of V1223 Sgr. Continual monitoring of this source is important to identify whether this activity is recurrent.

7.3.1.3 1H 2140+433/SS Cyg

SS Cyg (1H 2140+433 in IBIS2) is an optically bright DN observed to outburst every 40 days, characterised by an increase in optical magnitude from V~12 to V~8. The X-ray generation mechanism (described in Sec. 7.1.1) predicts a suppression of high energy emission during the regular optical outburst phases that typify these objects. The 20-30 keV IBIS light-curve has been correlated with the optical light-curve (validated AAVSO[1] data) to determine if the soft gamma-ray emission changes during the DN outbursts. Fig. 7.10 plots the optical, X-ray (*RXTE*/ASM quick-look results) and soft gamma-ray fluxes over the IBIS survey period and provides evidence

---

[1] `http://www.aavso.org/`

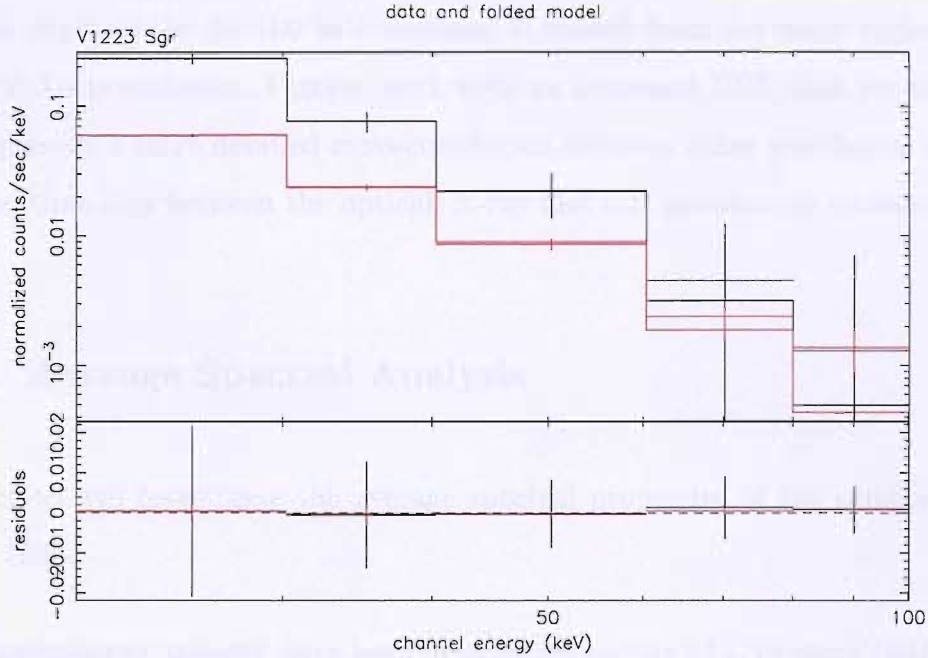

Figure 7.9: Comparing the outburst (black) and average survey (red) spectra of V1223 Sgr, fit with bremsstrahlung models. Values of best fit bremsstrahlung temperatures are listed in Table 7.3.

of strengthening of the 20–30 keV emission during optical quiesence. This confirms the finding of McGowan et al. (2004) from correlated X-ray (3–12 keV) and optical emission.

20–100 keV spectra have been extracted during outburst and quiescence (ranges of data marked 'O' and 'Qu' in Fig. 7.10) to quantify any spectral variation and are shown in Fig. 7.11 with the best fit bremsstrahlung model. The source is very faint during optical outburst and the data cannot be well fit either with this model or a simple power law (see Table 7.3 for best fit values of kT and Γ). The best fit values during optical quiescence are consistent with the average 2 year survey spectrum, only better constrained. The 20–100 keV flux is of an order of magnitude greater during quiescence than outburst, the $L_{20-100keV}$ increasing from 10^{31} erg s^{-1} to 2×10^{32} erg s^{-1}. Apart from confirming previous findings, it is interesting to see that the suppression of hard X-rays extends up to 100 keV for this system, suggesting that the origin of the 20–100 keV emission is indeed from the same region as the 2–10 keV X-ray emission. Further work with an increased IBIS data set should be able to provide a more detailed cross-correlation between other wavebands and help track the time-lags between the optical, X-ray and soft gamma-ray emission.

7.3.2 Average Spectral Analysis

This section will investigate the average spectral properties of the sample of CVs seen by IBIS.

Soft gamma-ray 'colours' have been determined for the 17 CVs using IBIS/ISGRI source counts in three energy bands (20–30, 30–40 and 40–100 keV) and have been plotted by sub-type in Fig. 7.12. While the IP colours are better defined, the polars appear softer in 'colour1' (30–40/20–30). Large error bars prevent any determination of whether polars may be harder in 'colour2' (40–100/30–40). The 20–100 keV spectra have been extracted and fit with both a simple power law model and a bremsstrahlung model. The best fits and associated fluxes for the objects are listed in Table 7.3. Also included in the Table are the fits for the burst of V1223 Sgr and for SS Cyg during optical quiescence and outburst. Both models were seen to fit equally well. Introducing an absorption parameter did not improve the fits. The relative values of the best fit parameters are illustrated in Fig. 7.13. From the results of the spectral fitting, it was concluded that V960 Sco was unlikely to be a true source detection and, as such, this oject has not been included further in the analysis. The IP fits are better defined due to their relative brightness compared to the polars. Nethertheless, a distinction cannot be made between the hardness of the polars and IPs. Futhermore, the weighted means of the best fits for photon index and bremsstrahlung temperature (Table 7.4) are consistent between polars and IPs, with the DN SS Cyg being marginally softer during optical quiescence.

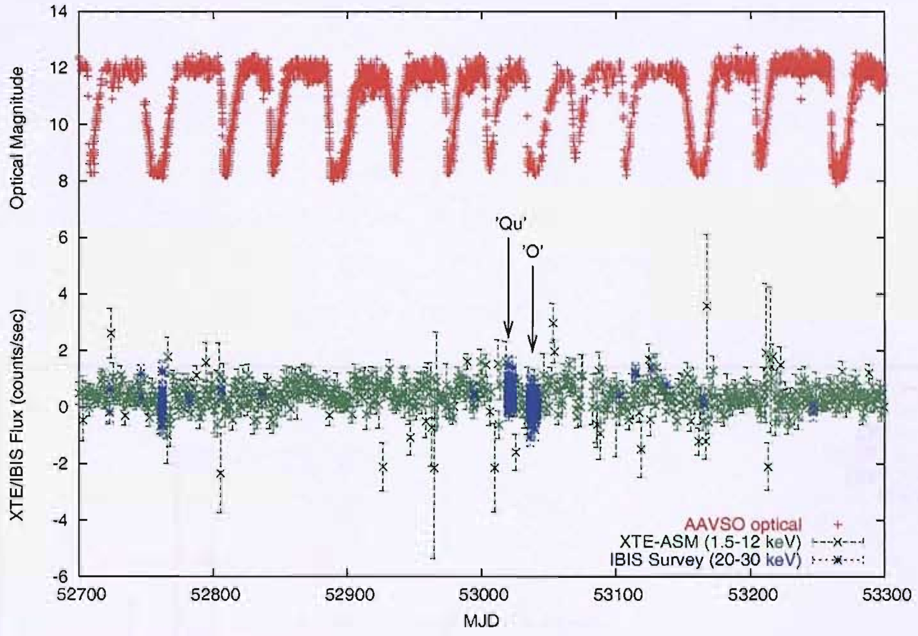

Figure 7.10: Optical, X-ray and soft gamma-ray light-curves of SS Cyg. Note the magnitude scale for the optical lightcurve.

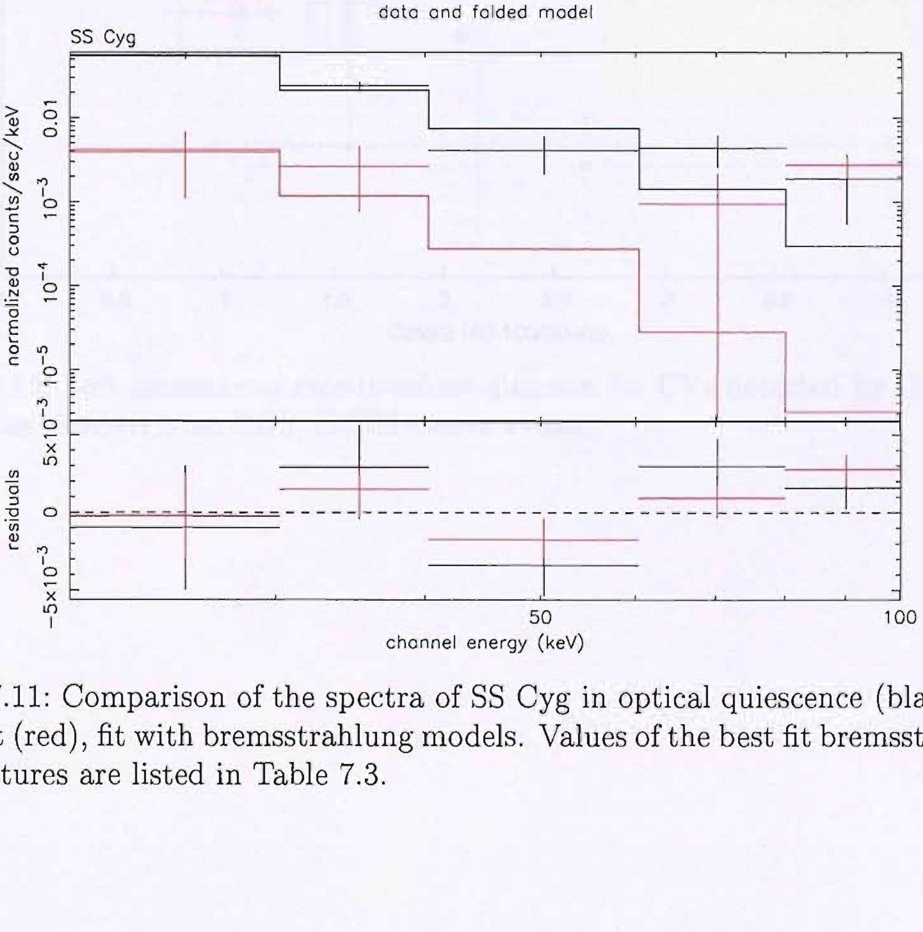

Figure 7.11: Comparison of the spectra of SS Cyg in optical quiescence (black) and outburst (red), fit with bremsstrahlung models. Values of the best fit bremsstrahlung temperatures are listed in Table 7.3.

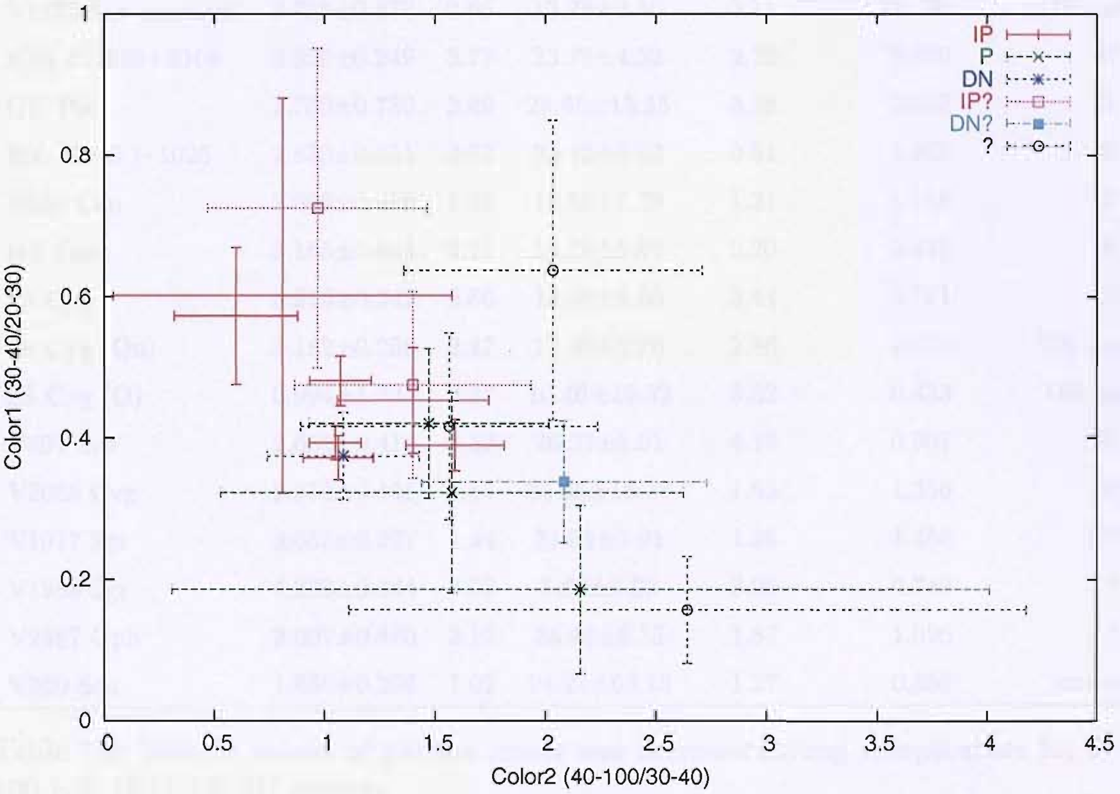

Figure 7.12: Soft gamma-ray colour-colour diagram for CVs detected by IBIS. The colours are derived from IBIS/ISGRI source counts.

	Γ	χ^2_ν	kT (keV)	χ^2_ν (3 d.o.f.)	Flux×10^{-11} (erg $s^{-1}cm^{-2}$)	Type
V709 Cas	2.842±0.119	0.45	23.32±2.18	1.91	4.476	IP
IGR J15479-4529	2.718±0.095	4.09	27.07±2.18	1.78	5.527	IP
V2400 Oph	3.129±0.112	4.47	18.63±1.39	4.98	3.268	IP
IGR J17303-0601	2.542±0.890	2.61	26.72±4.80	1.23	4.250	IP
V1223 Sgr	3.262±0.108	0.95	18.77±1.20	1.47	7.968	IP
V1223 Sgr (outburst)	3.725±0.370	0.65	13.78±2.50	0.71	26.160	IP outburst
IGR J21335+5105	2.956±0.249	3.77	23.78±4.32	2.10	3.600	IP
GK Per	2.750±0.730	3.49	28.65±15.55	3.28	2.542	IP
RX J1940.1-1025	2.830±0.351	0.23	25.42±7.02	0.51	3.365	P
V834 Cen	2.696±0.496	1.00	19.53±7.79	1.21	1.118	P
BY Cam	3.165±0.644	2.21	14.78±5.91	2.20	2.451	P
SS Cyg	3.215±0.242	2.86	13.56±8.05	3.44	2.781	DN
SS Cyg (Qu)	3.182±0.256	2.47	17.43±2.70	2.86	7.071	DN quiescence
SS Cyg (O)	0.994±1.225	3.27	10.46±15.32	3.82	0.433	DN outburst
V697 Sco	2.652±0.414	3.52	26.37±8.91	4.19	0.907	IP?
V2069 Cyg	2.370±0.441	1.54	35.66±16.77	1.65	1.350	IP?
V1017 Sgr	2.655±0.277	1.44	31.02±7.91	1.56	1.456	DN?
V1988 Sgr	4.223±0.444	4.00	5.68±1.02	3.06	0.742	?
V2487 Oph	3.007±0.470	2.19	25.48±8.55	1.87	1.026	?
V960 Sco	1.686±0.298	1.02	94.24±63.13	1.27	0.855	structure?

Table 7.3: Best fit values of photon index and bremsstrahlung temperature for 20–100 keV IBIS/ISGRI spectra.

Type	Γ	kT (keV)
IP	2.9±0.1	20.9±0.8
P	2.8±0.2	19.3±3.9
DN (SS Cyg)	3.2±0.25	17.4±2.7

Table 7.4: Weighted means of 20–100 keV spectral fits for Intermediate Polars and Polars for power law (Γ) and bremsstrahlung (kT) models compared to the DN SS Cyg during optical quiescence.

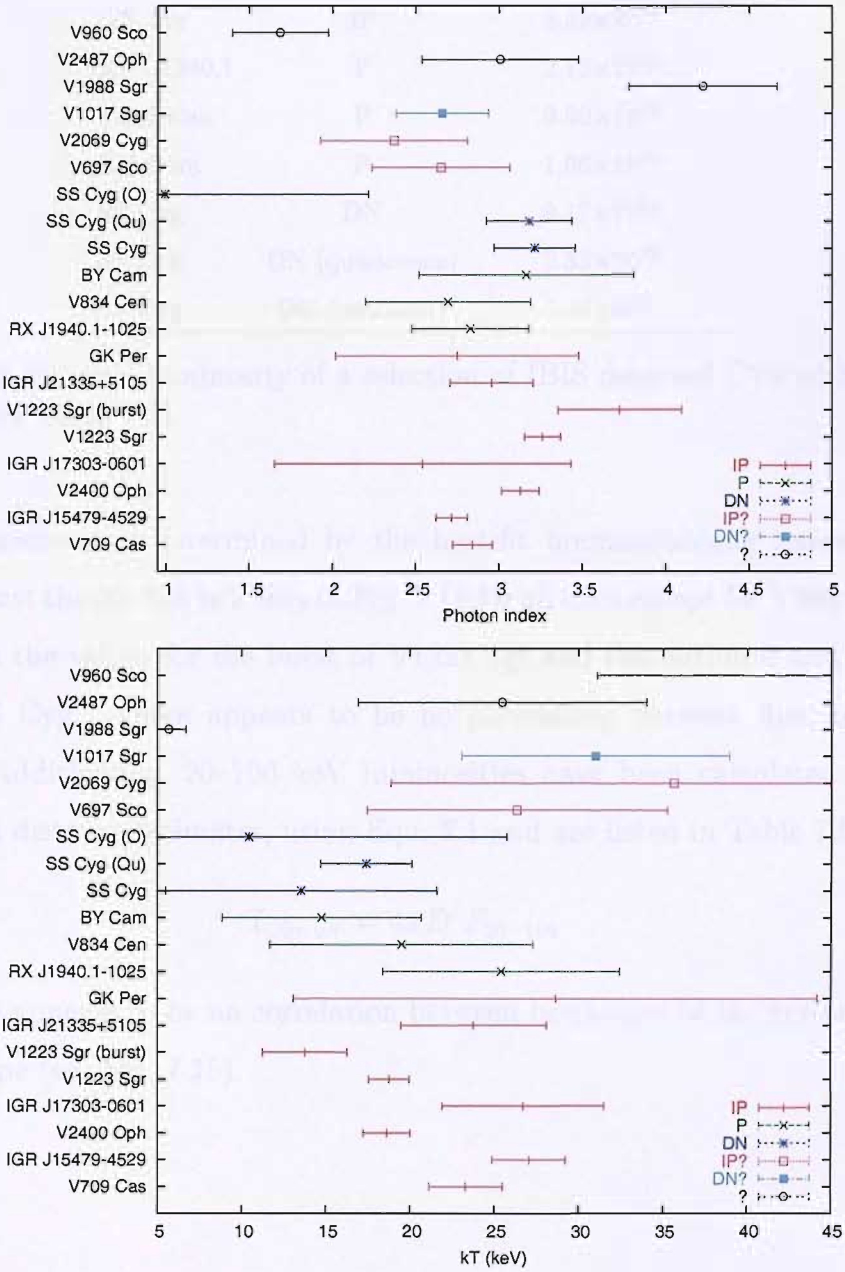

Figure 7.13: Results of the power law and bremsstrahlung fits to 20–100 keV spectra.

	type	$L_{20-100keV}$ erg s^{-1}
V1223 Sgr	IP	3.43×10^{33}
V1223 Sgr	IP (burst)	1.13×10^{34}
GK Per	IP	3.52×10^{32}
RX J1940.1	P	2.13×10^{32}
V834 Cen	P	9.90×10^{30}
BY Cam	P	1.06×10^{32}
SS Cyg	DN	9.17×10^{31}
SS Cyg	DN (quiescence)	2.33×10^{32}
SS Cyg	DN (outburst)	$1.41\text{x}10^{31}$

Table 7.5: 20–100 keV luminosity of a selection of IBIS detected CVs with distance estimates (see Table 7.2).

Source hardness as determined by the best-fit bremsstrahlung temperature is plotted against the 20–100 keV flux in Fig. 7.14 for all CVs except for V960 Sco. Also included are the values for the burst of V1223 Sgr and the outburst and quiescent states of SS Cyg. There appears to be no correlation between flux and source hardness. Additionally, 20–100 keV luminosities have been calculated for those sources with distance estimates, using Equ. 7.1 and are listed in Table 7.5.

$$L_{20-100} = 4\pi D^2 F_{20-100} \tag{7.1}$$

Again, there appears to be no correlation between brightness of the system and the spectral shape (see Fig. 7.15).

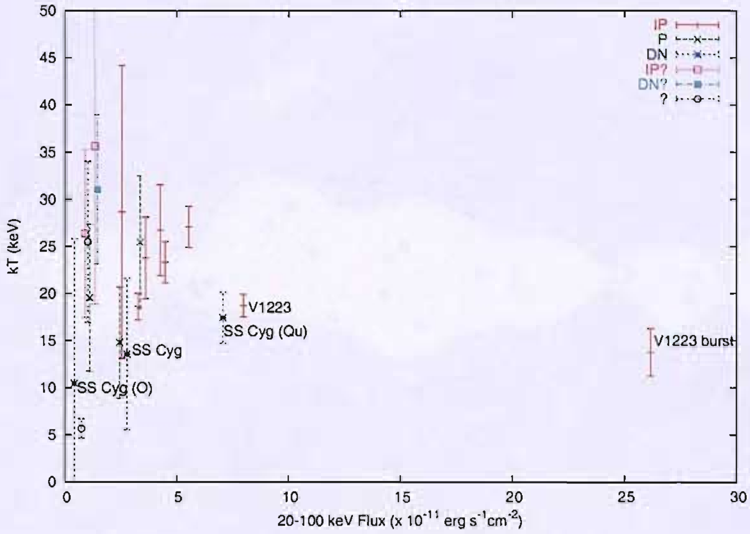

Figure 7.14: The soft gamma-ray spectral shape in terms of best-fit bremsstrahlung temperatures against 20–100 keV flux. SS Cyg is shown for average survey values together with optical outburst (O) and optical quiescence (Qu) values. Likewise for V1223 Sgr, the burst values are shown with the average survey values.

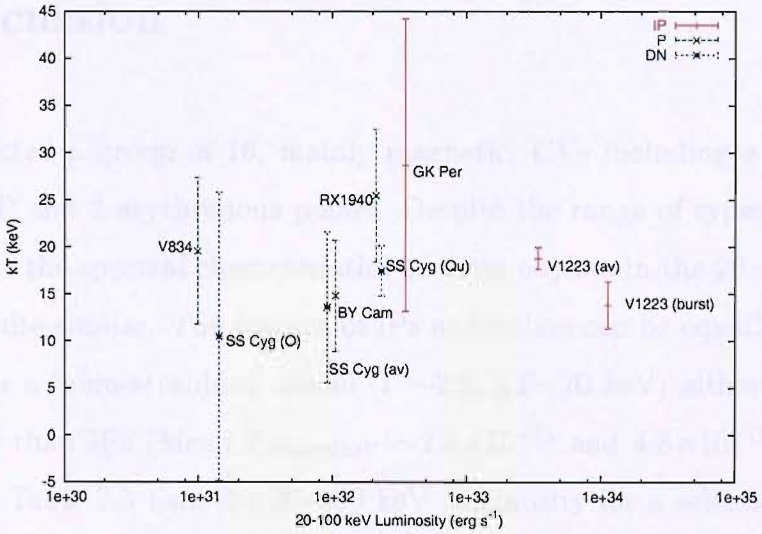

Figure 7.15: The soft gamma-ray spectral shape in terms of best-fit bremsstrahlung temperatures against 20–100 keV luminosity for sources with published distance estimates. SS Cyg is shown for average survey values together with optical outburst (O) and optical quiescence (Qu) values. Likewise for V1223 Sgr, the burst values are shown with the average survey values.

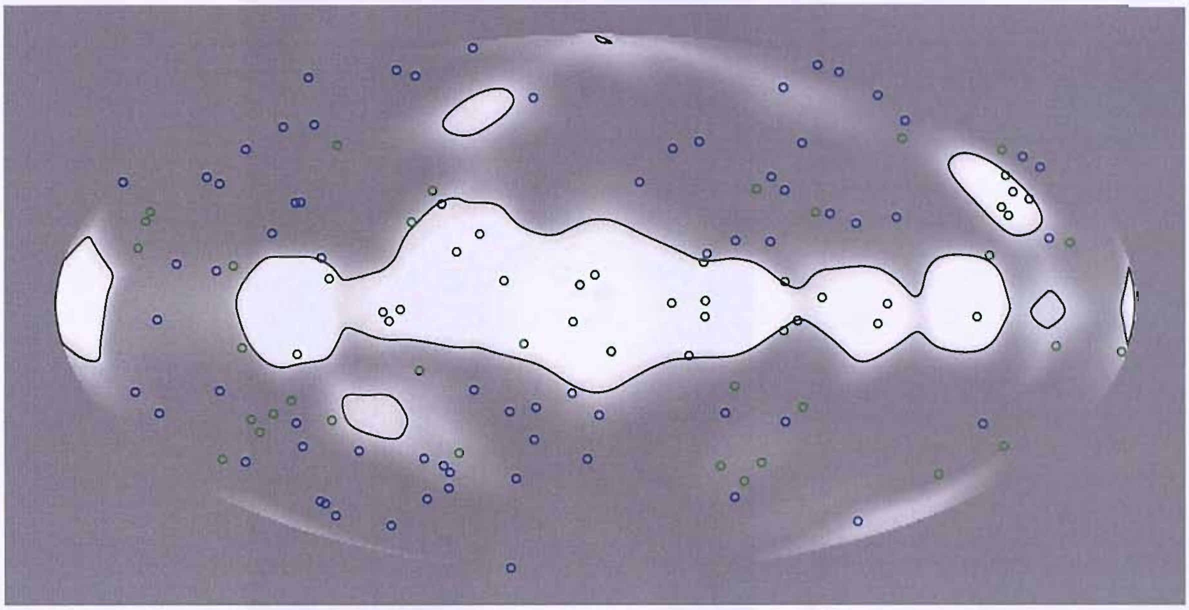

Figure 7.16: Population of magnetic CVs overlaid on the IBIS3pre exposure map. Contour represents 250 ksec of exposure. Green circles are intermediate polars and blue circles are polars.

7.4 Discussion

IBIS has detected a group of 16, mainly magnetic, CVs including a bright DN, a rare discless IP and 2 asychronous polars. Despite the range of types, this chapter has shown that the spectral characteristics of these objects in the 20–100 keV band are actually quite similar. The spectra of IPs and polars can be equally well fit with a power law or a bremsstrahlung model ($\Gamma \sim 2.8$; kT$\sim$20 keV) although the polars appear fainter than IPs (Mean $F_{20-100keV} \sim 2.3\times10^{-11}$ and 4.8×10^{-11} erg s^{-1}cm^{-2} respectively). Table 7.5 lists the 20–100 keV luminosity for a selection of sources. Unfortunately, due to the lack of distance estimates, a more detailed comparison between the relative luminosities of the sources (and sub-types) is not possible.

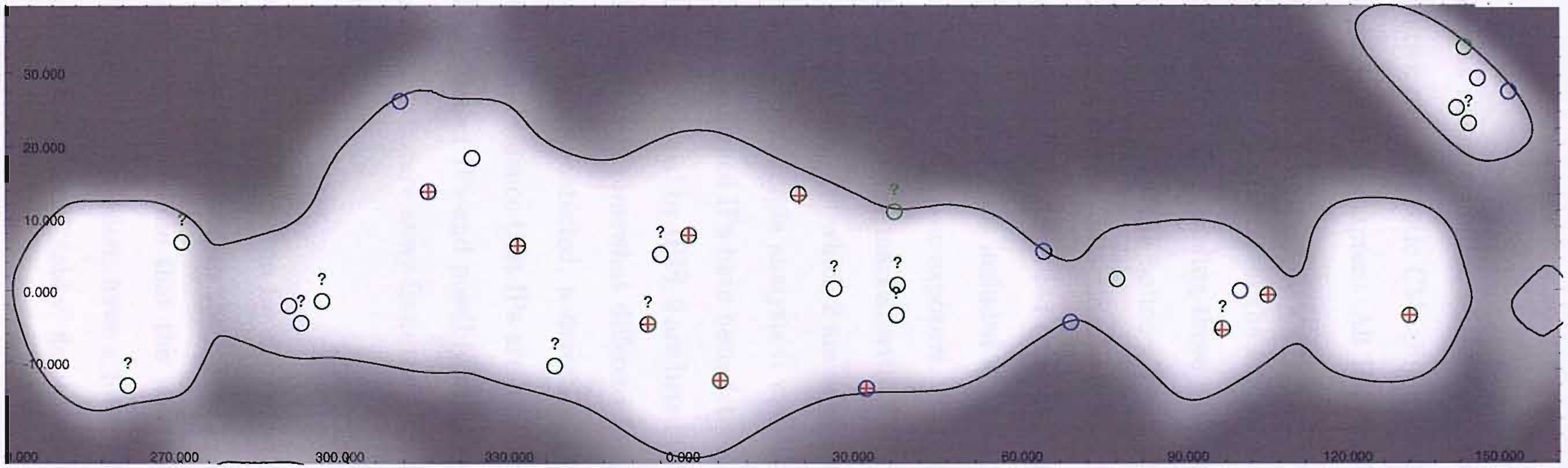

Figure 7.17: Polars (blue) and IPs (green) detected within 250 ksec of IBIS exposure (contour). IBIS detected sources (polars or IPs) are marked with a red cross.

It is useful to look at the distribution of the CVs detected by *INTEGRAL* compared to the complete set of magnetic CVs. Figure 7.16 is an exposure map of the IBIS3pre data set used in this chapter. All IBIS CVs detected above 5σ in the 20–100 keV energy range are found in regions for which the exposure is 250 ksec or above (contour marked). Overlaid on the exposure map are the locations of all currently known magnetic CVs including those with unconfirmed polar or IP classifications, as currently listed on the online CV database CVcat[1]. Figure 7.17 is a zoom in of Fig. 7.16 along the Galactic plane with the same 250 ksec exposure contour region. Sources marked with a red cross are the magnetic CVs detected by IBIS. GK Per and BY Cam are not included as their 20–100 keV significance was $<5\sigma$ and they lie in regions of lower exposure. Sources with unconfirmed IP and polar classification are additionally marked with '?'. A total of 20 IPs (of which 11 are unconfirmed) and 12 polars (of which 2 are unconfirmed) are located within the 250 ksec contour. From this simple analysis it can be seen that a significant proportion ($\sim$66%) of the confirmed IPs have been detected by IBIS in the 20–100 keV band. Of the 12 IPs not detected by IBIS, 9 are listed in the database as unconfirmed classifications. The picture is somewhat different for polars: IBIS detects only 2, leaving 8 confirmed polars undetected, a detection rate of 20%. This appears to confirm the observational evidence that IPs are harder sources than polars, as IBIS seems to preferentially detect IPs and possibly asynchronous polars. Consequently, deeper observations and exposure away from the Galactic plane should reveal more IP detections by IBIS.

As suggested in Sec. 7.1.2 the reason for the lack of hard X-ray/soft gamma-ray emission from polars may be related to the low $\dot{M}_{acc}$ and the high magnetic field. It is tempting therefore to conclude that the polars detected by IBIS, by virtue of the existence of >20 keV emission, have a lower B field and/or higher rate of accretion (therefore creating a less 'blobby' flow) than compared with other polars.

---

[1] `http://www.cvcat.net/`

Moreover, two of the three Polars observed by IBIS do not rotate sychronously. Asynchronous polars are a very rare sub-class of CVs consisting of just 4 confirmed members. The remaining 2 asynchronous polars are not currently detected by IBIS, but are located in regions of relatively low exposure. Asynchronicity in polars has been interpreted as a disruption due to a nova eruption (Schmidt et al. 1988; Mukai et al. 2003) or spin up of the WD caused by accreted angular momentum in high $\dot{M}_{acc}$ systems (e.g. *INTEGRAL*/IBIS detected polar, BY Cam, Silber et al. 1992; Schwarz et al. 2005). From the study of Doppler tomograms, Schwarz et al. have shown that the optical emission of BY Cam probably originates from an accretion curtain, as opposed to an accretion stream threaded on the magnetic field lines. They suggest that this implies that the accreted material enters the magnetosphere of the WD without being coupled to the magnetic field and predict an accretion rate a factor of two higher than expected from the orbital period of this system (~3.3 hr). According to the standard theory of CV evolution, CVs with P_{orb} <3 hr are older and have lower $\dot{M}_{trans}$ than longer P_{orb} systems as a consequence of disrupted magnetic braking (Kolb & Stehle 1996; Gänsicke 2005b). Interestingly, the least luminous of the polars detected by IBIS, V834 Cen, is a more typical phase-locked, short P_{orb} system. Apart from this source, all the other *INTEGRAL* CVs have P_{orb} >3 hr. The unusual periodicity of the asynchronous polar RX J1940.1–1025 ($P_{spin} > P_{orb}$), also observed by IBIS, has given rise to suggestions that it should be reclassified as an IP (Rana et al. 2005). The argument is supplemented by the strong hard X-ray emission detected from this source.

Gänsicke (2005b) has suggested that *INTEGRAL* might be a useful tool for detecting new IPs, complementing the (mainly Polar) *ROSAT* discoveries in the softer X-ray band. The present study confirms this. Particularly in the Galactic plane and centre, absorption inhibits the detection of these source from previous soft X-ray surveys, making IBIS an ideal resource for targeting the relatively X-ray hard IPs. Optical follow-up is, however, imperative to understand whether the wealth of unidentified sources are, in fact, CVs. *INTEGRAL* is well placed to monitor the long-term behaviour of the soft gamma-ray emission, as shown in Sec. 7.3.1. Furthermore, analysis of the 20–100 keV band emission and contemporaneous X-ray observations will expand our current knowledge of the difference between hard polars and those displaying a soft X-ray excess. The main limitation, however, for the discovery of new sources with IBIS at present is the large (∼2′–3′) error circle and lack of reliable fine timing capability for faint sources. It is possible that a portion of the ∼50 unclassified *INTEGRAL* sources are previously unidentified CVs. A follow-up campaign is underway with *XMM-Newton* and *Chandra* which will improve the location accuracy of the *INTEGRAL* sources.

Chapter 8

Conclusions

This thesis has described the techniques employed to produce the first and second IBIS/ISGRI survey catalogues and has presented subsequent analysis of some of the wealth of survey data. This work has been presented in the context of the current status of hard X-ray/soft gamma-ray astronomy outlined in Chapters 1 and 2.

Chapters 3 and 4 are concerned with the performance of the IBIS instrument. In particular, the energy resolution of the IBIS telescope in Compton mode has been determined; however, it was found that this mode could not be used as originally intended due to the in-flight background levels of the PICsIT detector. As a result, scientific results from the Compton mode have so far been very limited. Nethertheless, from a technical viewpoint, the spectral performance is in line with the pre-flight calibrations. Chapter 4 details the correction models developed to take into account the effect of the coded mask support structure which causes attenuation in photons as a function of both azimuth and off-axis angle. A satisfactory correction was developed by the author for the off-axis response which has been implemented into the *INTEGRAL* processing software (OSA) which reduces the systematic flux variations from ~40% to ~20%. Some progress was made in the azimuth response correction, but further improvements require additional calibration data scheduled for later in 2006.

The off-axis correction has a significant effect on the survey work presented in Chapter 5, since the survey data consists of observations of sources at a range of off-axis angles in the 30° IBIS field of view. The first survey catalogue is the result of the first year of Core Programme observations concentrated on the Galactic centre and plane. 123 sources were catalogued in the 20–100 keV energy range together with their fluxes in two energy bands. Data was processed using a version of the OSA software which does not include the off-axis correction, producing unreliable fluxes when mosaicing images of sources from multiple pointings at different off-axis angles. The correction algorithm was delivered with OSA v4.0 and the second catalogue data was processed with a subsequent release (OSA v.4.1). The second survey constitutes a significant improvement in exposure as well as processing techniques and lists 209 sources in the same energy band. As a result of the correction, more accurate fluxes and therefore spectra were also obtained, but due to the instrinsic variability of the sources detected, it is difficult to make a direct comparison of the average fluxes presented in the two catalogues.

The catalogued sources are dominated by X-ray binary systems (~60%) and a large set of as yet unclassified objects (~25%), thought to be additional Galactic binaries including a sub-set showing high intrinsic absorption. Analysis of the average spectral characteristics of the second survey sources is described at the end of Chapter 5. From average soft gamma-ray colour-colour diagrams (20–100 keV), average spectral differences could be found between HMXB and LMXB and also between the Atoll and Z sub-types of LMXB. As a result the analysis helps to discriminate between young and old neutron stars in binary systems, but not between old neutron stars and black holes. It was hoped that this analysis would also aid in identifying the origin of the many unclassified sources. Unfortunately, many of these sources are faint, leading to a limit on how well the colours could be constrained. Clearly this method cannot be used in isolation, but may be useful in combination with other source characteristics.

To date, *INTEGRAL* has made the first high energy detections of at least 100 new sources [1] (IGRs). Analysis of IBIS/ISGRI data of one such source, IGR J17285–2922 has been described in Chapter 6: the results suggest that the source is a LMXB possibly containing a black hole. A significant effort is underway to try and identify the many intriguing unclassified sources using other instruments such as *XMM-Newton*, *Chandra* and optical telescopes and from continued monitoring with the IBIS survey.

The final chapter is concerned with the detection of CVs by the IBIS survey. As a result of inspection of supplementary IBIS data, a total of 16 CVs have been observed. The sample mostly contains intermediate polars ($\geq$55%), but also includes polars ($\sim$20%), a dwarf nova and several systems without a confirmed CV sub-type. Spectral analysis concludes that the average 20–100 keV spectra of the magnetic CVs can be fit equally well with a power law ($\Gamma \sim 2.8$) or thermal bremsstrahlung model (kT$\sim$20 keV). It has been shown that the IBIS telescope is particularly able to detect intermediate polar systems which are a rare sub-class of magnetic CVs. Furthermore, a total of 3 polars have been detected, 2 of which are classed as asynchronous polars; highly unusual and poorly understood objects. Additional exposure will enable the soft gamma-ray emission from these systems to be investigated further and may provide important clues to the emission mechanisms in the different types of magnetic WD systems. Furthermore, it is suggested that a number of the unclassified *INTEGRAL* sources may be new CVs.

---

[1] `http://isdc.unige.ch/ rodrigue/html/igrsources.html`

Bibliography

Arnaud, K. A., Johnstone, R. M., Fabian, A. C., et al. 1987, MNRAS, 227, 241

Angelini, L. & Verbunt, F. 1989, MNRAS, 238, 697

Aschenbach, B. & Braeuninger, H. 1988, SPIE, 982, 10

Atteia, J.-L., Boer, M., Hurley, K., et al. 1987, ApJ, 320, 105

Augello, G., Iaria, R., Robba, N. R., et al. 2003, ApJ, 596, 63

Bamba, A., Yokogawa, J., Ueno, M., et al. 2001, PASJ, 53, 1179

Barlow, E.J., Bird, A.J., Clark, D.J., et al. 2005, A&A, 437, L27

Barlow, E.J. 1998, MSci Thesis, University College London

Barlow, W.A. 1969, "Photoconduction in Anthracene Single Crystals", PhD Thesis, University of Manchester

Barthelmy, S. D. 2004, Proc. SPIE, 5165, 175

Bassani, L., Malizia, A., Molina, M., et al. 2005, ATel # 537

Bassani, L., Molina M., Malizia, A., et al. 2006, ApJL, 636, L65

Bazzano, A., et al. 2006, in preparation

Beardmore, A. P., Osborne, J. P. & Hellier, C. 2000, MNRAS, 315, 307

Bélanger, G., Goldwurm, A., Goldoni, P., et al. 2004, ApJ, 601, L163

Bélanger, G., Goldwurm, A., Renaud, M., et al. 2005, ApJ, in press

Belloni, T. 2004, in "Interacting Binaries: Accretion, Evolution and Outcomes", eds. L. A. Antonelli, et al.

Bertin, E. & Arnouts, S. 1996, A&AS, 117, 393

Bird, A. J., Barlow, E. J., Bassani, L. et al. 2004, ApJL, 607, L33

Bird, A. J., Barlow, E. J., Bassani, L. et al. 2006, ApJ, 636, 765

Bildsten L. 1995, ApJ, 438, 852

Bonnet-Bidaud, J. M., Mouchet, M. & Motch, C. 1982, A&A, 112, 355

Bonnet-Bidaud, J. M., Mouchet, M., de Martino, D, et al. 2001, A&A, 374, 1003

Bonnet-Bidaud, J. M., Mouchet, M., de Martino, D, et al. 2005, A&A, 445, 1037

Brandt, S., Lund, N. & Rao, A. R. 1990, AdSpR, 10, 239

Buckley, D. A. H., Sekiguchi, K., Motch, C., et al. 1995, MNRAS, 275, 1028

Cadolle Bel, M., Rodriguez, J., Sizum, P. et al. 2004, A&A, 426, 657-667

Chanmugam, G., Ray, A. & Singh, K. P. 1991, ApJ, 375, 600

Charles, P.A. & Seward, F.D. 1995, Exploring the X-ray Universe, Cambridge University Press

Combi, J. A., Ribo, M., Mirabel, I. F., et al. 2004, A&A, 422, 103

Córdova, F. A-D. 1995, "Cataclysmic Variable Stars", X-ray Binaries, eds Lewin, W. H. G., van Paradjis, J., van den Heuvel, E. P. J., Cambridge University Press

Costa, E., Frontera, F., Heise, J., et al. 1997, Nature, 387, 783

Courvoisier, T. J. L., Walter, R., Beckmann, V. et al. 2003, A&A, 411, L53

Cowley, A. P., Crampton, D., Hutchings, J. B., et al. 1987, ApJ, 93, 195

Cropper, M. 1990, SSrv, 54, 195

Davelaar, J., Smith, A. & Becker, R.H. 1986, ApJ, 300, 59

Del Santo, M., Bazzano, A., Zdziarski, A. A. et al. 2005, A&A, 433, 613

de Martino, D., Matt, G., Mukai, K., et al. 2001, A&A, 377, 499

de Martino, D., Matt, G., Belloni, T., et al 2004, A&A, 415, 1009

Dermer, C. D. & Gehrels, N. 1995, ApJ, 447, 103

di Cocco, G., Bazzano, A., Cocchi, M., et al. 2004, ESA SP-552: 5th INTEGRAL Workshop on the INTEGRAL Universe, 459

Diehl, R., Halloin. H., Kretschmer, K., et al. 2006, Nature, 439, 45–47

Done, C., Madejski, G. M., Smith, D. A., et al. 1996, ApJ, 463, 63

Downes, R. A. & Shara, M. M. 1993, PASP, 105, 127

Downes, R. A., Webbink, R. F., Shara M. M., et al. 2001, PASP, 113, 764

Downes, R. A., Webbink, R. F., Shara, M. M., et al. 2005, VizieR Online Data Catalog, 5123, 0

Ebeling, H., Mullis, C. R. & Tully, R. B. 2002, ApJ, 580, 774

Esin, A. A., McClintock, J. E. & Narayan, R. 1997, ApJ, 489, 865

Fender, R.P. & Maccarone, T.J. 2004, to appear in Cosmic Gamma-Ray Sources, K.S. Cheng and G.E. Romero (eds.), Kluwer Academic Publishers, Dordrecht (astro-ph/0310538)

Finoguenov, A., Churazov, E., Gilfanov, M., et al. 1994, ApJ, 424, 940

Fishman, G. J. 1995, PASP, 107, 1145

Forman, W., Jones, C., Cominsky, L., et al. 1978, ApJS, 38, 357

Forot, M., et al. 2004, ESA SP-552: 5th INTEGRAL Workshop on the INTEGRAL Universe, 463

Frank, J., King, A. & Raine, D. 2002, Accretion Power in Astrophysics (3rd edition), Cambridge University Press

Friend, M. T., Martin, J. S., Connon-Smith, R. & Jones, D. H. P. 1990, MNRAS, 246, 654

Fusco-Femiano, R., dal Fiume, D., Feretti, L., et al. 1999, ApJL, 513, L21

Gänsicke, B. T., Marsh, T. R., Edge, A., et al. 2005, ATEL # 63

Gänsicke, B. T., Marsh, T. R., Edge, A., et al. 2005, MNRAS, 361, 141

Gallo, E., Fender, R. P. & Pooley, G. G. 2003, MNRAS, 344, 60

Galloway, D. K., Remillard, R., Morgan, E., et al. 2003, IAU Circ. 8081

Geckeler, R. D. & Staubert, R. 1997, A&A, 325, 1070

Gehrels, N., Chincarini, G., Giommi, P., et al. 2004, ApJ, 611, 1005

Giacconi, R., Murray, S., Gursky, H., et al. 1974, ApJS, 27, 37

Goldwurm, A., David, P., Foschini, L. et al. 2003, A&A 411, L223

Gonzalez-Riestra, R., Oosterbroek, T., Kuulkers, E. 2004, A&A, 420, 589

Gotthelf, E.V. & Vasisht G. 1998, NewA, 3, 293

Grebenev, S. A., Bird, A. J., Molkov, S. V., et al. 2005, ATEL # 457

Grimm, H.-J., Gilfanov, M. & Sunyaev, R. 2002, A&A, 391, 923

Gros, A., Goldwurm, A., Cadolle-Bel, M., et al. 2003, A&A, 411, L179

Gursky, H., Bradt, H., Doxsey, R et al. 1978, ApJ, 223, 973

Haberl, F., Motch, C., & Zickgraf, F.-J. 2002, A&A, 387, 201

Harmon, B. A., Wilson, C. A., Fishman, G. J., et al. 2004, ApJS, 154, 585

Harrison, T. E., McNamara, B. J., Szkody, P., et al. 1999, ApJL, 515, L93

Heise, J., Mewe, R., Brinkman, A. C. et al. 1978, A&A, 63, L1

Hellier, C. 1991, MNRAS, 251, 693

Hellier, C. & Buckley, D. A. H. 1993, MNRAS, 265, 766

Hellier, C., Beardmore, A.P. 2002, MNRAS, 331, 407-416

Hernanz, M. & Sala, G. 2002, Science, 298, 393

Herrero, A., Kudritzki, R. P., Gabler, R., et al. 1995, A&A, 297, 556

Hester, J. J., Mori, K., Burrows, D., et al. 2002, ApJL, 577, L49

Hill, A.B., Walter, R., Knigge, C., et al. 2005, A&A, 439, 255

Hurley, K., Sari, R., Djorgovski, S. G. 2002, "Cosmic Gamma Ray Bursts", to appear in Compact Stellar X-Ray Sources, eds. W.H.G. Lewin and M. van der Klis, Cambridge University Press (astro-ph/0211620)

Imamura, J. N., Steiman-Cameron, T. Y. & Wolff, M. T. 2000, PASP, 112, 18

in't Zand, J.J.M., Cornelisse, R., & Mendez, M. 2005, A&A, 440, 187

in't Zand, J.J.M., Jonker, P.G., Nelemans, G., et al. 2005, A&A, in press (astro-ph/0505256)

in't Zand, J.J.M., Verbunt, F., Heise, J., et al. 2004, Nuclear Physics B Proceedings Supplements, 132, 486

in't Zand, J.J.M., Verbunt, F., Kuulkers, E., et al. 2002, A&A, 389, 43 in't Zand, J.J.M. 1992, "A coded-mask imager as monitor of Galactic X-ray sources", PhD Thesis, University of Utrecht

ISDC 2005, The IBIS Analysis User Manual, ISDC/OSA-UM-IBIS v.5.0

ISDC 2004, The JEM-X Analysis User Manual, ISDC/OSA-UM-JEMX v.4.2

Ishida, M., & Fujimoto, R. 1999, Astronomische Nachrichten, 320, 352

Jager, R., Mels, W. A., Brinkman, A. C., et al. 1997, A&AS, 125, 557

Kaspi, V., Roberts, M. & Harding, A. 2004, "Isolated Neutron Stars", to appear in Compact Stellar X-Ray Sources, eds. W.H.G. Lewin and M. van der Klis, Cambridge University Press (astro-ph/0402136)

King, A. R., Ricketts, M. J. & Warwick, R. S. 1979, MNRAS, 187, 77P

Kirsch, M. G. F., Briel, U. G., Burrows, D., et al. 2005, Proc.SPIE, 5898, 22

Knight, F.K. 1982, ApJ, 260, 538

Knödlseder, J., Jean, P., Lonjou, V., et al. 2005, A&A, 441, 513

Kolb, U. & Stehle, R. 1996, MNRAS, 282, 1454

Knoll, G.F. 1989, Radiation Detection and Measurement, 2nd Ed, Wiley

Kuijpers, J. & Pringle, J. E. 1982, A&A, 114, L4

Kuiper, L., Hermsen, W., Cusumano, G., et al. 2001, A&A, 378, 918

Kuiper, L., Hermsen, W., Walter, R., & Foschini, L. 2003, A&A, 411, L31

Kuulkers, E., Norton, A., Schwope, A., & Warner, B. 2003, "X-rays frm Cataclysmic Variables", to appear in Compact Stellar X-Ray Sources, eds. W.H.G. Lewin and M. van der Klis, Cambridge University Press

Labanti, C., Di Cocco, G., Ferro, G., et al. 2003, A&A, 411, L149

Lamb, D. Q. & Masters, A. R. 1979, ApJL, 234, L117

Lamb, D. Q. 1985, ASSL Vol. 113: Cataclysmic Variables and Low-Mass X-ray Binaries, 179

Laurent, P., Paul, J., Claret, A., et al. 1994, A&A, 286, 838

Laurent P. 1998, The Onboard Compton Selection, IN-IB-Sap-RP-045

Lebrun, F., Leray, J. P., Lavocat, P. et al. 2003, A&A, 411, L141

Lebrun, F., Terrier, R., Bazzano, A, et al. 2004, Nature, 428, 293

Leo, W.R. 1992, Techniques for Nuclear and Particle Physics Experiments, Springer-Verlag

Levine, A. M., Lang, F.L., Lewin, W.H.G., et al. 1984, ApJS, 54, 581

Levine, A. M., Rappaport, S., Remillard, R., et al. 2004, ApJ, 617, 1284

Lewin, W. H. G., van Paradijs & J., Taam, R. E. 1993, SSRv, 62, 223

Liu, Q.Z., van Paradijs, J., van der Heuvel, E.P.J., et al. 2000, A&AS, 147, 25

Liu, Q.Z., van Paradijs, J., van der Heuvel, E.P.J., et al. 2001, A&A, 368, 1021

Lomb, N. R. 1976, Ap&SS, 39, 447

Lubinski, P., et al. 2005, ISDC private communication

Lum, K. S. K., Manandhar, R. P., Eikenberry, S. S., et al. 1994, IEEE Transactions on Nuclear Science, 41, 1354

Lund, N., Butz-Jorgentsen, C., Westergaard, N. J. et al. 2003, A&A, 411, L231

Lutovinov, A. & Revnivtsev, M. 2003, Astron. Lett. 29, 719

Lutovinov, A., Revnivtsev, M., Gilfanov, M. et al. 2004, A&A, 444 821L

Lutovinov, A., Rodriguez, J., Revnivtsev, M., et al. 2005, A&A, 433, 41

Lutovinov, A., Revnivtsev, M., Molkov, S., et al. 2005, A&A, 430, 997

Maccarone, T. J. 2005, MNRAS, 360, L68

Malizia, A., Bassani, L., Di Cocco, G., et al. 2004, ATel # 227

Malizia, A., Bassani, L., Stephen, J. B., et al. 2005, ApJL, 630, L157

Marcinkowski, R., Denis, M., Bulik, T., et al. 2004, INTEGRAL observation of GRB 030406 in the Compton mode, eConf C041213, 2201

Markwardt, C. B., Smith, E., & Swank, J. H. 2003, IAU Circ. 8080

Markwardt, C. B & Swank J. H. 2003, ATel # 156

Markwardt, C. B & Swank J. H. 2003, ATel # 133

Masetti, N., Palazzi, E., Bassani, L., et al. 2004, A&A, 426, 41

Masetti, N., Dal Fiume, D., Amati, L., et al. 2004, A&A, 423, 311

Masetti, N., Bassani, L., Bird, A. J., et al. 2005, Atel # 528

Mas-Hesse, J.M., Giménez, A., Culhane, J.L., et al. 2003, A&A 411, 261

McClintock, J. E. & Remillard, R. A. 2004, "Black Hole X-ray Binaries", to appear in Compact Stellar X-Ray Sources, eds. W.H.G. Lewin and M. van der Klis, Cambridge University Press (astro-ph/0306213)

McGowan, K. E., Priedhorsky, W. C., & Trudolyubov, S. P. 2004, ApJ, 601, 1100

Mirabel, I. F. & Rodriguez, L. F. 1994, Nature, 371, 46

Mirabel, I. F., Rodriguez, L. F., Cordier, B., et al. 1992, Nature, 358, 215

Mirabel, I. F. & Rodriguez, L. F. 1994, Nature, 371,46

Molina, M., Bassani, L., Malizia, A., et al. 2004, ATel # 263

Molina, M., Malizia, A., Bassani, L., et al. 2006, MNRAS submitted

Mukai, K., Hellier, C., Madejski, G. et al. 2003, ApJ, 597, 479

Nantalucci, L., Bird, A. J., Bazzano, A., et al. 2003, A&A, 411, L209

Nantalucci, L., Martinez-Núñez, S. 2005, INTEGRAL cross-calibration summary, private communication

Narayan, R., & Popham, R. 1993, Nature, 362, 820

Negueruela, I., Marco, A., Speziali, R., et al. 2000, IAU Circ. 7541

Negueruela, I. 2004, Contribution presented at the conference "The Many Scales of the Universe - JENAM 2004 Astrophysics Reviews", to be published by Kluwer Academic Publishers, eds. J. C. del Toro Iniesta et al. (astro-ph/0411759)

Orosz, J. A., Groot, P. J., van der Klis, M., et al. 2002, ApJ, 568, 845

Osaki, Y. 1974, PASJ , 26, 429

Parmar, A. N., Kuulkers, E., Oosterbroek, T., et al. 2003, A&A, 411, L421

Patel, S. K., Kouveliotou, C., Tennant, A., et al. 2004, ApJ, 602, 245

Patterson, J. 1994, PASP, 106, 209

Paul, J., Ballet, J., Cantin, M., et al. 1991, AdSpR, 11, 289

Press, W. H., & Rybicki, G. B. 1989, ApJ, 338, 277

Pringle, J. E., & Savonije, G. J. 1979, MNRAS, 187, 777

Psaltis, D. 2004, "Accreting Neutron Stars and Black Holes: a decade of discoveries", to appear in Compact Stellar X-Ray Sources, eds. W.H.G. Lewin and M. van der Klis, Cambridge University Press (astro-ph/0410536)

Raguzova, N. V. & Popov, S. B. 2005, Astronomical and Astrophysical Transactions Vol. 24 (astro-ph/05505275)

Rana, V. R., Singh, K. P., Barrett, P. E. & Buckley, D. A. H. 2005, ApJ, 625, 351

Remillard, R. A., Smith, D. A., Hurley, K. 2002, IAU Circ. 7880

Remillard, R. A. 2005, private communication

Revnivtsev, M. 2003, Astron. Lett., 29, 644

Revnivtsev, M., Churazov, E. M., Sazonov, S. Yu., et al. 2004, A&A, 425, 49

Revnivtsev, M., Lutovinov, A., Suleimanov, V., et al. 2004, A&A, 426, 253

Risaliti, G. & Elvis, M. 2004, "A Panchromatic View of AGN", to appear in Supermassive Black Holes in the Distant Universe, Ed. Barger, Kluwer Academic Publishers (astro-ph/0403618)

Rodriguez, L. F., Mirabel, I. F. & Marti, J. 1992, ApJL, 401, L15

Rodriguez, J., Tomsick, J. A., Foschini, L., et al. 2003, A&A, 407, 41

Rodriguez, J., Cabanac, C., Hannikainen, D. C., et al. 2005, A&A, 432, 253

Ritter, H., & Kolb, U. 1998, A&AS, 129, 83

Rupen, M. P., Brocksopp, C., Mioduszewski, A. J., et al. 2003, IAU Circ., 8054, 2

Sambruna, R. M., Parmar, A. N., Chiappeti, L., et al. 1994, ApJ, 424, 947

Scargle, J. D. 1982, ApJ, 263, 835

Schmidt, G. D. 1988, Polarized Radiation of Circumstellar Origin, 85

Schoenfelder, V., Bennett, K., Bloemen, H., et al. 1996, A&AS, 120, 13

Schwarz, R., Schwope, A. D., Staude, A. & Remillard, R. A. 2005, A&A, 444, 213

Segreto, A. 2003, private communication

Sekimoto, Y., Matsuzaki, K., Kamae, T., et al. 2000, PASJ, 52, L31

Serlemitsos, P. J., Jalota, L., Soong, Y., et al. 1995, PASJ, 47, 105

Shaw, S. E., Westmore, M. J., Hill, A. B., et al. 2004, A&A, 418, 1187

Sidoli, L., Vercellone, S., Mereghetti, S., et al. 2005, A&A, 429, 47

Silber, A., Bradt, H. V., Ishida, M., et al. 1992, ApJ, 389, 704

Skinner, G. K. & Ponman, T. J. 1994, MNRAS, 267, 518

Stephen J. B., Bassani, L., Molina, M. et al. 2005, A&A, 432, L49

Stephen J. B., Bassani, L., Malizia, A., et al. 2006, A&A, 445, 869

Strong, A. W., Diehl, R., Halloin, H., et al. 2005, A&A, 444, 495

Sturner, S. J. & Shrader, C. R. 2005, ApJ 625 923

Sugizaki, M., Mitsuda, K., Kaneda, H., et al. 2001, ApJS, 134, 77

Suleimanov, V., Revnivtsev, M., Ritter, H. 2005 A&A, 435, 191

Sunyaev, R., Churazov, E., Gilfanov, M., et al. 1991, ApJL, 383, L49

Swank, J. & Morgan, E. 2000, IAU Circ. 7531

Tanaka, Y. & Shibazaki, N. 1996, ARA&A, 34, 607

Titarchuk, L. 1994, ApJ 434, 570

Thorstensen, J. R. & Taylor, C. J. 2001, MNRAS, 326, 1235

Tomsick, J. A., Lingenfelter, R., Corbel, S., et al. 2004, ATel # 224

Torres, M. A. P., Garcia, M. R., McClintock, J. E., et al. 2004, ATel # 264

Ubertini, P., Lebrun, F., Di Cocco, G. et al. 2003, A&A, 411, L131

Ubertini, P., Bassani, L., Malizia, A, et al. 2005, ApJL, 629, L109

Urry, C.M. & Padovani, P. 1995, PASP, 107, 803

van Amerongen, S. & van Paradijs, J. 1989, A&A, 219, 195

van der Klis, M., 1995, "Rapid Aperiodic Variability in X-ray Binaries", X-ray Binaries, eds Lewin, W. H. G., van Paradjis, J., van den Heuvel, E. P. J., Cambridge University Press

van Paradijs, J., Penninx, W., Lewin, W. H. G. 1988, MNRAS, 233, 473 van Teeseling, A., Kaastra, J. S. & Heise, J. 1996, A&A, 312, 186

Vargas, M., Goldwurm, A., Denis, M., et al. 1996, A&AS, 120, 291

Vasisht, G. & Gotthelf, E. V. 1997, ApJ, 486, 129

Vedrenne, G., Roques, J. P., Shoenfelder, V. et al. 2003, A&A, 411, L63

Verbunt, F. & van den Heuvel, E.P.J. 1995, "Formation and Evolution of neutron stars and black holes in Binaries", X-ray Binaries, eds Lewin, W. H. G., van Paradjis, J., van den Heuvel, E. P. J., Cambridge University Press

Véron-Cetty, M.-P. & Véron, P. 2003, A&A, 412, 399

von Ballmoos, P., Evrard, J., Skinner, G. K., et al. 2001, ESA SP-459: Exploring the Gamma-Ray Universe, 649

Walter, R., Rodriguez, J., Foschini, L. et al. 2003, A&A, 411, L427-L432

Walter, R., Courvoisier, T. J.-L., Foschini, L., et al. 2004, Proc. 5th INTEGRAL Workshop, ESA-SP 522, 417

Walter, R. & INTEGRAL Survey Team 2004, AAS/High Energy Astrophysics Division 8

Walter, R., Bodaghee, A., Barlow, E. J. et al. 2004, ATel # 229

Warner, B. 1995, Cataclysmic Variable Stars, Cambridge University Press

Warner, B. & Woudt, P. A. 2002, PASP, 114, 1222

Watson, M. G., Rosen, S. R., O'Donoghue, D., et al. 1995, MNRAS, 273, 681

Wheatley, P. J., Mauche, C. W. & Mattei, J. A. 2003, MNRAS, 345, 49

White, N.E., Nagase, F. & Parmar, A.N., 1995, "The Properties of X-ray Binaries", X-ray Binaries, eds Lewin, W. H. G., van Paradjis, J., van den Heuvel, E. P. J., Cambridge University Press

Winkler, C., Courvoisier, T. J. L., Di Cocco, G. et al. 2003, A&A, 411, L1

Wijnands, R. & van der Klis, M. 1998, Nature, 394, 344

Wijnands, R. 2001, AdSpR, 28, 469

Woods, P., Kouveliotou, C., Finger, M. H., et al. 2002, IAU Circ. 7856

Woods, P.M. & Thompson, C. 2004, “Soft Gamma Ray Repeaters and Anomalous X-ray Pulsars: Magnetar Candidates”, to appear in Compact Stellar X-Ray Sources, eds. W.H.G. Lewin and M. van der Klis, Cambridge University Press (astro-ph/0406133)

Zhang, B. & Mészáros, P. 2004, International Journal of Modern Physics A, 19, 2385

Zombeck, M. V. 1990, Handbook of Astronomy and Astrophysics, Second Edition, Cambridge University Press

Zuckerman, B., Becklin, E. E., McLean, I. S., & Patterson, J. 1992, ApJ, 400, 665